Metal organic frameworks from unconventional metal feedstock for energy storage applications

by

Khavharendwe Melba Amukelani Rambau

A thesis submitted in partial fulfilment of the requirements for the degree of

DOCTOR OF PHILOSOPHY (Ph.D) IN PHYSICS

Faculty of Natural and Agricultural Sciences

University of Pretoria

Hatfied Pretoria

May 2021

Supervisor: **Dr. Nicholas M. Musyoka**

Co-Supervisor: **Prof. Ncholu Manyala**

Declaration

I, **Khavharendwe Melba Rambau** declare that this thesis, entitled *"**Metal organic frameworks from unconventional metal feedstock for energy storage application**"* which I hereby submit for the degree **Doctor of Philosophy (Ph.D.)** in the Department of Physics, University of Pretoria, South Africa has not previously been submitted by me for a degree at any other tertiary institution.

Signature…… Date…….

Acknowledgements

I would like to acknowledge my supervisor Dr. N. Musyoka and co-supervisor Prof. N. Manyala. If not for their vision, dedication and guidance the project will have not been possible.

I would also like to thank the Department of Science and Innovation (DSI), HySA Infrastructure and the CSIR for the financial support to make this study a success.

I also extend my gratitude to HySA Infrastructure team at the CSIR and the Carbon group at the University of Pretoria for the moral support. Special thanks to Dr Nithyadharseni Palaniyandy and Dr Delvina Japhet Tarimo for assisting me in my time of need.

Dedication

This thesis is dedicated to:

The love of my life and darling husband, Edwin Magidimisha. Thank you for being my strength when I am weak, for being my biggest cheerleader and for your unconditional love and support.

My Mother, Mrs Margret Demana. I am what I am today because of you, every victory I have is for you. None of this would have been possible if you had not believed in me.

Abstract

The study focuses on exploring ways to extract valuable metals from waste materials such as spent lithium-ion batteries (LIBs) and coal fly ash (CFA) and thus converting them into Metal-organic frameworks (MOFs) suitable for energy storage applications. The rise in clean energy demand requires that there be suitable storage systems that can be utilized. LIBs have a large energy density and a drawback exhibiting low power density and short cycle stability, which supercapacitors (SCs) complement by possessing high-power density with high operational charge and discharge rates at a high number of cycles. However, the main drawback of developing energy storage materials and devices is the cost of fabrication and operation. The study aims to introduce cost-effective ways of extracting valuable metals for the use of preparing porous MOFs for use in energy storage.

In the first instance, spent LIBs were physically dismantled and discharged before subjecting the cathode material to calcination to convert the metallic structure into metal oxides. The metal oxides were mixed with either hydrochloric acid (HCl) or sulphuric acid (H_2SO_4) to convert them into a metal salt that can react with an organic linker (under a conducive environment) to obtain manganese-based MOFs. The prepared MOFs exhibited structural, morphological and textural properties similar to manganese-based MOF obtained using commercial metal salts. The Mn-MOF(Cl_2) was the MOF prepared using HCl as a salt convertor and had better structural and textural properties. It was tested as an anode material in LIBs application and its electrochemical properties were compared to manganese-based MOF obtained using commercial metal salts (Mn-MOF(Com)).

Mn-MOF(Cl_2) achieved coulombic efficiency (CE) of approximately 99% and discharge capacity of 1355 mAh g^{-1} as compared to Mn-MOF(Com) obtained using commercial metal

salt, which had a discharge capacity of 772.55 mAh g^{-1} at 100 cycles. Mn-MOF(Cl_2) had good reversibility of the redox process and remarkable electrochemical performance ascribed to its flaky sheet-like structures, allowing shorter ion diffusion path, which compliments the strain incurred through severe volume variations amid frequent intercalation/de-intercalation of lithium ions.

In the second instance, coal fly ash was leached using an optimized method to obtain an aluminium sulphate leachate solution. The solution was used as a metal feedstock with fumaric acid as an organic linker in the synthesis of aluminium-based MOF (CFA-FumMOF). The CFA-FumMOF was synthesized as a mimic of aluminium fumarate MOF (Al-FumMOF). Despite the presence of other metals in the synthesis solution, the prepared coal fly ash derived MOF (CFA-FumMOF) exhibited almost similar characteristics to Al-FumMOF synthesized using commercial chemicals. Achieving a surface area of 1236 m^2/g with respect to Al-FumMOF (1266 m^2/g).

The prepared MOFs were subjected to direct carbonization to prepare MOF derived carbons (MDCs) for use in supercapacitors. The three-electrode measurements of Al-FumMOF and novel CFA-FumMOF were successfully prepared with a specific capacity of 28.62 mAh g^{-1} and 9.88 mAh g^{-1}, respectively at a specific current of 0.5 A g^{-1}. Their respective MDCs, Al-MDC and CFA-MDC obtained a specific capacitance of 111.94 F g^{-1} and 306.59 F g^{-1}, respectively at 0.5 A g^{-1}. When assembled into an asymmetric device, Al-FumMOF//Al-MDC had a specific capacity of 5.09 mAh g^{-1} at current densities of 0.5 A g^{-1}, with coulombic efficiency of 99.10%, indicating good cyclability and capacity retention of 46.80% after 5000 cycles. CFA-FumMOF//CFA-MDC achieved a specific capacity of 4.0 mAh g^{-1} at 0.5 A g^{-1}, with a good coulombic efficiency of 98.90% and capacity retention that gradually decreased to 42.36% after 5000 cycles.

In summary, the waste-to-MOF concept has attracted attention in the academia space and scientist have recorded the use of waste materials to obtain organic linkers and metals for MOF preparation. Herein, the authors wish to introduce a new synthesis route of using spent LIBs and CFA as metal feedstock to prepare MOFs. There are no reports of using spent LIBs to prepared Mn-based MOF, which is also used as anode for LIBs application. There are also no known reports on preparing Al-based-MOFs from CFA that are also used as sacrificial templates in preparation of MOF-derived-carbons. The electrochemical performance of these materials in LIBs and SCs application is the highest compared to the commercially prepared (pristine) materials. The reported synthesis routes exhibit innovative ways of utilization of cheap waste materials. The preparation of both Mn-MOF(Cl_2) and CFA-FumMOF signifies the potential for new market creation and relatively cheap ways to mitigate climate change.

Keywords

Metal Organic Frameworks

Coal fly ash

Leachate

Aluminium-based MOF

Fumarate-MOF

Supercapacitors

Manganese-based MOF

Spent cathode

Metal oxide

Lithium-ion Battery

Table of Contents

List of Figures

List of Tables

List of equations

Chapter 1: Introduction to Thesis

1. Introduction

1.1. Background of the Study

Porous materials such as zeolites, activated carbon and coordination polymers have gained considerable attention over the years [1]. Coordination polymers known as Metal-Organic Frameworks (MOFs) are the most desirable in the research field [1]. MOFs are crystalline in nature and formed by coordination between metal ions and organic linkers [2]. The organic linker is coordinated to the metal ions through the oxygen atoms, making a metal-oxygen carbon cluster called Secondary Building Units (SBU) [3,4]. The variety of metals and organic linkers give MOFs the advantage of possessing functional tunable pore sizes. They possess BET ultrahigh surface areas of up to 10 000 m^2/g, which is ideal for application in energy storage studies [5,6]. With astounding properties, MOFs still face a limitation in upscaling and commercialization due to the high cost of production and the unavailability of environmentally friendly feedstock [7]. Researchers have embarked on substituting commercial organic linkers with those prepared from waste materials. Ting et al., prepared MOF-5 using spent terephthalic acid (H_2BDC) that was used as a precursor for the preparation of Polyethylene terephthalate (PET) in the Vietnam chemical industry [8]. The spent H_2BDC had to be re-crystallized at 300 ^oC and utilized to make MOF-5 yielding a surface area of 1424 m^2/g. Our group also researched the utilization of PET flakes as a source of H_2BDC [9]. The PET was depolymerized using ethylene glycol to synthesize of Zr-MOF. The obtained surface area was 814 m^2/g, which is comparable to Zr-MOF prepared using commercially prepared H_2BDC. There have been a few reports on the substitution of conventional metal salts as a source of metal ions using metals oxides. Qi et al., utilized various metal oxides such as ZnO and MgO and were aged with oxalic dehydrate and ground to spark reactivity that led to the formation of 2D and 3D MOFs [10].

Other metal oxides were explored by Zhao et al., preparing HKUST-1 using hydroxyl double salt (HDS), which is derived from a reaction between one divalent metal oxides with a different divalent cation [11]. The HDS was combined with a copper salt, H_2BTC in DMF and ZnO in room temperature yielding a crystalline HKUST-1 with a surface area of 1895 m^2/g within 10 s of the reaction. In this regard, there is a need for a new development of environmentally friendly feedstocks with cost-effective methods. This thesis provides a broad context of obtaining metal feedstock from waste materials such Lithium-Ion Battery (LIBs) and Coal Fly Ash (CFA). A detailed approach is given on the extraction of the metals from these wastes, the MOF synthesis procedure, MOF derived carbons (MDCs) and their energy storage applications.

1.2. Problem Statement

Coal fly ash (CFA) is a by-product of coal combustion. South Africa is heavily dependent on the combustion of coal to generate energy. Approximately 50 million tons of CFA is produced in South Africa, of which only 10% is utilized in Portland cement constituent and road construction industry, with the remainder distributed to slurry dams and landfills [12,13]. This poses an environmental threat as CFA particles leach out toxic metals during rainfall, which contaminates the soil, groundwater and vegetation. This predicament costs the government money and needs proper handling [14]. The utilization of coal as a source of energy leads to the emission of greenhouse gases, which in turn lead to global warming. This has led to a quest to find renewable and green energy generators to mitigate this problem. Scientists have focused on the development of renewable energy, looking at solar, wind, biomass and geothermal [15]. With such technological developments, this intermittent energy needs to be stored, thus there has been the development of supercapacitors (SCs), hydrogen storage systems, lead-acid batteries, and Lithium-ion batteries (LIBs) [16]. Lithium-ion batteries are the most famous and

are mainly used in household appliances, cell phones and with the demand to decarbonize the world, the utilization of electric vehicles has increased significantly. With such transition in electric vehicles and electronic development, there is an increase in the utilization of LIBs with little control of the waste batteries [15,16]. After their life cycle, spent LIBs are disposed of in landfills, which can lead to health and environmental hazards and thus crippling the economy [17]. Spent LIBS cathodes can be recycled using various processes or regenerated into new cathode material [18,19]. Despite the current mitigation plan for spent LIBs, there is still a gap in recovering valuable metals present in spent LIBs.

The above scenarios shed light on how the world has developed from the utilization of coal, which generates CFA as waste. Similarly, in the world's attempt to transition from the use of coal, there is the utilization of LIBs, which also create wastes after its life cycle. Based on these arguments, it was seen fit to conduct the study reported in this thesis, on introducing novel methods of recovering valuable metals that can easily be used to prepare MOFs for use in energy storage.

1.3. Motivation

CFA consist of melted minerals forming crystalline phases such as quartz, mullite and hematite [20]. These crystalline phases consist of dominant chemical compositions such as SiO_2, Al_2O_3 and Fe_2O_3 [20,21]. With these metals available in significant amount, CFA becomes attractive for metal extraction. Aluminium has been successfully extracted in a form of $Al(OH)_3$. This can be done by pre-desilication, calcination, dissolution and carbonation process, giving an $Al(OH)_3$ with a morphology of spherical bayerite with a particle size of above 50 µm [22]. CFA is still used to synthesize zeolites (or aluminosilicate crystalline material) by extracting SiO_2 and Al_2O_3 through the fusion process [23]. Aluminium can also be extracted through acid

leaching using inorganic acids such as H_2SO_4 and HCl, which makes it simpler to obtain and utilize for other applications [24,25]. In this study, careful attention was given to aluminium-fumarate MOFs (Al-FumMOFs). It was first commercialized by BASF and commonly known as Basolite (A520) [26]. It possesses a high surface area, which makes it an ideal candidate for various applications such as adsorption, catalysis and energy storage [27]. Utilizing coal fly ash as a source of aluminium salt for the synthesis of Al-FumMOFs could assist in curbing the CFA waste problem.

In the same instance, the most common LIBs consist of lithium (Li), nickel (Ni), manganese (Mn) and cobalt (Co). These metals can easily be recovered using hydrometallurgy and pyrometallurgy processes as metal carbonates, metal hydroxides and alloys [28,29]. Amongst the aforementioned metals, manganese is the most attractive in LIBs. Mn is abundant in nature, inexpensive to obtain, environmentally friendly and safer due to its stability [30–32]. For these reasons, the most preferred LIBs are Mn containing due to their exceptional electrochemical performance and better thermal stability complimented by the presence of Mn [33]. Although, it is one of the cheapest metals, there has not been substantial research on its recycling. Given the important role Mn plays in energy storage (LIBs), it is therefore imperative to find ways to recycle and utilize Mn in LIBs application. In this study, a distinct focus is given on Mn-based MOFs. These MOFs are known to improve the energy density and thermal stability of LIBs [34]. Obtaining such materials with exceptional qualities from spent LIBs will lead to creating new markets and innovative route to use waste material in preparing Mn-based MOFs and LIBs electrodes.

1.4. Research Questions

Based on the scenarios presented in section 1.3, the study aims to answer the following questions.

- Can CFA leachate solution be successfully utilized as a source of metal salt to mimic aluminium-fumarate MOF (Al-FumMOF)?
- Can spent LIBs cathode material be a viable source of Mn for the preparation of Mn-based MOFs?
- How do the structural and textural properties of the coal fly ash derived MOF (CFA-FumMOF) and spent LIB derived MOF (Mn-MOF (Cl_2)) be comparable to pristine Al-FumMOF and Mn-MOF(Com)?
- What are the electrochemical performance characteristics of these materials in the application of LIBs and supercapacitors?

1.5. Objectives

The study aims to synthesize porous metal-organic frameworks using unconventional metal feedstock such as coal fly ash and spent lithium-ion battery for energy storage purposes. The following are the objectives:

1. Leach CFA using sulphuric acid (H_2SO_4) to obtain aluminium sulphate ($Al_2(SO_4)_3$) as a metal salt to synthesize CFA-FumMOF.
2. Obtain MOF derived carbon (MDC) material using CFA-FumMOF as a template.

3. Utilize the obtained CFA-FumMOF as a positive electrode and its carbon derivative (CFA-MDC) as a negative electrode to prepare an asymmetric supercapacitor device.
4. Extract manganese metal from spent lithium-ion battery cathode material using inorganic acids (H_2SO_4 and HCl).
5. Do a comparative study on which metal salt (H_2SO_4 or HCl based) gives a quality Mn-based MOF.
6. Utilize the best Mn-based MOF from spent LIBs as an anode for the preparation of lithium-ion batteries.

1.6. Research Approach

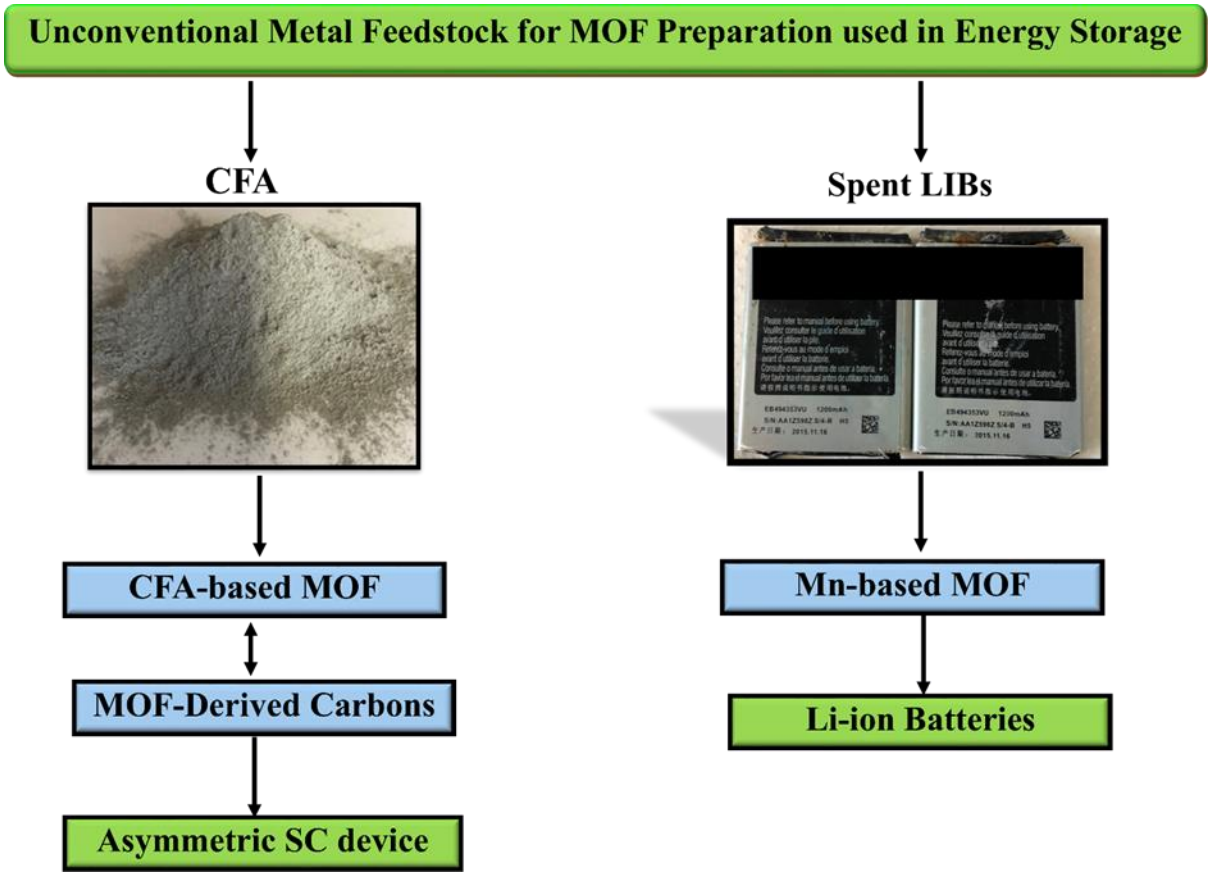

Figure 1.1: Flow chart describing the research approach.

There was literature review and experimental designs to achieve the objectives. The review then focused on how conventional MOFs are synthesized to determine the best way possible for synthesizing the MOFs using the unconventional metal feedstock. The research was broken down into two stages as represented by Figure 1.1. The first stage was to determine the best possible route of obtaining $Al_2(SO_4)_3$ from coal fly ash and synthesizing the coal fly ash derived MOF (CFA-FumMOF). The stage also involved direct carbonization of the CFA-FumMOF to obtain a high surface area carbonaceous material as a negative electrode material for the preparation of an asymmetric supercapacitor device. To determine how effective CFA-FumMOF, the pristine Al-FumMOF was also prepared under the same conditions, carbonized, and tested the electrochemical performance in SCs. The second stage involved converting the spent cathode material into a metal salt, through the process of calcination and acid precipitation. To determine in which salt form Mn is favourable, Mn was precipitated using H_2SO_4 and HCl. The precipitated salts are used as metal feedstock for the synthesis of Mn-based MOF. The best suited Mn-based MOF was used as anode material for the preparation of Li-ion batteries. For comparison purposes, Mn-MOF from commercial feedstock was also prepared and discussed.

1.7. Scope and Delimitation

The experiments were conducted on a laboratory scale and in small quantities. The coal fly ash was obtained from an external supplier. The coal combustion process study to obtain coal fly ash was not conducted due to the scope of the study. CFA was leached with H_2SO_4 based on the literature review. Aluminium sulphate ($Al_2(SO_4)_3.18H_2O$) was used as a commercial metal salt to synthesize Al-FumMOF based on literature review and the synthesis procedure was also adopted from previous studies. MOF derived carbons were prepared in conditions adapted from previous reports. The asymmetrical supercapacitor devices were prepared using fumarate-

MOFs as a positive electrode and their carbons derivatives as a negative electrode. Fumarate-MOFs were tested as anode materials in lithium-ion battery studies. However, due to their poor performance, their results were not documented. The spent LIBs were obtained from an external source and life cycle studies were not conducted due to the scope of the study. $MnCl_2$ salt was used as a commercial metal salt to synthesize Mn-MOF(Com) in comparison to the one obtained from spent LIBs (Mn-MOF(Cl_2)). Mn-based MOFs were not tested for supercapacitors device due to their low surface area and poor performance based on the previous reports.

1.8. Thesis Outline

Chapter one is an introduction to the study. It provides a broad context of the study while highlighting the problem statement, motivation, research questions and objectives of the study. The chapter also covers the scope and delimitations of the study. Chapter two provides an in-depth literature review on how CFA is currently recycled and utilized to solve industrial problems. It also describes how spent LIBs are recycled and regenerated to be utilized for the second time in the energy storage industry. It further describes the possible ways of extracting metals from both CFA and spent LIBs and how closely related these metals can be used to synthesize high valent MOFs and other types of MOFs. The chapter also covers MOFs that have been prepared using waste materials as metal feedstock and highlighting the success thereof. The chapter further introduces how various MOFs have been used as anode/cathode for LIBs and SCs and how their derived carbons play a pivotal role in electrochemical performance. Chapter 3 gives a detailed explanation of the experimental resources, set-up, methods and characterizations. Chapter four provides the obtained structural and textural results of the CFA-FumMOF in comparison to the pristine (Al-FumMOF). It then further discusses the properties of the MOF derived carbons (MDCs) from CFA-FumMOF and Al-

FumMOF. It also provides the electrochemical performance of the asymmetrical supercapacitor device of CFA-FumMOF and Al-FumMOF. It further provides the structural and textural results and discussion of the Mn-based MOF from spent LIBs as compared to the commercial obtained Mn-based MOF. It further discusses the electrochemical performance of Mn-based MOFs from spent LIBs and commercially obtained as anode material for Li-ion battery application. Chapter 5 discusses the conclusions and findings obtained from the overall research altogether with future work.

Chapter Summary

This chapter gives a brief overview of the research study, the motivation, objectives, research approach, scope and delimitations and thesis outline. This chapter fully describes what the reader should expect and the fundamentals behind the purpose of the study.

Chapter 2: Literature Review

2. Introduction

Fossil fuels remain the dominant supplier of electrical energy worldwide [35]. Combustion of fossil fuel for electricity generation has proved to be reliable and a cheap power source, which has a drawback of being the single largest global greenhouse gas producer with an average of 1000 g lifecycle CO_2 emission per kWh of electricity [36–38]. For such a stance, the world has encountered social, political and environmental strain to lower carbon emissions [39–42]. Many countries have endorsed regulations that requires industries with a high carbon footprint to purchase carbon allowances as a stance to introduce accountability. This has led many countries into signing legally binding documents such as the Kyoto and Paris agreement, which aims to reduce greenhouse gasses emission by 2060 [43,44]. This would require a significant change in energy harnessing and a transition towards renewable energy (RE).

The world energy outlook reported that for global temperature rise to be limited to 2 °C by 2100, the world needs to attain carbon-neutral energy in which RE provides 60% of energy by the end of the century and 715 million electric vehicles utilized by 2040 [45–47]. This is a clear indication that the world is making a transition towards REs. Currently, many countries have amalgamated intermittent RE in their electrical power systems having benefits of improved power quality, voltage profile, stability and reliability [48–51]. RE have minor drawbacks due to the unpredictable nature of the resources for RE, which gives a variable output with uncontrollable availability. REs are also restricted and in most cases situated at a distance from load centers [52,53]. Such REs are known as variable renewable energy sources (VRES), which are namely solar and wind [52,54]. To resolve these issue, grid-compatible energy storage systems need to be developed, which consist of high capacity, high energy density, long-life

cycle, reliability and cost-effectiveness [45,55]. Having energy storage systems enables efficient economic performances, load levelling, peak shaving, power quality improvement and reliability [55]. Energy storage systems can be categorized as mechanical, chemical, thermal, electrochemical and electrical [56–58]. Mechanical storage systems operate through the conversion of electrical energy into mechanical energy at off-peak hours via the principle of potential or kinetic energy [59,60]. At peak times the mechanical energy is converted back to electrical energy to supply demand. Thermal energy storage systems operate by storing heat or cold storage medium using various conditions such as temperature, place and power [61–63].

Chemical energy storage systems operate by breaking and forming chemical bonds between atoms and molecules during the energy release period [54,64]. Electrochemical energy storage systems operate by converting chemical energy into electrical energy [65–67]. These systems range from secondary batteries and rechargeable batteries. The electrodes within the system consist of different electrochemical potentials that undergo redox reaction, which result in the generation of external electric current during the discharge period. Supercapacitors are also classified as both electrochemical and electrical energy storage system [65,68,69]. They consist of high surface area electrodes and can achieve high capacity/capacitances and low energy densities while maintaining high power density. These energy storage systems have existed for decades and have gradually developed as the energy demand increased with the increasing population. For the purpose of this work, the author will focus on the development of electrochemical energy storage systems, specifically lithium-ion batteries (LIBs) and supercapacitors (SCs). The main drawback of developing these energy systems is the cost of fabrication and operation [55]. Therefore, the ultimate goal for the author is to develop storage materials through innovative ways of recycling and obtaining high performing electrochemical materials that are also environmentally friendly. For this sole purpose, the literature review covers the conventional recycling methods of coal fly ash and lithium-ion batteries and

exploring their possibilities as metal feedstock for the preparation of metal-organic frameworks (MOFs). The chapter also covers the utilization of MOFs for the application in lithium-ion batteries and supercapacitors.

Chapter 2: Part A

2.1. Coal fly ash formation, properties and classification

Due to an increase in energy demand in the past years, the utilization of coal has increased significantly translating to an increase in coal fly ash (CFA) [70,71]. Despite being a by-product that is detrimental to the environment, CFA has desirable traits. The physical, chemical, and mineral composition of CFA are associated with the combustion processes such as pulverized combustion and fluidized bed. Amongst the aforementioned, the pulverized combustion process (PCP) is of significance due to the quality of the CFA formed [72–74]. The PCP operates at maximum temperatures ranges of 1200-1500 °C to provide maximum efficiency that leads to the formation of CFA as depicted by Figure 2.1. The CFA formation happens in stages, at low temperatures, moisture on the coal surface evaporate and volatile materials are released. As the temperatures increases, the coal softens and continues to release the volatile components. When the temperatures reach above 600 °C, the coal undergoes thermal swell and complete devolatilization, which results in coke formation. In the last stage, the coal grains deteriorate, and the remaining coal residue fully combust. In this stage, the by-products begin to form. Distinctively, the by-products consist of 70 to 90% of CFA, and the remainder consists of bottom ash. During the final degassing stage, there is the formation of spherical particles that form part of the CFA. The CFA is evacuated with the flue gas through the electrostatic precipitators in which it is collected [75–78]. Generally, constituents of CFA obtained from PCP are unburned carbon, aluminosilicates, cenospheres, and magnetite. The

cenospheres are spherical shapes formed by rapid cooling during freefall conditions and consist of a mineral composition of mullite ($3Al_2O_32SiO_2$). The rest of the constituents form agglomerates due to high-temperature sintering reactions with the mineral composition of quartz (SiO_2), mullite ($3Al_2O_32SiO_2$) and magnetite (Fe_3O_4) [79–81]. Amongst the dominant minerals, there are oxides such as CaO, MgO, K_2O and trace elements such as Cr, Pb, Ni, Ba, Sr, V, and Zn. According to the American Society for Testing and Materials (ASTM), CFA can be classified as either Class F or Class C [82]. Class F consists of greater than 70% of the sum of SiO_2, Al_2O_3, and Fe_2O_3, with Class C consisting of a sum between 50-70% of the mentioned minerals. Class F CFA originates from the combustion of high ranking bituminous coals and anthracites, which gives the CFA pozzolanic properties associated with hardening when in contact with $Ca(OH)_2$ and water. Class C CFA is formed by the combustion of low-ranking lignite and sub-bituminous coals possessing cementitious properties associated with self-hardening in contact with water [83–85].

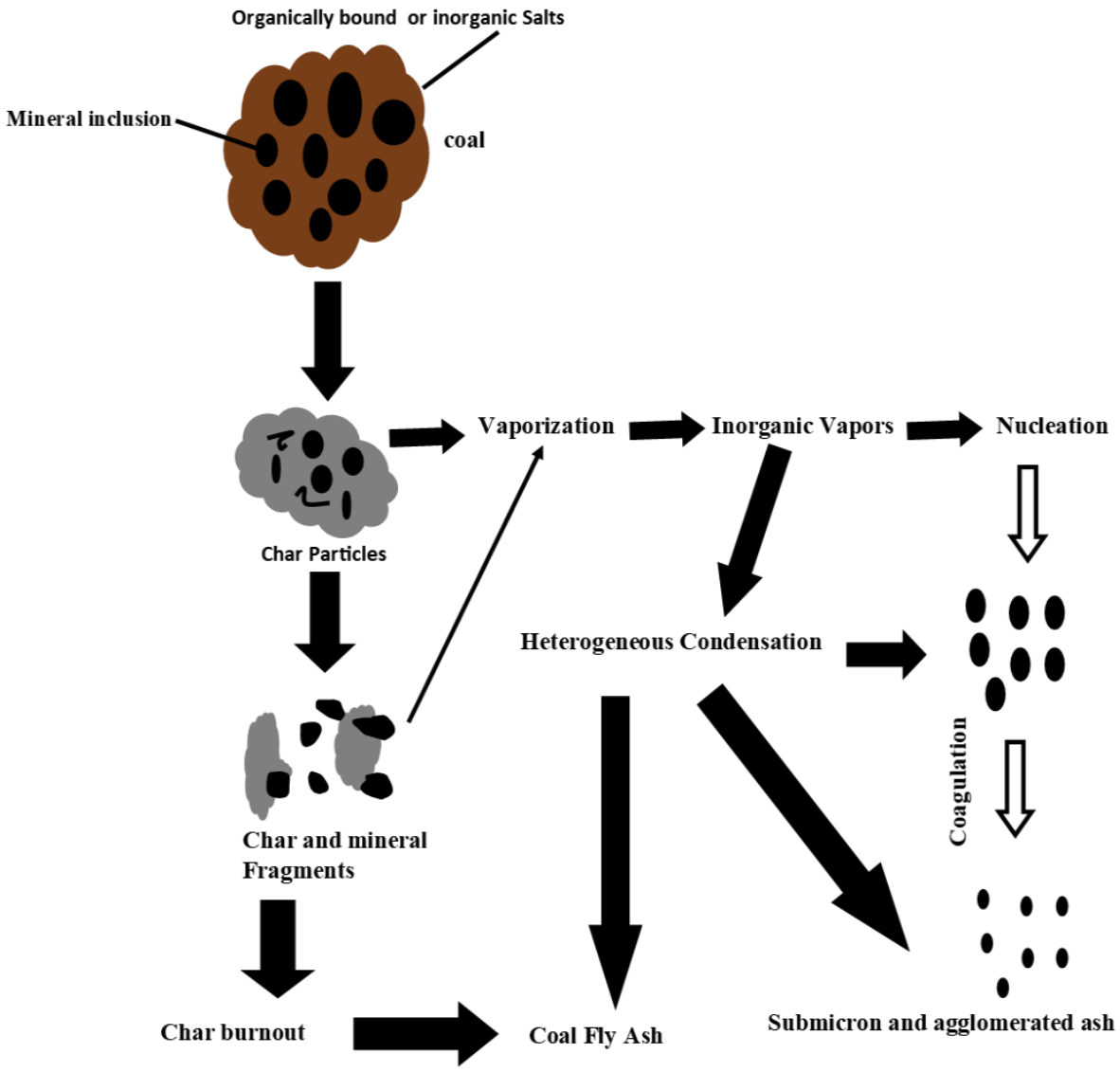

Figure 2.1: Formation of CFA during the pulverized combustion process.

2.2. Coal Fly Ash Applications

Globally, the utilization of CFA in different sectors is only a quarter with respect to its production. However, over the years the CFA market has increased and has been estimated to grow from USD 3.4 billion in 2018 to USD 4.5 Billion in 2023. The highest market is found in the Asia Pacific region with countries such as China, India, Australia, and Indonesia followed by North America. These Figures indicate a gradual transition to the recycling of CFA

for environmental conservation and the reduction of ecological imbalances [85,86]. Figure 2.2 depicts the various industries that CFA is currently being used as raw materials. These range from practical application in the construction and research sector for adsorption application.

Figure 2.2: Application of CFA in current industries.

2.2.1. Soil Amelioration

The physicochemical properties of CFA are an ideal addition to the soil to improve its physical, chemical, and biological properties. Ideally, the soil has high bulk density, poor infiltration, and soil structure, whereas CFA possesses small particles that stimulate aeration, percolation, and water retention [86,87]. Adriano et al., reported a significant increase in water holding capacity and plant available water with the CFA application rate of 560 000 Kg/ha and 1120 000 Kg/ha, respectively [53]. This is due to the presence of the cenospheres, which promotes soil microporosity and enhancing soil air space [88].

2.2.2. Construction Industry

CFA plays a significant role in the cement industry as a source of raw material or an additive. Class F CFA has pozzolanic and cementitious properties thus making it an ideal candidate for clinker replacement in Portland cement, which enhances the concrete properties [89–91]. The utilization of CFA with low carbon content, assist in water reduction during production as compared to Portland cement. CFA can reduce the CO_2 emission that could have been in the preparation of Portland cement [92–94]. In the same aspect, CFA is commonly used in road construction as a means of embankments. It is lightweight, which makes compaction and handling easy. This property enables only up to 60% pressure exerted during embankment as compared to soil. The pozzolanic properties offer reliable strength and offering very little settlement. It consists of a high angle of shearing resistance upon more compaction, increasing slope stability. When compacted, the permeability of CFA can range between 10^{-4} to 10^{-6} cm/s, which is comparable to the values of silty sand to silty clay soil and decreases with time due to hardening properties, which assist in drainage [95–97].

2.2.3. Glass and Ceramics Industry

The main components of glass and glass-ceramics are CaO, SiO_2, and Al_2O_3 and since they are the most dominant metal oxides in CFA, then it is feasible to utilize them as raw materials in this industry. The other present metal oxides assist in nucleation and crystallization while the cenospheres increase the reactivity [98,99]. Sheng et al., produced glass, utilizing CFA as raw material with an addition of 10 wt% Na_2O. The oxide acts as a glass modifier that assists in controlling the viscosity and thermal behaviour of the glass. The glass exhibited good durability

and heavy metals were solidified into the glass framework [100]. Zhang et al., did a composite of glass-ceramic, utilizing CFA consisting of metal oxides SiO_2-Al_2O_3-Fe_2O_3-CaO. A glass modifier (Na_2O) was added, and the mixture melted at 1350 °C for the formation of glass. Further annealing at 770 °C creates ceramization of the glass forming a glass-ceramic. The material exhibited good durability, good mechanical properties, and non-toxic [101]. He et al., replaced kaolinite with CFA in ceramic cordierite production. Industrial Al_2O_3 and MgO were mixed with the CFA and methylcellulose, which was pressed into disks and sintered at temperatures between 1125 – 1320 °C. Cordierite glass-ceramic exhibited low linear thermal expansion coefficient and high compressive strength and served as an ideal substitute for products such as cordierite honeycombs, cordierite kiln furniture, or heat exchangers [102].

2.2.4. CFA as Adsorbent

CFA is utilized as a low-cost adsorbent in industries such as wastewater treatment in the removal of heavy metals and organic compounds such as phenols and dyes. The aluminosilicates properties such as a high surface area with porosity make CFA an ideal candidate. CFA has the potential of removing metals such as Pb, Zn, Hg, Ni, and Cu from wastewater [103–106]. To describe the adsorption processes, scientists use the Freundlich and Langmuir models. The Freundlich model describes that the metal ion concentration on the adsorbent surface will increase, as there is an increase in the initial concentration of the metal ions, whereas Langmuir describes that adsorbent surfaces contain finite adsorption sites [107]. Sočo et al., followed Langmuir and Freundlich models to conduct a study on heavy metal (Ni and Co) removal in wastewater using CFA as adsorbent [107]. The study indicated that the adsorption of metals is dependent on the pH of the solution in which the surface charge of the adsorbent is affected altogether with the degree of ionization and speciation of the adsorbate.

The adsorption efficiency of Ni(II) and Cu(II) increase with an increase of pH level of 8.0. The maximum adsorption efficiency ranged between 98.0 and 98.4% at pH 8-10 for Cu(II) and 97.7% at pH 8 for Ni(II) with a maximum contact time of 2 hours and 1 hour, respectively. The Freundlich correlation coefficient is higher for the adsorption of Ni(II) on CFA. The model study exhibited physisorption monolayer adsorption in which the Ni(II) and Cu(II) adsorbed through particle diffusion mechanism.

2.2.5. Recovery of Rare Earth Elements (REE)

CFA consist of a considerable amount of rare earth metals that can be suitable for extraction based on the demand of REE and the large quantities of CFA denoted as waste. REE are classified as either light rare earth elements (LREE) or heavy rare earth elements (HREE) due to the electron configuration [108,109]. LREE includes metals such as La, Ce, Pr, Nd, Pm, Sa, Eu, and Gd whereas HREE includes Tb, Dy, Ho, Er, Tm, Yb, Lu, Sc, and Y. These REEs are used in the manufacturing of lasers, magnets, fluorescent materials, and most importantly in the defence industry to manufacture radar systems and satellites [110–114]. REEs can be extracted from CFA using physical or chemical extraction.

a) Physical separation

In physical extraction, REEs are extracted using techniques that segregate CFA according to particle size, magnetic fraction components, and density separations (flow-sink) [115,116]. The particle size separation operates by sieving the CFA with equipment containing various sieve sizes connected to an electromagnetic vibrator. This is based on the principle that CFA consists of different particle sizes that in turn consists of different phases with different REEs embedded within [117,118]. Magnetic fraction separation is a process of segregating materials according

to their magnetic susceptibility. The material can be classified either as paramagnetic, diamagnetic, or ferromagnetic depending on the reaction towards magnetic fields of different intensities. Paramagnetic materials are attracted to the highest intensity of the magnetic field, diamagnetic materials repel away from the magnetic field and ferromagnetic materials possess high magnetization properties in the presence of low magnetic field strength [119,120]. The float-sink technique involves segregating material particles by their density (using gravity principles) in a suitable heavy liquid [121,122].

b) Chemical separation

Chemical separation involves the use of hydrometallurgical processes such as leaching, solvent extraction, and ion exchange [123]. Leaching is a process of utilization of lixiviant to dissolve metallic values. The most common lixiviant are inorganic acids such as hydrochloric acid (HCl), nitric acid (HNO_3) and sulfuric acid (H_2SO_4) [123,124]. Kumari et al., did a comparative study on REE leaching of CFA using the three inorganic acids. The results indicated the leaching efficiencies in the order of $HCl>HNO_3>H_2SO_4$ [125]. However, despite being the least efficient, H_2SO_4 is less volatile and a cost-effective lixiviant. As a means of increasing the REE extraction rate, acid leaching can be combined with alkali compounds such as Na_2CO_3, NaCl, Na_2O_2, NaOH, KOH, and $Ca(OH)_2$ [126,127]. Tang et al., did an alkali fusion and acid leaching on CFA using Na_2CO_3 and HCl [128]. CFA was thermally fused with Na_2CO_3 in a muffle furnace. The fusion process activates the inert material in CFA by transforming quartz and mullite into soluble silicates. At optimum leaching conditions of 3M HCl, solid-liquid ratio 1:2, the total leaching efficiency of REE was 72.78%.

2.2.6. Preparation of Porous Materials from CFA

CFA has been used as feedstock to prepare porous materials such as zeolites and mesoporous silica materials.

a) Zeolites

Zeolites are porous crystalline structures characterized by a framework of linked tetrahedral aluminosilicates containing oxygen atoms bonded to cations (Si^{4+} and Al^{4+}) [129]. The arrangement leads to the formation of a 3D structure that contains cavities forming channels and cages, which are filled with H_2O molecules, or other exchangeable cations. These cavities give zeolites the special properties of adsorption of molecules and the presence of Si(IV) and Al(IV) complements the negative charge giving zeolites the property of high cation exchange capacities. Zeolites occur naturally through forces of nature such as volcanism in volcanic sediments, alkaline deserts and lake sediments. The most common natural zeolites are clinoptilolite, erionite, chabazite, mordenite and phillipsite [130,131]. However, there have been studies of synthetic zeolites using synthetic resources and also using waste products such as CFA. The richness of CFA in aluminosilicates makes it an obvious candidate in synthesizing zeolites. Generally, the synthesis of zeolites from CFA depends on the dissolution of aluminosilicates with alkaline solutions. Murayama et al., did a comparative study of hydrothermal synthesis of zeolite using alkali solutions of NaOH, Na_2CO_3 and KOH [132]. The CFA was added to the alkali solutions with concentration ranging from 1 to 4 M with a solid-liquid ratio of 1:4 at 120 °C. When observing the solution of NaOH, the crystallinity of the zeolite P increased with an increase of concentration of up to 3 M. At this point, there is a phase transition from zeolite P to HS (hydroxysolidalite). In Na_2CO_3, there is a small degree of crystallization of zeolite P and does not change with an increase in reaction time. In KOH, after 3 hours of reaction, there was no crystallization but instead, crystallization of chabazite

crystals occurred after 10 hours of reaction. These results indicated that different alkali medium, lead to different results in zeolites. Na_2CO_3 had a low degree of crystallization due to the low dissolution of CFA in the carbonate solution and low pH.

The formation of chabazite crystals was due to the presence of K^+ in KOH solution, which subsequently led to the formation of a different zeolite structure at a long reaction time. The overall study suggests the formation of zeolites is dependent on the dissolution of aluminosilicates, which in turn is the temperature (25 – 120 °C), condensation (time) and crystallization (concentration of OH^- in solutions makes a significant difference) dependent. Hollman et al., introduced a novel technique for CFA zeolite synthesis that involves a two-stage hydrothermal method [133]. Unlike direct alkali reaction, the process involved the desilication of CFA to remove unwanted Si. The stripped Si is used for zeolite synthesis by adjustment of Si/Al ratio using industrial obtained Al. Lastly, the remainder of the fly ash residue is converted into pure zeolite using the conventional method of alkali hydrothermal synthesis. There have been other methods developed such as pre-fusion step prior to hydrothermal synthesis and the development of microwave-assisted zeolite synthesis [134,135]. These profound synthesis methods allow tailor-made zeolites for applications such as water treatment, catalysis and adsorption [136–138].

b) Mesoporous Silica Materials

Mesoporous silica materials are made up of metal nodes such as Si and Al comprising of pore sizes in the range of 2-50 nm. Their synthesis process includes the use of surfactants that self-assembles into micelles at conducive environment and form a template for metal condensation, which can easily be removed through dissolution and leaving a porous structure as indicated in figure 2.3 [139]. The company Mobil Research and Development Corporation synthesized the first mesoporous silica. The procedure included the use of the liquid crystal template

mechanism of aluminosilicates gels and designated as Mobil Composition Matter (MCM-41) [139]. MCM-41 consists of a hexagonal structure with a pore diameter of 2.5 to 6 nm. Other forms of MCMs have been synthesized through the variation of the precursor and synthesis conditions. MCM-48 consists of cubic structure and MCM-50 consists of a lamella-like arrangement.

University of California, Santa Barbara synthesized an aluminosilicate material from non-ionic triblock copolymers and poly(alkylene oxide) block copolymers as a templates. The obtained materials were designated as Santa Barbara Amorphous type materials (SBA) and divided into SBA-11 (cubic structure), SBA-12 (3-d hexagonal, SBA-15 (hexagonal) and SBA -16 (cubic cage structure). The materials have slightly larger pores than MCMs (4.6 – 30 nm) and thicker silica walls [139,140]. These porous materials have huge applications in pharmaceuticals, drug delivery and biomedical purpose. CFA is an ideal candidate for the synthesis of mesoporous silica materials. Their synthesis procedure is almost identical to zeolite synthesis, with a slight difference that there is no crystallization stage rather templates are added to redirect the structure. Kumar et al., reported the use of CFA to prepare MCM-41, aluminium containing MCM-41 (Al-MCM-41) and siliceous SBA-15 type material [141]. In the study, CFA was fused with NaOH (1:1.2). The fused material was mixed with water to obtain supernatant that is used as a source of Si. For the synthesis of MCM-41, the supernatant was mixed with the surfactant cetyltrimethylammonium bromide (CTAB) and hydrothermally treated for 4 days. To obtain Al-MCM-41, a post-synthesis process was done through the addition of trimethylaluminium ($Al(CH_3)_3$). SBA-15 material was prepared using the remainder surfactant triblock polymer $(EO)_{20}(PO)_{70}(EO)_{20}$.

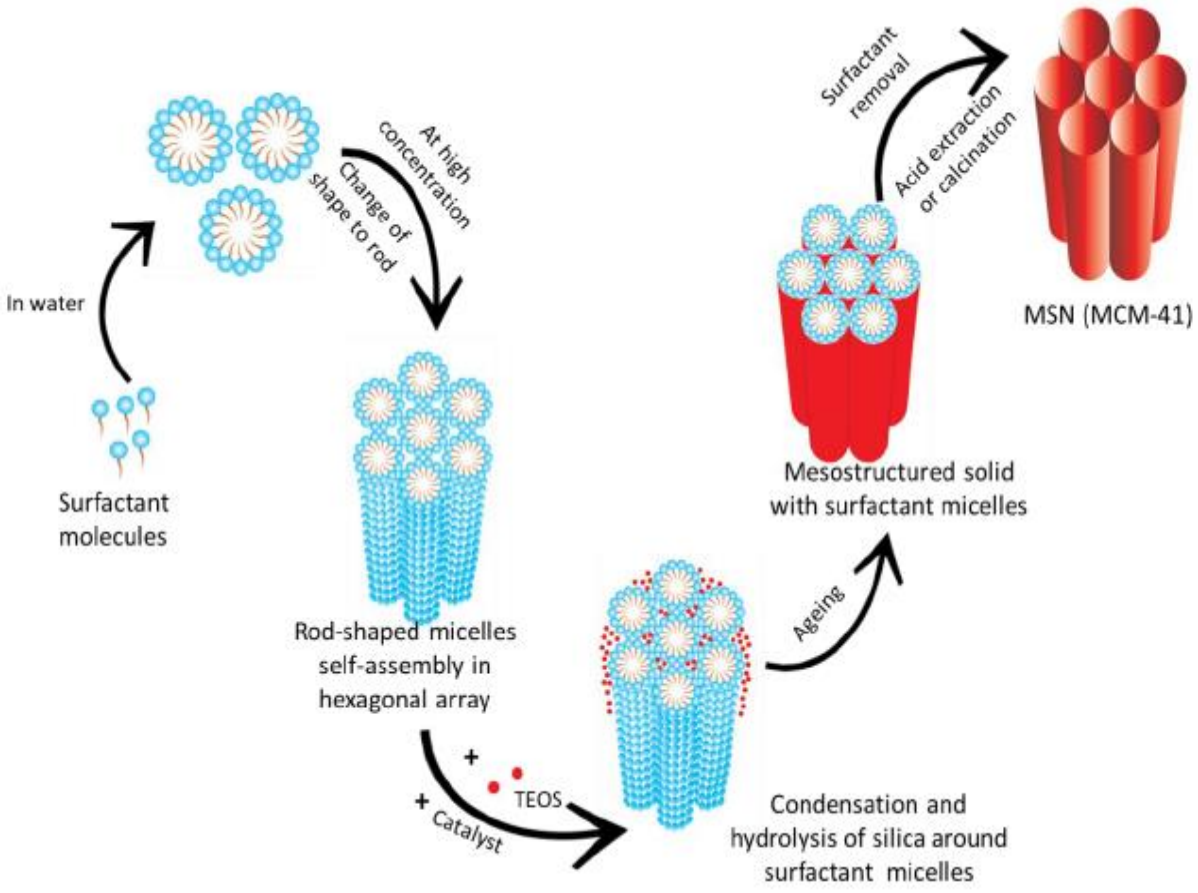

Figure 2.3: Preparation of Mesoporous material MCM-41[139]**.**

2.2.7. Recovery of Aluminium (Al) and Iron (Fe)

Apart from REE, CFA consist of other valuable metals such as Al, Fe, Ti, V, Ge, Ga, and trace metals such as Cr, Cd and Cu [25]. All these metals are valuable and can be utilized in various applications, therefore their extraction is paramount. Aluminium is one of the most dominant elements in CFA, which involve leaching and sintering for effective recovery. The leaching process includes the use of mineral acids such as H_2SO_4, HNO_3 and HCl [142]. Li et al., studied the efficient recovery of Al using H_2SO_4. A volumetric ratio of acid to CFA of 5:1 was treated at temperatures of 200 ~ 210 °C with agitation speed of 300 r/min [25]. The solid and liquor were separated obtaining the intermediate product aluminium sulphate located at the surface of

the solid. Through the process of concentrating the aluminium sulphate solution, there was formation of aluminium sulphate crystals. The crystals were sintered and transformed to γ-Al_2O_3 and subsequently to α-Al_2O_3 through the Bayer digesting process. Singh et al., recovered iron and aluminium oxides from CFA using magnetic separation process and HCl leaching [143]. In the first stage, Fe_2O_3 was recovered through a magnetic separator with a force field between 0.14 to 0.16 T. The process recovered 50.50% of Fe_2O_3 which is about 7.5% of the total CFA. The remainder of the CFA was leached with 6N HCl to obtain Fe_2O_3 and Al_2O_3. The highest leaching efficiency of aluminium and iron ions were obtained at a temperature of 107 °C, a solid-liquid ratio of 1:4 and contact time of 5 hours. To obtain the metals as oxides, the leachate was subject to ammonium hydroxide digestion. The precipitated material consisted of 6.27% Fe_2O_3 and 91.93% Al_2O_3 with 1.8% impurities containing Ti and Si.

Sangita et al., did a comparative study on leaching CFA with the inorganic acids HCl, HNO_3 and H_2SO_4 [144]. The study indicated that in HCl, aluminium and iron extraction increases from 3.71 to 5.78% with an increase in concentration from 2 to 11.3 *N*. In HNO_3, aluminium increased from 2.78 to 4.37% with a considerable amount of iron from 12.57% to 54.99% with an increase in concentration from 2 to 14 *N*. The sulphuric acid study indicated a steady increase in aluminium extraction from 4.08 to 41.71%, with an increase in iron from 42.7% for 91.67% with an increase in concentration from 4 to 41.1 *N*. There were traces of other metals such as Ca, Mg, Na, K and Ti due to the increase in hydronium ion concentration. The overall study suggested that, H_2SO_4 is a better leachate with a maximum efficiency of 68.68% of aluminium at solid ratio of 1:3. On the other hand, sintering process involves the treatment of CFA with sintering agents such as lime (CaO) at high temperatures to form soluble alumina [145]. Alumina is separated by leaching the sinter while treating the sinter prepares a solution with high alumina quantity. Padilla et al., did a study using CFA and sintering it with CaO at temperatures above 1100 °C to form calcium aluminate [146]. The aluminate was dissolved in

extractants such as Na_2CO_3 and NaOH retaining calcium silicate as a solid residue. The leachate solution consisted of rich alumina ions and was subsequently precipitated as $Al(OH)_3$ through CO_2 contact. Other authors have reported the combination of leaching and sintering in the extraction of aluminium [147]. By sintering the CFA before leaching, the mullite crystalline phase disintegrates liberating Al_2O_3 to be available for leaching. Shemi et al., did a leach-sinter-leach technique using H_2SO_4 for leaching and CaO for sintering [148]. In the first stage, the CFA was first leached giving an optimum aluminium extraction of 24.8%. The remainder of the residue was sintered with CaO, which subsequently transformed the mullite into leachable mineral. The second stage successfully leached the sintered material giving the overall aluminium extraction of 88.2%.

2.3. Extracted Metals from CFA as possible Metal feedstock for MOFs

With all the possible ways of leaching out aluminium from CFA, the extracted metals from CFA can be a possible substitute of conventional metal source for the synthesis of MOFs. Generally, MOFs are self-assembling porous materials constructed with metal clusters linked by organic ligands as depicted in Figure 2.4 [4]. This coordination result in permanent porosity, tunable pore sizes and high surface area materials [149]. The most common MOFs consist of carboxylate-based ligands with high-valent metal ions such as Ti^{4+}, Zr^{4+}, Fe^{3+}, Cr^{3+} and Al^{3+} [150]. This leaves a possibility of utilizing CFA leachate containing these ions to prepare high valent MOFs.

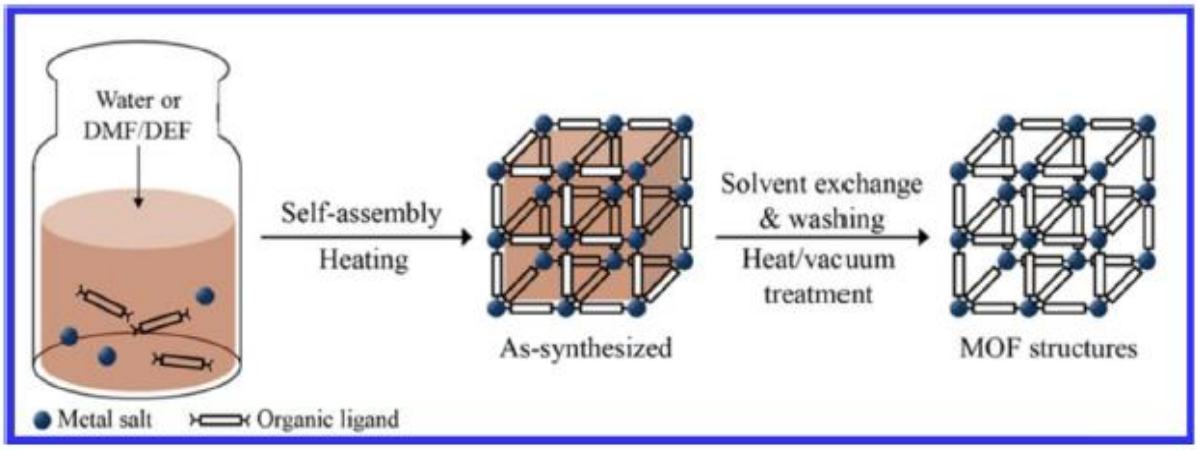

Figure 2.4: Self-assembly of metals and organic linkers to form MOFs during solvothermal synthesis [151]**.**

2.3.1. High Valent MOFs

The most common high valent MOFs are Fe, Zr, Ti and Al-based [150]. They possess a high charge and ionic radii that enables them to have stronger bonding with carboxylate groups forming rigid and robust structure. This trend follows the hard/soft acid-base principle where low-oxidation state metals tend to form an unstable complex with hard bases but forming more stable complex with high oxidation state metals. High valent MOFs tend to be more chemically and hydrothermally stable. For these reasons, they are highly desired from their counterpart mono and divalent metal ions producing the most stable MOFs [150,152]. This property puts them in a pedestal for the application in energy storage.

a) Titanium-based MOFs (Ti-MOFs)

Ti-based MOFs are the less explored high valent MOFs due to their complexity in synthesis, chemistry and coordination structural diversity [153]. Ti^{3+} is stable under reductive conditions and can easily oxidize to form Ti^{4+} when exposed to oxygen [153]. Ti^{4+} consists of strong polarizing ability and low electronegativity and therefore it is more reactive and can easily

hydrolyze in humidity [153]. These properties make it difficult for the synthesis of MOFs causing rapid uncontrollable nucleation forming irregular framework formation, which generally ends as amorphous nonporous coordination polymers [153]. However, this has led the discovery of Ti nanoclusters [153]. Serre et al., reported the first Ti-based MOF named MIL-91(Ti) [154]. The material was prepared by hydrothermal synthesis of $TiO_2.H_2O$ and *N, N*- piperazinebismethylenephosphonic acid in an HF solvent for 4 days. The framework consists of coordination of corner-sharing TiO_6 octahedra and protonated bisphosphonate groups (PO_3-CH_2-NHC_4H_{10}-NH-CH_2-PO_3) having two types of linkages. The PO_3C group act as a bridging linker that coordinate the two oxygen atoms with the metal ion [154]. Wang et al., prepared amino-functionalized Ti-based MOFs to optimize their properties. This was done through the hydrothermal synthesis route involving the treatment of $Ti(OC_3H_7)_4$ and H_2BDC-NH_2 mixture in DMF at 150 °C. The material was crystalline, with mesoporous structure and high surface area (1343.9 m^2/g) [155].

Despite all the synthesis methods present and various titanium metal precursors, there is still unpredictability of the resultant MOF due to the complex Ti-coordination chemistry. Methods such as post-synthetic cation exchange were developed to mitigate this limitation. This process involves cation exchange of Ti with known MOFs structures constructed with other metal ions to obtain specific type of Ti-based MOF. Lau et al., did a post-synthetic procedure by exchanging Zr^{4+} ion in UIO-66 with Ti^{4+} (using $TiCl_4(THF)_2$) as a metal source, to enhance CO_2 uptake [156].

For further improvement on the principle of post-synthetic procedures, Zou et al., developed a high valence metathesis (HVMO) and oxidation strategy for targeted Ti-based MOFs using PCN-333(Sc), MIL-100(Sc), MOF-74(Zn) and MOF-74(Mg) as templates [157]. This strategy relies on examining the prerequisites of the targeting metal ion and the template MOF. In the

prerequisites for metal species; i) the high valent metal ion should possess a suitable reduced state that is achieved easily; ii) To ensure successful crystallization, the lower oxidation species should undergo metal metathesis at a substantial rate; and iii) The reduced species should be stable in the exchanging environment. In looking at the MOF template; i) Metal species within the MOF template should be stable and not be reduced by the exchanging metal ion; ii) Template should possess open metal sites temporarily coordinated by solvent molecules to assist in the acceleration of metathesis rate; iii) Both metal species in template and targeting ion should possess similar coordination environment; and iv) the bond between metal and linker should possess lability for complete exchange process. The HVMO process was successful while maintaining crystallinity of the exchanged MOFs.

b) Aluminium-based MOFs (Al-MOFs)

There are various types of aluminium-based MOFs that have been developed to date [158]. Their properties as one of the highly porous structures in MOFs record and their chemical and thermal stability attract research attention for various applications. Aluminium-based MOF was pioneered by Ferey et al., from Materials Institute Lavoisiers (MIL) by creating what is known today as MIL-53[Al(OH)(BDC)] [159]. The group further developed MIL-69 [Al(OH)(O_2C—$C_{10}H_6$-CO_2).H_2O] through the hydrothermal treatment of aluminium nitrate and 2,6-naphthalenedicarboxylic acid [160]. The materials consisted of 3D framework of infinite trans chains of corner–sharing $AlO_4(OH)_2$ octahedra connected by 1,4-benzenedicarboxylate groups. These materials have exhibited the properties of the breathing effect due to the pore expansion during dehydration and as results has sparked intensive research towards the aluminium MOF family.

Senkovska et al., from the Dresden University of Technology (DUT) introduced a new Al-based MOF using 2,6- naphthalenedicarboxylate (ndc) or 4.4-biphenyldicarboxilate (bpdc) as

linkers forming DUT-(4) known as Al(OH)(ndc) and DUT-5 known as Al(OH)(bpdc) [158]. DUT-5 is isorecticular to Mil-53 and MIL-69 and by introducing N, N-dimethylformamide (DMF) as solvent instead of water, it annihilates the breathing property and create permanent porosity. Other reported Al-based MOFs are MIL-96, MIL-100, MIL-110 synthesized with BTC linker at different pH, MIL-122 with organic linker 1, 4, 5, 8-NTC, CAU-1 and MIL-101 with organic linker H_2N-BDC [158].

c) Iron–based MOFs (Fe-MOFs)

Iron-based MOFs are the most used high valent MOFs. Similar to the rest of the group, Fe-based MOFs synthesis procedure is complex. Fe-MOFs can be of poor crystallinity due to the formation of polar Fe-O bond that decelerates the coordination complexation reaction between the Fe ions and the organic linker [161]. To obtain high crystallinity MOFs, there should be control of structural regularity during the synthesis procedure. MIL-53(Fe) is the most common iron-based and consists of a low surface area, however, can be flexible in the presence of guest molecules which make it an ideal candidate for adsorption. The material consists of 3-dimensional framework made from infinite chains FeO_6 connected to carboxylate linker [161,162]. Other Fe-MOFs are MIL-101(Fe), MIL-100(Fe) and MIL-88B(Fe) which can easily be prepared by solvothermal process [163,164]. MIL-53(Fe) required H_2BDC as linker in DMF, MIL-100(Fe) required trismesic acid as linker in HF, MIL-101(Fe) required H_2BDC in DMF, and MIL-88B(Fe) required H_2BDC linker in DMF and NaOH [163,165,166]. The MOFs require $FeCl.6H_2O$ as metal source.

The main difference that brings out crystallinity in the preparation of these MOFs is the different reaction times, which are generally long and the extensive temperatures [162,167–169]. Bauer et al., prepared isorecticular Fe-MOFs in an attempt to improve pore wall through chemical modification [170]. This process was done by functionalizing organic linker

molecules (NH_2-H_2BDC) using a solvothermal process. The process was successful in producing Fe-MIL53-NH_2, Fe-MIL88B-NH_2, and Fe-MIL101-NH_2 and indicating how the reaction medium and temperature are influential in structural formation of the MOFs. However, as much as this process was successful in determining important parameters, it still entails the longevity of the synthesis procedure. The microwave synthesis procedure is an ideal for synthesis due to the reduction of temperature and time. This means there is rapid crystallization, phase selectivity and diverse morphology and easy tunable reaction parameters [165]. Ma et al., did a solvothermal synthesis of MIL-88B(Fe) using microwave-assisted heating of the reactants in DMF [163]. The process occurred at 150 °C between the times of 1 to 10 minutes. Optimum reaction conditions yielded high crystallinity of MIL-88B(Fe) and great phase purity. Dry gel conversion (DGC) method is also preferred as opposed to conventional synthesis route. Ahmed et al., was the first to report the synthesis of MIL-100(Fe) using the (DGC) [164]. The starting materials were pre-shaped dry gels (Fe/H_3BTC) without the use of any acid and salt. The high concentration of the precursors and the evaporation of water at the bottom of the reactor ensured the rapid crystallization of MIL-100(Fe). Tannert et al., combined both microwave-assisted and DGC synthesis procedure to prepare MIL-100(Fe) [166]. This was an attempt to address time, energy and environmental-related issues associated with synthesis of MOFs. The precursors are placed at the top of the reactor on a sieve with the bottom of reactor filled with small amount of solvent. This ensures that the solvent is recovered for re-use with little to no contamination. The microwave then directly heats the reactants leading to localization of heat that ensures rapid crystallization and hence addressing time and energy-related issues.

d) Zirconium-based MOFs (Zr-MOFs)

Zr-MOFs are distinctive from the rest of high valent MOFs due to feasible synthetic conditions and reproducibility [171]. Cavka et al., from the University of Oslo (UiO) reported the first Zr-MOF [172]. The material was constructed by Zr metal with H_2BDC as linker and was named UiO-66. The material possessed high thermal stability (up to 500 °C), in which only hybrid frameworks was achieved. Each SBU consist of six Zr cations coordinated to μ_3-O and μ_3-OH forming an octahedron geometry (Zr-oxo-hydroxo). Each SBU is connected with each other through the dicarboxylate linker forming 12 coordination sites. The high thermal stability of the material is associated the Zr-O strong bonds and the rearrangements of Zr_6 clusters during dihydroxylation and rehydration of μ_3-OH. Whereas the high coordination number enhances the mechanical stability and gives better resistance to shear stress [172]. Cavka et al., further demonstrated that other Zr-MOF structures can be prepared by increasing the length of the linkers without tempering with the thermal stability property of the Zr-MOF. The isoreticularly MOF prepared was UiO-67 by substitution of H_2BDc linker with a longer 4,4-biphenyl dicarboxylate (BPDC) linker and UiO-68 used terphenyl 4,4′-dicarboxylate (TPBC) as linker [173]. The point within the framework is found between benzene rings and terminal carboxyl group whereas the linker and metal ions remain connected thus thermal stability maintained. UiO-66, UiO-67 and UiO-68 have different ligand length but consist of similar network topology [174].

As impressive as the structure is, it contains ligand defects that are rare in other MOFs. Zr-O bond polarizes to form a covalent character due to the high charge density of Zr^{4+}, which in turn slows down the ligands exchange reaction between Zr metal and carboxylate group forming defects [174]. In most attempts, the formation of Zr-MOF was difficult resulting in the formation of microcrystalline compounds and the utilization of different linkers other than

H_2BDC led to poor crystalline materials. The introduction of modulated synthesis strategy led to the formation of phase-pure single crystals [174]. This procedure involves the controlling of the coordination system between the metal ion and organic linker through interception using a modulator that consist of the same chemical functionality as the linker. The modulator act as a rival against the present linker, which reduces the nucleation process allowing the growth of single crystals. These processes have greatly increased the reproducibility, crystallinity and morphology of Zr-MOFs [175].

Schaate et al., reported on benzoic acid (HBC), acetic acid and water as modulators in the synthesis of Zr-BDC, Zr-BPDC and their isorecticular materials [176]. In the formation of Zr-BDC, the increase in modulator concentration led to an increase in individual and big crystals whereas for MOFs with longer ligands (Zr-BPDC) formation of well-defined crystals required much higher concentration of modulator, which also increase reproducibility [176]. Ren et al., reported on the utilization of formic acid as modulator, which accelerated the crystalline formation of UiO-66. During the reaction, Zr undergoes hydrolysis leading to the formation of $Zr_6O_4(OH)_4(OC)_{12}$ SBU, which accelerates nuclei formation growing larger crystals [177]. Modulators can be used for preparing defect engineered MOFs by creating accessible metal site and adjusting pore properties. Wu et al., used a modulator to increase pore volume from 0.44 to 1.0 cm^3/g by obtaining uninhabited linker sites. Furthermore, there was substantial surface area increase from 1000 to 1600 m^2/g [178].

2.3.2. MOFs from unconventional metal feedstock

There are various studies that have been conducted in extracting waste metals for the use of preparation of MOFs. This study has attracted attention in attempts to have cost-effective ways of preparing MOFs [179]. These metal precursors are readily available and the presence of various metals and impurities does not interfere on the overall products. Zhan et al., reported

the first stance, in the preparation of vanadium-based MOFs (V-MOFs) using oil refinery waste (carbon black) consisting of high concentration of vanadium (V) [179]. The carbon black was first leached using NaOH and HCl. There after there was an addition of sodium dithionite before the addition of the H_2BDC and H_2NDC organic linker resulting in MOFs denoted as V-BDC-i and V-NDC-i. On another stance, cetyltrimethylammonium bromide (CTAB) was added as capping agent in order to control the morphology of obtained MOFs and the MOFs were denoted as V-BDC and V-NDC. Subsequently, CTAB addition showed improved morphology with the MOFs exhibiting crystals with nanofibers and nanorods whereas V-BDC-i and V-NDC-i MOFs exhibited irregular morphological shapes. Joshi et al., reported on the synthesis of aluminium-based MOFs using aluminium-containing products such as aluminium foil and beverage cans [180]. In the first instance, aluminium foil is used as a support for growing MOF/aluminium nanocrystals composite on a one-pot synthesis method. The produced MOFs were Mil-53 (Al) obtained using H_2BDC organic linker and MIL-96 (Al) obtained using BTC as organic linker. These MOFs had mesh-like morphology that can be applied in gas adsorption. Unsupported aluminium-based MOFs were also prepared by addition of HCl as leaching agent on the synthesis process. Beverage cans from coca cola were use used in the same one-pot synthesis method and obtained as non-supported MIL-53(Al) and MIL-96(Al) using H_2BDC and BTC as organic linker, respectively. These MOFs were highly microporous with BET surface are close to 800 m^2 g^{-1}. Song et al., used electroplating sludge (EPS) and waste PET as metal source and organic linker, respectively for preparing nickel-based MOF (Ni-MOF) nanocrystals. EPS consist of other metals such as Fe^{3+} and Cu^{2+} coexisting with Ni^{2+}, however this had little significance on the final product since their concentration is low in the leachate [181]. EPS was leached using high concentration HCl to obtain Ni^{2+} and the MOF was prepared using convention solvothermal method. The obtained MOF had 2D layered morphology corresponding well with one synthesised using commercial

products. It was also discovered that Fe^{3+} and Cu^{2+} also coordinated with BDC linkers, which resulted in change in electronic structure (band gap).

These reports on MOFs obtained from waste materials motivated the need to explore other metal sources such as coal fly ash for MOF preparation. There are reports on the use of activated CFA as composite material to stabilize chromium-based MOF (MIL-101) [306]. This is the only known record on the use CFA in MOF preparation and no record of the utilization of coal fly ash (CFA) as a source of metal nodes for MOFs synthesis, which is the gap the study aims to address. This concept is approached through the process of metal extraction using inorganic acids, namely H_2SO_4. As already indicated in section 2.2.7, H_2SO_4 has optimum leaching efficiency for aluminium and therefore aluminium was selected as a leached metal to prepare aluminium fumarate MOF. Al-fumarate MOFs possess high surface areas, minimal dead volume and high stability towards water, which can be used in broad application [26].

2.4. MOFs and their Carbon derivatives for Electrochemical storage in Supercapacitors (SCs)

The porous nature of the MOF structure is ideal for storage of electrolyte ions, specifically, their metal cations enable electrolyte and redox-active site. MOFs have been used in SCs as active materials and as precursors for MOF derived carbons (MDCs) as presented in Figure 2.5. Several studies have covered different types of MOFs and their carbon derivatives in the SCs application.

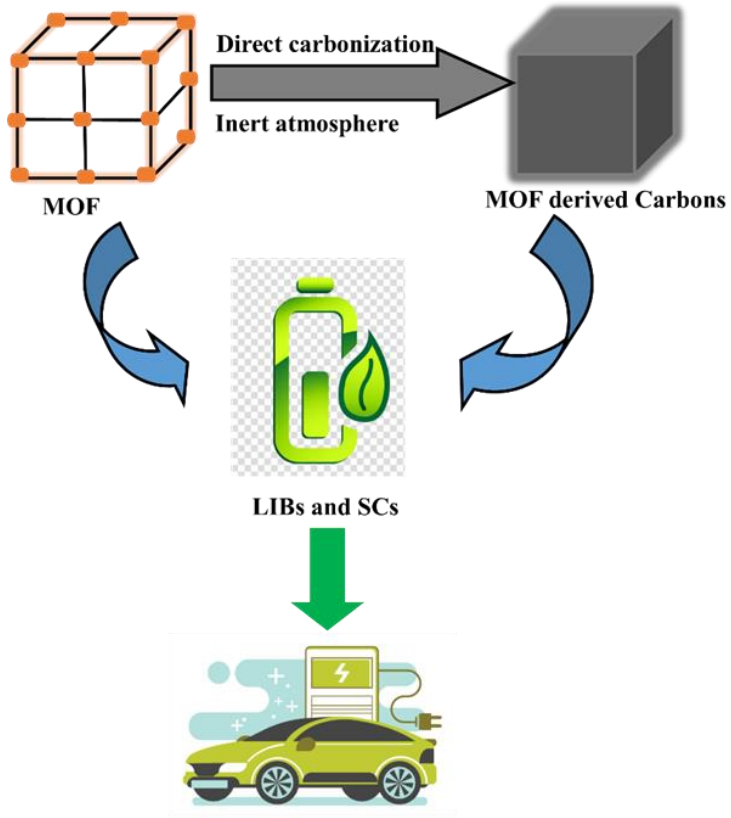

Figure 2.5: Representation of MOF transformation to porous carbons and how they can be used for LIBs and SCs.

2.3.2. General Supercapacitors (SCs) applications

Supercapacitors are devices that operate on the principle of electrochemical energy conversion. These devices possess high-power density and cyclic stability with low energy density. Lithium-ion batteries (LIBs) possess low power density and cyclic stability and high energy density and therefore, supercapacitors act as complementary devices towards LIBs [182]. A supercapacitor device consists of an electrode, electrolyte (aqueous or organic) and separator. The electrode is the most important part of the device because the entire electrochemical performance relies on its properties. The electrode should be highly conductive, possess high surface area, thermally stable and corrosion resistant. Therefore, intensive study and selection is needed for a proper electrode. Supercapacitors can be classified as either pseudocapacitors (PCs) or electrochemical double layer capacitors (EDLCs) [183].

PCs provide high electrochemical activities mainly redox reactions with high capacitance value. Most PCs materials are oxide materials and conductive polymers. EDLCs form an interface between the electrode and electrolyte where charge is stored through the electrostatic adsorption of ions. Materials that exhibit EDLC properties are mainly nanoporous materials and carbon-based materials. Before preparation of the device, a three-electrode system is utilized for optimization of the working parameters such as working potential, electrolyte and appropriate mass before cell assembly. The system consists of the active electrode, reference and counter electrode in an electrolyte [184,185]. After the determination of these variables, one can assemble a symmetric or asymmetric supercapacitor device or cell. In the assembly the positive and negative electrode are separated by a separator infused in electrolyte, and pressed by spring and spacer for proper tight closure of the device.

When a material display either pseudocapacitors (PCs) or electrochemical double layer capacitors (EDLCs) behaviour, then, a specific capacity or capacitance is calculated using a GCD curve using the equations below [185].

$$Q_s = \frac{I_d \times \Delta t}{3.6} \quad (1)$$

$$C_s = \frac{I_d \times \Delta t}{\Delta V} \quad (2)$$

Where Q_s is the specific capacity, C_s is specific capacitance, I_d as specific current (A g^{-1}), Δt is discharge time (s) and ΔV is change in potential (V).

The specific energy (E_d) is calculated using equation (3) for the device with a linear charge/discharge profile and equation (4) for non-linear charge/discharge profile [185].

$$E_d = \frac{1}{2} C_s \Delta V^2 = \frac{C_s \times \Delta V^2}{7.2} \quad (3)$$

$$E_d = \frac{1}{3.6m} \int V dt \quad (4)$$

Where *I* is the current (mA), $\int V dt$ is the area under discharge curve and m (mg) is the mass of the active electrode.

The specific power (P_d) of the device can be calculated using

$$P_d = \frac{E_d}{\Delta t} \times 3600 \quad (5)$$

An asymmetric device consists of negative and positive electrode with different materials exhibiting different capacity/capacitance behaviour. The capacity/capacitance of the material influences the working voltage, therefore it is paramount for mass balancing in order to balance the charge of each working electrode. When a positive electrode consists of non-linear charge/discharge profile and the negative electrode with linear charge/discharge, the charge balancing equation $Q_+ = Q_-$ is written as follows:

$$Q_+ = Q_- \rightarrow m_+ \times 3.6 Q_{s+} = m_- \times \Delta V_- \times C_s \rightarrow \quad (6)$$

Where, Q_+ and Q_- is stored charge in positive and negative electrode, respectively. Q_{s+} and C_{s-} are the specific capacity for the positive and negative electrode, respectively. ΔV_- is the potential window for the negative electrode and masses of the positive and negative electrode are represented as m_+ and m_-, respectively. Equation (6) can be simplified easily as

$$\frac{m_-}{m_+} = \frac{3.6 \times Q_s}{\Delta V_- \times C_{s-}} \quad (7)$$

The coulombic efficiency C_E was calculated using equation below:

$$C_E = \frac{t_d}{t_c} \times 100\% \quad (8)$$

Where t_c is the charge time and t_d the discharge time [185].

a) High valent MOFs as Electrodes for Supercapacitor

Pristine MOFs have been studied in the use of SCs. Generally, MOFs exhibit pseudocapacitive behavior due to faradic redox between active electrode and electrolyte. Their theoretical specific capacitance can reach up to 2000 F/g [186]. High valent MOFs have also been investigated due to their exceptional chemical stability. Tan et al., utilized UiO-66(Zr) as an active electrode for a three-electrode system [186]. The material showed a specific capacitance of 1144 F g^{-1} at a scan rate of 5 mV s^{-1} in a 6 M KOH electrolyte. The materials exhibited the pseudo-capacity behaviour, with smaller particles of the MOFs promoting fast redox reactions and short diffusion paths for electrons and ions. The high surface area (1047 m^2 g^{-1}) played a crucial role in accommodating large number of charges to facilitate high capacitances. The material had the capacity retention of 654 F g^{-1} over 2000 cycles. Babu et al., evaluated the electrochemical behaviour of Basolite F300 or Fe(BTC)-MOF in a three-electrode system [187]. It was observed that the electrochemical behaviour is mainly influenced by reductive dissolution rather than ion insertion. The study indicated that the material preferred platinum as working electrode in the presence of an aqueous acid with CE-type mechanism that involves the liberation of Fe(III).

MOFs are known to be insulating in nature, non-conductive, and therefore often time made into composites or hybrid materials to compensate for the insulation. Majumder et al., prepared a hybrid material consisting of Mil-53(Al) and reduced graphene oxide (rGO) to increase conductivity and obtain superior charge storage [188]. The composite materials possessed a specific capacitance of 280 F g^{-1} at 0.5 A g^{-1}. By utilizing a symmetric two-electrode system, the material exhibited energy density of 6.66 Wh kg^{-1} and power density of 3655 W kg^{-1} with

a capacitance retention of 50% after 5000 cycles. The good electrochemical performance is attributed to the hierarchical pore features of the MIL-53(Al), with exposed metal sites that act as redox active sites supported by the uniform distribution on rGO sheets. Zhang et al., hybridized carbon nanotubes (CNTs) with Mn-MOF to prepare an electrode [189]. This led to an increase in conductivity and specific capacitance of the Mn-MOF from 43.2 F g^{-1} to 203.1 F g^{-1}. The symmetrical device showed an energy density of 6.9 Wh kg^{-1} and power density 2240 W kg^{-1} with 88% capacity retention after 3000 cycles at 5 A g^{-1}.

b) MOF Derived Carbons (MDCs) as Electrode for SCs

MOFs possess porous structures that can be utilized as sacrificial templates for generation of porous carbons [150,152]. The advantages of using MOFs is the ability to tailor the composition and structure of the MOF through various linker and metals, which in turn creates MDCs with multiple pore channels and high surface area [190]. These MDCs are ideal candidates for electrode preparation due to the enhanced stability and electrochemical conductivity [190]. The MDCs synthesis can occur in two methods: i) template impregnation and ii) direct carbonization. In impregnation method, the template is impregnated with carbon containing liquid that acts as a carbon precursor. Radhakrishnan et al., reported on the impregnation of Al-based porous coordination polymer with furfuryl alcohol and carbonized under inert atmosphere [191]. The carbonization process stimulated the formation of γ-alumina nanoparticles, which was easily removed by chemical treatment (HF) to obtain microporous carbon. Direct carbonization method involves calcining MOF at high temperatures under inert conditions where the MOF structure decomposes and act as source of carbon. Most metals vaporise at those working temperature and the remainder are chemically removed.

Porous carbons have been utilized in SCs due to the EDLCs properties. MDCs have been studied for the use of SCs using various kinds of MOFs as template. Su et al., utilized Fe-MOF

for the preparation of MDCs [192]. The Fe-MOF was prepared by the reaction between 1,4,5,8-naphthalenetetracarboxylic dianhydride ligand and $FeCl_2$ under hydrothermal conditions. The material used as sacrificial template through N_2 treatment at 700 °C and chemically treated afterwards. The MDCs retained the hexagonal-nonodisk morphology of the parent material and high graphitic degree with surface area of 817 m^2/g. They exhibited good electrochemical performance with specific capacitance value of 182 F/g. The morphology of the MDCs assists in the shortening of ion transportation length and eases the ion diffusion within the mesoporous structure due to the improved electrical conductivity which results from graphitization structure. Yan et al., did a comparative study of MDC from Al-MOF against MDCs from HKUST-1 and MOF-5 [193]. Al-MOF MDC gave the highest surface area of 1103 m^2/g and specific capacitance of 232.8 F/g at current density of 100 mA g^{-1}. Sun et al., prepared MOF derived hierarchically porous carbons with a controlled pore structure using a double template method [194]. Al-MOF was prepared using the solvothermal approach and was used as the first template. The Al-MOF was then encapsulated with Cu^{2+} ions using a double solvent method. The loaded Cu^{2+} in the MOF assist as a pore forming agent by in situ transformation of Cu^{2+} into nanoparticles through carbonization. Cu^{2+} ions also influence the particle size and transformation of Al ions in the MOFs into Al_2O_3 oxide during carbonization. This then enables pore size control of the generated porous carbon after chemical treatment. These properties enhanced the electrochemical performance with specific capacitance of 185 F/g at 10 mV s^{-1}. In general, the electrochemical performance of MDCs is highly dependent on the porous structure with interconnected pores and the graphitization of the material. MOF doping by organic linker extension or metal encapsulation creates hierarchical porous structures that can thoroughly enhance the specific capacitance [194].

Chapter 2: Part B

2.4. Lithium-Ion Batteries (LIBs) Structure and Chemistry

The LIBs consist of a positive electrode (cathode), a negative electrode (anode), separator and the electrolyte. The electrolyte acts as a medium that propagates the lithium ions from the anode towards the cathode [195]. As a result, there is a flow of electrons and this process is considered as the discharging state of the battery and the opposite happens when the battery is charging. Lithium-ion batteries are constructed to provide specific and desirable properties concerning its intended application. The most important traits are energy density, power, life cycle and the most importantly the cost of production. All of these properties are selected or considered when preparing the positive electrode (cathode). The cathode material can consist of lithium and metal oxides or lithium with phosphate. The cathode materials are divided into three categories, the layered, spinel and olivine structured cathode materials [195,196]. Table 1 consists of the most common different types of LIBs with their uses throughout the world. The layered cathodes are described as LMO_2 where M=Ni, Co and Mn. Their layered structure creates a significant number of diffusion routes for the Li-ions giving the good electrochemical performance [197]. The lithium cobalt oxide $LiCoO_2$ was the first commercially available in 1991 by SONY and has been very successful. The Li and Co occupy octahedral sites stacked alternately in layers forming hexagonal symmetry. This arrangement gives them a high capacity, high nominal voltage and low self-discharge. This cathode material can be prepared easily, is chemically stable and is also insensitive to moisture. With all the desirable traits, the Co is quite expensive and has low thermal stability, which can cause the cell to explode [196–198].

Lithium nickel oxide ($LiNiO_2$) is also one of the earliest commercialized batteries and has the same layered structure as $LiCoO_2$, however with minor differences. The $LiNiO_2$ is much

cheaper, less toxic than its rival and has high energy density thus it can provide between 20-30% of reversible capacity. The $LiNiO_2$ has also limiting properties, the synthesis procedure is quite tedious since the nickel ions are in the Ni^{3+} state and need to be evenly dispersed without crossing it the Li^+ in the lithium plane. The structure of the $LiNiO_2$ can also be easily damaged over several charge-discharge cycles [196,199]. The Ni^{3+} can be easily reduced thus making thermally unstable as $LiCoO_2$ [197]. To minimize such limitations and to increase thermal stability and electrochemical performance there have been other elements that have been used as additives such as aluminium and magnesium forming the most common cells which are lithium nickel manganese cobalt (NMC) and lithium nickel cobalt aluminium oxide (NCA) [200]. These materials have an excellent electrochemical performance with capacity ranging from 140 mAh g^{-1} to 180 mAh g^{-1}. Despite their good performance, there is still a danger of thermal runaway more especially if overcharged [201]. The Lithium manganese oxide ($LiMn_2O_4$) has a cubic spinel structure and was one of the early discovered materials which have fewer advantages compared to LCO and LNO. The Mn is found at low cost, less toxic, has a theoretical capacity of 148 mAh/g and its spinel structure does not get damaged as much as LCO during cycling [196,199,201]. The framework consists of interstitial space that creates 3D channels for high-rate lithium-ion conduction giving it good electrochemical performance [202]. It is however limited with its poor life cycle and there has been research on trying to improve the life cycle, structural stability and electrochemistry. This can be done through cationic exchange and it was found that the introduction of Ni can improve the charge-discharge cycle [195,196].

Lithium iron phosphate ($LiFePO_4$) is an olivine structure which has low voltage but possesses higher capacity (170 mAh g^{-1}), less toxic and safer due to its stable structure, therefore, are highly used for practical applications in electrical vehicles (EVs) [197,203]. The cathode can withstand high temperature, oxidation and acidic environment and no thermal runaway. It has

a limitation in room temperature creating low lithium-ion diffusion giving low electrochemical performance [196]. There have been studies to improve these characteristics such as the addition of carbon on the matrix and decreasing the particle size so that the contact area with the electrolyte can be effective for Li^+ propagation.

Table 2.1: Different types of LIBs and their applications [204,205]

Types of LIBs	**Application**
$LiMn_2O_4$	Military/aerospace, Computer memory preservation, Power tools, medical devices, powertrains
$LiCoO_2$	Mobile phones, tablets, laptops, cameras, Military/aerospace
Li-S	Not widely used, Military/aerospace
$LiNiMnCoO_2$	E-bikes, medical devices, EVs, industrial
$LiFePO_4$	Stationary with high currents and endurance
$LiNiCoAlO_2$	Medical, industrial, EV (Tesla)
Li_2TiO_3	UPS, EV, solar street lighting

2.4.1. Environmental Effects of Landfill disposal of Spent LIBs

Disposing LIBs in landfills has a very detrimental effect. Most of the disposed LIBs are not completely discharged which can cause fire hazards and explosions [206]. LIBs electrolytes and solvents are known to leak which then contaminates the environment. Most commonly found solvents in LIBs are propylene carbonate, ethylene carbonate and diethyl carbonate.

These electrolytes are known to cause respiratory irritation, skin irritation, sore throat and coughing [207]. The metal oxides of the electrodes can also lead to acute poisoning which affects livers and kidneys. Prolonged exposure to manganese and cobalt-containing oxides can lead to headache, insomnia, photo contact dermatitis and others [207]. These products can affect the nervous system and in severe cases can cause renal failure and even death [207–209]. The metallic lithium can also react vigorously when exposed to water or moisture producing lithium hydroxide and hydrogen [210,211]. Other external factors can lead to the disposal of LIBs in a landfill as a hazard. These factors can be from mechanical abuse (crushing and impact), thermal abuse (heating and ignition) and self-induced. Self–induced can be seen through overcharging and over-discharge [212,213]. When the battery is overcharged, there is formation of metallic lithium that is deposited on the positive electrode. When the battery is over-discharged or under-voltage, there still remains the intercalated lithium on the negative electrodes. The copper current collector will then dissolve forming copper dendrites which will lead to internal short circuit [212]. Lithium salts such as $LiPF_6$ can decompose to form LiF and PF5 and when these products mix with decomposed solvents and the electrode surface, they form gaseous products such as CO_2, oxalate carbonates, CO, C_2H_4, CH_4 and complex fluorinated oligoethylene [214,215]. LIBs can be punctured by nails and other sharp things while in the landfills. This can cause internal short circuits, that stimulates the electric energy to be released and the temperature rises rapidly as the heat from short circuit increase which can cause explosions and fires [216].

Yokoshuma et al., conducted a nail penetration test using a nail and the aftermath of the penetration was observed using an X-ray scanner for battery cells [217]. When the battery cells were penetrated, inner short circuit happened causing the electrolyte to boil and it was observed that white gas was vigorously generated causing the cell pouch to swell. There was an increase in temperature above 100 ºC causing the tip of the nail to melt. Mao et al., also did a test on the

effects of penetration having nail and the battery samples had cathode material containing $Li(Ni_{0.5}Co_{0.2}Mn_{0.3})O_2$ and $LiMn_2O_4$ with an anode of natural graphite [218]. The group discussed the fire behaviour of the LIBs upon penetration in seven stages: i) Generation of gases upon penetration, ii) Spark generation on penetrated site, iii) Formation of jet flame, iv) Jet flame ejection from the cell, v) Vigorous ejection of jet flame, vi) Stable combustion, vii) Subsiding and extinguishing of flame.

2.4.2. Recycling Methods

The most important phase of LIBs recycling is the pre-treatment, which is catagorized under pyrometallurgical recovery process , thus separating LIBs according to different chemistries of the anode and cathodes, which include manual dismantling [219,220]. These are usually done cryogenically for safety reasons. Crushed materials can also be separated utilizing magnetism, floatation and also manually. The anode and cathode materials need to be separated from collector plates and this is done by treatment with N-methylpyrrolidone (NMP). The binder that is used to paste the cathode and anode materials on the collector plates can be removed by thermal treatment at low temperatures [28,221]. The obtained separated material which includes plastics, casing cathode and anode materials consist of valuable metals. To obtain individual metals is quite difficult hence these materials still go further treatment using hydrometallurgical process [28].

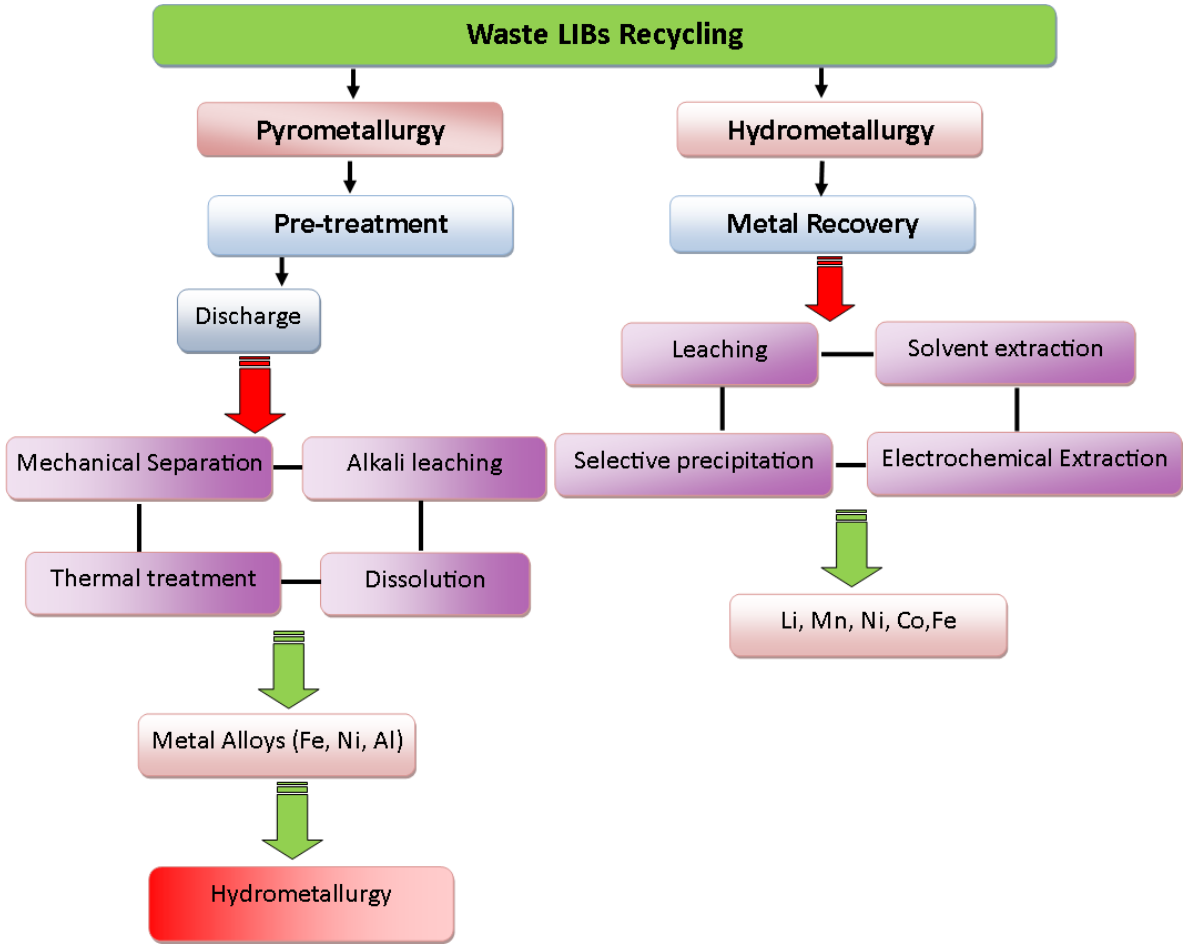

Figure 2.6: Flow chart indicating recycling stages and processes.

2.4.3. Pyrometallurgical Recycling

This recycling method uses thermal treatment or incineration of the LIBs at mild and high temperatures. The by-product is the generation of alloys using reducing agents such as coke. This process includes alkali fusion, calcination and roasting [222]. Prior to these processes, the spent LIBs are subject to pre-treatment methods such as discharge and mechanical separation. Figure 2.6 summarizes the waste LIBs recycling processes and their inter-connection.

a) Mechanical Separation

It is a pre-treatment method that involves reducing and sorting of materials according to particle size and physical properties. It is the most common method that is currently used in most industrial LIBs recycling [223–225]. Wang et al., did a study on the shredding of LIBs consisting of $LiCoO_2$, $LiFePO_4$ and $LiMn_2O_4$ using a commercial granulator after been discharged and submerged in liquid nitrogen [220]. The large particle sizes (> 6 mm) materials consisted of plastics and casing, copper foils consisted of particle sizes ranging from 2.5 - 6 mm and between 1 - 2.5 mm. The ultrafine black powder consisted of graphite and the cathode materials with small particle sizes of < 0.5 mm. The study showed that the process can increase the shredded material concentration according to the fraction of particle size. It was also observed that their concentration in specific materials varied with respect to different cathode material. This indicated that the incoming waste in LIBs need to be sorted according to their specific chemistries which would give materials of great purity thus the study proposed the labelling of LIBs to indicate the chemistries. It was observed that after the process of shredding and mechanical separation, finer products consist of graphite and cathode material while the copper and aluminium make up the coarse products with the plastic and casing as the large pieces' products.

b) Alkali Leaching

This can be done by using alkaline solutions to produce hydroxides when heated, just before acidic leaching happens [226]. This is another effective way of segregation of Al and Cu current collectors from the cathode material and graphite anode. Nayl et al., used 4 M NH_4OH to decompose the cathode materials at 60 ºC for 60 minutes with leaching efficiency of 97.8% for Al and 64.7% for Cu [227]. The other valuable metals (Mn, Co, Ni and Li) remained in the alkali paste and were effectively leached using 2 M H_2SO_4.

c) Dissolution Approach

This process is another economical form of successfully segregating the current collectors. This is done by using different solvents to dissolve binders and other additives. Song et al., utilized a low-cost solvent N, N-Dimethylformamide (DMF) for the dissolution of the binder and recovery of Al and Cu foils [228]. The materials were immersed in 150 mL of DMF and heated at 70 °C and stirred for 2 hours. The cathode material was recovered, however, there were still traces of PVDF binder indicating incomplete dissolution. The PVDF binder was only removed through the heating of cathode material at low temperatures. Ultrasonic treatment is well known for surface cleaning and researchers have utilized it to increase the peel-off efficiency. Sencanski et al., did a dissolution study on the separation of Al current collector from the cathode material [229]. The foil was immersed in NMP under ultrasonic bath for 60 minutes to dissolve the PVD binder. With this procedure, only 68% of the cathode material was recovered, however under controlled ultrasonic treatment. The procedure is considered expensive due to the utilization of the solvent and the energy needed to facilitate the ultrasonic treatment. He et al., did a comparative study on the utilization of ultrasound for Al collector and cathode material separation using various organic solvents [230]. The peel-off efficiencies increased with the following order of organic solvents, NMP>DMAC>DMF>ethanol. A peel-off efficiency of 99% was obtained when NMP was used at the optimum conditions of 70 °C, 240 W and 90 minutes.

d) Thermal Treatment

This process involves the thermal treatment of the materials at mild temperatures. This is done to change the crystalline phase of the cathode and also to get rid of the volatile material, binders and carbon [28,221]. Yang et al., did a study on the successful recovery of Al, Cu and active cathode and anode materials without contamination through thermal treatment by controlling

temperature between 550 ºC and 600 ºC [231]. The thermogravimetric mass spectrometer reveals that the binder polyvinylidene fluoride (PVDF) decomposed at temperatures below 500 °C. At temperatures between 500 and 550 °C, there is an evolution of CO_2 gas that is associated with the redox reaction between acetylene black and $LiNi_{1/3}Co_{1/3}Mn_{1/3}O_2$ and at this point, the active cathode material is reduced. The cathode anode graphite materials were successfully separated from the Al and Cu foil respectively at 600 °C. This successful approach enabled the efficient leaching of metal recovery at optimum conditions of 90 °C, 2 hours and $4MH_2SO_4$. This process has illustrated the ability to successfully separate cathode materials from their current collectors without or with insignificant contamination. The reduction process also prepares the materials for efficient leaching by decomposing the binder and other additives.

e) Mechanochemical Approach

The mechanochemical strategy involves the process of grinding LIBs material through ball milling to achieve a high surface area. The chemistry lies in the mechanical force applied by grinding causing physicochemical and chemical transformations. The process distorts the crystal structure of solids by revealing a hidden surface causing a chemical transformation. The procedure is simple, environmentally and economically friendly [232–235]. Wang et al., did a study on various co-grinding reagents to determine which reagents gives high recovery efficiency of Li and Co from $LiCoO_2$ [236]. PVC was the least performing co-grinder giving the least amount of recovery of Li and Co. NaCl was able to convert 30% of Li and Cl to water-soluble LiCl. Co was not successfully converted to chloride form due to the detachment of the ionic bond of NaCl from the mechanical force applied. This type of formation is attributed to the reduced atom radius and better polarity of Li enabling it to bond with Cl, while Co (low reactivity) cannot be converted to the water-soluble compound. NH_4Cl leached Li and Co partially due to its decomposition induced by the mechanical force enabling Cl to react with Li

and Co through solid-solid reaction. $FeCl_3$ performed better than the former co-grinders. $FeCl_3$ is a strong acid salt which reduced the surface activation energy and was able to convert both Li and Co to water-soluble ions. However, EDTA was established as the best chelating agent in co-grinding with $LiCoO_2$. The ball-milled material was leached with water and Li (99%) and Co (98%) were recovered as Co_3O_4 and Li_2CO_3 through precipitation. The above leaching procedure was achieved at optimum conditions of mass ratio 1:4 ($LiCoO_2$: EDTA), 4 hours of milling, rotary speed of 600 r/min and the ball-to-powder ratio of 80:1 [236].

2.4.4. Hydrometallurgical Recycling

This process involves the dissolution of metallic fraction from its solid form into a solution where specific materials can be extracted and separated. The method includes leaching batteries in order to recover the metals and separated using the precipitation, electrolyte deposition and solvent extraction [222].

a) Leaching

Leaching is one of the traditional methods of extracting valuable metals from LIBs. The cathode materials are submerged into either inorganic or organic acid. The most commonly used inorganic acids are H_2SO_4, HCl and HNO_3 [220]. Sohn et al., did a study on the leaching of $LiCoO_2$ in H_2SO_4 [237]. The extraction efficiency of Li was 70% and Co was only 40%. During the extraction process, Co is converted to Co^{3+} and has low solubility. However, when hydrogen peroxide was added, the leaching rate of Co increased. Hydrogen peroxide converts the metal into its divalent state, thus Co^{3+} is reduced to Co^{2+} which is soluble in the acidic solution [222]. Besides the use of H_2SO_4, other inorganic acids have been studied to determine their leaching efficiencies. Lee et al., also conducted reductive leaching of $LiCoO_2$ using HNO_3

[211]. The addition of hydrogen peroxide had increased the leaching efficiency by 45% for Co and 0% for Li. The overall leaching efficiency was 99% from both Li and Co at 75 ºC, 30 min and 1 M HNO_3. The group also conducted kinetic studies that showed that the dissolution rate of both Li and Co are inversely proportional to their ionic concentration, indicating that dissolution of the $LiCoCO_2$ is dependent on the surface chemical reaction. Joulié et al., indicated that amongst the three inorganic acids, HCl gives the best leaching efficiency [238]. The leaching step is dependent on the nature of species used to leach and its interaction with the matrix of the sample. HCl consists of chloride ions that enhance the dissolution of metals due to the ability of the ions to alter the structure of the surface layer.

b) Selective Precipitation

Precipitation is one of the methods that fall under hydrometallurgical recycling. This step usually follows after acid leaching; the metals can be separated or extracted from the leachate using solvated species that causes the salts to precipitate as depicted in Figure 2.7 [237]. Contestabile et al., did Co precipitation study on $LiCoO_2$ that was leached using 4 M HCl for 1 hour at 80 ºC [239]. The Co was precipitated using 4 M NaOH and recovered as $Co(OH)_2$. The precipitation process starts at pH 6 and ends at pH 8. Nayl et al., studied the precipitation of Mn, Ni, Co and Li from sulphate leachate [227]. A solution of 2 M of NaOH was first added to the leachate and the pH was adjusted with the addition of Na_2CO_3. $MnCO_3$ was precipitated at pH 7.5, $NiCO_3$ at pH 9 and $Co(OH)_2$ at pH 11-12. Many studies focus on the recovery of Li and Co but few studies focus on the recovery of Mn, Ni, Cu and Fe. This is due to the fact that these metals require co-precipitation and a lot of pH adjustments which is tedious work.

However, several authors have taken time to explore the routes of these metals. Li et al., used oxalic acid to leach $LiFePO_4$ battery at 0.3 M of oxalic acid, 80 ºC, 60 minutes and solid to liquid ratio of 60 g/L [240]. During the leaching step, Fe (II) does not oxidize but instead

precipitate forming FeC_2O_4. The rest of the products such as $Li_2C_2O_4$, Li_3PO_4 and $Fe_3(PO_4)_2$ are found within the leachate since the cathode materials react completely with the oxalic acid. Cheng et al., did a study on various Li-ion batteries such as LMO, LCO, LFP and NCM [241]. The study focused on leaching the batteries using phosphoric acid and the precipitation of Li, Ni, Co and Mn. After adjusting the optimum leaching conditions, it was observed that lithium can easily be dissolved in phosphoric acid with traces of other metals such as Mn^{2+} and Ni^{2+}. Manganese and nickel were precipitated using oxalic acid since their Ksp values are lower than that of Li^+. Li^+ was recovered by pH adjustment and was precipitated as Li_3PO_4. Dutta et al., precipitated Mn, Fe and Cu from $LiCoCO_2$ battery using 2 M H_2SO_4 as a leaching agent [242]. After optimization conditions of 10% of H_2O_2, 30 ºC, 2 hours and 75 g/L, the leached solution consisted of 3.64 g/L Mn, 1.48 g/L Cu, 0.2 g/L Fe, 2.44 g/L Li and 14.56 g/L Co. The focus was in the recovery of Co from the leached solution, however, the rest of the metals were still precipitated. Fe and Mn were precipitated using $(NH_4)_2S_2O_8$ in 4 hours at the pH range of 4-4.2.

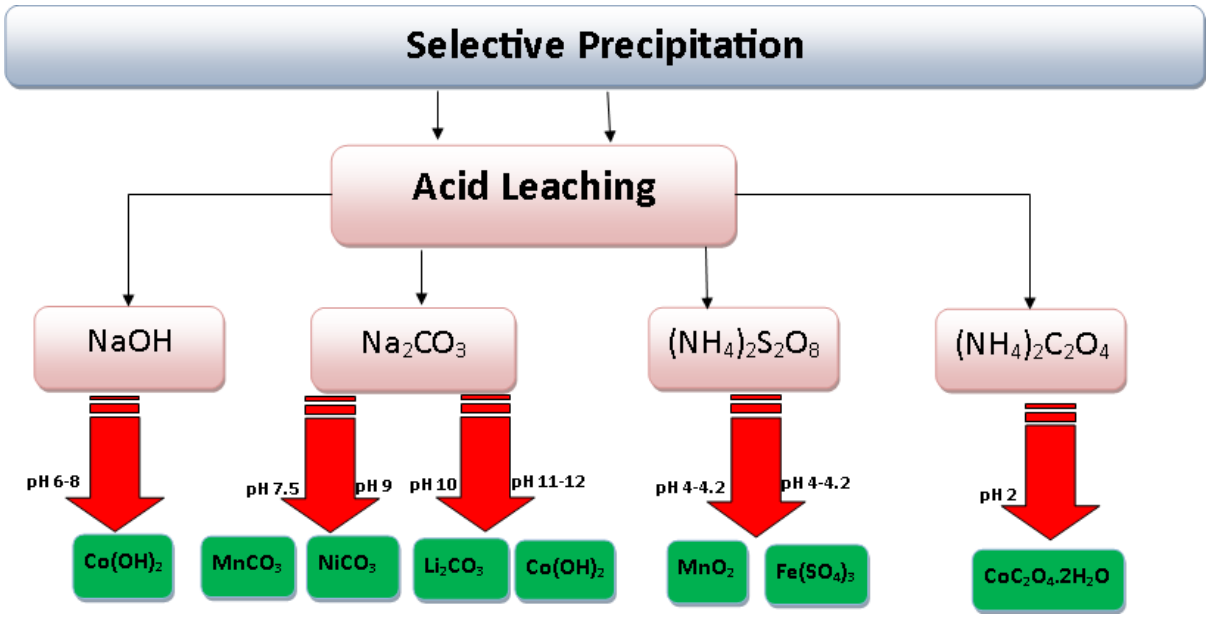

Figure 2.7: Selective precipitation based on various precipitation agents to obtain Co, Mn, Ni, Li from various spent LIBs.

c) Solvent Extraction

The process involves a mixture containing two phases (organic and aqueous). When complexing agents are added to the solution, the hydrophobic complexes convert to organic phases allowing the separation of materials due to different textures. The most common extracting solvents are PC-88A, D_2EHPA and Cyanex 272 in which Li, Co and Cu are easily extracted [243]. Cyanex 272 is used with kerosene as a diluent and the procedure consists of 2 steps, where aluminium is extracted at pH 2.5 - 3 and the extraction of cobalt at pH 4.5 and the remainder Li in the solution is precipitated with sodium carbonate. Cheng et al., reported of solvent extraction from NMC from sulphuric acid leachate using Cyanex 272 to extract and separate Co and Ni at pH 6 [244]. Co and Mn were extracted and separated at pH 9 using D_2EHPA [227,244]. After Dutta et al., had precipitated Fe and Mn using $(NH_4)_2S_2O_8$ the leachate contained Cu that was solvent extracted [242]. Cu was extracted from the leachate (pH 4) using 15% LIX 84 IC diluted in kerosene. When the solution reached equilibrium at pH 2, the different phases of the solvents separated into layers with one layer containing 99.99% of Cu [242,245]. Li et al., extracted Mn in kerosene using 15 vol% D_2EHPA and 5% TBP as organic phase modifiers [246]. Kerosene was saponified at a rate of 60% with 0.5 mol/L ammonia. The pH of the leached solution was adjusted to 2.25 using 2 mol/L of NaOH. The study showed that Mn extraction rate increases significantly to 99.9% as the phase ratio was adjusted to 1:1. The Mn^{2+} that were in the organic phase were stripped with a two-step stripping process using 0.156 mol/L H_2SO_4 enabling Ni^{2+} and Co^{2+} to be in aqueous phase while Mn^{2+} remained in the organic phase with a recovery rate of 84.6%. In the second stage of stripping, a $MnSO_4$ solution was obtained that contained small traces of Co.

2.4.5. Application of Recycled LIBs Materials

Metals from LIBs are successfully recycled from the different processes and can be sold as individual parent materials or can be used to obtain other products. In most cases, companies recycle the materials just to regenerate or re-synthesize new cathode material that can be applied in EVs and other applications. The re-synthesis process includes the use of sol-gel and sintering.

a) Sol-gel Method

The sol-gel method involves the utilization of a chelating agent to adjust the molar ratios of the metals in the leachate, adjusting the pH and stirring until a gel-like product forms which after calcination can be used as a cathode material [247]. This is considered as one of the easiest and direct route of resynthesizing the cathode material. Li et al., did a sol-gel re-synthesis by comparing acetic and maleic acid as leaching and chelating agents to re-synthesize $Li(Ni_{1/3}Co_{1/3}Mn_{1/3})O_2$ [247]. The maleic acid leaching process gave the leaching efficiencies of 99.45% Li, 98.45% Co, 98.58% Ni and 98.16% Mn whereas acetic acid leaching gave 98.83% Li, 97.85% Co, 97.93% Ni, and 97.74% Mn at optimum conditions. The molar ratios of the metals present were adjusted using CH_3COOLi, $(CH_3COO)_2Ni$, $(CH_3COO)_2Co$, and $(CH_3COO)_2Mn$ and the pH adjusted to 7. The cathode material from maleic acid had better electrochemical performance when discharged at 0.2 C with initial capacity of 151.6 mAh g^{-1} and after 150 cycles, its capacity was 127.3 mAh g^{-1}. The discharge capacities at 2 C and 5 C were 133.6 and 120.2 mAh g^{-1}, respectively.

The same group also did a study using lactic acid as leaching agent and acetic acid as chelating agent, obtaining approximately 98% recovery of Ni, Co, Mn and Li [248]. The precursor was prepared by sol-gel and the regenerative cathode material ($LiNi_{1/3}Co_{1/3}Mn_{1/3}O_2$) exhibited great electrochemical performance having a reversible discharge capacity of 138.2 mAh g^{-1} at 0.5 C

after 100 cycles with capacity retention of 96%. The material performed better than the cathode material prepared from commercial products. The electrochemical performance of regenerative material prepared by sol-method depends on the chelating agents. The chelating agents affect the particle size and the homogeneity of the material by ensuring there is enough interaction between the metal ions and polar side groups that promotes the crystallinity of the material during the heat treatment [249,250]. The small particle sizes and uniformity enables diffusion of Li^+ ion resulting in fast reaction and kinetics [250]. The acetic acid used by Li et al., is a weak chelating agent, such agents tend to form impurities when utilized at high pH such 7 creating large particles thus affecting the crystallinity. This in turn affects the electrochemical performance of the material [247,250]. Lactic acid chelating method was also successful due to the presence of carboxyl group that is adjacent to hydroxyl group having similar properties to citric acid [248,250].

b) Solid-state Sintering

Another direct method often used is solid-state sintering. The process involves the mixing lithium carbonate and the recovered metal oxide at relevant molar ratios, then heating the mixture at higher temperatures [251]. Meng et al., did a sintering process in order to regenerate $LiCoO_2$. The spent $LiCoO_2$ cathode material was leached at optimum conditions [252]. The cobalt was precipitated from the leachate using ammonium oxalate and obtained as $CoC_2O_4.2H_2O$, which through an oxidation process, Co_3O_4 is formed and used as a precursor. The leachate remains lithium rich and Li^+ which can be obtained as Li_2CO_3 by precipitation using Na_2CO_3. Li_2CO_3 and Co_3O_4 were mixed at a specific molar ratio and heat treated at 900 °C for 20 h. The prepared cathode material had an initial charge and discharge of 124.9 mAh g^{-1} and 119.7 mAh g^{-1} at 0.2 C.

Weng et al., did a preparation of $Li[Ni_{1/3}Co_{1/3}Mn_{1/3}]O_2$ which had excellent electrochemical performance, by first using a method of co-precipitation using Na_2CO_3 as aqueous solution precipitant and $NH_3.H_2O$ as chelating agent [253]. The precursor was then mixed with Li_2CO_3 at molar ratio of 1:0.5 and sintered at 920 ºC for 15 hours. The initial discharge capacity of the regenerated material was 152.7 mAh g^{-1} which is comparable to commercially prepared cathode material with a value of 157.3 mAh g^{-1}. The recycled prepared material exhibited a 94% discharge capacity retention rate at the end of 50^{th} cycle. Meng et al., developed a process that gives high performing recycled cathodes without the production of secondary pollutants [254]. The process involved the incorporation of mechanochemical activation prior to solid state sintering. The spent NMC is recovered by calcining the cathode material to segregate it from the foil and mixing the material with Li_2CO_3 at a ratio of 1.20:1 through a mechanochemical activation process. Mechanochemical activation enhances the diffusion of lithium ions from Li_2CO_3 and the nickel ions from the spent NMC, which in turn diminishes the cationic disordering and promote the regeneration process by enhancing the reconstruction of the layered structure. This progress then leads to better electrochemical performance of the cathode material. The sintering process occurred at 800 ºC for 10 hours, it was observed that below this temperature the sintering between the NMC cathode and the Li_2CO_3 is not complete and at temperatures above 800 ºC the cathode materials structures are destroyed. The regenerated material reached a discharge capacity of 165 mAh g^{-1} at 0.2 C at first cycle with a capacity retention of above 80%. This value is far much greater than those reported using conventional methods of leaching [254].

2.5. Extracted metals from spent LIBs as possible metal feedstock for MOFs

The listed recycling methods for spent LIBs indicate that extraction of metals such as nickel (Ni), manganese (Mn) and cobalt (Co) is possible and can be repurposed for other applications such as the preparation of MOF. This is a subtle and new study, and it offers different prospects of a new industry in the recycling of LIBs. With the energy demand on the rise and the increase of electrochemical energy storage systems and electric vehicles, this is an opportunity to create new markets. The section below discusses the MOFs such as Ni, Mn and Co-based, current reports of MOFs derived from spent batteries and previous reports of Ni, Mn and Co-based MOFs used as anode materials for LIBs application.

2.5.1. Nickel, Manganese and Cobalt-based MOFS

Ni, Mn and Co-based MOFs are common and used mainly in gas adsorption and gas sensing due to their active sites that enable gas molecule bonding [255]. They have a common factor considered as divalent MOFs. Co-based MOFs consist of carboxyl and hydroxyl groups coordinated to form an arrangement of one-dimensional parallel hexagonal channels [256]. The material consists of coordinated solvent molecules that can be vacated through thermal treatment leaving a stable framework with open pore and coordinative unsaturated metal cation. These available metal sites can bond with guest molecules making the material lucrative for gas adsorption. Strauss et al., prepared Co-MOF-74 based on Co^{2+} metal ions connected to 2.5-dioxido-1,4-benzenedicarboxylate prepared through solvothermal synthesis [257]. The MOF contains one-dimensional pore system with a pore diameter of 1.1-1.2 nm with a hexagonal honeycomb-like lattice and open metal sites. The material was infiltrated with tetrathiafulvalene (TTF) using the host-guest concept. The material was used for CO_2 gas sensing showing exceptional performances due to its increase in resistivity.

Yaghi et al., reported on preparation of Ni- MOF through solvothermal method of mixing Ni acetate hydrate and 1,3.5-benzenetricarboxylic acid (BTC) [258]. Thermal treatment of the material led to dehydration forming a monohydrate material with one–dimensional channels and pore sizes that are comparable to zeolitic material and molecular sieves. The material indicated successful H_2O and ammonia inclusion within its pore structure and rejected any molecule larger than its pores or any molecules without a reactive lone pair.

Ranjbar et al., did a study on Mn-MOFs by observing the effects of different organic linkers using hydrothermal synthesis [259]. Mn-MOF prepared using 2,6- Pyridinedicarboxylic acid linker had a morphology of rod-like microstructure, Mn-MOF prepared from 1,2,3-benzenetricarboxylic acid linker contained morphology of rod-like nanostructures and Mn-MOF prepared from 1,3,5-benzenetricarboxylic acid had a morphology of spherical nanoparticles. The linkers not only affected the morphologies but also rendered different textural properties. These materials exhibited high SO_2 and CO_2 adsorption.

2.5.2. MOFs prepared from using recycled Battery Materials

The recycling of valuable metals for preparation of porous materials is a demanding topic in the research world and few studies have reported MOFs from unconventional metals. However, only few have been reported on spent LIBs. Vellingiri et al., reported on the use of waste alkaline battery to extract the divalent metal (Zn^{2+}) that is used for MOF-5 synthesis [260]. The spent material was leached using HNO_3 obtaining a leachate solution consisting of Zn^{2+}, Mn^{2+} and Fe^{2+}. The zinc ion was precipitated using NaOH and obtaining a zinc hydroxide that was used as metal source with BDC linker for MOF-5 coordination. The resultant MOF-5 was not stable in DMF solution. The second attempt was on precipitation using NaOH and ascorbic acid as reducing agent, achieving 83% Zn^{2+} separation. The MOF-5 synthesized with this

leachate was stable toward DMF and chloroform washing with crystalline structure comparable with commercially prepared MOF-5. An upscaling study was done of waste prepared MOF-5 with quantitative solvent recovery and it was determined that 1 kg can be produced at a cost of 42 USD (United States dollar). Perez et al., simulated battery waste solution ($LiNiMnCoO_2$ battery) for the preparation of MOF [261]. The simulant solution was prepared using $Ni(SO_4),6H_2O$, $Mn(SO_4),6H_2O$ and $Co(SO_4),6H_2O$ commercial salts and were reacted using two different organic linkers, 1, 4-benzenedicarboxylic acid (BDC) and 1,3,5-benzene-tricarboxylic acid (BTC). The metal salts were dissolved in 1 equivalence in DMF solution forming an NMC solution. For comparative studies, each metal salt was dissolved individually to prepare Ni-BDC, Ni-BTC, Mn-BDC, Mn-BTC, Co-BDC and Co-BTC. This was done to compare the ligand effect on the coordination and chelating ability toward the different metal ions. In the BDC solvent, NMC-MOF consisted of hexagonal structure with 68% Mn and 40% Co and Ni composition. The structure consisted of large particles (100 µm) surrounded by smaller nanoparticles (5 µm) which are sensitive towards humidity. The Ni-BDC did not possess any crystallinity but rather indicating an amorphous phase with Mn and Co-BDC showed crystallinity. It was observed that BDC linker can separate Mn and Co in the same materials whilst precipitating Ni as small particle. The NMC-BTC MOF, Co-BTC and Mn-BTC consisted of rod-shaped structures with high degree of crystallinity except for Ni-BTC. The overall structure prepared in BTC are highly stable and consisting of an overall structure consisting of well-coordinated metal nodes. The battery simulation study formed a direction and influence of the PhD study. Thus, the study focuses on a method of converting spent LIB electrodes to Mn-based MOF in order to mimic Mn-1, 4-benzenedicarboxylic acid MOF through pre-existing methods of pyrometallurgy [221,223, 228]. However, there are no reports on this direct approach to prepare Mn-1, 4-benzenedicarboxylic acid MOF from spent LIBs and also utilized for the LIBs application.

2.5.3. Ni, Mn and Co-based MOFs as anode for LIBs application

Ni, Mn, Co are transition metals that are redox-active possessing various oxidation states and have been investigated as anode materials for LIBs application [259,262]. Zhang et al., reported on Ni-based MOF consisting of porous channels for ion diffusion prepared on a one-pot hydrothermal synthesis [263]. The MOF was used as an anode exhibiting a reversible specific capacity of 620 mAh g^{-1} at 100 mA g^{-1} after 100 cycles with a coulombic efficiency of 100%. Generally, Ni-based MOFs exhibit excellent cycling performance, however they also possess poor thermal stability and low discharge/charge potential. In an attempt to improve porous structure and electrochemical performance of Ni-based MOFs, An et al., used 3,3',5,5'-tetramethyl-4,40–bipyrazole (H_2Me4bpz) as an organic linker that offers rotation characteristic and structural stability [264]. The resultant Ni-MOF was a two-dimensional layered structure due to the coordination mode of azo metal salt. The ligand assisted in enhancing the lithium-ion insertion/extraction and the electrochemical stability even after cycling.

The first Co-based MOF used for LIBs was reported by Gou et al., with $Co_2(OH)_2$BDC- MOF [265]. The obtained MOF had good cycling stability while maintaining a capacity of 650 mAh g^{-1} at 50 mA g^{-1} over 100 cycles. Hu et al., reported high reversible capacity of 1090 mAh g^{-1} at current density 0.2 A g^{-1} of Co-MOF as anode [266]. The MOF still achieved a capacity of 611 mAh g^{-1} as the current density increases to 100 mA g^{-1}. The materials exhibited good cycling properties due to the oxidation state which Co stays in (Co^{2+}) during lithiation and delithiation process enabling Li^+ insertion within the organic moiety with no interaction with Co ions.

Manganese-based MOF consist of exceptional electrochemical performance. Liu reported on a microporous structure prepared by reacting 2,3,5,6-tetrafluoroterephthalatic acid(H_2tfbdc) and

4,4′-bipyridine(4,4′-bpy) with manganese (II) [34]. The Mn-based MOF exhibited an irreversible high capacity during first discharge with reversible lithium storage capacity of 390 mAh g^{-1} from the fourth cycle. Its high performance was hindered by the conversion reaction of the MOF during the cycling stage. Maiti et al., reported of reported of high performing Mn-1,3,5-benzenetricarboxylate MOF prepared through solvothermal synthesis using H_2BDC as organic linker [267]. The MOF achieved a high specific capacity of 694 and 400 mA g^{-1} at 0.1 and 1 A g^{-1} with good cyclability and structural retention. Hu et al., prepared Mn-MOF an exceptional using manganese chloride ($MnCl_2$) and 1,4-benzenedicarboxylic acid as linker through solvothermal synthesis [268]. The MOF was subjected to thermal activation prior to electrochemical testing. The MOF exhibited a high lithium storage capacity of 974 mAh g^{-1} after 100 cycles at current density 100 mA g^{-1}.

2.5.4. Other Pristine MOFs as anode for LIBs application

The first pristine MOF to be utilized as anode material was MOF-177(Zn) reported by Li et al., [269]. The electrochemical reaction resulted in the destruction of the MOF structure during the lithiation and delithiation reaction. This led to its poor cyclic performance with an initial high discharge capacity of 400 mAh g^{-1} at current density of 50 mA g^{-1}, which then dropped drastically to 105 mAh g^{-1} in the second cycle. This first step led to the opportunities to explore various MOFs (like high valent MOFs) as electrode materials. Tang et al., prepared UiO-66 (Zr) as nanoparticle to reduce diffusion length for lithium ions while increasing the contact area for conductive carbon phase [270]. The material was prepared as a cathode and maintained a specific discharge capacity of 118 mAh g^{-1} for 30 cycles. Generally, MOFs utilize redox active metal nodes to store charges in LIBs. However, UiO-66(Zr) electrode was prepared in such a way that it completely relies on anions for electrode reaction. It was also discovered that the

lithiation sites are situated at node oxygens and linker carboxylate oxygen, indicating that during this process charge transfers from Li to node oxygenes and carboxylates. This process assists in stabilizing the MOF structure avoiding destruction as appose to MOFs dependent on single redox-active metal nodes.

MIL-53(Fe) was the first to be reported by Ferey et al., as cathode materials in LIBs. The material had an initial reversible capacity of 80 mAh g^{-1} while maintaining 70 mAh g^{-1} after 50 cycles [271]. The low capacities are associated to the limitation of lithium insertion amount in which x=0.6 in $Li_xFe^{III}(OH)_{0.8}F_{0.2}O_2CC_6H_4CO_2.H_2O$. Combelles et al., studied the electrode limitation of Mil-53(Fe) using density functional calculations and local chemical bond analyses [272]. The findings indicated that the material possess weak antiferromagnetic properties when at temperature 0 K with Fe ions in high-spin state. Lithiation and delithiation occurs in a two-step insertion/conversion mechanism. In the insertion step, the capacity of the single-phase reaction increases with an increase in fluorine content. In the following step, the reaction ends, as there is stabilization of a localized Fe^{2+} /Fe^{3+} mixed-valence state at the inorganic chains. The conversion reaction is encouraged by the insertion of Li at the $Li_{0.5}$MIL-53(Fe) because of complete loss in local interactions of the linkers and metal ions of the MOF framework. Wang et al., prepared Al-MOFs using two different salts [$(Al(NO_3)_3.9.H_2O$ and $AlCl_3.6H_2O$] as anode for LIBs [273]. The prepared MOFs consisted of hierarchal tremella-like structure arranged as nanosheets. The materials reached a capacity of 392 mAh g^{-1} after 100 cycles at current density of 37.5 mA g^{-1}. At high current density of 37.5 A g^{-1} retained a capacity of 258 mAh g^{-1}. The materials possessed structural stabilities that contributed to excellent cyclic performance. Various studies have been conducted on pristine MOFs as electrode materials and mechanisms of Li storage have been deduced to the conversion mechanism and insertion mechanism. The conversion mechanism strongly relies on the stability of the framework hence the selection of appropriate ligand is crucial. This is because reversible formation of the MOF is paramount to

obtain high Li storage and electrochemical performance with good recyclability. Therefore, the framework should be strong enough for the transformation and avert the formation of poorly reversible oxides. In the insertion mechanism, the Li storage is reliant on the valence metal ions and organic linkers with functional groups that can easily interact with the Li ions.

Chapter summary

This chapter gave a detailed discussion on how coal fly ash is generated and currently being used as a substitute for various feedstocks and the generation of new materials. As shown in the review, the utilization has industrial application such as soil amelioration and preparations of ceramics and glass. It also indicated that intensive research is required for the optimization of porous materials and valuable metal leaching. It was observed that, CFA consist of metals that can be extracted and returned into the market to assist in boosting the South African economy.

The research also reveals chemical structures and how LIBs function. It covers the detrimental effects on the environment that discarding spent LIBs on landfills. Recycling processes and methodologies are clearly described. The metal extraction methods such as pyrometallurgy and hydrometallurgy cover the different strategies of how they are interconnected to achieve metal recovery. The chapter also details how LIBs can be easily regenerated using methods such as sol-gel, solid-state sintering and co-precipitation.

The review also indicates how these metals extracted from CFA and spent LIBs can be used as metal feedstock to prepare MOFs. High valent MOFs such as Al-MOF and Fe-MOFs can be easily prepared using Al and Fe from CFA. Other divalent MOF such as Mn-MOF can also be

prepared using spent cathode materials such as LMNO. These materials have various applications. However, the thesis aims to explore them for energy storage purposes, specifically LIBs and SCs. The review indicates how various high valent MOFs and divalent MOFs are utilized as pristine materials for the preparation of anodes and cathode for LIBs and SCs. MOFs can act as sacrificial templates for obtaining porous carbons. These porous carbons possess superior porosity over conventionally obtained porous carbons and exhibit high electrochemical stability and performance for LIBs and SCs. The review highlights the possible ways in which CFA and spent LIBs are commonly used and how they can be used to further grow their markets. Therefore, the novelty of the research lies in the use coal fly ash and spent LIB as a source of metal feedstock to prepare Al-based MOF and Mn-based MOF, respectively. Due to the exceptional structural and textural properties of the pristine MOFs (commercially ready), it can be expected that the novel MOFs will exhibit exceptional electrochemical performance in LIBs and SCs application.

Chapter 3: Experimental

3. Introduction

This chapter discusses the materials, experimental set-ups and characterization techniques. It provides a detailed approach to the synthesis routes and provides fundamental principles on characterization techniques.

3.1. Preparation of Coal Fly ash derived MOF (CFA-FumMOF) and its carbon derivative (CFA-MDC)

This section illustrates how CFA was leached using H_2SO_4 to extract valuable metals for the preparation of coal fly ash derived MOF (CFA-FumMOF). Metals such as Al, Fe, Ti and other trace metals are soluble, and their concentration can be found in the leached solution. The synthesis procedure of CFA-FumMOF is discussed.

3.1.1. Materials

Coal fly ash samples were obtained from a South African power station (Medupi). Sigma Aldrich supplied sulphuric acid (98%), fumaric acid (99%) and sodium hydroxide (99%). Associated Chemical Enterprises supplied aluminium sulphate octadecahydrate (99%), hydrofluoric acid (40%) and hydrochloric acid (37%). Argon and nitrogen were supplied by Afrox South Africa.

3.1.2. CFA-FumMOF synthesis

Aluminium metal from CFA was extracted using an inorganic acid leaching process. The fundamentals of inorganic acid leaching are discussed in chapter 2 (section 2.2.7). 100 g of Coal Fly ash (CFA) was mixed with 200 mL (18 M) of sulfuric acid (H_2SO_4). The mixture was

heated at 230 ºC with stirring for 24 h. Thereafter, the temperature was increased above 340 ºC to evaporate sulfuric acid. After evaporation, the fly ash was heated for an additional 30 minutes to be completely dry. The resultant mixture was then mixed with water on a ratio of 1:6 (CFA: H_2O) w/vol and stirred at 90 ºC for 30 minutes [274]. This step is crucial so that Al is obtained in a form of aluminium sulphate. If not the case, there will be no MOF materialization rather the recrystallization of fumaric acid as depicted by Figure 3.1. The mixture was then filtered, and the resulting filtrate (79.5 mL) was set aside to be used for MOF synthesis. The MOF synthesis procedures were conducted following a slight modification from previous reports [275]. In a different beaker, 6.45 g of fumaric acid and 4.75 g of NaOH were mixed with 95.5 mL of deionized water. Both solutions were heated at 60 ºC for 1 hour. The solutions were then mixed at 60 ºC and stirred for an additional 2 h. After the reaction, the mixture was filtered, washed with deionized water and dried at 105 ºC for 24 h. For comparison purposes, aluminium fumarate MOF was prepared using aluminium sulphate octadecahydrate ($Al_2(SO_4)_3.18H_2O$) as metal feedstock. The CFA derived MOF is denoted as CFA-FumMOF and the commercially prepared aluminium fumarate MOF is denoted as Al-FumMOF.

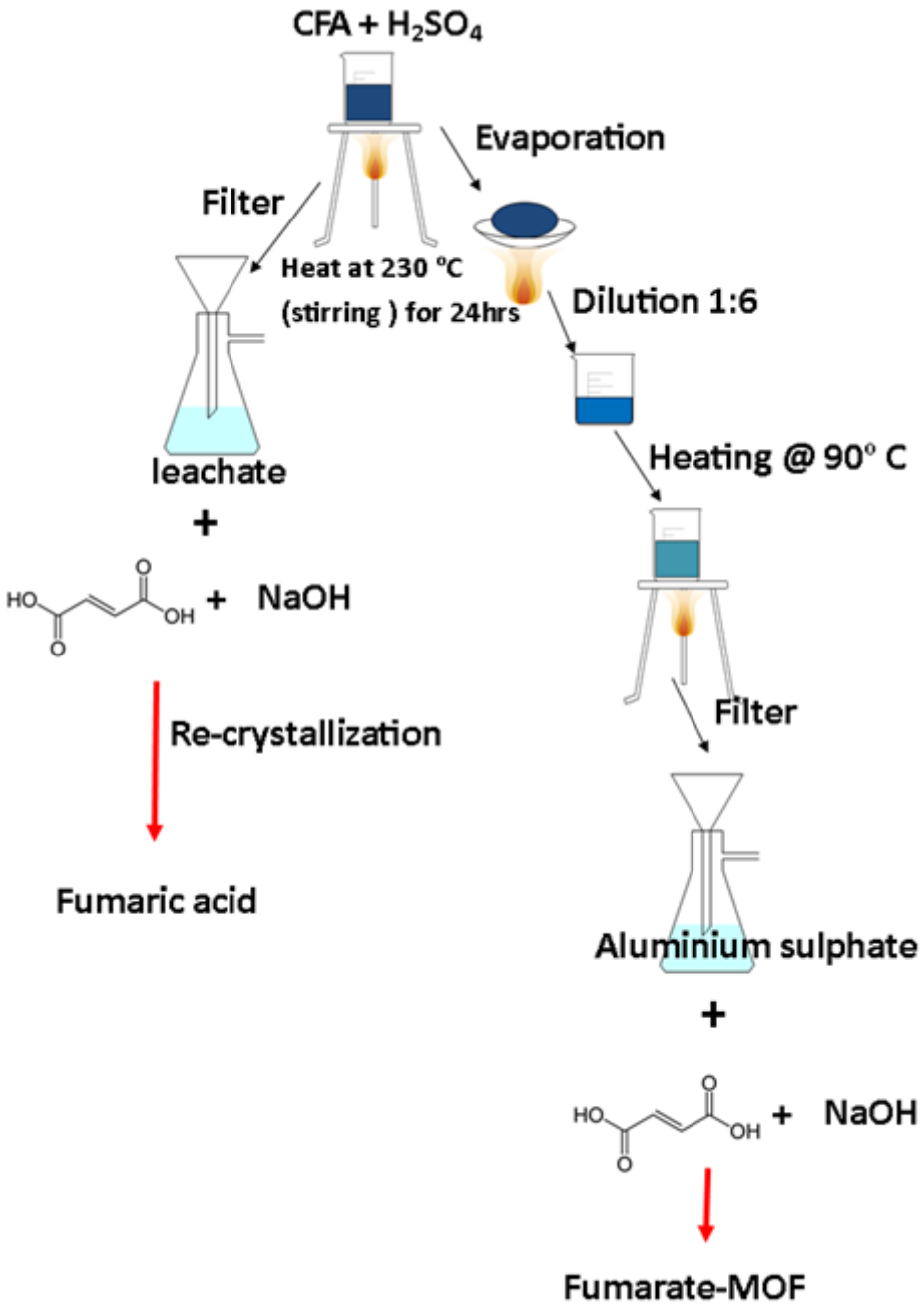

Figure 3.1: Experimental setup of CFA leaching and CFA-FumMOF preparations.

3.1.3. Direct carbonization of MOFs to obtain MOF-derived Carbons (MDCs)

Direct carbonization of porous materials and the process of MOF derived carbons have been discussed in details in chapter 2 (section 2.3.2 b). For the preparation of the MOF derived carbons (MDCs), the obtained MOFs were placed in a tube furnace and heated under argon at

800 ºC for 2 h thereafter cooled to room temperature. The black materials were washed in 10% HF for 4 hours and refluxed at 10% HCl at 70ºC overnight. The materials were washed thoroughly with deionized water and collected for characterization. The obtained carbon material from Al-FumMOF and CFA-FumMOF were denoted Al-MDC and CFA-MDC, respectively.

3.2. Preparation of CFA-FumMOF and MDCs for Supercapacitors (SCs) application

The CFA-FumMOF obtained from CFA was used as a positive electrode and its carbon derivative (CFA-MDC) was used as a negative electrode for the preparation of the SCs device. To analyse how effective their performance is, pristine Al-FumMOF and its carbon derivative (Al-MDC) were also prepared as anode and cathode, respectively for SCs analysis.

3.2.1. Three electrode configuration

A three-electrode system was configured to optimize the performance of the working electrode as depicted in figure 3.2. To prepare the working electrode, 80% of the active material (prepared MOFs or MDCs) was mixed with 10% of polyvinylidene fluoride and 10% of carbon black. Drops of N-methylpyrrolidone (NMP) were added to form a slurry using mortar and pestle. The slurry was then pasted over a nickel foam with an area of 1×1 cm^2. The coated nickel foams were then dried at 60 °C for 12 hours. The configuration included a glassy carbon counter electrode, saturated calomel electrode, and a working electrode (active material) and was tested in a 6 M KOH aqueous electrolyte. The Al-FumMOF and CFA-FumMOF were analysed as positive electrodes and Al-MDC and CFA-MDC were analysed as negative electrodes. Their capacitive performance was performed with the aid of a Bio-Logic VMP300

potentiostat (Knoxville TN 37930, USA) controlled by EC-Lab V1.40 software in a three-electrode set-up.

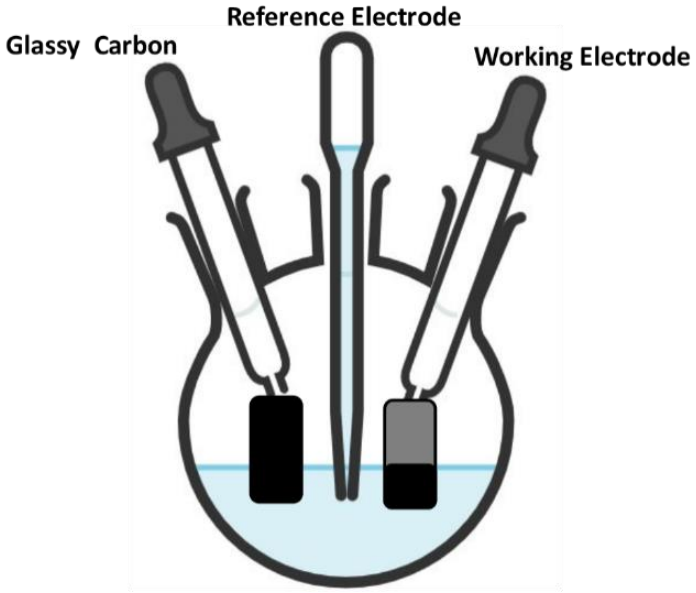

Figure 3.2: Three electrodes configuration for SCs analysis.

3.2.2. Two electrode configuration

In the two-electrode configuration, CFA-FumMOF was prepared as a positive electrode with its carbon derivative (CFA-MDC) as the negative electrode on the device. The configuration is presented in Figure 3.3. Similarly, for comparison purposes, Al-FumMOF was prepared as the positive electrode and its carbon derivative (Al-MDC) as a negative electrode. The devices were assembled in a coin cell (thickness: 0.2 mm and diameter: 16 mm) with a microfiber filter paper as a separator in a 6 M KOH electrolyte. Their capacitive performance was performed with the aid of a Bio-Logic VMP300 potentiostat (Knoxville TN 37930, USA) controlled by EC-Lab V1.40 software.

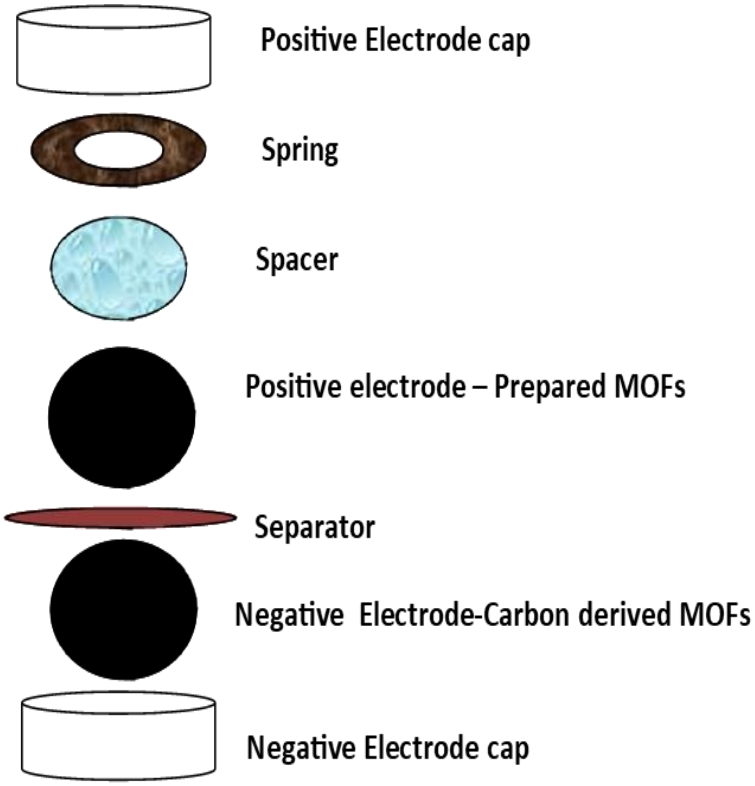

Figure 3.3: Two electrode configuration for asymmetrical SC application.

3.3. Preparation of Manganese-based MOFs from spent LIBs

3.3.1. Materials

Spent LIBs were obtained from a renowned model of smartphones. 37% of hydrochloric acid (HCl), 98% sulfuric acid (H_2SO_4), 95% ethanol, sodium sulphate (Na_2SO_4), N, N-Dimethylformamide (DMF), N-Methyl-2-pyrrolidone (NMP), benzene-1,4-dicarboxylic acid (H_2BDC) and manganese chloride salt ($MnCl_2$) were purchased from associated chemical enterprise in South Africa.

3.3.2. Manganese-based MOF synthesis

To recover spent cathode material, the batteries were subjected to mechanical separation and calcination as described in chapter 2, section 2.5.2 (a) and (d). Figure 3.4 presents a full detail on the extraction of metals and synthesis of Mn-based MOF from spent LIBs. Spent LIBs were discharged in 2 M Na_2SO_4 for 24 hours and dismantled. The cathode material was immersed in NMP and heated for 1 hour at 100 ºC. The recovered cathode material was calcined at 550 ºC for 30 minutes to burn out impurities and convert metals into metal oxides. The metal oxides were converted into salts by the addition of either H_2SO_4 (1 M) and HCl (1.75 M). The resulting mixture was dried at 90 ºC for 5 hours. The salts were mixed with H_2BDC at a ratio of 2:3. The MOF synthesis reaction occurred in 40 mL of DMF at 120 ºC for 48 hours (for H_2SO_4 salt) and 24 hours (for HCl salt). The materials were washed with DMF for 4 hours at 80 ºC and washed twice with ethanol at 60 ºC for 24 hours. The resulting MOFs were labelled as Mn-MOF(Cl_2) and Mn-MOF(SO_4) for use of HCl and H_2SO_4 salts respectively. For comparison purposes, commercial salt ($MnCl_2$) was used to prepare Mn-MOF(Com) and characterized.

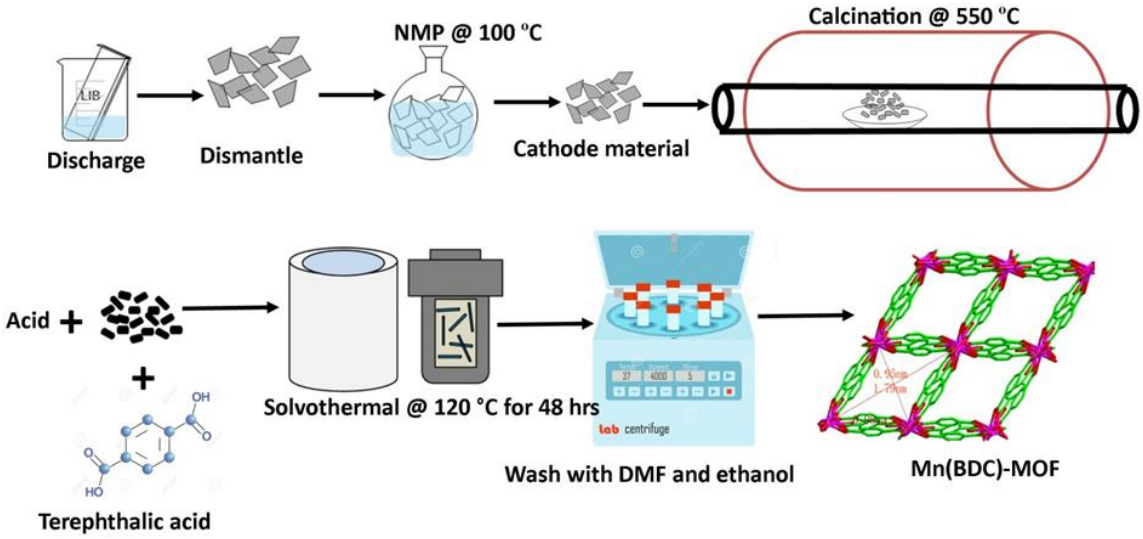

Figure 3.4: Synthetic procedure of preparing Mn-based MOFs from spent LIBs

3.4. Preparation of Mn-MOF(Cl_2) as anode for LIBs application

Due to the structural and textural properties of the synthesized Mn-based MOFs, Mn-MOF(Cl_2) was considered the best candidate for LIBs application. Mn-MOF(Com) was also utilized as an anode for comparison purposes.

3.4.1. Anode preparation and cell assembly

The working electrode was prepared by mixing 70% of the active material, 20% of the carbon black and 10% of carboxyl methyl cellulose (CMC) into a homogeneous powder. Deionized water (1.5 mL) was added to create a slurry. The slurry was pasted on a copper foil using the doctor-blading technique. This technique was originally developed in 1952 to prepare film with a specific thickness on a substrate (copper foil) [276]. In the technique, a sharp blade is placed at a distance on a metal surface. The slurry is then placed in front of the blade and the blade is

dragged across the surface creating a wet film of the slurry. The copper foil was then dried overnight and pressed into wafers. The coin cells were prepared in an argon-filled glove box, with the standard condition of O_2 and H_2O < 0.5 ppm. Figure 3.5 shows the internal arrangement of cell configuration, Lithium foil was used as a counter electrode, 1 M LiPF6 in EC: DMC: DEC (1:1:1 Vol%) as electrolyte and Celgard 2300 polypropylene-based membrane was used as a separator. The fabricated cells were evaluated using galvanostatic-cycling performances, cyclic voltammetry (CV), and electrochemical impedance spectroscopy (EIS) by MACCOR series 4000 tester and a Bio-Logic VMP3 potentiostat/galvanostat, respectively.

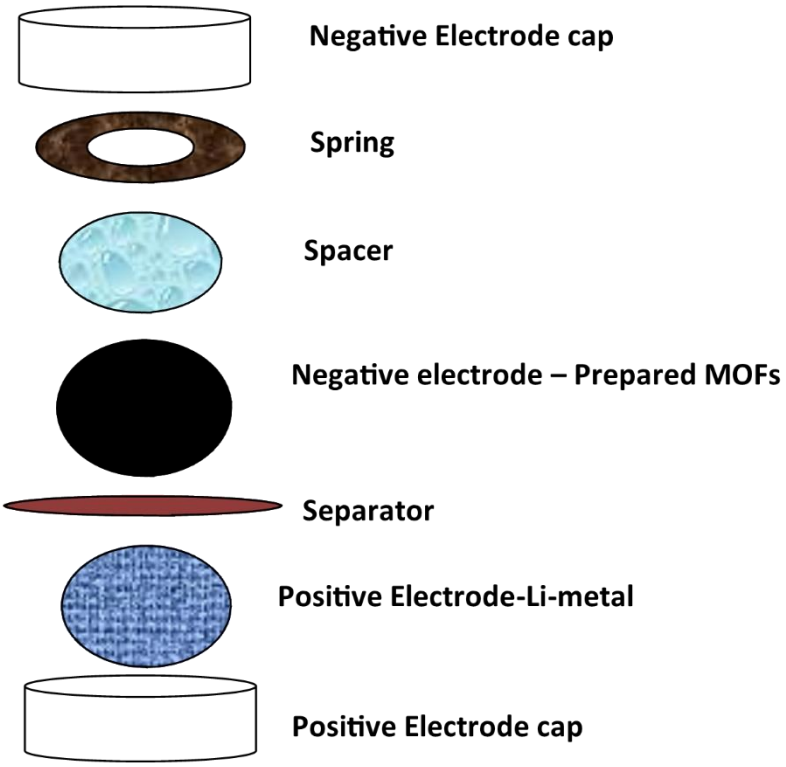

Figure 3.5: Cell assembly configuration for LIBs analysis.

3.5. Material characterization

3.5.1. Scanning electron microscopy (SEM) and energy-dispersive X-ray spectroscopy (EDS)

SEM is a technique that utilizes high-energy electron morphology observation in atomic and nanometer scale [277]. The fundamental principle of SEM technique is presented in Figure 3.6. The technique provides high-resolution images that can be coupled with elemental details. The image processing is dependent on signals produced from interaction between the specimen and electron beam. These signals consist of secondary electrons, backscattered electrons, characteristic electrons, auger electrons, cathodoluminescence, transmitted electrons and specimen current [278]. Secondary electrons are the loosely bound electrons that are emitted when the beam interacts with the specimen. They have low energy (3-5 eV) and released from the specimen within nanometers of the material. They are used to brand a specific position of the electron beam also giving topographical information. Backscattered electrons consist of energy greater than 50 eV and provide compositional and topographic information. This information differs from the ones provided by secondary electrons due to the depth in which backscattered electrons are released. Other electrons such as auger electrons, cathodoluminescence, transmitted electrons and specimen current are used for microstructural analysis [279]. Energy-dispersive X-ray spectroscopy (EDS) is a technique utilized to quantify the elemental and chemical composition of a specimen. The system is interconnected with the SEM and uses characteristic x-rays that are emitted from the specimen's inner shell due to the high-energy beam of charged particles [280]. The detector identifies the X-rays and presents them through a spectrum in which each element can be matched with referenced spectra. The morphology and elementals composition of the obtained MOFs and MDCs was analyzed using

an Auriga Cobra Focused-Ion-Beam Scanning Electron Microscope (FIB-SEM). The materials were initially coated with chromium before analysis.

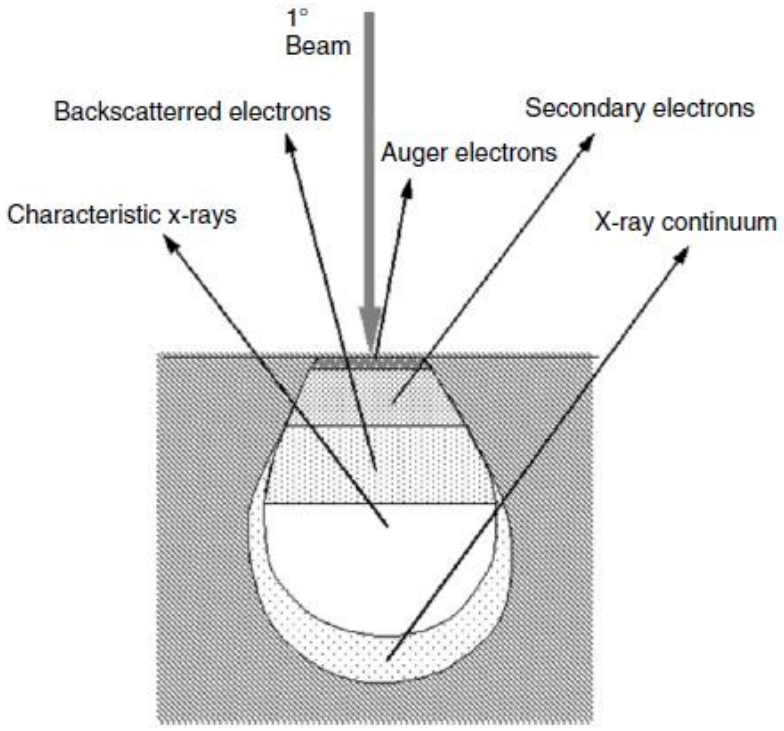

Figure 3.6: Diagram indicating beam interaction with a specimen during SEM analysis [276].

3.5.2. X-Ray diffraction (XRD)

XRD is a non-destructive technique for analysing crystalline materials. The technique produces information such as structural (average grain size, crystallinity, strain and crystal defects), phases and crystal orientation [281]. The technique releases information based on the constructive interference of monochromatic X-rays with the crystalline sample. The instrument consists of a cathode ray tube that produces the necessary X-rays which are filtered to produce monochromatic radiation, the collimator then concentrates and directs the monochromatic

radiation towards the sample. As the radiation interacts with the sample there is constructive interference when conditions satisfy Bragg's law (equation 9)

$$n\lambda = 2dsin\theta \quad (9)$$

where n is an integer, λ is the wavelength of the X-rays, d is the interplanar spacing and θ is the diffraction angle [282,283]. In this research, X-ray diffraction (XRD) patterns were obtained using a PANalytical X'Pert Pro powder diffractometer with Pixcel detector using Ni-filtered Cu-Kα radiation (0.154 nm) in the range of 2θ = 1–90° at a scanning rate of 0.1°s^{-1} and the diffractograms were analysed using Rietveld refinement via TOPAS (v3.1).

3.5.3. Fourier-transform infrared (FT-IR) spectroscopy

FTIR is a form of infrared spectroscopy that gives information about the analysed specimen using absorption or transmitted peaks associated with frequencies of vibrations between atomic bonds of the material [284]. The spectroscopy utilizes the Fourier mathematical procedure to decipher interferogram into a spectrum as depicted in Figure 3.7. Generally, different materials have a different combination of atoms and functional groups giving each material a unique IR spectrum that stands as its signature. In principles, the atomic bonds of different elements absorb light at a different frequency, which is measured using infrared spectroscopy creating an infrared spectrum. Thus, the functional groups will absorb the infrared light causing a stretch in the bond at a specific wavenumber range. The data is presented as a spectrum showing stretches as a function of infrared absorption frequency at a range of 400-4000 cm^{-1} [284,285]. The FTIR instrument is coupled with a detector, sample cell, amplifier A/D converter, computer and radiator. Radiation propagates through the interferometer to the detector to magnify the received signal and transform it into a digital signal through the A/D convertor,

which is then amplified and transmitted to the computer [286,287]. In this thesis, FTIR was performed using Attenuated Total Reflection-Fourier Transform Infrared (ATR-FTIR) spectrum (spectrum 100 FTIR spectrometer, PerkinElmer Inc) by four scans with a resolution of 4 cm^{-1}.

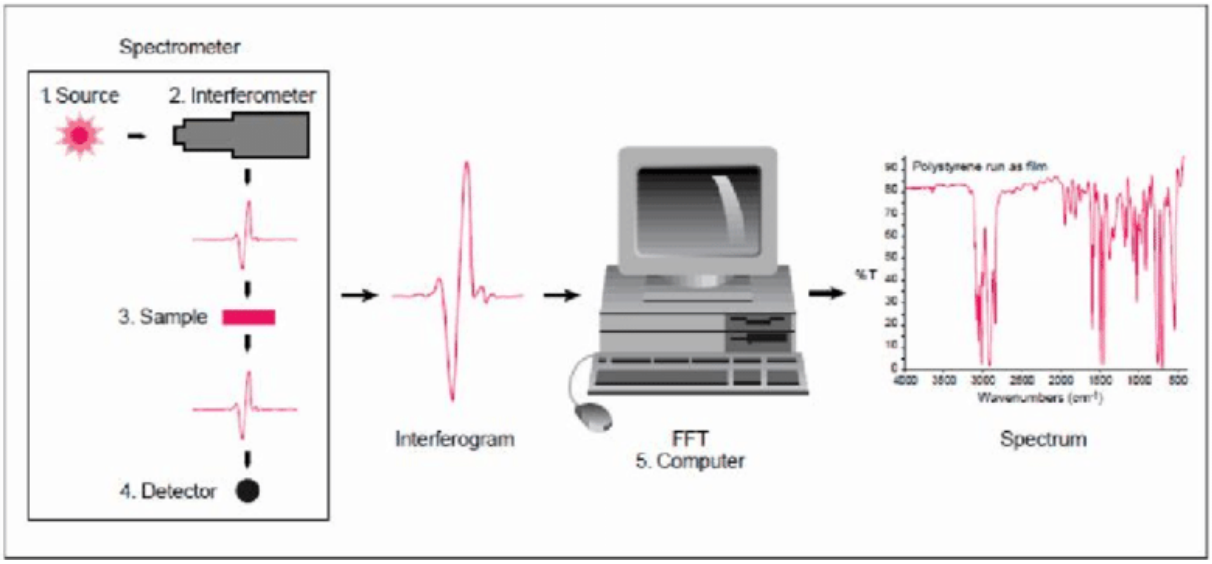

Figure 3.7: FTIR principle and instrumental operation [286].

3.5.4. Energy dispersive X-ray fluorescence (EDXRF)

EDXRF is a non-destructive elemental analysis technique used mainly in research and other industrial fields. The technique operates by exciting fluorescing atoms of the materials using energetic electrons, ions or photons [288]. When the material is excited, the radiation is strong enough to displace a tightly bound inner electron, which is replaced by an outer electron. The binding energy of the inner electron orbital decreases resulting in the release of energy. This emitted energy is called fluorescent radiation and contains specific information of transition between electron orbitals of a particular element [289,290]. This information can be used to

determine various elemental compositions within a material. In this study, the elemental composition of the materials was analyzed by an X-ray energy dispersive fluorescence spectrometer (XRF, PANalytical Epsilon 3 spectrometer). Analysis was carried out on the range of Na-Am (sodium to americium). The instrument is equipped with an X-ray tube Rh 9 W, 50 kV, 1 mA, 4096- channel spectrum analyzer, 6 measurement filters (Cu-500, Cu-300, Ti, Al-50, Al-200, Ag) and high-solid state detector SDD (50 μm thickness) cooled by a Peltier cell.

3.5.5. Raman spectroscopy

Raman spectroscopy utilizes light interaction with matter to obtain information about intra- and inter-molecular vibrations for comprehension of the crystal lattice and molecular backbone structure [291]. Raman spectroscopy originates from the Raman effect, which is a phenomenon that occurs when light interacts with molecules of the gas, liquid or solid resulting in photons scattered and approximately 1 photon in 10 million scatters at a frequency different from incident photon. In principle, Raman operates by observing molecular bond polarization that occurs during light interaction with a molecule inducing distortion of the electron cloud [292]. The change in polarizability occurs at specific energy transitions of molecular bonds, which in turn give rise to Raman active modes. These are represented by the Raman spectrum, which consists of Raman scattering light intensity and wavelength position. In this study, a WITec alpha 300 RAS+Confocal micro-Raman microscope (Ulm, Germany) was utilized to analyse the synthesized samples. To avoid sample heating, the system was operated at a laser power of 5 mW and wavelength of 532 nm in a spectral acquisition time of 150 s.

3.5.6. X-Ray photoelectron spectroscopy (XPS)

XPS is a surface analysis technique that provides information about a material's chemical status of the atoms accompanied by superficial elemental analysis [293]. The solid material is irradiated with an X-ray beam with an energy of hv. A mono-energetic photon from the energy beam displaces an electron from an atom of the surface of the material and photons that possess high energy are able to reach the deeper region of the material resulting in the release of electrons with a specific kinetic energy. The XPS spectrum consists of a detailed plot of the number of electrons emitted against their kinetic energy. Individual elements within the material produce characteristic peaks (which correspond to electron configuration) at specific binding energy values that enable identification. The binding energy is calculated using Ernest Rutherford equation as follows

$$B.E = hv - E_{k.e} - W_f \quad (10)$$

Where $B.E$ is the energy of the emitted electron, hv is the energy of the X-ray photons being used, $E_{k.e}$ is the kinetic energy and the W_f is the work function of the material [294]. In this study, the instruments Thermo, ESCAlab 250Xi, with X-rays of monochromatic Al kα (1486.7 eV), Xray power (300 W), spot size 900 µm, Survey spectrum analysed at 100 eV, high resolution at 20 eV and pressure $<10^{-8}$ mbar was used.

3.5.7. Thermogravimetric analysis (TGA)

TGA is a technique of measuring mass loss percentage as a function of temperature in a controlled atmosphere [295]. During the process, the sample is mounted on a pan that is supported on a balance. This pan is located inside a furnace in which the mass of the material is determined per temperature change. In this thesis, TGA was performed using the Hitachi

STA 7300 with alumina crucibles under air at a temperature rate of 10 °C/min at a temperature range of 0 °C to 1000 °C.

3.5.8. Nitrogen adsorption and desorption studies

N_2 adsorption was conducted under the fundamentals of BET theory. The theory stipulates that gas adsorption occurs on the surface of the materials due to the van der Waals forces [296]. Adsorption can be classified as either physical or chemical adsorption. Physical adsorption is associated with the van der Waals forces, whereas chemical adsorption corresponds to the chemical reaction that occurs between the solid and the gas. The amount of gas adsorbed by materials can be translated as the surface area of the material [296,297]. BET surface area measurements were conducted by volumetric analysis at liquid nitrogen temperature (77 K) using Micromeritics ASAP 2020. The BET surface areas of the materials were calculated in the region $0.01< P/P_0 <0.25$. Before each gas sorption analysis, samples were degassed at 150 °C under vacuum for 8 hours. Pore size distribution of the materials was obtained using non-local density functional theory (NLDFT), micropore volume was determined using the t-plot and pore volume using the Horvath–Kawazoe (HK) method.

Chapter summary

This chapter is subdivided into five subsections discussing the experimental set-up, synthesis parameters and characterization methods. The first subsection discusses the leaching process of CFA and the preparation of CFA-derived MOF (CFA-FumMOF) in an attempt to imitate aluminium fumarate MOF. For comparison, Al-FumMOF was also prepared using commercial feedstock. The section further discusses how the prepared MOFs from CFA and commercial

feedstock were converted to porous carbon materials. The next subsection discusses the preparation of nickel foam electrodes for SCs applications using two and three-electrode configurations. The chapter further discusses the utilization of spent LIBs as feedstock for the preparation of Mn-based MOFs. For comparison purposes, Mn-based MOF from commercial feedstock was also prepared. These materials were then further used as anode electrodes for LIBs application. The chapter ends by describing the characterization techniques and their principles.

Chapter 4: Results and Discussion

4. Introduction

This chapter discusses the results obtained from synthesis, characterization, Lithium-ion battery and supercapacitor applications. These results have been published and some are still under review as articles in peer-reviewed journals.

4.1. Manganese-based Metal-Organic Framework from Spent Li-Ion Batteries and its Electrochemical Performance as Anode in Li-ion Battery

4.1.1. Summary of Work

LIBs have been recycled using hydrometallurgy and pyrometallurgy techniques to recover valuable metals [222,223,298]. However, LIBs are usually recycled for the regeneration of the spent cathode using methods such as co-precipitation, sintering and sol-gel [224]. The regenerative processes are profitable such that the obtained materials possess capacities and capacity retention that is equivalent to commercially available cathodes.

There are various reports on the regeneration of LMNO batteries as a way to preserve manganese (Mn) [229]. Mn plays a major role in the preparation of LIBs. There are plenty of natural reserves of Mn and it is inexpensive to harness. It has been used for the preparation of Metal-Organic Frameworks (MOFs) for various applications including LIBs. A high performing Mn-based MOF (Mn-1,3,5-benzenetricarboxylate MOF) was reported by Maiti et al., [267]. The material was synthesized through solvothermal synthesis using H_2BDC as organic linker [267]. The MOF achieved a specific capacity of 694 and 400 mA g^{-1} at 0.1 and 1 A g^{-1} with good cyclability and structural retention. In this thesis, the author reports on the recycling of spent LIBs by converting cathode materials into Mn salts using HCl and H_2SO_4,

which has never been reported elsewhere. A comparative study is done between Mn-MOF obtained using commercial salts and those prepared from spent LIBs. The Mn-MOF obtained from HCl as salt convertor (Mn-MOF(Cl_2)) was chosen for electrochemical measurements due to good morphological, structural and textural properties.

4.1.2. Results and Discussion

Journal of The Electrochemical Society, 2021 **168** 010527
1945-7111/2021/168(1)/010527/10/$40.00 © 2021 The Electrochemical Society ("ECS"). Published on behalf of ECS by IOP Publishing Limited

Manganese-Based Metal Organic Framework from Spent Li-Ion Batteries and its Electrochemical Performance as Anode Material in Li-ion Battery

Khavharendwe Rambau,[1,2] Nicholas M. Musyoka,[1,z] Nithyadharseni Palaniyandy,[3] and Ncholu Manyala[2,z]

[1]*HySA Infrastructure Centre of Competence, Centre for Nanostructures and Advanced Materials (CeNAM), Chemicals Cluster, Council for Scientific and Industrial Research (CSIR), Pretoria 0001, South Africa*
[2]*Department of Physics, Institute of Applied Materials, SARCHi Chair in Carbon Technology and Materials, University of Pretoria, Pretoria 0002, South Africa*
[3]*Energy Centre, Smart Places Cluster, Council for Scientific and Industrial Research (CSIR), Pretoria 0001, South Africa*

Herein, we report a method of recycling spent lithium-ion batteries (LIBs) cathode materials by utilizing them as a metal feedstock for the synthesis of Mn-based metal-organic frameworks (Mn-MOF). Spent cathodes were converted to manganese salts using acids (HCl and H_2SO_4) and reacted with commercial benzene-1,4-dicarboxylic acid (H_2BDC), as an organic linker. The LIB-derived metal salts were compared to commercial available $MnCl_2$ salt in the formation of Mn-MOFs. Mn-MOFs from spent LIBs (MOF(Cl_2) and Mn-MOF(SO_4)) exhibited similar morphological, structural and textural properties when compared to that obtained from commercial $MnCl_2$ salt. HCl obtained MOF (Mn-MOF(Cl_2)) was analysed for electrochemical properties due to its superior structural properties. It achieved coulombic efficiency of approximately 99% and discharge capacity of 1355 mAh g^{-1} as compared to Mn-MOF obtained using commercial salt (Mn-MOF(Com)) with a discharge capacity of 772.55 mAh g^{-1} at 100 cycles. The developed LIBs recycling strategy has the potential for contributing to existing LIBs recycling strategies and as well to the circular economy.
 [DOI: 10.1149/1945-7111/abd285]

Manuscript submitted September 16, 2020; revised manuscript received November 10, 2020. Published January 18, 2021.

Supplementary material for this article is available online

The world is facing the problem of climate change due to the utilization of fossil fuel to generate energy.[1,2] This has led to a quest to find renewable and green energy sources to minimize the generation of greenhouse gases.[3] Scientists have focused on the development of different types of renewable energy sources such as solar, wind, biomass and geothermal.[4–6] The produced green energy often requires appropriate storage systems. Scientists have successfully developed energy storage systems such as Supercapacitors and Li-ion batteries (LIBs).[7,8] LIBs are renowned for their high energy density and cycling ability.[9,10] They are mainly utilized in household appliances and cell phones. Besides, with the demand to decarbonize the world, their application in electric vehicles (EVs) has increased significantly.[11–13] Projections indicate that by 2035 EVs will reach 190 million units and by 2040 the EVs usage will reach 320 million, comprise 16% of global passenger vehicles.[14,15] Large sales of EVs also indicate that large quantities of spent Li-ion batteries (LIBs) will be generated at the end of their life cycle. Most spent LIBs are disposed of in landfills, which can lead to health and environmental hazard and thus crippling the economy.[16] The cost of obtaining raw material for LIBs, preparation from brine and hard rock, is between $1800/ton and $5000/ton and it projected that it could cost only $1130/ton if obtained from recycled LIBs material.[17] This is an indication that recycling cannot only benefit the environment but will also have economic benefits. The spent LIBs can be recycled through the process of pyrometallurgy, which involves thermal treatment of spent LIBs at elevated temperature using reducing agents such as coke and limestone.[18] The process is limited to high energy utilization, can cause environmental pollution and has a high process cost. In order to improve the means of recycling, industries such as Toxco and Accurec developed the hydrometallurgy process.[19,20] The process involves the dissolution of metals by utilizing inorganic acids for metal leaching, solvent extraction and co-precipitation, among other processes.[21,22] The process was advanced to be greener by utilizing inorganic acids as disillusion medium giving minimal energy consumption and lesser toxic gas fumes. These processes successfully extract metals that can be sold or used to obtain other products. The most common reason for LIB recycling is the regeneration of LIBs cathode materials.[23] The regeneration process varies from sintering, sol-gel and co-precipitation.[24–26] These processes are lucrative that the regenerative materials maintain discharge capacities and capacity retention that is comparable to cathodes prepared from pristine commercial products. The recycled materials can also be used in the preparation of air-electrodes and supercapacitors.[27,28] Manganese is one of the most important metals in the preparation of LIBs since it is abundant and quite cheap to obtain. It is also useful in the preparation of Metal-organic Frameworks (MOFs) for various applications. MOFs are crystalline porous materials consisting of metal cations and multidentate organic linkers and have many applications. Mn-MOFs can be used as anodes for LIBs. In previous studies, Mn-1,3,5-benzenetricarboxylate MOF was reported as an anode for LIBs, exhibiting high specific capacities of 694 and 400 $mAhg^{-1}$ at current densities of 0.1 and 1 Ag^{-1},[29] respectively. A one-dimensional polymer [Mn(tfbdc)$(Im)_4$] prepared from manganese acetate, imidazole (Im) and tetrafluoroterephthalic acid (H_2tfbdc) was used as an anode. The material achieved a high capacity of 525 mAg^{-1} with a coulombic efficiency of 95% at 150 cycles at a current density of 50 mAg^{-1}.[30] These materials possess good cycling and are good anodic materials. Herein, we report the recycling of spent LIBs into Mn salts using HCl and H_2SO_4 for their utilization as feedstock for the preparation of Mn-MOFs. The MOFs are compared to Mn-MOF obtained using commercial salts. Mn-MOF(Cl_2) obtained from spent LIBs using HCl possessed good structural, morphological and textural properties and was tested for its electrochemical performance in comparison to the Mn-MOF obtained using commercial salts.

Experimental

Materials and synthesis.—Spent LIBs were obtained from a renowned model of smartphones. 37% of hydrochloric acid (HCl), 98% sulfuric acid (H_2SO_4), 95% ethanol, sodium sulphate (Na_2SO_4), N,N- Dimethylformamide (DMF), N-Methyl-2-pyrrolidone (NMP), benzene-1,4-dicarboxylic acid (H_2BDC) and manganese chloride salt ($MnCl_2$) were purchased from associated chemical enterprise in

[z]E-mail: NMusyoka@csir.co.za; ncholu.manyala@up.ac.za

South Africa. Spent LIBs were discharged in 2 M Na_2SO_4 for 24 h and dismantled. The cathode material was immersed in NMP and heated for 1 h at 100 °C. The recovered cathode material was calcined at 550 °C for 30 min to burn out impurities and convert metals into metal oxides.[31] The metal oxides were converted into salts by the addition of either H_2SO_4 (1 M) or HCl (1.75 M). The resulting mixture was dried at 90 °C for 5 h. The salts were mixed with H_2BDC at a ratio of 2:3. The MOF synthesis reaction occurred in 40 ml of DMF at 120 °C for 48 h (for H_2SO_4 salt) and 24 h (for HCl salt). The materials were washed with DMF for 4 h at 80 °C and washed twice with ethanol at 60 °C for 24 h. The resulting MOFs were labelled as Mn-MOF(Cl_2) and Mn-MOF(SO_4) for use of HCl and H_2SO_4 salts respectively. For comparison purposes, commercial salt ($MnCl_2$) was used to prepare Mn-MOF(Com).

Materials characterization.—The morphology of the obtained MOFs was analysed using an Auriga Cobra Focused-Ion-Beam Scanning Electron Microscope (FIB-SEM). X-ray diffraction (XRD) patterns were obtained using a PANalytical X'Pert Pro powder diffractometer with Pixcel detector using Ni-filtered Cu-Kα radiation (0.154 nm) in the range of $2\theta = 1°–60°$, and at a scanning rate of $0.1° \ s^{-1}$. FTIR was performed using Attenuated Total Reflection-Fourier Transform Infrared (ATR-FTIR) spectrum (spectrum 100 FTIR spectrometer, PerkinsElmer Inc.) by four scans with a resolution of $4 \ cm^{-1}$. Thermogravimetric Analysis (TGA) was performed using the Hitachi STA 7300 with alumina crucibles under air at a temperature rate of 10 °C min^{-1}. The elemental composition of the materials was analysed by X-ray fluorescence spectrometer (XRF, ARL ADVANT'X series). X-ray photoelectron spectroscopy (XPS) analysis was conducted using an AXIS ultra DLD spectrometer (KratosAnalytica) with a monochromatic Al Kα excitation source (1486.6 eV) and the data was analysed by XPS peak 4.1. BET surface area measurements were conducted by volumetric analysis at liquid nitrogen temperature (77 K) using Micromeritics ASAP 2020. The pore size distribution of the materials was obtained using non-local density functional theory (NLDFT), micropore volume was determined using the t-plot and pore volume using the Horvath–Kawazoe (HK) method.

Electrochemical measurements.—The working electrode was prepared by mixing 70% of the active material, 20% of carbon black and 10% of carboxyl methyl cellulose (CMC) into a homogeneous powder. Deionized water (1.5 ml) was added to create a slurry. The slurry was pasted on copper foil using the doctor-blading technique. The copper foil was then dried overnight and the pressed into wafers. The mass loading of the active materials are 2.5–3.5 mg for both materials. The coin cells were prepared in an argon-filled glove box, with the standard condition of O_2 and $H_2O < 0.5$ ppm. Lithium foil was used as a counter electrode, 1 M $LiPF_6$ in EC: DMC: DEC (1:1:1 Vol%) as an electrolyte and Celgard 2300 polypropylene-based membrane was used as a separator.

Results and Discussion

The morphological properties of the prepared Mn-based MOFs are presented in Figs. 1a–1c. As expected, the obtained MOF materials exhibited laminar structures that were homogeneous and consistent with previous reports.[32] The sheet-like laminar structures of Mn-MOF(SO_4) were found to be thicker than those of Mn-MOF(Cl_2) which can be due to minor contaminants as indicated by XRD. Figures 1d–1g presents the EDS spectrum and the elemental mapping of the LIB-derived Mn-based MOFs. Observations indicate that both Mn-based MOFs consisted of a significant amount of Mn, O, C and trace amounts of metal contaminants. The presence of these elements elucidates the possibility of the coordination of Mn with the organic linker.

The XRD patterns of the prepared materials are presented in Fig. 2. It can be observed that the Mn-MOF(Com) had a comparable pattern to that of the simulated version of the Mn-MOF with characteristic peaks at $2\theta \sim 10.42°$, 14.2°, 18.9°, 21.1° associated with the 011, 110 and 111 planes. In Figs. 2b and 2c, the prepared LIB-derived Mn-MOFs consist of these characteristic peaks with minor shifts due to insignificant crystallographic expansion associated with minor contaminants. Other unidentified peaks can be noted to appear at $2\theta = 22.31°$, and 25.60° (marked by #) and could be due to various phase formation of the MOF.[33]

Comparisons of thermal stability of Mn-MOF(Com) and LIB-derived Mn-MOFs are presented in Fig. 3a. Moisture removal from the materials is observed to occur at temperatures below 200 °C. From 290 °C to ~400 °C, the observed weight loss is associated with DMF solvent evaporation. The organic linker starts to decompose at about 420 °C. The residual material, which did not burn out completely, is due to the conversion of metal species to their oxide form.[34] Similar thermal decomposition trend was observed for the LIB-derived MOFs which is a confirmation of successful bonding of the metal constitutes with the organic linker. Noteworthy, the TGA profiles of Mn-MOF(Cl_2) had a close resemblance to that of Mn-MOF(Com) as already confirmed by XRD. However, it can be observed that Mn-MOF(SO_4) had a relatively low weight loss of about 30% which could be due to the presence of unreacted metal species. The FTIR spectra in Fig. 3b shows various functional groups present in the prepared MOFs. There are visible peaks at the range of 1529.25 $-1658.60 \ cm^{-1}$ and 1382.09 $-1421.60 \ cm^{-1}$, which are associated with the asymmetric and symmetric stretching vibration of $–COO^-$. These peaks appear when there is complete complexation of acidic COOH with Mn ions, which results in deprotonation.[35] The broad peak appearing between 3000 and $3500 \ cm^{-1}$ is associated with the O-H group from water molecules as confirmed by TGA.[35] The peaks at 739.24 and $880.20 \ cm^{-1}$ can be associated with ring-out-of plane vibration of the BDC organic linker, which serves as an indication of coordination of Mn ions.[35] Noteworthy, the FTIR spectra of Mn-MOF(Cl_2) had almost similar vibrational profile when compared to that of Mn-MOF(Com). To further confirm the possible coordination of the manganese metal with the organic linker, the materials were subjected to XPS analysis to determine the different elemental states.

The survey spectra presented in Figs. 4a and 4c indicated peaks at 284.3, 531.7, 400.1 and 642.2 eV, which are associated with C1s, O1s, N1s and $Mn2p_{3/2}$, respectively. Figures 4b and 4d shows the C1s scans of Mn-MOF(Cl_2) and Mn-MOF(SO_4) that illustrates the presence of the carboxylate group (O-C = O) at 288.3 eV, carbon group (C-C) at 284.75 eV and (C-O) at 286.37 eV, as well as O1s scans (Fig. S1) available online at stacks.iop.org/JES/168/010527/mmedia) at 531.49 eV (C-O), 532.76 eV (C = O) which is associated with the organic linker. The $Mn2p_{3/2}$ and $Mn2p_{1/2}$ peaks at 653.74 and 641.42 eV (Fig. S1) indicate possible coordination of manganese ion with the oxygen atom from the organic linker.[35] XRF results in Table SI further substantiate the presence of Mn in both Mn-MOF(Cl_2) and Mn-MOF(SO_4) with trace metals such as NiO and TiO_2.

The comparative N_2 sorption isotherms are presented in Fig. 5. According to the IUPAC classification,[36] the N_2 isotherms indicates a type III isotherm category consisting of H3 hysteresis loop which is attributed to the morphology of aggregates of plate-like particles as indicated by SEM, which leads to the formation of slit-shaped pores. From Table I, Mn-MOF(Com) was found to have a surface area of $34.47 \ m^2 \ g^{-1}$ and a pore volume of $0.1322 \ cm^3 \ g^{-1}$. On the other hand, MOFs prepared from spent LIBs had the surface area of $29.36 \ m^2 \ g^{-1}$ for Mn-MOF(Cl_2) and $29.47 \ m^2 \ g^{-1}$ for the Mn-MOF(SO_4). The relatively low surface areas for both MOF (Com) and LIB-derived MOFs was possibly due to the occlusion of solvent molecules within the MOF structure which indicate that more activation of the samples would be required.

Due to the morphology of Mn-MOF(SO_4) consisting of thick sheet-like laminar structures and the presence large quantity of unreacted metal oxides as indicated by XRD, TGA and FTIR, it can be speculated that these factors can hinder Li^+ migration. As a result, Mn-MOF(SO_4) was not characterized for electrochemistry.

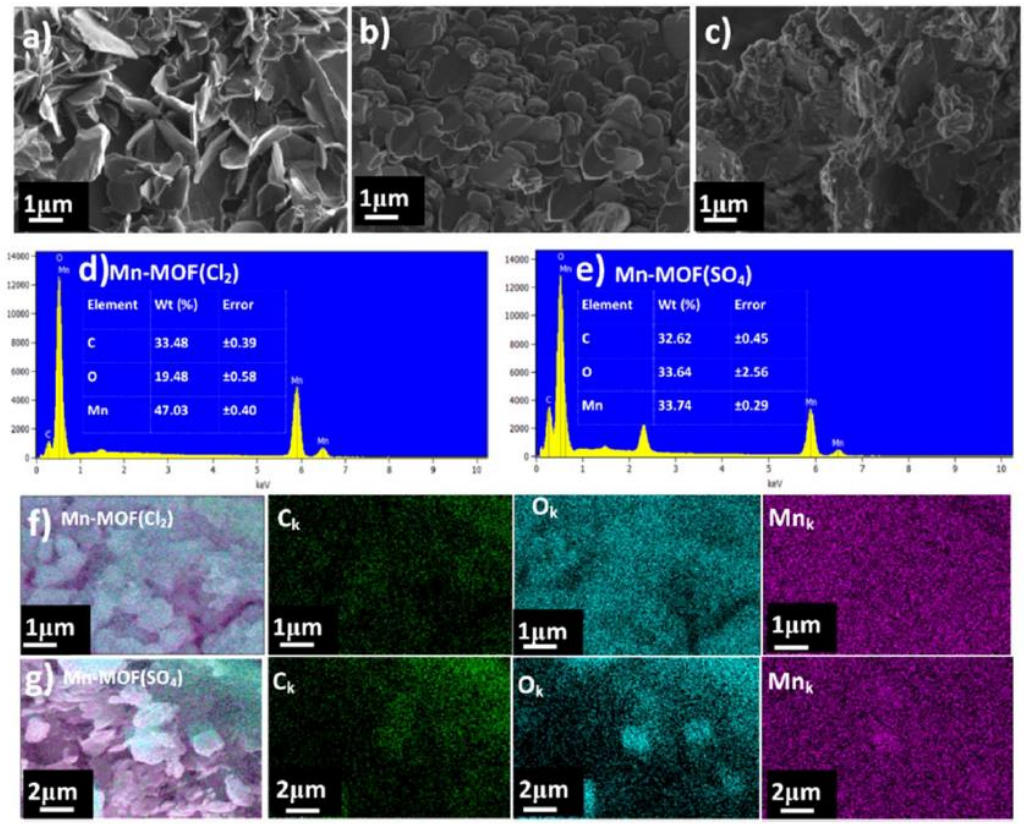

Figure 1. SEM images of (a) Mn-MOF(Com) LIB-derived Mn-MOFs (b) Mn-MOF(Cl_2), (c) Mn-MOF(SO_4) as well as their comparative EDS spectra (d), (e) and their elemental mapping (f), (g).

Cyclic voltammetry (CV) measurements and galvanostatic charge-discharge cycling were performed with using Li metal as a reference/counter electrode. Figures 6a and 6b depict the first five consecutive CV curves of Mn-MOF(Com) and Mn-MOF(Cl_2) at scan rate 0.1 mV s^{-1} and voltage window of 0.01–3.0 V. The first cycle of Mn-MOF(Com) consists of two cathodic peaks at 0.63 V and 0.13 V. The peak at 0.63 V disappears after the first discharge creating an initial irreversible capacity. This is due to the formation of a solid electrolyte interface (SEI) layer that fades with the following cycles. The peak at 0.13 V is associated with the intercalation of Li^+ into the organic group within the MOF. The anodic peak is observed at 1.03 V that suggest the extraction of Li^+ and the oxidation of Mn^{3+} ions. Mn-MOF(Cl_2) reduction peaks are at 1.18 V,0.68 V and 0.19 V. Following the initial cycle, the peaks 0.68 V and 0.19 V shift to 0.84 V and 0.32 V, respectively, whereas the peak at 1.18 V completely disappears after the formation of SEI.[35] The anodic peak for Mn-MOF(Cl_2) is situated at 1.08 V. The initial discharge-charge curves of Mn-MOF(Com) and Mn-MOF(Cl_2) are shown in Figs. 6c and 6d, obtained at a voltage range of 0.001–3.0 V and current density of 100 mA g^{-1}. The initial discharge curves of Mn-MOF(Com) and Mn-MOF(Cl_2) consist of a slope at 0.8 V and 1.23 V, respectively. This is due to the formation of lithium carboxylates $Li_2C_6H_4O_4$ and $Li_2C_8H_4O_4$ that are formed by the insertion of Li^+ into the organic moiety.[29] This indicates that the linker participates in redox reaction through carboxylate groups for the enablement of Li insertion and extraction. The materials further consist of a plateau formation approximately at 0.6 V and 1 V, respectively which is due to the reduction of Mn^{2+} and the formation of metallic manganese.[37,31] These observations correspond with CV in Figs. 6a and 6b. The low discharge plateau of Mn-MOF(Com) indicates good anodic characteristics. Figures 6c and 6d illustrates, the first discharge capacity of Mn-MOF(Com) is 2053 mAh g^{-1} and Mn-MOF(Cl_2) is 2511 mAh g^{-1} which is higher than the theoretical capacity of 970 mAh g^{-1}. In the initial charge curve, there is a slope just below 0.9 V for both MOFs and giving a charge capacity of 847.88 mAh g^{-1} for Mn-MOF(Com) and 1378.60 mAh g^{-1} for Mn-MOF(Cl_2). This leads to low initial columbic efficiency (CE) of 41.30% for Mn-MOF(Com) and 54.90% for Mn-MOF(Cl_2). Low CE is attributed to several components such as irreversible conversion reaction, loss of water and interfacial storage.[38] Furthermore, the high initial columbic efficiency of the Mn-MOF(Cl_2) may be due to the solid electrolyte interface (SEI), which is caused mainly due to the decomposition of the electrolyte. Moreover, the SEI formation could be due to the smaller particle size of Mn-MOF(Cl_2), exhibited uniform and smaller particle than that of Mn-MOF(Com) indicated by SEM analysis leading to high surface reaction with electrolyte. Other reasons due to the intrinsic nature of the material can also contribute to the high initial columbic efficiency.[39,40] Subsequently, the plateaus decreased to 0.4 V for both MOFs, which is ideal for the prevention of Li metal dendrite formation and high energy density sustainability.

Figures 7a and 7b shows the cycle performance between the two MOFs, Mn-MOF(Com) and Mn-MOF(Cl_2) for 100 cycles at a current density of 100 mA g^{-1}. Both Mn-MOF(Com) and Mn-MOF(Cl_2) managed to achieve a coulomb efficiency of approximately 99% after 10 cycles. Mn-MOF(Cl_2) exhibited the highest discharge capacity of 1355 mAh g^{-1} with the pristine (Mn-MOF (Com)) delivering 772.55 mAh g^{-1} after 100 cycles as indicated in Fig. 7d. The high performance of Mn-MOF(Cl_2) was unexpected and can be due to factors such as structural stability and the presence

Journal of The Electrochemical Society, 2021 168 010527

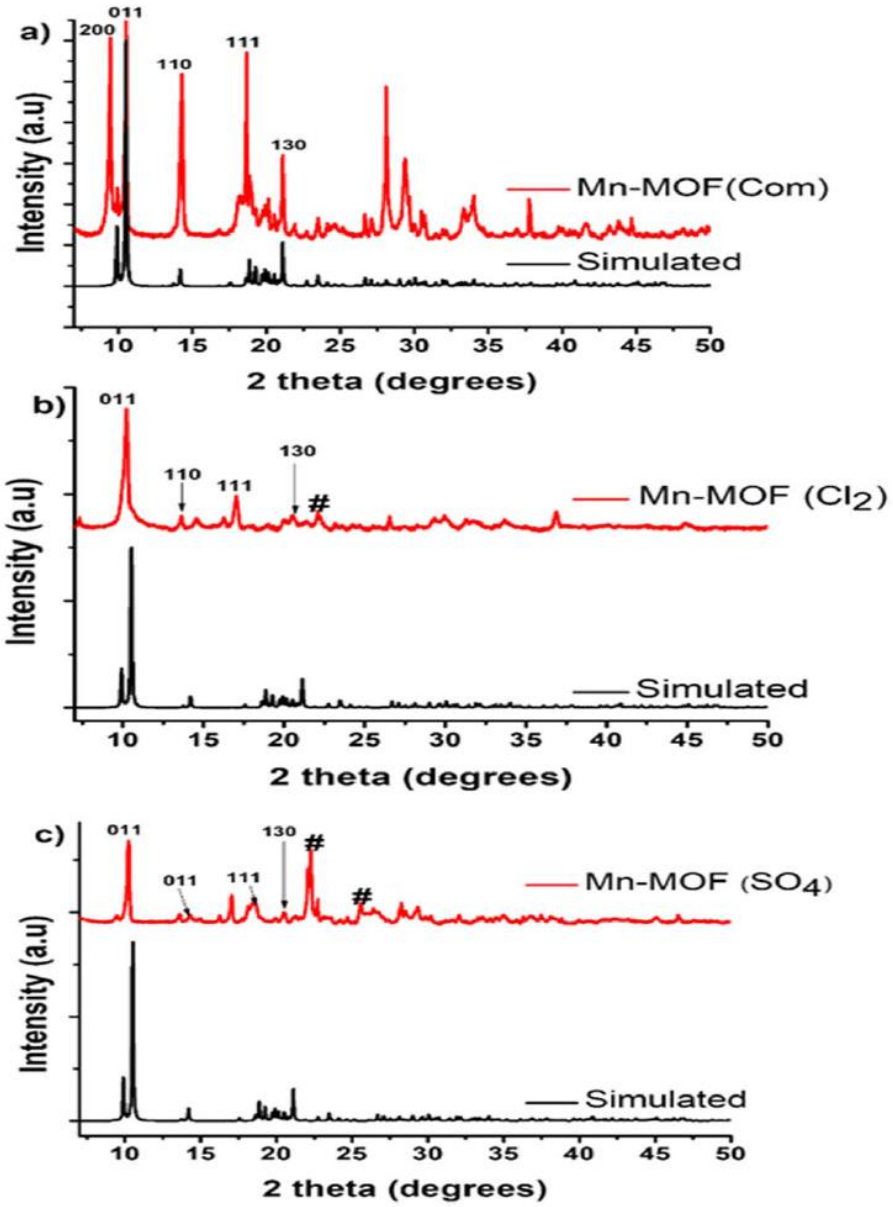

Figure 2. XRD patterns of (a) Mn-MOF(Com), (b) Mn-MOF(Cl_2) and (c) Mn-MOF(SO_4).

of unreacted metal oxides as indicated by XRD. Albeit, the CE of the initial charge and discharge were low, the specific capacity gradually increases and eventually obtaining capacity retention of approximately 90% and high CE(~99%). Increase in specific capacity during the initial cycling (from 10 to 25 cycles) performance of the Mn-MOF(Com) and Mn-MOF(Cl_2) is ascribed to the equilibration and activation of the electrode or the particle size reduction of the active materials.[41] Moreover, it is also associated to the development of inorganic SEI film through exhaustion of electrolyte on the electrode surface, reversible growth and dissociation of a polymeric gel-like layer formed through kinetically activated electrolyte degradation.[41] With proximity of 100% CE (Fig. 7c), Mn-MOF(Cl_2) indicates good reversibility of the redox process. The remarkable electrochemical performance of MOF(Cl_2) ascribed to its flaky sheet-like structures, allowing shorter ion diffusion path, which compliments the strain incurred through severe volume variations amid frequent intercalation/de-intercalation of lithium ions.[29,41,39] This indicates that Mn-MOF(Cl_2) can be an ideal candidate for anode material and also as a substitute for commercially prepared Mn-based MOFs.

The rate capacities are also illustrated in Fig. 7d. The current density used were from 100 mA g^{-1} to 2.5 A g^{-1} as indicated in Table II. Mn-MOF(Com) starts with charge/discharge of 656.91/1836.94 mAh g^{-1} and gradually decays to 421.81/441.56 mAh g^{-1} at 100 mA g^{-1}. After various cycles at different current density, it returns to 678.10/678.89 mAh g^{-1}. Mn-MOF(Cl_2) had charge/discharge value of 2031.39/4282.7 mAh g^{-1} which gradually decreased to 1774.04/1810.88 mAh g^{-1} and returned to 1930.09/1971.62 mAh g^{-1} and stabilized. The materials also exhibited 99% CE at different current densities, further confirming good

Journal of The Electrochemical Society, 2021 168 010527

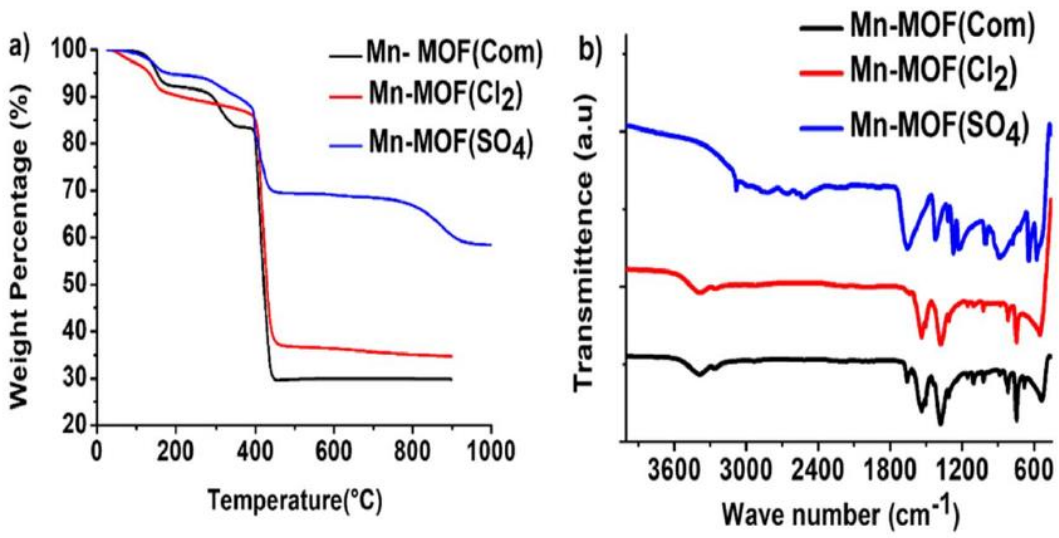

Figure 3. Comparative (a) TGA plots and (b) FTIR spectra of Mn-MOF(Com) and LIB-derived Mn-MOFs.

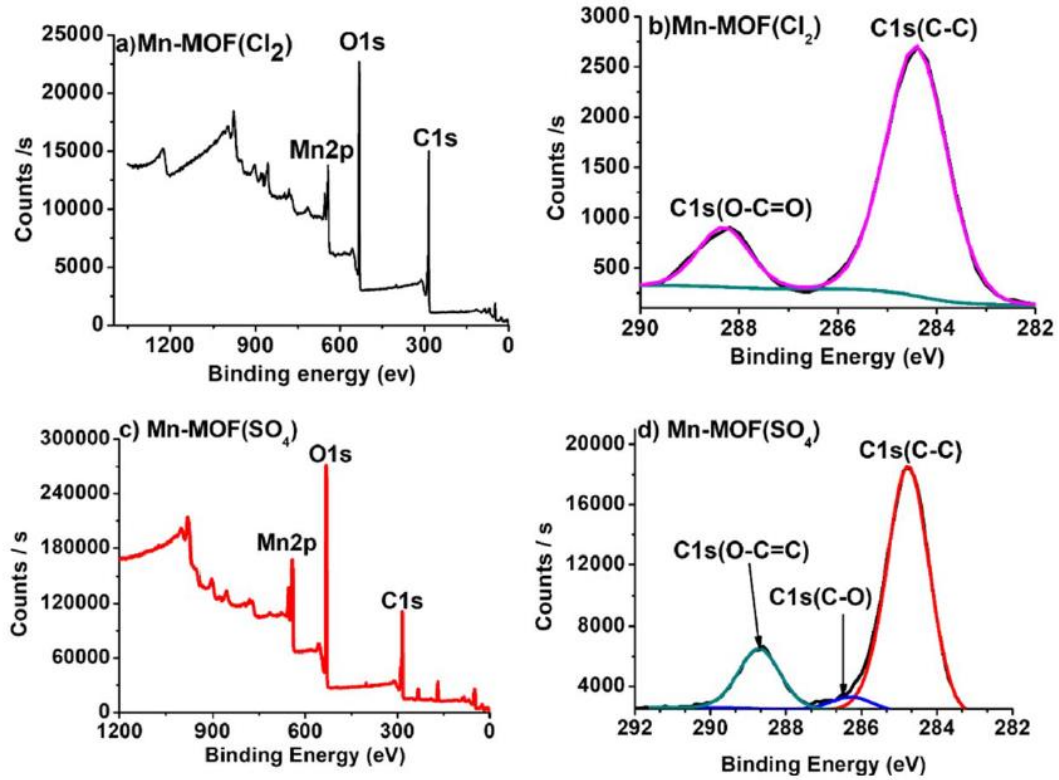

Figure 4. Survey XPS spectra of (a) Mn-MOF(Cl_2) and (c) Mn-MOF(SO_4) and respective C1s plots of (b) Mn-MOF(Cl_2) and (d) Mn-MOF(SO_4).

reversibility of the redox process. It can be observed that the Mn-MOF (Cl_2) has the ability for good cycling and high specific capacity as compared to the conventionally prepared Mn-MOF(Com). This is due to the morphology contribution of sheet-like structure with minor aggregation enabling short ion diffusion to active sites resulting in superior rate capability and confirmed by SEM.

Ex-situ XRD (Figs. 8a and 8b) was performed before and after 100th cycle. It can be observed that there is broadening of peaks at 33.1° and 28.5° indicate that Mn-MOF(Com) experienced amorphization after fully discharging to 0.01 V and can remain stable in an amorphous state. However, Mn-MOF(Cl_2) retained a sharp peak at 26.3° and amorphous peak at 33.1°, indicating partial retention of structure and amorphization.[35,42,43] This is substantiated with the SEM (Figs. 8c 8d) images, which consist of thickened laminar structures and amorphous agglomerates. Albeit the morphology

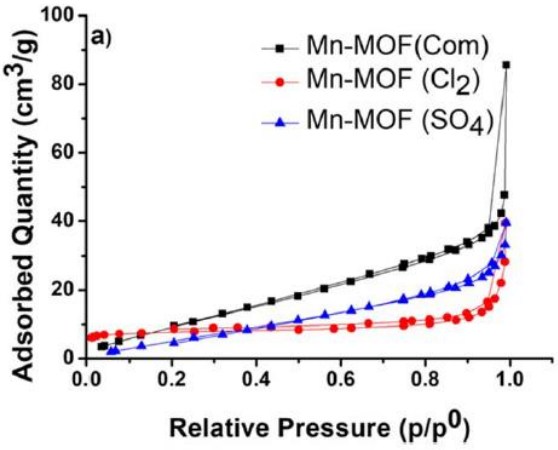

Figure 5. Comparative N_2 sorption isotherms of Mn-MOF(Com) and LIB-derived Mn-MOFs.

change, the material remained porous enough for assistance in the kinetic properties of the materials.

The electrochemical impedance spectroscopy EIS (Fig. 9) was conducted for Mn-MOF(Com) and Mn-MOF(Cl_2) to understand the kinetics of materials and fitted with an electrical equivalent circuit. The coin cells were analysed before and after the 100 cycles. Generally, the circuit consists of a combination of electrolyte resistance Rs, surface film (R_{sf}), charge transfer resistance (Rct) and constant phase elements (CPE_{sf}, CPE_{ct}, CPE_{dl}).[31] R_{sf} is associated with the resistance of Li^+ ion movement through the SEI film, Rct is associated with the charge transfer between the interfaces. The constant phase elements are associated with surface film capacitance (CPE_{sf}), CPE_{ct} is associated with charge transfer resistance capacitance and double-layer capacitor (CPE_{dl}) illustrating the inhomogeneous nature of the electrodes corroborated with α values (> 0.5). Warburg impedance (W_s) is associated with the solid-state diffusion of Li^+ ions through the material lattices and C is described as the intercalation capacitance.[44,45] The fitted data from EIS data and equivalent circuit are detailed in Table III. Before cycling, the R_s value of Mn-MOF(Cl_2) is lower than Mn-MOF(Com) suggesting better wettability of Mn-MOF(Cl_2). R_s value decreased after 100 cycles from each materials indicating improved connec-

Table I. Textural properties of the prepared MOFs.

Sample	BET SA ($m^2\,g^{-1}$)	Micropore Vol ($cm^3\,g^{-1}$)	Pore Vol ($cm^3\,g^{-1}$)
Mn-MOF(Com)	34.47	0.0165	0.1322
Mn-MOF(Cl_2)	29.36	0.00857	0.06112
Mn-MOF(SO_4)	29.47	0.00857	0.06115

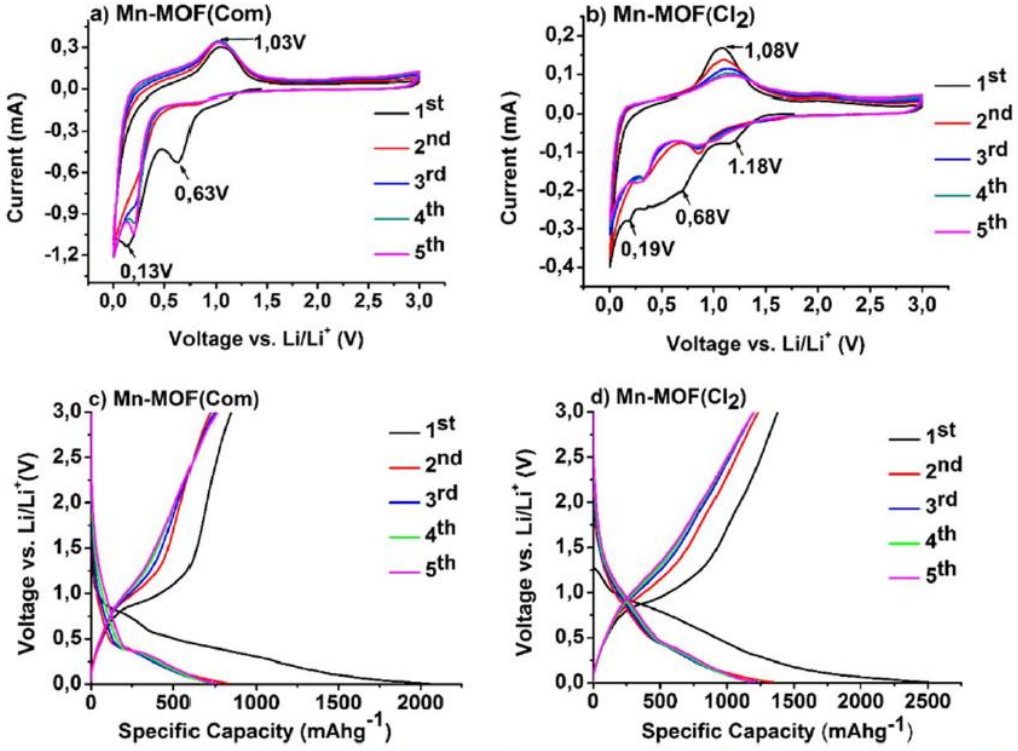

Figure 6. Cyclic voltammograms of (a) Mn-MOF(Com) and (b) Mn-MOF(Cl_2) at scan rate 0.1 mV s^{-1}. First five galvanostatic charge-discharge voltage profiles of (c) Mn-MOF(Com) and d) Mn-MOF(Cl_2) cycled at current density 100 mA g^{-1}.

Journal of The Electrochemical Society, 2021 168 010527

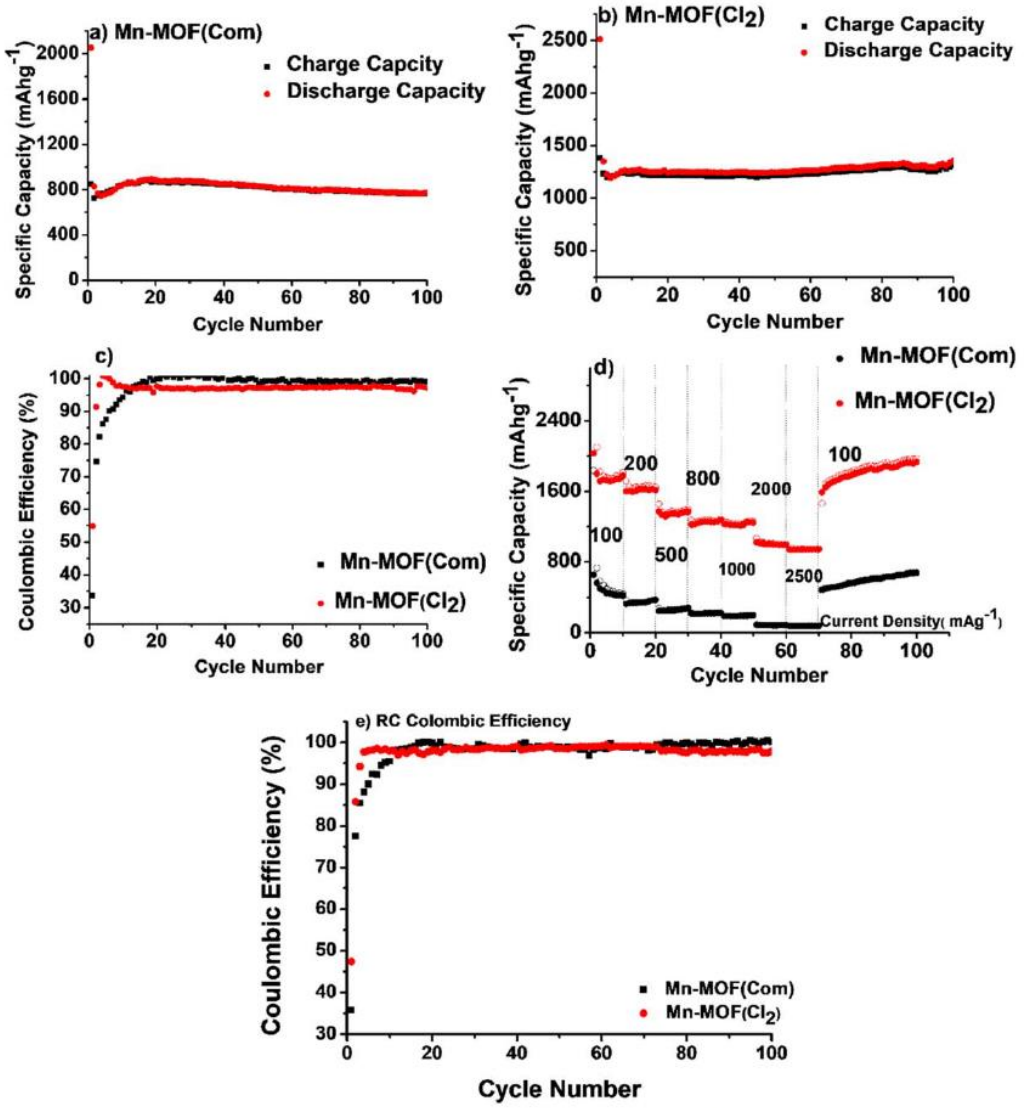

Figure 7. Cyclic performances of (a) Mn-MOF(Com) and (b) Mn-MOF(Cl_2) at current density 100mAg^{-1}. (c) Coulombic efficiency, (d) Rate performance and (e) Coulombic efficiency obtained from rate performance of Mn-MOF(Com) and Mn-MOF(Cl_2) at voltage range 0.01–3 V.

tivity. However, R_s value of Mn-MOF(Cl_2) was lower than Mn-MOF(Com) indicating its high performance. The charge transfer resistance of the materials decreased significantly after 100 cycles. Mn-MOF(Cl_2) possessed the lowest (17.02 Ω) with a notable vertical line in the low-frequency region indicating less diffusion length and effortless insertion and de-insertion of Li^+ ions. Consequently, reaching high specific capacity, which is in good agreement with the rate capability test. The values of CPE_{sf} and CPE_{ct} ranged from 10–27 μF with CPE_{dl} ranging from 4–14 μF. The EIS has provided significant perspective towards the charge transfer properties of Mn-MOF(Com) and Mn-MOF(Cl_2). This further substantiates high-performance properties of Mn-MOF(Cl_2).

Conclusions

In summary, Mn-based MOFs were successfully synthesized from metal feedstock obtained from spent LIBs. Amongst the obtained MOFs, Mn-MOF(Cl_2) showed traits that were consistent with the MOF prepared using a commercial $MnCl_2$ salt, based on its morphological, structural and textural properties. Mn-MOF(Cl_2) exhibited good electrochemical performance with a discharge specific capacity of 1355 mAh g^{-1} and 99% coulombic efficiency. When scaled up, the developed process has the possibilities for contributing to the recycling alternatives for spent LIBs.

Acknowledgments

KR and NMM would like to acknowledge the financial support from the South African Department of Science and Innovation (DSI) for research activities under the HySA Infrastructure (Project No. CNMH01X). NMM also thanks to the Council for Scientific and Industrial Research (CSIR) for financial support (Project No. C1GEN25). NM acknowledge the financial support by South African Research Chairs Initiatives (SARChI) of the Department of Science and Innovation and the National Research Foundation (NRF) of South Africa (grant no. 61056). Any opinions, findings

Journal of The Electrochemical Society, 2021 168 010527

Table II. Rate performance current densities with corresponding specific capacity values.

	Mn-MOF(Com)		Mn-MOF(Cl_2)	
Charge Density (mAg^{-1})	Charge Capacity ($mAhg^{-1}$)	Discharge Capacity ($mAhg^{-1}$)	Charge Capacity ($mAhg^{-1}$)	Discharge Capacity ($mAhg^{-1}$)
100	421.81	441.56	1774.04	1810.88
200	373.42	373.87	1614.10	1646.23
500	281.58	277.21	1369.25	1393.18
800	226.28	223.96	1276.23	1287.43
1000	197.89	195.84	1242.67	1260.21
2000	85.45	83.47	994.38	1002.83
2500	79.98	79.12	939.15	947.30

Journal of The Electrochemical Society, 2021 168 010527

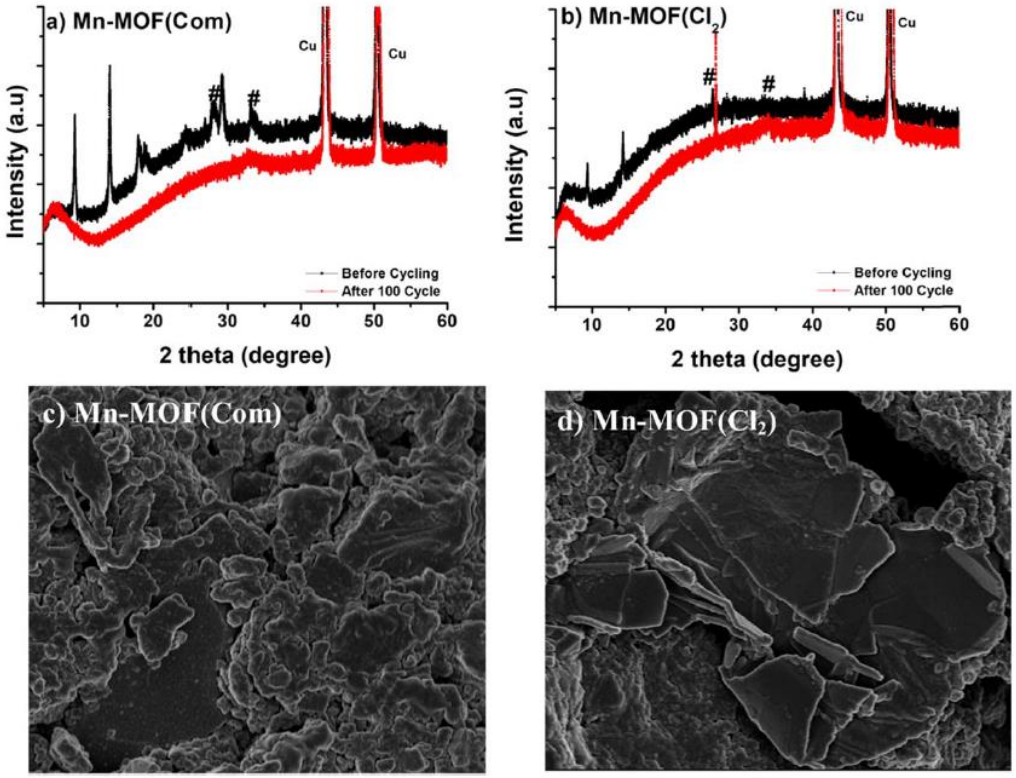

Figure 8. XRD patterns (a), (b) and SEM images of prepared MOFs at discharge 0.01 V after 100 cycles.

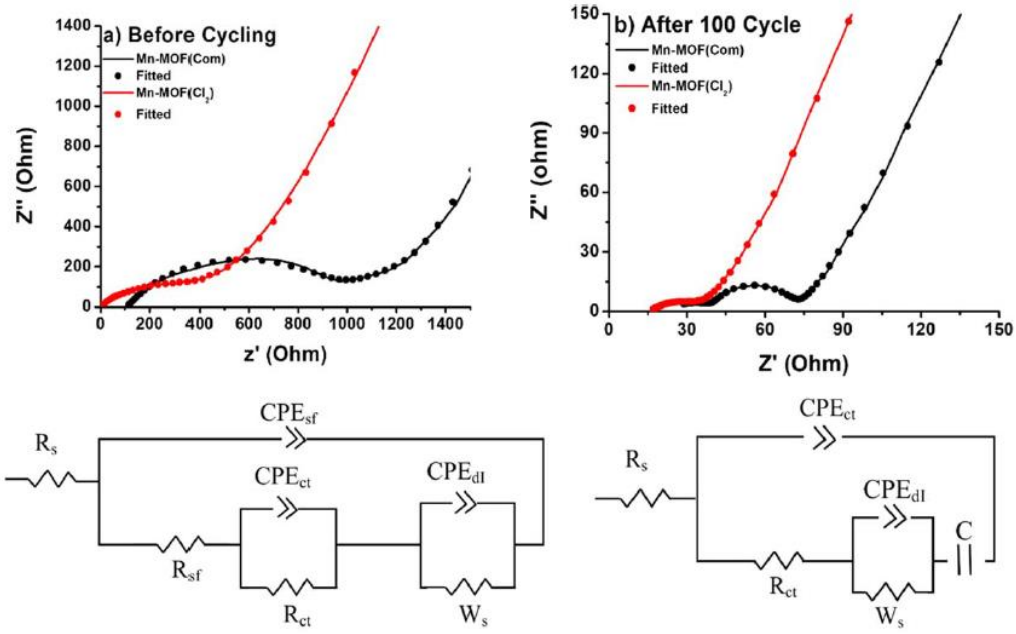

Figure 9. Impedance spectra of prepared MOFs (a) before and (b) after 100 cycles.

Table III. Fitted impedance values of Mn-MOF(Com) and Mn-MOF(Cl_2) using equivalent electric circuit.

Material	Before/After 100 Cycle	R_s (±5Ω)	R_{sf} (±5Ω)	R_{ct} (±5Ω)	W_s (±10Ω)
Mn-MOF(Com)	Fresh cell	108.6	891.6	759.1	350.5
	After 100 cycle	15	35	100	220.6
Mn-MOF(Cl_2)	Fresh cell	4.5	10.5	511	310.8
	After 100 cycle	15.0	—	22.0	115.0

and/or recommendations expressed here are those of the authors and not of the funding bodies.

ORCID

Nicholas M. Musyoka https://orcid.org/0000-0001-9830-9265

References

1. M. Janić, *J. Air Transp.Manag.*, **69**, 247 (2018).
2. Q. Chen, M. Lv, Z. Tang, H. Wang, W. Wei, and Y. Sun, *J. CO_2 Util.*, **14**, 9 (2016).
3. M. S. Masnadi, J. R. Grace, X. T. Bi, C. J. Lim, and N. Ellis, *Appl. Energy*, **140**, 209 (2015).
4. A. Al-Dousari, W. Al-Nassar, A. Al-Hemoud, A. Alsaleh, A. Ramadan, N. Al-Dousari, and M. Ahmed, *Energy*, **176**, 194 (2019).
5. M. Leveni, G. Manfrida, R. Cozzolino, and B. Mendecka, *Energy*, **180**, 818 (2019).
6. S. Shilpi, D. Lamb, N. Bolan, B. Seshadri, G. Choppala, and R. Naidu, *J. Environ. Manage.*, **239**, 83 (2019).
7. L. Liu, Y. Feng, and W. Wu, *J. Power Sources*, **410**, 77 (2019).
8. P. Ladpli, R. Nardari, F. Kopsaftopoulos, and F. K. Chang, *J. Power Sources*, **414**, 529 (2019).
9. N. Nitta, F. Wu, J. T. Lee, and G. Yushin, *Mater. Today*, **18**, 264 (2015).
10. J. Zhang, Y. Chen, R. Chu, H. Jiang, Y. Zeng, Y. Zhang, and H. Guo, *J. Alloys Compd.*, **787**, 1062 (2019).
11. G. Zubi, R. Dufo-López, M. Carvalho, and G. Pasaoglu, *Renewable Sustainable Energy Rev.*, **89**, 308 (2018).
12. W. Chen, J. Liang, Z. Yang, and G. Li, *Energy Procedia*, **158**, 4368 (2019).
13. M. Bila, C. Opathella, and B. Venkatesh, *J. Energy Storage*, **6**, 185 (2016).
14. M. J. C. Quartz, (2019), accessed 2019-09-04, https://qz.com/1620614/electric-car-forecasts-are-all-over-the-map/.
15. F. Sioshansi and J. Webb, *B.E. J. Econ. Anal. Policy*, **61**, 15 (2019).
16. Y. Yu, B. Chen, K. Huang, X. Wang, and D. Wang, *Int. J. Environ. Res. Public Health*, **11**, 3198 (2014).
17. C. H. Jo and S. T. Myung, *J. Power Sources*, **426**, 265 (2019).
18. X. Zheng, Z. Zhu, X. Lin, Y. Zhang, Y. He, H. Cao, and Z. Sun, *Engineering*, **4**, 370 (2018).
19. F. Saloojee and J. Lloyd, (2015), accessed 2019-10-15, https://sagreenfund.org.za/wordpress/wp-content/uploads/2015/07/Lithium-Battery-Recycling-Literature-Review-CM-Solutions.pdf.
20. J. Xiao, J. Li, and Z. Xu, *Environ. Sci. Technol.*, **54**, 25 (2019).
21. M. Joulié, R. Laucournet, and E. Billy, *J. Power Sources*, **247**, 555 (2014).
22. W. S. Chen and H. J. Ho, *Metals*, **8**, 321 (2018).
23. P. Liu, L. Xiao, Y. Tang, Y. Zhu, H. Chen, and Y. Chen, *Vacuum*, **156**, 324 (2018).
24. C. K. Lee and K. I. Rhee, *J. Power Sources*, **109**, 21 (2002).
25. X. Song, T. Hu, C. Liang, H. L. Long, L. Zhou, W. Song, and J. W. Liu, *RSC Adv.*, **7**, 4790 (2017).
26. X. Zhang, Y. Xie, H. Cao, F. Nawaz, and Y. Zhang, *J. Waste Manag.*, **34**, 1724 (2014).
27. Y. Mao, X. Shen, Z. Wu, L. Zhu, and G. Liao, *J. Alloys Compd.*, **816**, 152604 (2020).
28. T. Or, S. W. Gourley, K. Kaliyappan, A. Yu, and Z. Chen, *Carbon Energy*, **2**, 43 (2020).
29. S. Maiti, A. Pramanik, U. Manju, and S. Mahanty, *ACS Appl. Mater. Interfaces*, **7**, 16363 (2015).
30. G. Sun, L. Yu, Y. Hu, Y. Sha, H. Rong, B. Li, and Q. Liu, *Cryst. Growth Des.*, **19**, 6510 (2019).
31. N. Palaniyandy, K. Rambau, N. Musyoka, and J. Ren, *J. Electrochem. Soc.*, **167**, 090510 (2020).
32. S. Sundriyal, S. Mishra, and A. Deep, *Energy Procedia*, **158**, 5824 (2019).
33. D. Wu, W. Yan, H. Xu, E. Zhang, and Q. Li, *Inorganica Chim. Acta*, **460**, 98 (2017).
34. Y. Wu, X. Song, J. Zhang, S. Xu, L. Gao, J. Zhang, and G. Xiao, *Chem. Eng. Sci.*, **201**, 297 (2019).
35. H. Hu, X. Lou, C. Li, X. Hu, T. Li, Q. Chen, M. Shen, and B. Hu, *New J. Chem.*, **40**, 9752 (2016).
36. K. S. Sing, *Pure Appl. Chem.*, **57**, 619 (1985).
37. Q. Liu, L. Yu, Y. Wang, Y. Ji, J. Horvat, M. L. Cheng, and G. Wang, *Inorg. Chem.*, **52**, 2822 (2013).
38. N. Palaniyandy, F. P. Nkosi, K. Raju, and K. I. Ozoemena, *J. Electroanal. Chem.*, **833**, 92 (2019).
39. P. Nithyadharseni, M. V. Reddy, B. Nalini, and B. V. Chowdari, *Mater. Lett.*, **150**, 27 (2015).
40. P. Nithyadharseni, M. V. Reddy, B. Nalini, T. R. Ravindran, B. C. Illai, M. Alpana, and B. V. Chowdari, *Mater. Res. Bull.*, **70**, 485 (2015).
41. C. Li, X. Hu, W. Tong, W. Yan, X. Lou, M. Shen, and B. Hu, *ACS Appl. Mater. Interfaces*, **9**, 29838 (2017).
42. H. Song, L. Shen, J. Wang, and C. Wang, *Nano Energy*, **34**, 57 (2017).
43. S. A. Melchior, N. Palaniyandy, I. Sigalas, S. E. Iyuke, and K. I. Ozoemena, *Electrochim. Acta*, **297**, 973 (2019).
44. M. V. Reddy, S. Madhavi, G. S. Rao, and B. V. Chowdari, *J. Power Sources*, **162**, 1321 (2006).
45. P. Nithyadharseni, M. V. Reddy, B. Nalini, M. Kalpana, and B. V. Chowdari, *Electrochim. Acta*, **161**, 268 (2015).

4.1.3. Conclusion

In conclusion, spent LIBs were successfully utilized as metal feedstock for the preparation of Mn-based MOFs. The Mn-MOF obtained from HCl as salt convertor (Mn-MOF(Cl_2)) had properties similar to Mn-based MOF prepared using a commercial $MnCl_2$ metal salt, based on its morphological, structural and textural properties. It further showed exceptional electrochemical performance corroborated by discharge specific capacity of 1355 mAh g^{-1} and 99% coulombic efficiency. This study has a potential to be scaled up as a means of creating novel ways of recycling spent LIBs.

4.2. Preparation of Coal Fly Ash Derived Metal-Organic Frameworks and their Carbon Derivatives

4.2.1. Summary of Work

Herein, the authors present a novel approach of utilizing coal fly ash (CFA) leachate as a metal feedstock for MOF preparation. Approximately 50 million tons of CFA is produced in South Africa, of which only 10% is utilized in the Portland cement constituent and road construction industry, with the remainder distributed to landfills and slurry dams [299–301]. This poses an environmental threat as CFA particles leach out toxic metals during rainfall, which contaminates the soil, groundwater and vegetation. This predicament costs the government money and needs proper handling [302–304]. Albeit the cons of CFA, they possess metals such as aluminium (Al) in the form of amorphous aluminosilicate glass and mullite mineral ($3Al_2O_3.2SiO_2$) [305,306]. Such properties have enabled CFA to be used in various applications including catalysis. It has been reported that CFA was activated through heat and fused with chromium-based MOF (MIL-101(Cr)) to form a stable composite [306]. Apart from this case, there are no reports of CFA being utilized as metal feedstock for MOF synthesis. Therefore, the author presents a novel way of synthesizing coal fly ash derived MOF. Direct carbonization was applied to the coal fly ash derived MOF for porosity, and surface area enhancement by conversion to carbon material or MOF derived carbons (MDCs). This process is a common way of obtaining hierarchical porous carbons possessing high surface area, large pore volume with good thermal and chemical stability [307]. The method involves heat-treating MOFs under inert conditions at high temperatures. This enables the MOF structure to disintegrate acting as a sacrificial template for carbon. Most metals vaporize at those working temperatures and the remainder are chemically removed remaining with a porous carbon. This

thesis reports on the comparative investigation of CFA derived MOFs with aluminium fumarate MOF together with their carbon derivative.

4.2.2. Results and Discussion

Materials Today Communications 27 (2021) 102433

Contents lists available at ScienceDirect

Materials Today Communications

journal homepage: www.elsevier.com/locate/mtcomm

Preparation of coal fly ash derived metal organic frameworks and their carbon derivatives

Khavharendwe M. Rambau [a,b], Nicholas M. Musyoka [a,*], Rafal Panek [c], Wojciech Franus [c], Magdalena Wdowin [d,*], Ncholu Manyala [b,*]

[a] HySA Infrastructure Centre of Competence, Centre for Nanostructures and Advanced Materials (CeNAM), Chemicals Cluster, Council for Scientific and Industrial Research (CSIR), Meiring Naude Road, Brummeria, Pretoria, 0001, South Africa
[b] Department of Physics, Institute of Applied Materials, SARCHI Chair in Carbon Technology and Materials, University of Pretoria, South Africa
[c] Department of Geotechnics, Faculty of Civil Engineering and Architecture, Lublin University of Technology, Nadbystrzycka 40, 20-618, Lublin, Poland
[d] Mineral and Energy Economy Research Institute, Polish Academy of Sciences, Wybickiego 7A, 31-261, Kraków, Poland

ARTICLE INFO

Keywords:
Coal fly ash
Aluminium fumarate metal organic framework
Coal fly ash derived metal organic framework
Metal organic framework derived carbons

ABSTRACT

In this study, a new strategy for preparing metal organic frameworks (MOFs) using coal fly ash (CFA) as a metal feedstock is introduced. Aluminium and other metal species were leached out from CFA using sulfuric acid and reacted with fumaric acid following a procedure that had been optimized to mimic Aluminium fumarate MOF (Al-FumMOF). Despite the presence of different metals in the synthesis solution, the prepared coal fly ash derived MOF (CFA-FumMOF) exhibited almost similar characteristics to Al-FumMOF synthesized using commercial chemicals. In this case, the surface area of 1236 m^2/g was obtained for CFA-FumMOF, whereas that of Al-FumMOF was 1266 m^2/g. For pore enhancement, the prepared CFA-FumMOF was subjected to direct carbonization and resulted in improved surface area (i.e. increase from 1236 m^2/g to 2017 m^2/g). The developed innovative strategy of using CFA leachate in MOF synthesis has the potential for lowering the cost of producing MOFs as well as create a new route for value-addition of the waste CFA for many applications.

1. Introduction

MOFs are composed of secondary building units of metal clusters and organic linkers connected to form 3D lattices with cavities [1,2]. There are various organic linkers and metal clusters that can be utilized in the synthesis of numerous types of MOFs [3–5]. These different building units give MOFs desirable properties such as permanent porosity, tunable pore sizes and stability (chemical, thermal and hydro) and have made MOFs to be attractive for application such as sensors, photovoltaics, catalysis and energy storage [6–15]. Despite the impressive properties and applications, the biggest challenge for MOFs commercialization is their high cost of production due to few options for environmentally friendly feedstock (metal salts and linkers). In addition to the present drawback, the upscaling conditions are complicated thus making it difficult for wide-spread MOF commercialization [16].

The most utilized organic linkers are carboxylates, phosphonate, sulfonates and heterocyclic compounds, while metal clusters are usually derived from specific metals salts [17]. The utilization of commercially available metal salts and organic linkers is a conventional norm. However, these feedstocks are quite expensive and often not environmentally friendly. There have been efforts to introduce greener and inexpensive synthesis routes that involve substitution of harmful organic solvents such as dimethylformamide (DMF) with less harsh solvents such as ethanol, water and inclusion of solvent-free reaction routes such as ball milling [18,19]. MOFs obtained through these synthesis routes are still crystalline and possess comparable properties with those prepared using conventional routes [20,21]. Other greener, inexpensive, and energy-efficient synthesis routes such as sonochemical, microwave and electrochemical have also been designed and are currently implemented in MOFs synthesis routes [22–25].

Recently, pristine organic linkers such as terephthalic acid (H_2BDC) have been substituted with those obtained from wastes such as discarded textile fibres as well as spent polyethylene terephthalate (PET) bottles and product [26,28]. This approach presents a potentially attractive means of cutting the cost of MOFs production. There are also attempts to substitute commercial metal oxides and salts as feedstocks by utilizing mineral feedstocks that are ground to spark reactivity that leads to the formation of 2D and 3D MOFs [29,30]. There are few reports on the use

* Corresponding authors.
E-mail addresses: NMusyoka@csir.co.za (N.M. Musyoka), wdowin@min-pan.krakow.pl (M. Wdowin), ncholu.manyala@up.ac.za (N. Manyala).

https://doi.org/10.1016/j.mtcomm.2021.102433
Received 15 July 2020; Received in revised form 30 April 2021; Accepted 4 May 2021
Available online 7 May 2021

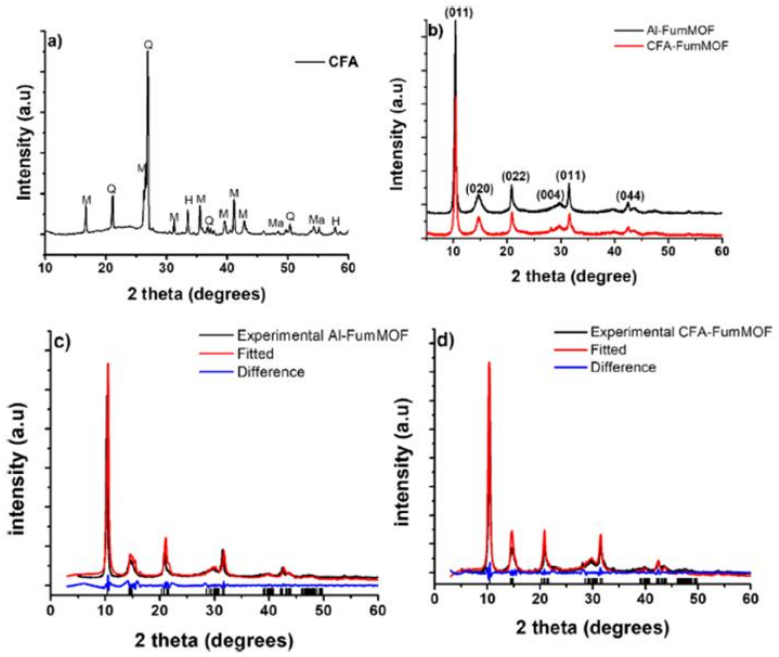

Fig. 1. a) XRD Pattern of CFA b) Comparative XRD Patterns of prepared Al-FumMOF and CFA-FumMOF c, d) Comparisons of simulated patterns with those of prepared Al-FumMOF and CFA-FumMOF (M – mullite, Q- quartz, H-hematite, Ma – magnetite).

of divalent metal ions that are derived from waste materials such as alkaline batteries, oil refinery carbon black waste, wastewater and aluminium foils as metal feedstock for MOF preparation [31]. Of interest to this study is coal combustion by-products as a potential source of metal salts for MOF synthesis.

Coal fly ash (CFA) is one of the by-products of coal combustion, a source of energy for many countries. South Africa produces close to 50 million tons of CFA of which only 10 % is utilized, with the rest dumped in slurry dams [32–34]. With such a large amount in slurry dams, CFA is considered an environmental hazard due to the potential for leaching out toxic metals to the soil and underground water [35–37]. Despite these disadvantages, CFA consists of a considerable amount of aluminium (Al) in the form of mullite mineral ($3Al_2O_3.2SiO_2$) and amorphous aluminosilicate glass [38,39]. These mineralogical composition properties have enabled CFA to be used as a catalyst after activation and other applications. For example, activated CFA was previously used as a composite material to stabilize chromium-based MOF (MIL-101) [39]. However, to the best of our knowledge, no studies have reported on the utilization of coal fly ash (CFA) as a source of metal nodes for MOFs synthesis and hence the novel aspect of the current study.

To further enhance the surface area and porosity of the CFA-derived MOF, the resulting MOF was subjected to direct carbonization to convert it into a high surface area carbonaceous material referred to as MOF-derived carbon (MDC). Direct carbonization is an attractive method of obtaining hierarchical porous carbons that possess large pore volumes as well as good thermal and chemical stabilities [40]. This method involves heating a MOF sample at high temperatures, under inert conditions, where the MOF structure decomposes and acts as a carbon source. Therefore, this communication also reports on the comparative properties of CFA-derived MOFs with their carbon derivative.

2. Experimental

2.1. Materials

Coal fly ash samples were obtained from a South African power station. Sulphuric acid (H_2SO_4, 98 %), fumaric acid ($C_4H_4O_4$, 99 %) and sodium hydroxide (NaOH, 99 %) were supplied by Sigma Aldrich. Aluminium sulphate octadecahydrate ($Al_2(SO_4)_3.18H_2O$, 99 %), hydrofluoric acid (HF, 40 %) and hydrochloric acid (HCl, 37 %) were supplied by associated chemical enterprises company. Afrox South Africa supplied argon and nitrogen.

2.2. Synthesis of coal derived MOFs

The CFA leaching method was adapted from studies by Missengue et al [27]. In this case, 100 g of CFA was mixed with 200 mL of H_2SO_4. The mixture was heated at 230 °C with stirring for 24 h. Thereafter, the temperature was increased above 340 °C to evaporate H_2SO_4. After evaporation, CFA was heated for an additional 30 min to be completely dry. The resultant mixture was then mixed with water on a ratio of 1:6 (CFA: H_2O) w/vol and stirred at 90 °C for 30 min. This step is crucial so that Al is obtained in the form of aluminium sulphate. If not the case, there will be no MOF materialization rather the recrystallization of fumaric acid as depicted by Figs. S1 and S2. The mixture was then filtered, and the resulting filtrate (79.5 mL) was set aside to be used for MOF synthesis (solution A). In a different beaker, 6.45 g of fumaric acid (organic linker) and 4.75 g of NaOH were mixed with 95.5 mL of deionized water (Solution B). The MOF synthesis procedure was conducted following a slight modification of a previous study [41]. In this case, both solutions A and B were independently heated at 60 °C for 1 h. Thereafter, the two solutions were mixed (still heating at 60 °C) and stirred for 2 h. After the reaction, the mixture was filtered, washed with deionized water and dried at 105 °C for 24 h. For comparison purposes,

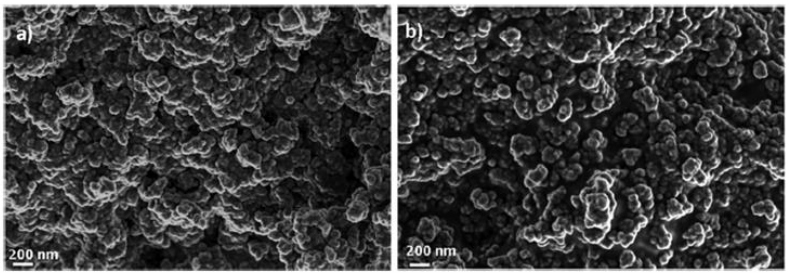

Fig. 2. SEM images of a) Al-FumMOF and b) CFA-FumMOF.

aluminium fumarate MOF was also prepared using $Al_2(SO_4)_3.18H_2O$ as metal feedstock. The CFA derived MOF is denoted as CFA-FumMOF, whereas aluminium fumarate MOF prepared from commercial chemicals is denoted as Al-FumMOF.

2.3. Preparations of MDCs

For the MOF-derived carbons (MDCs) preparation, the obtained MOFs were placed in a tube furnace and heated under argon flow at 800 °C for 2 h, then cooled to room temperature. The resulting black material was washed using 10 % HF for 4 h and subsequently refluxed using 10 % HCl at 70 °C overnight. The resulting material was then thoroughly washed with deionized water and collected for characterization. The obtained carbon material from Al-FumMOF and CFA-FumMOF were denoted Al-MDC and CFA-MDC, respectively.

2.4. Characterization

The morphological characteristics of the obtained MOFs and MDCs was analyzed using an Auriga Cobra Focused-Ion-Beam Scanning Electron Microscope (FIB-SEM). X-ray diffraction (XRD) patterns were obtained using a PANalytical X'Pert Pro powder diffractometer with Pixcel detector using Ni-filtered Cu-Kα radiation (0.154 nm) in the range of $2\theta = 1–90°$ at a scanning rate of $0.1°s^{-1}$ and the diffractograms were analyzed using Rietveld refinement via TOPAS (v3.1). The Raman analysis was performed using Jobin-Yvon T64000 Raman spectrometer. FTIR was performed using Attenuated Total Reflection-Fourier Transform Infrared (ATR-FTIR) spectrum (spectrum 100 FTIR spectrometer, PerkinsElmer Inc) by four scans with a resolution of $4\,cm^{-1}$. The elemental composition of the materials was analyzed by X-ray energy dispersive fluorescence spectrometer (XRF, PANalytical Epsilon 3 spectrometer) within the range of Na-Am (sodium to americium). The instrument is equipped with X-ray tube Rh 9 W,50 kV, 1 mA, 4096-channel spectrum analyzer, 6 measurement filters (Cu-500,Cu-300, Ti, Al-50, Al-200, Ag) and high-solid state detector SDD (50 µm thickness) cooled by a Peltier cell. Thermogravimetric Analysis (TGA) was performed using the Hitachi STA 7300 with alumina crucibles under air at temperature rate of 10 °C/min. For XPS analysis, Thermo ESCAlab 250Xi Spectrometer was used with X-rays of monochromatic Al kα (1486.7 eV), Xray power (300 W) and spot size 900 µm. The survey spectrum was analysed at 100 eV, high resolution at 20 eV and pressure <10−8 mbar. BET surface area measurements were conducted by volumetric analysis at liquid nitrogen temperature (77 K) using Micromeritics ASAP 2020. Before each gas sorption analysis, samples were degassed under vacuum at 150 °C (MOF) and 200 °C (MDC) for 8 h. Pore size distribution of the materials was obtained using non-local density functional theory (NLDFT), micropore volume was determined using the t-plot and pore volume using the Horvath–Kawazoe (HK) method.

3. Results and discussion

3.1. Morphological and structural analysis

The XRD patterns in Fig. 1 presents the structural properties of CFA and the prepared MOFs. Peaks associated with mullite (M), quartz (Q) and hematite (H) in Fig. 1a) indicate the presence of aluminium, silica and iron in CFA [37,38]. The CFA also has an amorphous aluminosilicate phase as depicted by the hump appearing at 15−30° 2θ range. From Fig. 1b), c) and d), the CFA-FumMOF crystallinity is closely comparable to the pristine Al-FumMOF with very subtle differences as shown with fitted patterns. The refined lattice parameters of the synthesized Al-FumMOF are a =6.9 Å, b =11.9 Å, c =14.4 Å whereas those of the

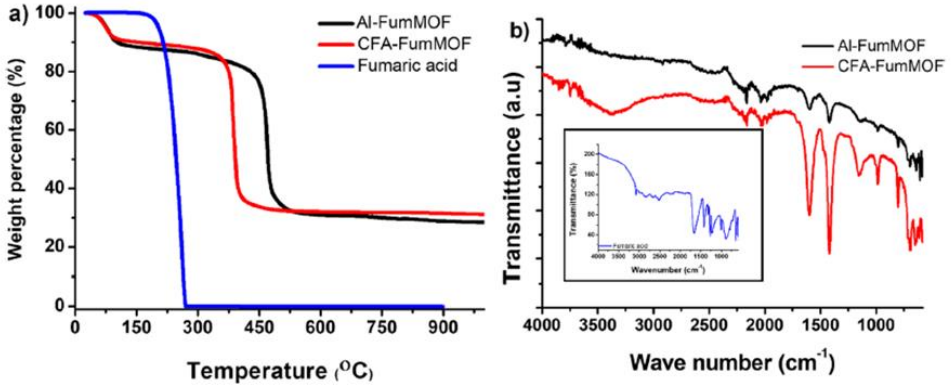

Fig. 3. a) TGA plots for the prepared MOFs and Fumaric acid and b) FTIR spectra for the prepared MOFs and fumaric acid (insert).

Table 1
XRF analysis of Chemical composition of CFA and CFA-FumMOF.

Compounds	Coal fly ash Concentration (wt. %)	CFA-FumMOF Concentration (wt. %)
SiO_2	52.9	0.1
Al_2O_3	26.4	19.3
P_2O_5	1.4	0.3
Fe_2O_3	3.5	9.2
K_2O	0.9	<0.1
CaO	8.9	<0.1
TiO_2	2.1	0.6
Cr_2O_3	0.1	<0.1
MnO	0.1	<0.1
CuO	0.9	<0.1
ZrO_2	0.1	0.3
ZnO	0.4	0.4

obtained CFA-FumMOF are a =6.8 Å, b=12.1 Å, c = 14.3 Å. These lattice parameters are in good agreement with the crystallographic information file of aluminium fumarate MOF (Table S1). This finding affirms the crystallinity of the obtained material, which conforms to the octahedral structure that possesses infinite number consecution of Al-OH-Al structures that are connected by the fumarate linker forming rhombohedral channels [41,42]. These results serve as an indication that the topology is maintained and that both CFA-FumMOF and Al-FumMOF are almost similar, as suggested by the SEM images presented in Fig. 2a) and b). In this case, their morphology consists of small clusters which are consistent with the commercial Basolite A520 [41,43].

Thermogravimetric analysis was conducted to determine the structural change of the materials with temperature, as shown in Fig. 3a). The organic linker was found to be stable up to about 268 °C, and thereafter, it decomposes completely. The initial weight loss of the prepared MOFs was observed between temperatures 76 °C and 80 °C, which can be attributed to moisture loss. The degradation of the organic linker (weight loss of about 26 %) is observed at 469 °C and 385 °C for Al-FumMOF and CFA-FumMOF, respectively, which is in accordance with previous results [44]. The prepared MOFs were not burned out completely but rather turning the remainder of the materials into residual metal oxides [41,44,45]. These results confirm the coordination of the organic linker with the metals.

FTIR spectra of the fumaric acid (insert) and the prepared MOFs are compared in Fig. 3b.. Fumaric acid has an O—H vibration from 3300 to 2500 cm^{-1} and C═O stretch at 1671 cm^{-1} associated with the COOH group [46]. The prepared MOFs possess the broad peak centered at 3500 cm^{-1}, which is attributed to the O—H vibration of the residual H_2O compound as confirmed by the TGA results. The peaks at 1420 and 1602 cm^{-1} indicate the asymmetric and symmetric stretching vibrations of COO-. The presence of Al metals is confirmed by the Al—OH stretch at 580 cm^{-1} [47,48]. Raman spectroscopy further confirmed the obtained results as indicated by Fig. S3. Signature peaks of MOFs were observed at 1464.7 and 1669.2 cm^{-1}, which indicate the coordination bonding of symmetric stretching and asymmetric stretching of COO- which is already confirmed by FTIR. The peak at 3067 cm^{-1} is consistent with those in fumaric acid functional groups, indicating the possible coordination between the metal center and the organic linkers [44]. These results further confirm the possible coordination of Al—OH from the CFA leachate with the organic linker forming CFA-FumMOF.

The chemical composition of the utilized South African CFA and the obtained CFA-FumMOF is presented in Table 1. Aluminium, silicon, iron and calcium are present in the CFA in the form of mullite, quartz, hematite and lime, respectively [49–51]. The results also indicate that the dominant metal in CFA-FumMOF is Al, followed by Fe and other trace metals in small quantity. As expected, the organic linker coordinated mainly with Al due to its abundant quantity, valence state, the favourable synthesis conditions. It can be speculated that isomorphic substitution could have occurred between Fe^{3+} and Al^{3+} due to the proximity of their ionic radii (Al^{3+}: 0.5, Fe^{3+}: 0.6) [57]. According to Pearson's hard/soft acid/base (HSAB) principle, Hard Lewis acids prefer to bond with Hard Lewis bases whereas Soft Lewis acids prefer to bond with Soft Lewis bases [52,53]. This principle stipulates that high-valence metal ions with high energy density will increase the electrostatic interaction between metal and linker. This in turn forms a stable complex given the linker is in the high-valent carboxylate groups, and the coordination environment remains constant [54–56], elucidating the isomorphic substitution of the metals. However, this would require further confirmatory studies.

To further investigate the successful coordination of Al and the organic linker in CFA-FumMOF, XPS analysis was conducted, and the results are presented in Fig. 4a) and b). The full survey spectrum of CFA-FumMOF confirms the presence of C (285.2 eV), Al (74.8 eV) Fe (710.1 eV) and O (532.7 eV) elements without detecting the presence of any other metals, possibly due to their uneven distribution. The deconvolution spectra of C1s core level displays the presence of the carbons associated with benzoic ring (C—C) at 284.9 eV, C—O bond at 285.8 eV and the carboxylate group (O—C = O) at 289.3 eV, which reinforces the presence of the organic linker [47]. The O1s and Al_2p deconvoluted spectra in Fig. S4 indicate the presence of Al-O bonding which further substantiates the successful coordination of Al and the organic linker.

3.2. Morphological and structural analysis of MDCs

The XRD patterns of the MOF-derived carbon materials are presented in Fig. 5a) whereas their corresponding SEM images are shown in Fig. 6a) and b). The peaks that were associated with the synthesized parent MOFs (seen in Fig. 1) were not present after the MOF carbonization.process. This finding indicates that successful MOF-derived carbon materials were formed. In this case, the MOF precursor is completely carbonized at high temperatures. The Al metal species and

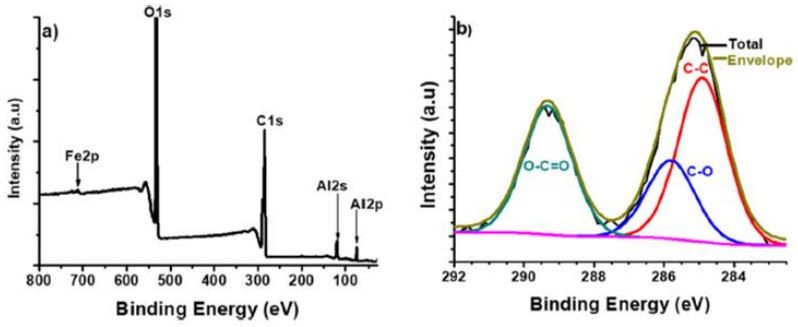

Fig. 4. a) XPS full survey scan for CFA-FumMOF and b) XPS spectra for carbon peaks on CFA-FumMOF.

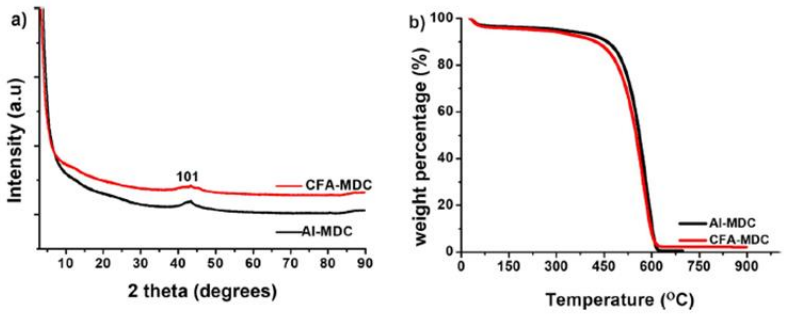

Fig. 5. a) XRD patterns of MDCs and their b) TGA plots.

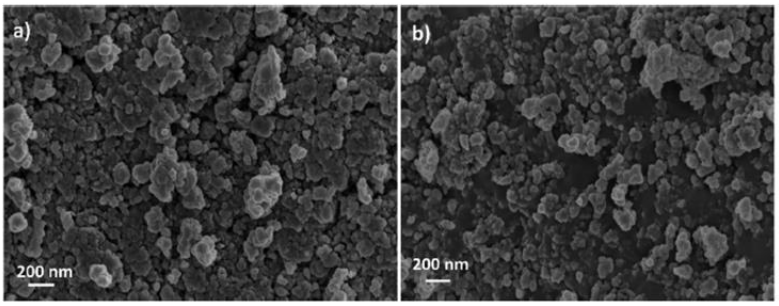

Fig. 6. SEM Images of a) Al-MDC and (d) CFA-MDC.

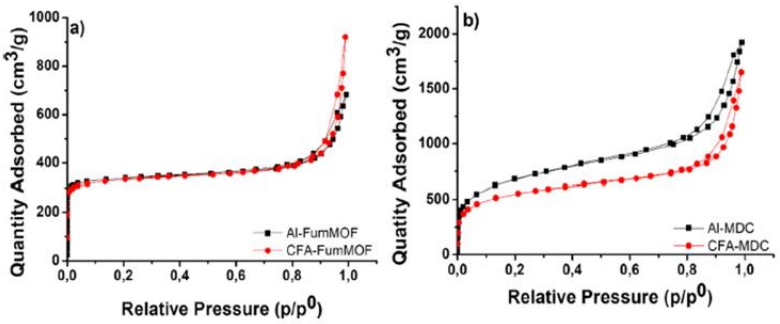

Fig. 7. N_2 sorption Isotherm for a) prepared MOFs and b) MDCs.

other trace metals are converted into their oxide form, soluble in HF and HCl and washed out during the washing step. From the XRD patterns of the MDCs presented in Fig. 5a), there is the presence of a 101 peak at $2\theta = 44°$ which can be attributed to the graphitic nature of the carbons [58,59]. The comparative SEM images of the parent MOFs and MDCs shown in Fig. 6a) and b) confirms the similarity of their morphological characteristics. The retention of the morphology indicates that the structure of the MOF did not collapse even after successful carbonization [58,60]. The thermal gravimetric analysis corroborates the complete conversion of MOF-to-Carbon, as shown in Fig. 5b). In this case, the TGA showed negligible weight loss (<5 wt.%) at the initial temperature due to the loss of moisture trapped within the pore structure. The material remains stable until the decomposition of carbon occurs at 600 °C. It is noteworthy that the material burned out completely, indicating that it was purely carbonaceous [58]. With these results at hand, it can be confidently confirmed that the conversion of Al-FumMOF and CFA-FumMOF to carbon material was accomplished.

3.3. Textural properties of prepared MOFs and MDCs

N_2 sorption analysis was conducted as presented in Fig. 7a) and b) to

Table 2
Textural properties of the prepared MOFs and their derived carbons.

Sample	BET SA (m^2/g)	Micropore Vol (cm^3/g)	Pore Vol (cm^3/g)
Al-FumMOF	1266	0.5	1.1
CFA-FumMOF	1236	0.5	1.4
Al-MDC	2438	0.8	3.0
CFA-MDC	2017	0.7	2.6

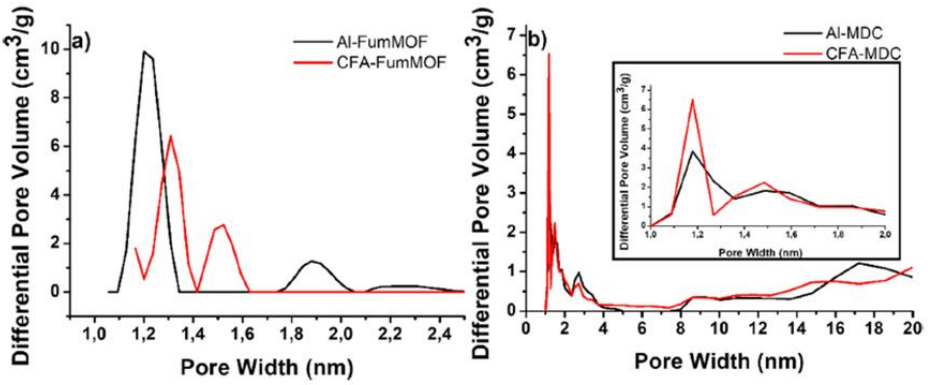

Fig. 8. Pore size distribution (PSD) plots of a) Prepared MOFs and b) MDCs.

determine the surface area and porosity characteristics of the prepared MOFs and their carbon derivatives. According to the IUPAC classification, the sorption plots exhibits both type I and IV isotherms [61]. The isotherms consist of a sharp step of adsorption at low pressures, which indicates the presence of micropores. A hysteresis loop indicates the existence of mesopores at pressures $p/p_0>0.8$, which occurs due to capillary condensation within these pores [62,63]. According to De Boer hysteresis loop classification, the obtained hysteresis loops are a type H1 that indicates that the pore structures are cylindrically shaped with narrow pore size distribution [64,65].

The surface area of the Al-FumMOF and CFA-FumMOF was found to be 1266 m^2/g and 1236 m^2/g, respectively (Table 2). Regardless of the different sources of metals for the MOFs preparation, the textural properties were closely comparable and almost similar to other previous reports [41,66]. After direct carbonization of the MOFs, there is enhancement of the textural properties as indicated by Fig. 7b) and Table 2. The isotherms of the obtained MDCs also have similar characteristics when compared to the parent MOFs which indicates close similarities of their pore geometries. However, the resulting MDC isotherms had high N_2 adsorption at low pressures than the parent material [58]. The Surface area was also noted to increase significantly to 2438 m^2/g and 2017 m^2/g for Al-MDC and CFA-MDC, respectively.

The textural properties are corroborated by the pore size distribution (PSD) presented in Fig. 8a) and b). The pore sizes of the prepared MOFs consist of a narrow bimodal pore distribution in the micropore range with dominant pores centered between 1.2 and 1.8 nm for both Al-FumMOF and CFA-FumMOF, respectively. It is further observed that there is a pore shift towards 1.3 nm and 1.5 nm for CFA-FumMOF, which could be due to the widening of the pores, possibly because of the presence of other elements with high ionic radii. The resulting MDC had narrower polymodal micropore distribution centered at 1.2 nm, 1.2 nm and 1.5 nm. These observations substantiate the high surface areas that are as depicted in Table 2 and are comparable to previous reports [66–68].

4. Conclusion

The synthesis of CFA-FumMOF using CFA derived leachate, as metal feedstock, was successful. Despite the presence of mixed metals in the synthesis solution, the prepared CFA-FumMOF exhibited almost similar characteristics to the commercial Al-FumMOF based on its morphological, structural and textural properties. The obtained CFA-FumMOF had a surface area of 1236 m^2/g, which is comparable to the commercially prepared Al-FumMOF (1266 m^2/g). MOF-derived carbons were also obtained through direct carbonization of the parent MOFs. The carbonization process successfully yielded enhanced porosity of the material with surface area of 2438 m^2/g and 2017 m^2/g for Al-MDC and CFA-MDC, respectively. This study presents an innovative strategy for preparing low-cost MOFs using waste materials and can benefit the environment by recycling CFA and creating new value-added materials. With optimization and further studies, there is a high potential for the preparation of good quality MOFs from CFA that can be used for many other applications.

CRediT authorship contribution statement

Khavharendwe M. Rambau: Investigation, Methodology, Writing - original draft, Visualization. **Nicholas M. Musyoka:** Conceptualization, Supervision, Funding acquisition, Writing - review & editing. **Rafal Panek:** Methodology, Writing - review & editing. **Wojciech Franus:** Supervision, Resources. **Magdalena Wdowin:** Writing - review & editing, Funding acquisition. **Ncholu Manyala:** Supervision, Writing - review & editing.

Declaration of Competing Interest

The authors report no declarations of interest.

Acknowledgements

KR and NMM would like to acknowledge the financial support from the South African Department of Science and Innovation (DSI) for research activities under the HySA Infrastructure as well as the National Research Foundation (NRF) for funding South Africa-Poland bilateral collaboration (Project No. CNMH01X and EIMH04X). MW, WF, and RP also thank the Polish National Centre for Research and Development (NCBR) for providing funding for the SA-Poland collaboration (Grant No. PL-RPA/SFZCHSA/06/2016). NM acknowledge the financial support by South African Research Chairs Initiatives (SARChI) of the Department of Science and Technology and the National Research Foundation (NRF) of South Africa (Grant No. 61056). Any opinions, findings and/or recommendations expressed here are those of the authors and not of the funding bodies.

Appendix A. Supplementary data

Supplementary material related to this article can be found, in the online version, at doi:https://doi.org/10.1016/j.mtcomm.2021.102433.

References

[1] P.A. Kobielska, A.J. Howarth, O.K. Farha, S. Nayak, Metal–organic frameworks for heavy metal removal from water, Coord. Chem. Rev. 358 (2018) 92–107.
[2] R.B. Lin, S. Xiang, B. Li, Y. Cui, G. Qian, W. Zhou, B. Chen, Our journey of developing multifunctional metal-organic frameworks, Coord. Chem. Rev. 384 (2019) 21–36.
[3] Y.Z. Chen, R. Zhang, L. Jiao, H.L. Jiang, Metal–organic framework-derived porous materials for catalysis, Coord. Chem. Rev. 362 (2018) 1–23.
[4] S. Natarajan, P. Mahata, Metal–organic framework structures–how closely are they related to classical inorganic structures? Chem. Soc. Rev. 38 (2009) 2304–2318.
[5] D.J. Tranchemontagne, J.L. Mendoza-Cortés, M. O'Keeffe, O.M. Yaghi, Secondary building units, nets and bonding in the chemistry of metal–organic frameworks, Chem. Soc. Rev. 38 (2009) 1257–1283.
[6] F.X. Coudert, A.H. Fuchs, Computational characterization and prediction of metal–organic framework properties, Coord. Chem. Rev. 307 (2016) 211–236.
[7] K. Wang, D. Feng, T.F. Liu, J. Su, S. Yuan, Y.P. Chen, H.C. Zhou, A series of highly stable mesoporous metalloporphyrin Fe-MOFs, J. Am. Chem. Soc. 136 (2014) 13983–13986.
[8] D. Feng, K. Wang, Z. Wei, Y.P. Chen, C.M. Simon, R.K. Arvapally, D. Yuan, Kinetically tuned dimensional augmentation as a versatile synthetic route towards robust metal–organic frameworks, Nat. Commun. 5 (2014) 5723.
[9] M.D. Allendorf, V. Stavila, Crystal engineering, structure–function relationships, and the future of metal–organic frameworks, Cryst. Eng. Commun. 17 (2015) 229–246.
[10] A.J. Howarth, A.W. Peters, N.A. Vermeulen, T.C. Wang, J.T. Hupp, O.K. Farha, Best practices for the synthesis, activation, and characterization of metal–organic frameworks, Chem. Mater. 29 (2016) 26–39.
[11] Y.Z. Chen, R. Zhang, L. Jiao, H.L. Jiang, Metal–organic framework-derived porous materials for catalysis, Coord. Chem. Rev. 362 (2018) 1–23.
[12] H. Wang, Q.L. Zhu, R. Zou, Q. Xu, Metal-organic frameworks for energy applications, Chemistry 2 (2017) 52–80.
[13] J. Zhu, T. Xia, Y. Cui, Y. Yang, G. Qian, A turn-on MOF-based luminescent sensor for highly selective detection of glutathione, J. Solid State Chem. 270 (2019) 317–323.
[14] R. Kaur, A.L. Sharma, K.H. Kim, A. Deep, A novel CdTe/Eu-MOF photoanode for application in quantum dot-sensitized solar cell to improve power conversion efficiency, J. Ind. Eng. Chem 53 (2017) 77–81.
[15] D. Jiang, M. Chen, H. Wang, G. Zeng, D. Huang, M. Cheng, Z. Wang, The application of different typological and structural MOFs-based materials for the dyes adsorption, Coord. Chem. Rev. 380 (2019) 471–483.
[16] J. Ren, X. Dyosiba, N.M. Musyoka, H.W. Langmi, M. Mathe, S. Liao, Review on the current practices and efforts towards pilot-scale production of metal-organic frameworks (MOFs), Coord. Chem. Rev. 352 (2017) 187–219.
[17] W. Lu, Z. Wei, Z.Y. Gu, T.F. Liu, J. Park, J. Park, M. Bosch, Tuning the structure and function of metal–organic frameworks via linker design, Chem. Soc. Rev. 43 (2014) 5561–5593.
[18] J. Zhang, G.B. White, M.D. Ryan, A.J. Hunt, M.J. Katz, Dihydrolevoglucosenone (cyrene) as a green alternative to N, N-dimethylformamide (DMF) in MOF synthesis, ACS Sustain. Chem. Eng. 4 (2016) 7186–7192.
[19] H. Yang, S. Orefuwa, A. Goudy, Study of mechanochemical synthesis in the formation of the metal–organic framework $Cu_3(BTC)_2$ for hydrogen storage, Microporous Mesoporous Mater. 143 (2011) 37–45.
[20] F.A.A. Paz, J. Klinowski, Hydrothermal synthesis and structural characterization of a novel cadmium-organic framework, J. Solid State Chem. 177 (2004) 3423–3432.
[21] R. Seetharaj, P.V. Vandana, P. Arya, S. Mathew, Dependence of solvents, pH, molar ratio and temperature in tuning metal organic framework architecture, Arab. J. Chem. 12 (2019) 295–315.
[22] A. Tahmasian, A. Morsali, S.W. Joo, Sonochemical syntheses of a one-dimensional Mg (II) metal-organic framework: a new precursor for preparation of MgO one-dimensional nanostructure, J. Nanomater. 2013 (2013) 10.
[23] F. Zhang, T. Zhang, X. Zou, X. Liang, G. Zhu, F. Qu, Electrochemical synthesis of metal organic framework films with proton conductive property, Solid State Ion. 301 (2017) 125–132.
[24] T.W. Murinzi, E. Hosten, G.M. Watkins, Synthesis and characterization of a cobalt-2, 6-pyridinedicarboxylate MOF with potential application in electrochemical sensing, Polyhedron 137 (2017) 188–196.
[25] B.M. Connolly, J.P. Mehta, P.Z. Moghadam, A.E. Wheatley, D. Fairen-Jimenez, Prom synthesis to applications: metal-organic frameworks for an environmentally sustainable future, Curr. Opin. Green Sustain. Chem. 12 (2018) 47–56.
[26] V. Ting, V. Doan, in: Use of Waste TPA in the Synthesis of a Metal Organic Framework (MOF) for Use in Hydrogen Storage, Scientific Conference on Oil Refining and Pertrochemical Engineering, Hanoi, Viet Nam, 2014. Oct 8-10.
[27] R.N.M. Missengue, P. Losch, G. Sedres, N.M. Musyoka, O.O. Fatoba, B. Louis, L. F. Petrik, Transformation of South African coal fly ash into ZSM-5 zeolite and its application as an MTO catalyst, CR Chim. 20 (2017) 78–86.
[28] X. Dyosiba, J. Ren, N.M. Musyoka, H.W. Langmi, M. Mathe, M.S. Onyango, Preparation of value-added metal-organic frameworks (MOFs) using waste PET bottles as source of acid linker, Sustain. Mater. Technol. 10 (2016) 10–13.
[29] F. Qi, R.S. Stein, T. Friščić, Mimicking mineral neogenesis for the clean synthesis of metal–organic materials from mineral feedstocks: coordination polymers, MOFs and metal oxide separation, Green Chem. 16 (2014) 121–132.
[30] J. Zhao, W.T. Nunn, P.C. Lemaire, Y. Lin, M.D. Dickey, C.J. Oldham, G.N. Parsons, Facile conversion of hydroxy double salts to metal–organic frameworks using metal oxide particles and atomic layer deposition thin-film templates, J. Am. Chem. Soc. 137 (2015) 13756–13759.
[31] E.S.M. El-Sayed, D. Yuan, Waste to MOFs: sustainable linker, metal, and solvent sources for value-added MOF synthesis and applications, Green Chem. 22 (2020) 4082–4104.
[32] G. Wang, P.A. Jensen, H. Wu, F.J. Frandsen, Y. Laxminarayan, B. Sander, P. Glarborg, KOH capture by coal fly ash, Fuel 242 (2019) 828–836.
[33] N.J. Wagner, A. Matiane, Rare earth elements in select Main Karoo Basin (South Africa) coal and coal ash samples, Int. J. Coal Geol. 196 (2018) 82–92.
[34] S. Wang, H. Wu, Environmental-benign utilization of fly ash as low-cost adsorbents, J. Hazard. Mater. 136 (2006) 482–501.
[35] B. Lokeshappa, A.K. Dikshit, Behaviour of metals in coal fly ash ponds, APCBEE Proc. 1 (2012) 34–39.
[36] G. Singh, S. Kumar, M.K. Singh, S.K. Mohapatra, Environmental impact assessment of ash disposal system of a thermal power plant, Int. J. Hydrogen Energy 41 (2016) 15887–15891.
[37] D.K. Gupta, U.N. Rai, R.D. Tripathi, M. Inouhe, Impacts of fly-ash on soil and plant responses, J. Plant Res. 115 (2002) 401–409.
[38] W. Franus, M.M. Wiatros-Motyka, M. Wdowin, Coal fly ash as a resource for rare earth elements, Environ. Sci. Pollut. Res. 22 (2015) 9464–9474.
[39] A. Chatterjee, X. Hu, F.L.Y. Lam, Catalytic activity of an economically sustainable fly-ash-metal-organic-framework composite towards biomass valorization, Catal. Today 314 (2018) 137–146.
[40] X. Yan, X. Li, Z. Yan, S. Komarneni, Porous carbons prepared by direct carbonization of MOFs for supercapacitors, Appl. Surf. Sci. 308 (2014) 306–310.
[41] J. Dechnik, C. Janiak, S. De, Aluminium fumarate metal-organic framework: a super adsorbent for fluoride from water, J. Hazard. Mater. 303 (2016) 10–20.
[42] N. Tannert, C. Jansen, S. Nießing, C. Janiak, Robust synthesis routes and porosity of the Al-based metal–organic frameworks Al-fumarate, CAU-10-H and MIL-160, J. Chem. Soc. Dalton Trans. 48 (2019) 2967–2976.
[43] M. Gaab, N. Trukhan, S. Maurer, R. Gummaraju, U. Müller, The progression of Al-based metal-organic frameworks-From academic research to industrial production and applications, Microporous Mesoporous Mater. 157 (2012) 131–136.
[44] Y. Wang, Q. Qu, G. Liu, V.S. Battaglia, H. Zheng, Aluminum fumarate-based metal organic frameworks with tremella-like structure as ultrafast and stable anode for lithium-ion batteries, Nano Energy 39 (2017) 200–210.
[45] G.C. Shearer, S. Chavan, J. Ethiraj, J.G. Vitillo, S. Svelle, U. Olsbye, K.P. Lillerud, Tuned to perfection: ironing out the defects in metal–organic framework uio-66, Chem. Mater. 26 (2014) 4068–4071.
[46] L. Zhou, X. Zhang, Y. Chen, Facile synthesis of Al-fumarate metal–organic framework nano-flakes and their highly selective adsorption of volatile organic compounds, Mater. Lett. 197 (2017) 224–227.
[47] J. Li, W. Huang, M. Wang, S. Xi, J. Meng, K. Zhao, Q. Chen, Low-crystalline bimetallic metal–organic framework electrocatalysts with rich active sites for oxygen evolution, ACS Energy Lett. 4 (2018) 285–292.
[48] D. Kim, K.S. Song, O. Buyukcakir, T. Yildirim, A. Coskun, Bimetallic metal organic frameworks with precisely positioned metal centers for efficient H_2 storage, Chem. Commun. 54 (2018) 12218–12221.
[49] A.K. Tripathy, C.K. Sarangi, B.C. Tripathy, K. Sanjay, I.N. Bhattacharya, B. K. Mahapatra, B.K. Satpathy, Aluminium recovery from NALCO fly ash by acid digestion in the presence of fluoride ion, Int. J. Miner. Process. 138 (2015) 44–48.
[50] D. Valeev, A. Mikhailova, A. Atmadzhidi, Kinetics of iron extraction from coal fly ash by hydrochloric acid leaching, Metals 8 (2018) 533.
[51] S. Sangita, C.R. Panda, Acid leaching technique for the possible recovery of aluminium and other metal values from coal fly ashes, J. Indian Chem. Soc. 93 (2016) 481–487.
[52] S. Yuan, L. Feng, K. Wang, J. Pang, M. Bosch, C. Lollar, Q. Wang, Stable metal–organic frameworks: design, synthesis, and applications, Adv. Mater. 30 (2018), 1704303.
[53] T. Devic, C. Serre, High valence 3p and transition metal based MOFs, Chem. Soc. Rev. 43 (2014) 6097–6115.
[54] K. Wang, D. Feng, T.F. Liu, J. Su, S. Yuan, Y.P. Chen, H.C. Zhou, A series of highly stable mesoporous metalloporphyrin Fe-MOFs, J. Am. Chem. Soc. 136 (2014) 13983–13986.
[55] D. Feng, K. Wang, Z. Wei, Y.P. Chen, C.M. Simon, R.K. Arvapally, D. Yuan, Kinetically tuned dimensional augmentation as a versatile synthetic route towards robust metal–organic frameworks, Nat. Commun. 5 (2014) 5723.
[56] S. Yuan, J.S. Qin, C.T. Lollar, H.C. Zhou, Stable metal–organic frameworks with group 4 metals: current status and trends, ACS Cent. Sci. 4 (2018) 440–450.
[57] F. Trousselet, A. Archereau, A. Boutin, F.X. Coudert, Heterometallic metal–organic frameworks of MOF-5 and UiO-66 families: insight from computational chemistry, J. Phys. Chem. C 120 (2016) 24885–24894.
[58] T. Segakweng, N.M. Musyoka, J. Ren, P. Crouse, H.W. Langmi, Comparison of MOF-5-and Cr-MOF-derived carbons for hydrogen storage application, Res. Chem. Intermed. 42 (2016) 4951–4961.
[59] B. Liu, H. Shioyama, T. Akita, Q. Xu, Metal-organic framework as a template for porous carbon synthesis, J. Am. Chem. Soc. 130 (2008) 5390–5391.
[60] R.R. Salunkhe, Y. Kamachi, N.L. Torad, S.M. Hwang, Z. Sun, S.X. Dou, Y. Yamauchi, Fabrication of symmetric supercapacitors based on MOF-derived nanoporous carbons, J. Mater. Chem. A 2 (2014) 19848–19854.
[61] K.S. Sing, Reporting physisorption data for gas/solid systems with special reference to the determination of surface area and porosity (Recommendations 1984), Pure Appl. Chem. 57 (1985) 603–619.
[62] B. Seoane, A. Dikhtiarenko, A. Mayoral, C. Tellez, J. Coronas, F. Kapteijn, J. Gascon, Metal organic framework synthesis in the presence of surfactants: towards hierarchical MOFs? Cryst. Eng. Comm. 17 (2015) 1693–1700.

[63] H. Bu, Y. Ju, J. Tan, G. Wang, X. Li, Fractal characteristics of pores in non-marine shales from the Huainan coalfield, eastern China, J. Nat. Gas Sci. Eng. 24 (2015) 166–177.
[64] J.H. De Boer, The Structure and Properties of Porous Materials, Butterworth & Co Publishers Ltd, London, 1958, pp. 68–94.
[65] M.M. Labani, R. Rezaee, A. Saeedi, A. Al Hinai, Evaluation of pore size spectrum of gas shale reservoirs using low pressure nitrogen adsorption, gas expansion and mercury porosimetry: a case study from the Perth and Canning Basins, Western Australia, J. Pet. Sci. Eng. 112 (2013) 7–16.
[66] J.A. Coelho, A.M. Ribeiro, A.F. Ferreira, S.M. Lucena, A.E. Rodrigues, D.C. D. Azevedo, Stability of an Al-fumarate MOF and its potential for CO_2 capture from wet stream, Ind. Eng. Chem. Res. 55 (2016) 2134–2143.
[67] M. Hu, J. Reboul, S. Furukawa, N.L. Torad, Q. Ji, P. Srinivasu, Y. Yamauchi, Direct carbonization of Al-based porous coordination polymer for synthesis of nanoporous carbon, J. Am. Chem. Soc. 134 (2012) 2864–2867.
[68] W. Chaikittisilp, K. Ariga, Y. Yamauchi, A new family of carbon materials: synthesis of MOF-derived nanoporous carbons and their promising applications, J. Mater. Chem. A 1 (2013) 14–19.

Supporting information

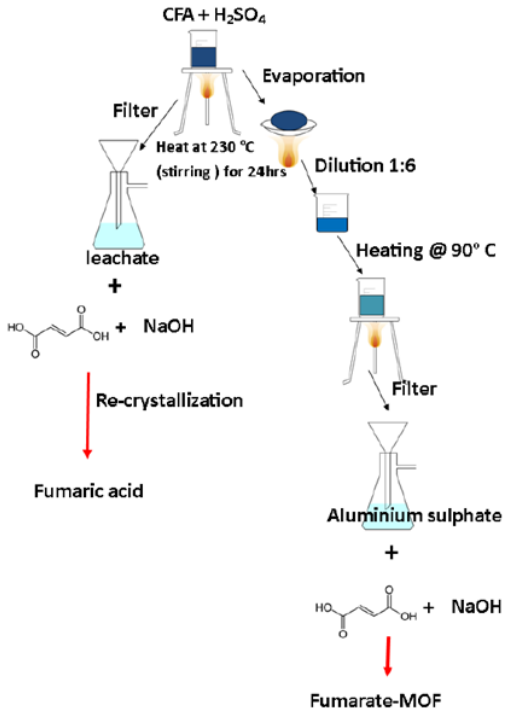

Figure S1. Reaction procedure depicting the outcome of each procedure

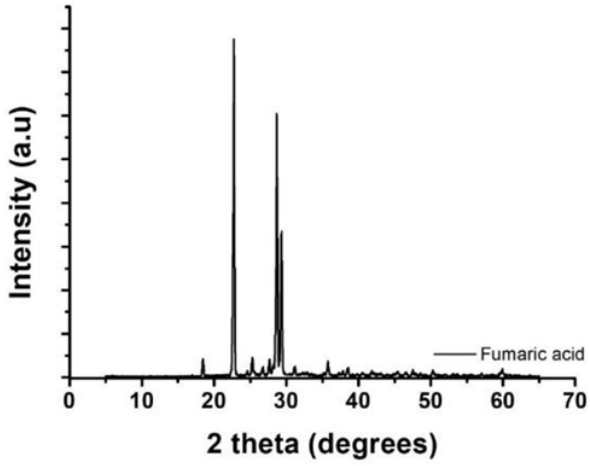

Figure S2. Fumaric acid obtained when calcination is not done during the leaching process

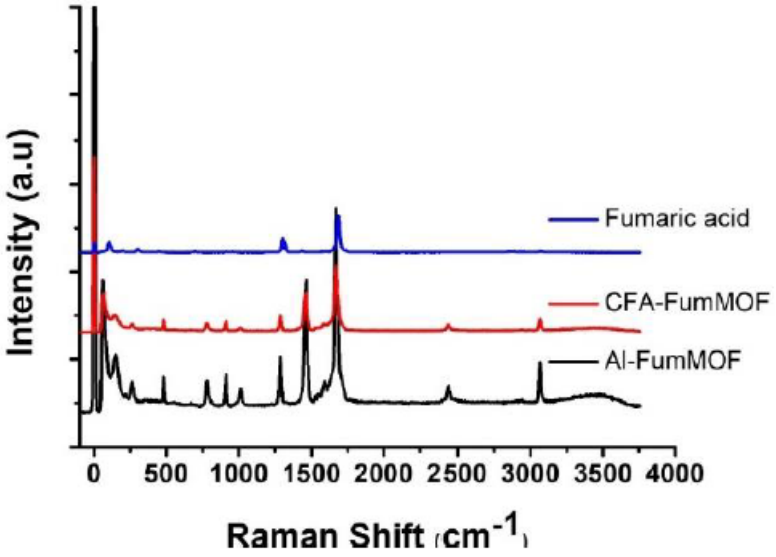

Figure S3. Raman spectra for the prepared MOFS and Fumaric acid

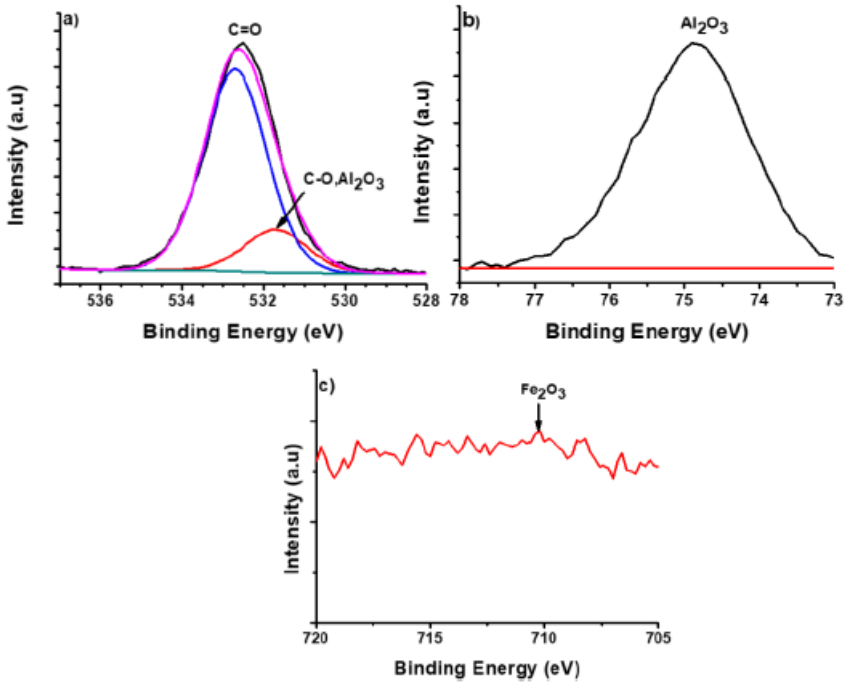

Figure S4. XPS spectra of a) O1s scan , b) Al2p Scan and c) Fe2p Scan for CFA-FumMOF

Table S1. The Reitveld refinement values of Aluminium fumarate MOF (obtained from CIf file)

Lattice parameters

a (Å)			6.8419000				
b (Å)			12.0877000				
c (Å)			14.2070000				
beta (°)			122.547				
Site	Np	X	Y	Z	Atom	OCC	Beq
Al1	0	0,5000	0,5000	0,0000	Al	1	1
Al2	0	0,0000	0,5000	0,0000	Al	1	1
O1	0	0,1801	0,5173	0,9402	O	1	1
O2	0	0,2471	0,4002	0,1159	O	1	1
O3	0	0,5384	0,3688	0,0844	O	1	1
O4	0	0,4506	0,0933	0,3797	O	1	1
O5	0	0,7828	0,1133	0,3994	O	1	1
C1	0	0,4298	0,347	0,1338	C	1	1

4.2.3. Conclusion

The investigation of utilizing CFA leachate as metal feedstock for the synthesis of coal fly ash derived MOF (CFA-FumMOF) was successful. The presence of mixed metals in the solution had little influence on the final structure. However, isomorphic substitution was determined, were Fe ions possessed some of the Al metal position within the structure. Despite this phenomenon, it was seen that CFA-FumMOF exhibited almost similar characteristics to the commercial Al-FumMOF based on its morphological, structural and textural properties. CFA-FumMOF achieved a surface area of 1236 m^2/g, which is comparable to Al-FumMOF (1266 m^2/g) prepared from commercially available products. The direct carbonization method was

used to obtain MOF-derived carbons from parent MOFs. After successful carbonization, the materials achieved a surface area of 2438 m^2/g and 2017 m^2/g for Al-MDC and CFA-MDC, respectively. This study shows an innovative was of synthesizing MOFs from cheap metal feedstock, which can benefit the economy and environment. The study can be optimized and has a potential to be commercialized to prepare good quality MOFs that can be used for various applications.

4.3. Asymmetric supercapacitor based on novel coal fly ash derived MOF as anode and its derived carbon as cathode

4.3.1. Summary of work

There have been studies in the use of waste materials such as biomass, polyethylene plastic and unconventional materials, which are converted to porous materials for SCs application [308–310]. Xu et al., reported of an activated carbon from apricot shell at 6 M KOH giving a high double layer capacitance of 339 F g^{-1} [311]. Rufford et al., did a study on activated carbon from sugarcane bagasse giving a specific capacitance of 300 F g^{-1} [312]. Porous materials such as Metal-Organic Frameworks (MOFs) have been also been investigated and developed for SCs application. MOFs are prepared by chemical coordination between and metal and organic linker to create an open crystalline framework with permanent porosity [313,314]. Most have been used as electrodes materials and have given acceptable electrochemical performance due to their tunable porosity. They can also be utilized as sacrificial templates to obtain metal oxides and highly porous carbons that can be used in SCs application [315]. Metal oxides can be obtained through calcination under air whereas carbon materials can be obtained through wet impregnation or direct carbonization under inert atmosphere. There are records of specific capacitance as high as 232 F g^{-1} at 0.1 A g^{-1} of MOF derived carbons [307]. In here, the authors do a comparative SCs study on the use of waste derived MOF, from coal fly ash (CFA-FumMOF), with structural properties similar to aluminium fumarate MOF as candidates for electrode material. These materials undergo direct carbonization process to obtain MOF derived carbons (MDCs) material. These MDCs are used as negative electrode materials in an asymmetrical device in which their respective parent materials (MOFs) are the positive electrode.

4.3.2. Results and Discussion

WILEY-VCH

ARTICLE

Asymmetric supercapacitor based on novel coal fly ash derived Metal Organic Frameworks as positive electrode and its derived carbon as negative electrode.

K. M. Rambau,[a,b] D. J. Tarimo, [b] O. Fasakin, [c] N. Manyala*[b], N. M. Musyoka *[a]

[a] Dr,N.M, Musyoka and Ms K.M Rambau
HySA Infrastructure Centre of Competence , Centre for Nanostructures and Advanced Materials (CeNAM), Chemicals cluster
Council for Scientific and Industrial Research (CSIR)
Pretoria , South Africa
NMusyoka@csir.co.za

[b] Prof, N, Manyala and Dr, D.J. Tarimo
Department of Physics,
Institute of Applied Materials, SARCHI Chair in Carbon Technology and Materials
University of Pretoria, South Africa.
ncholu.manyala@up.ac.za:

[c] Dr, O Fasakin
Department of Physics and Engineering Physics.
Obafemi Awolowo University
Ile-Ife, 220005, Nigeria

Supporting information for this article is given via a link at the end of the document.

Abstract: Herein, we report a comparative study between aluminium fumarate metal organic framework (Al-FumMOF) and a novel coal fly ash derived aluminium MOF (CFA-FumMOF) with their respective MOF derived carbons (MDCs) for electrochemical performance in supercapacitor application. In the half-cell configuration, Al-FumMOF possessed the specific capacity value of 28.62 mAh g^{-1} and CFA-FumMOF with 9.88 mAh g^{-1} at a specific current of 0.5 A g^{-1} in 6 M KOH electrolyte. The carbon derivative from CFA-FumMOF possessed the highest specific capacitance of 306.59 F g^{-1} at 0.5 A g^{-1} as compared to carbon obtained from Al-FumMOF (111.94 Fg^{-1}). Each MOF was prepared with its respective carbon derivative for an asymetrical capacitor device with the specific capacity of 5.09 mAh g^{-1} at 0.5 A g^{-1}.

Introduction

Fossil fuels remain the dominant supplier of electrical energy worldwide [1]. Combustion of fossil fuel for electricity generation has proved to be indispensable, reliable and a cheap power source, which has a drawback of being a single largest global greenhouse gas producer with an average of 1000 g lifecycle CO_2 emission per kWh of electricity [2-4]. For such stance, the world has encountered social, political and environmental strain to lower carbon emissions [5-8]. Many countries have endorsed regulations that involve industries with high carbon footprint to acquire carbon allowances and enables emission regulation. This has led many countries to enter a concord of Kyoto and Paris agreement that aims at reduction of greenhouse gasses emitted by fossil fuels by 2060 [9-10]. This would require a significant change on energy harnessing and a transition towards renewable energy (RE). World energy outlook reported that for global temperature rise to be limited to 2°C by 2100, the world needs to attain carbon-neutral energy in which RE provide 60 % of energy by the end of the century and 715 million electric vehicles utilized by 2040 [11-13]. This is a clear indication that the world is making a transition towards REs. Currently, many countries have amalgamated intermittent RE in their electrical power systems having benefits of improved power quality, voltage profile, stability and reliability [14-17]. RE have minor drawbacks due to the unpredictable nature of the resources of RE, which gives a variable output with uncontrollable availability. REs are also restricted and in most cases situated in a distance from load centers [18-19]. Such REs are known as variable renewable energy sources (VRES), which are namely solar and wind [18, 20]. To resolve these issue grid-compatible energy storage systems need to be developed, which consist of high capacity, high energy density, long-life cycle, reliability and cost effectiveness [21-22]. Having energy storage systems enables efficient economic performances, load leveling, peak shaving, power quality improvement and reliability [21]. Energy storage systems can be categorized as mechanical, chemical, thermal, electrical and electrochemical [23-25]. Electrochemical is the most common and reliable energy storage systems, which include Lithium ion batteries (LIBs) and Supercapacitors (SCs) [26-28]. LIBs have a draw back in exhibiting high energy density and good rate performance, whereas SCs have high-rate performance and low energy density [29]. Since the main drawback of developing SCs is energy density, it is paramount to find new materials that are cost effective and can improve the energy density [21]. There have been studies in the use of waste materials such as biomass, polyethylene plastic and unconventional materials, which are converted to porous materials for SCs application [30-32]. Xu et al reported on activated carbon from apricot shell at 6 M KOH giving a high double layer capacitance of 339 F g^{-1} [33]. Rufford et al reported on activated carbon from sugarcane bagasse giving a specific capacitance of 300 F g^{-1} [34]. Porous materials such as Metal Organic Frameworks (MOFs) have also been successfully applied and developed for SCs. MOFs are prepared by chemical coordination between metal and organic linker to create an open crystalline framework with permanent porosity [35-36]. Most have been used as electrodes materials providing acceptable electrochemical performance due to their tunable porosity. They can also be utilized as sacrificial templates to obtain metal oxides and highly porous carbons that can be used in SCs application [37]. Metal oxides can be obtained through calcination under air

whereas carbon materials can be obtained through wet impregnation or direct carbonization under inert atmosphere. There are records of specific capacitance as high as 232 F g^{-1} at 0.1 A g^{-1} of MOF derived carbons [38]. In here, the authors reported a comparative SCs study on the use of waste derived MOF, from coal fly ash (CFA-FumMOF), with structural properties similar to Aluminium fumarate MOF as candidates for electrode material. These materials undergo direct carbonization process to obtain MOF derived carbons (MDCs) material. These MDCs are used as negative materials in an asymmetrical device in which their respective parent materials (MOFs) are the positive electrode. It is noteworthy to the reader that the morphological, structural and textural properties of these materials have been discussed in a previous report [53] and this report will only cover the electrochemical performance of the materials. This communication covers the proof of concept in utilizing cost effective methods and green synthesis of MOFs and derived carbons in the application of SCs.

Results and Discussion

The electrochemical performance of the synthesized MOF materials were evaluated using a three-electrode configuration in 6 M KOH electrolyte. Figure 1 (a) represents the cyclic voltammetry (CV) curves at a scan rate of 20 mV s^{-1} in the positive potential window range of 0.0 to 0.4 V for Al-FumMOF and the novel CFA-FumMOF. The CV curves exhibit two redox peaks, which are attributed to the electrochemical redox reaction of the metallic Al (with numerous valence states) and the concentration of KOH electrolyte, which consist of OH^- group with highest ionic conductivity amongst anions. The depicted redox peaks from the CV curves are associated with the Faradic nature of the Al-FumMOF. The novel CFA-FumMOF also exhibited the Faradic behavior observed from the pristine material. The oxidation peaks were observed at 0.34 V and 0.35 V, and reduction peaks at 0.24 V and 0.20 V for Al-FumMOF and CFA-FumMOF, respectively. The galvanostatic charge/discharge (GCD) curves in figure 1 (b) at a specific current of 0.5 A g^{-1} exhibit a non-linear curve with a potential plateau, which corresponds with the CV curves indicating battery type SCs. By observation of both CV and GCD curves, it can be seen that the current response and discharge time of Al-FumMOF are higher than the novel CFA-FumMOF. This can be due to the presence of Fe^{3+} metal embedded within the CFA-FumMOF structure. Our group reported on the structural properties of CFA-FumMOF and speculated on the isomorphic substitution of Fe towards Al in the MOF structure [53]. It is expected that the presence of Fe would increase conductivity and stability; however, in this instance the opposite is true. The concept of bimetallic MOFs to enhance electrochemical performance relies on various principles; (i) quantity of the dopant or new metal introduced; (ii) the structural and morphological changes of the MOF after introduction of the new metal and (iii) synergy of the two metals within the structure [39-42]. Due to these reasons, there are no free holes created that improved the electrical conductivity instead, the Fe ion operates as in any Fe-based MOF, which has poor electrochemical performance. As a result, the presence of Fe ions inhibits the flow of electrons. Figure 1 (c) depicts the specific capacity against specific current evaluated using equation (1) whereby both materials indicate good rate capability with a gradual decrease in specific capacity due to in ability of the electrolyte ions to access the pores. Al-FumMOF possess highest specific capacity value of 28.62 mAh g^{-1} compared to that of CFA-FumMOF with 9.88 mAh g^{-1} at specific current of 0.5 A g^{-1}. The electrochemical performance of Al-FumMOF and the novel CFA-FumMOF is relatively better when compared to other reported Al-based MOFs [48, 50-51]. Previous reports on aluminium-based MOF known as MIL-53(Al) indicated the specific capacitance of 6.5 F g^{-1} at 0.5 A g^{-1}, this can also be attributed to its agglomerated morphology as opposed to the laminar structure possessed by both Al-FumMOF and CFA-FumMOF, which enables ease transportation of electrolyte ions. Figure 1 (c) shows the coulombic efficiency for Al-FumMOF and CFA-FumMOF in 2000 cycles at 2 A g^{-1}. The half-cell configuration maintained an efficiency of 99.31 % for Al-FumMOF and 98.52 % for CFA-FumMOF. It is obvious that Al-FumMOF has high cycling stability as compared to the novel CFA-FumMOF. It is also noteworthy that the synthesized MOFs in this paper are achieved through green chemistry as opposed to other Al-based MOFs.

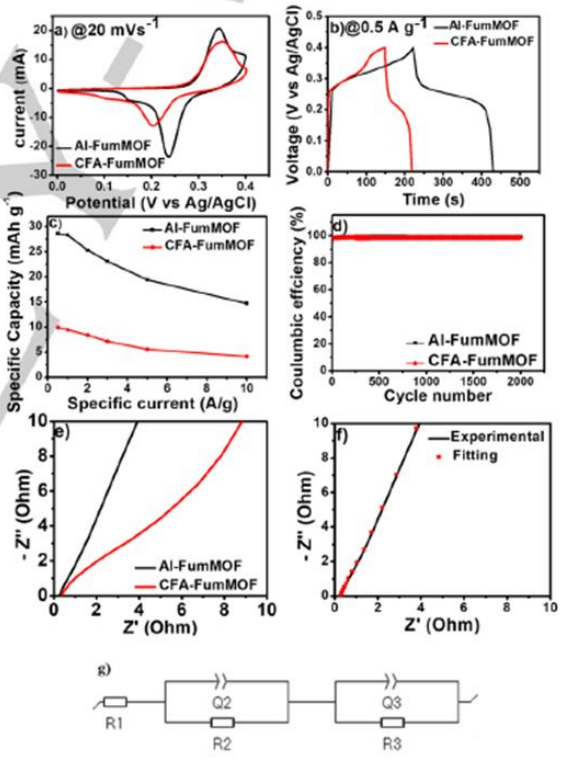

Figure 1. (a) CV curves at a scan rate of 20 mV s^{-1}, (b) GCD curves at a specific current of 0.5 A g^{-1}, (c) Specific capacity against specific current, (d) Cycling performance and (e) EIS Nyquist plot for Al-FumMOF and CFA-FumMOF, respectively in 6 M KOH in a positive potential window. (f, g) EIS Nyquist plot fitting and its equivalent circuit for Al-FumMOF.

Figure 1 (e) presents the EIS Nyquist plot of Al-FumMOF and CFA-FumMOF. It can be observed from the figure that Al-FumMOF exhibits a short diffusion length stipulating a fast charge

transport as compared to CFA-FumMOF. The EIS was used to obtain Equivalent series resistance (ESR), which is the total resistance of the ionic resistance of electrolyte, the electrolyte/electrode interface resistance and electrode/current collector interface resistance. The ESR values where obtained from Z' axis intersect and are 0.21 Ω and 0.44 Ω for Al-FumMOF and CFA-FumMOF, respectively. The ESR value of Al-FumMOF corroborates the good electrochemical performace as compared to CFA-FumMOF.The charge transfer resistance (R_{ct}) is associated with the charge transfer between the interfaces and was obatined from the semi circle at high frequency region with the values of 0.08 and 0.12 for Al-FumMOF and CFA-FumMOF, respectively. The EIS Nyquist plot of Al-FumMOF was fitted with the circuit presented in figure 1 (g).The ESR value from the circuit is represented by R1 at high-frequency region with charge transfer resistance (R_{ct}) represented by R2 . R3 is associated with leakage resistance (R_l), with Q2 and Q3 associated with real capacity. The fitted ESR vlaue is 0.28 Ω and R_{ct} value is 0.10 Ω, which corresponds to experimental values. The MOF derived carbons (MDCs) were also analyzed for their electrochemical properties using a three-electrode configuration in 6 M KOH in a negative potential window range of -1.0 to 0.0 V.

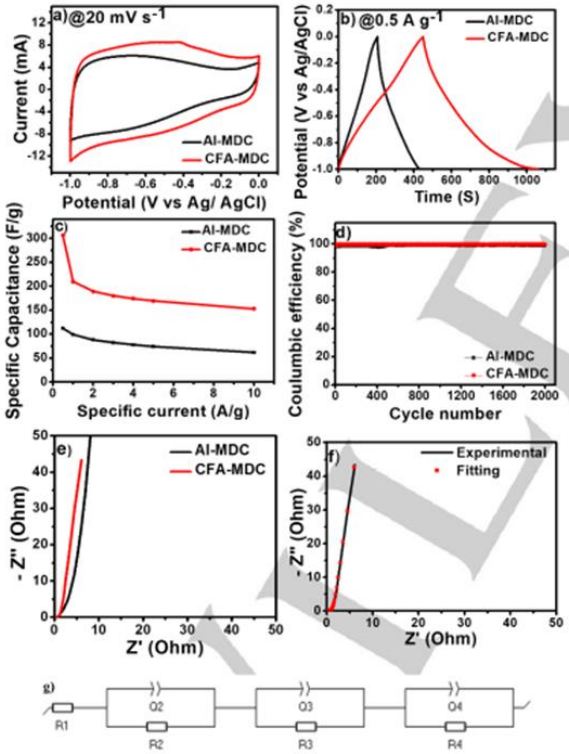

Figure 2. (a) CV curves at a scan rate of 20 mV s^{-1}, (b) GCD curves at a specific current of 0.5 A g^{-1}, (c) Specific capacitance against specific current (d) Cycling performance, (e) EIS Nyquist plot for Al-MDC and CFA-MDC, respectively in 6 M KOH in a negative potential window. (f, g) EIS Nyquist plot fitting for CFA-MDC.

Figure 2 (a) shows the comparative CV curves of Al-MDC and CFA-MDC, which suggest EDLC behavior corroborated with the relatively rectangular shape of the curve. It can also be observed that the CFA-FumMOF consisted of the longest discharge time compared to Al-MDC at 0.5 A g^{-1}, indicating better electrochemical performance (Figure 2 (b)). Generally, the electrochemical performance of carbon materials is dependent on its surface area. The surface area of both carbons are relatively the same (2438 m^2/g for Al-MDC and 2017 m^2/g for CFA-MDC) [53]. However, CFA-MDC appears to have high specific capacitance of 306.59 F g^{-1} at 0.5 A g^{-1} as compared to Al-MDC with the value of 111.94 F g^{-1} as evaluated using equation (2). These values are consistent with other reports of MOF derived carbons from aluminium based MOFs. Zhang et al reported on MDC obtained from MIL-53(Al) giving a specific capacitance of 298 F g^{-1} at 1 mV s^{-1} in 1 M H_2SO_4 [43]. Yan et al reported on MDC from Al(OH)(1.4-NDC).$2H_2O$, which reached a specific capacitance of 232.8 F g^{-1} at a specific current of 0.1 A g^{-1} [44]. Also, the specific capacitance of the MDCs may differ due to the pore sizes of the parent MOFs. On the other hand, the metal node (Al) maybe similar, but the porous structure of the MOF may differ due to the organic linkers used for coordination, which result in similar MOFs with different pore sizes and as a result, the MDCs porous structure may differ. The as prepared carbons (Al-MDC and CFA-MDC) had the presence of narrower polymodal micropore distribution centered at 1.2 nm and 1.5 nm with CFA-MDC possessing wider mesopores. The mesoporous structure enabled free and easy access of electrolyte ions [5]. The GCD curve in figure 2 (b) for CFA-MDC also assume a near symmetrical triangular shape associated with good columbic efficiency as depicted in figure 2 (d). CFA-MDC has columbic efficiency of 99.62 % and Al-MDC of 98.79 % indicating good cyclability. Figure 2 (e) represent the EIS Nyquist plot of Al-MDC and CFA-MDC. CFA-MDC is exhibiting short diffusion length which already corresponds to the specific capacitance. The experimental ESR values were 1.16 Ω and 0.26 Ω for Al-MDC and CFA-MDC, respectively. The small ESR value of CFA-MDC is associated with good wettability. The fitting of CFA-MDC is depicted in figure 2 (f) with the circuit in figure 2 (g). The ESR value is represented by R1 and charge transfer resistance (R_{ct}) represented by R2, leakage resistance (R_l) is represented by R3 and R4, with Q2 and Q3 associated with real capacity. From the fitting of CFA-MDC, the ESR value is 0.31 Ω and R_{ct} value is 0.27 Ω, which corresponds well to the experimental values of 0.38 and 0.24 Ω, respectively. The prepared MOFs were used as the positive electrode and their respective carbon derivatives were used as a negative electrode for a full cell device. The asymmetric device of Al-FumMOF//Al-MDC was assembled with mass balancing using equation (4) giving a ratio of 3.0:1.0 and working with a total mass electrode of 7.1 mg/cm^2. The assembly was done with a standard 2032 grade coin cell sandwiched with a filter paper as separator and 6 M KOH as electrolyte. Figure 3 (a) display the CV curve at a scan rate of 40 mV s^{-1} of Al-FumMOF at a positive potential window of 0.0-0.4 V and Al-MDC at a negative potential window of -1.0-0.0 V. The curve gives an illustration of EDLC and Faradic behavior of the device, with EDLC contribution visible in both positive and negative currents, however, Faradic contributions showing dominance with much higher positive current. Subsequently, creating a battery-like behavior in the device. The CV curves of the device are

represented in figure 3 (b) at different scan rates of 5 to 100 mV s^{-1}.

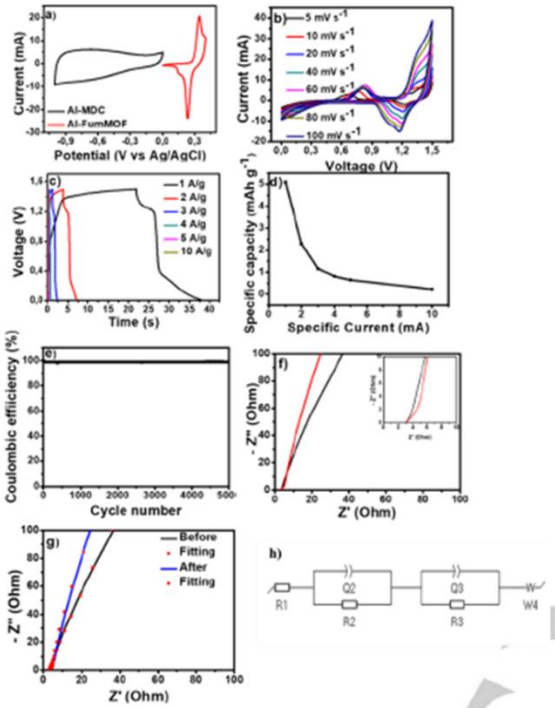

Figure 3. Al-FumMOF//Al-MDC asymmetric device: (a) CV of positive and negative electrodes at scan rate of 20 mV s^{-1}, (b) CV curves at different scan rates, (c) GCD curves at different specific currents, (d) Specific capacity versus specific current (e) Cycling stability versus cycle number for the device, f) EIS Nyquist plot and (g) Fitting of EIS Nyquist plot before and after cycling.

The curves illustrate a merger between EDLC and Faradic contribution associated with hybrid asymmetric supercapacitors. The GCD curves at different specific currents ranging from 0.5 to 10 A g^{-1} are depicted in figure 3 (c) and showing the potential steps confirming the Faradic behavior from the CV curves. As a result, the specific capacity of the device was calculated using equation (1) obtaining a value of 5.09 mAh g^{-1} at a specific current of 0.5 A g^{-1} (figure 3 (d)). The capacities dropped as the specific current increased due to the limited ion migration associated with diffusion on the outer surface of the material for charge storage at higher specific current [45]. It can be observed that there is a drop from the specific capacities in the device as compared to the three-electrode system, which is due to an increase in electronic field in the cell configuration working at high potential window, which is subsequently increased by the increase in specific current. This result in an overall interruption in the collaboration of Faradic and EDLC processes [46]. The specific energy and power of the device evaluated using equation (5) and (6) at 1 A g^{-1} were 10.12 Wh kg^{-1} and 552.09 W kg^{-1}, respectively. This is expected as an indication of low specific capacity. Figure 3 (e) illustrates the coulombic efficiency of 99.10 %, indicating good cyclability after 5000 cycles. Figure 3 (f) illustrates the Nyquist plot showing fitting and experimental data. The circuit (figure h) consist of R1, R2 and R3 that represent equivalent series resistance (ESR), charge transfer resistance (R_{ct}) and leakage resistance (R_l), respectively. Q2 and Q3 are associated with real capacity and with the Warburg (W) element in series with circuit. R2 and Q2 is associated with the resistance rate and Faradaic electrochemical activity occurring between the electrode and electrolyte. The experimental ESR values are 3.00 Ω and 3.06 Ω and R_{ct} values are 0.64 Ω and 1.69 Ω for before and after cycling stability. The values corresponds with the fitted ESR value of 3.14 Ω and 3.17 Ω with R_{ct} values of 0.99 Ω and 1.23 Ω. It is noteworthy that the R_{ct} value before cycling is small compared to after cycling. This indicates that the material becomes more resistive after 5000 cycles and hence give poor performance.

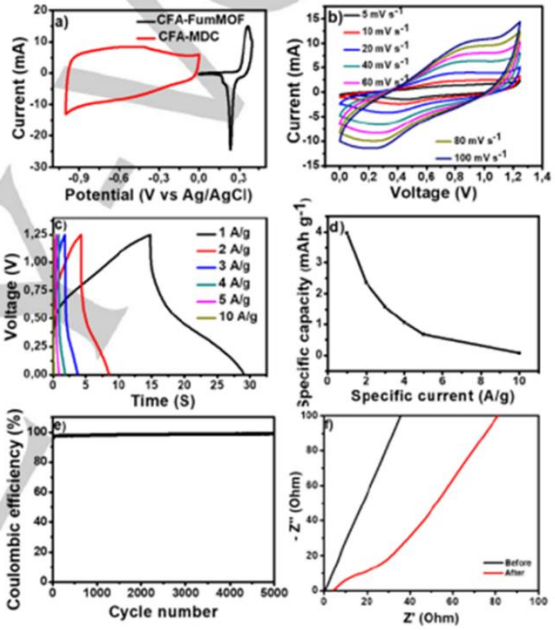

Figure 4. CFA-FumMOF//CFA-MDC asymmetric device: (a) CV of positive and negative electrodes at scan rate 20 mV s^{-1}, (b) CV curves at different scan rates (c) GCD curves at different specific currents, (d) Specific capacity versus specific current, (e) Cycling stability versus cycle number for the device, and (f) EIS Nyquist plot before and after cycling.

The asymmetric device of CFA-FumMOF//CFA-MDC was assembled with mass balancing using equation (5) giving a ratio of 5.0:1.0 and working with a total mass electrode of 6.8 mg/cm^2. The cell was assembled under the same conditions mentioned prior. Figure 4 (a) is illustrating the CV curves for CFA-FumMOF in the potential window of 0.0-0.4 V and CFA MDC at -1.0-0.0 V. The CFA-FumMOF electrode shows the Faradic behavior corroborated by redox peaks with CFA-MDC demonstrating the pseudocapacitive behavior demonstrated by relatively rectangular shape, indicating a reversible capacitive behavior [47-49]. The CV curves of the asymmetrical device of CFA-FumMOF//CFA-MDC are shown in figure 4 (b) at scan rates from 5 to 100 mV s^{-1}. The curves illustrate the nonlinear

psuedocapacitive behavior, which operated from a potential window of 0.0-1.45 V. The GCD profiles represented by figure 4 (c) at different specific currents from 0.5 to 10 A g^{-1} illustrates a quasi-linear curve with Faradic contribution, which corresponds well to the CV curves. The specific capacity recorded is 4.0 mAh g^{-1} at 0.5 A g^{-1} (figure 4 (d)). The device obtained a good coulombic efficiency of 98.90 % after 5000 cycles as depicted in figure 4 (e). The specific energy and power of the device calculated using equation (5) and (6) at 1 A g^{-1} are 2.48 Wh kg^{-1} and 625 W kg^{-1}, respectively. There are no known reports on the use of pristine aluminum-based MOF as supercapacitor device. However, there is a single report on the use of an optimized aluminium MOF, which is involved integration of the MOF structure with reduced graphene oxide (rGO) [48]. This study reported the energy density of 6.66 Wh kg^{-1} and power density of 3655 W kg^{-1}. The rGO assisted in reducing agglomeration of the MOF creating more active sites interacting with electrolyte and increasing charge storage. It can therefore be stipulated that an optimization process of CFA-FumMOF and Al-FumMOF could yield an improved electrochemical performance and energy density. In three electrode configurations, the prepared MOFs illustrated a faradic behavior and their derived carbons illustrated a typical EDLC behavior as expected. Their electrochemical performance were relatively improved as compared to other reported aluminium-based MOFs [48, 50-51]. Therefore, the specific capacity and capacitance reported herein are the highest in record. However, on the electrochemical device there is poor performance and to observe the compatibility of the prepared MOFs with other carbon materials, an asymmetrical device with the MOFs as positive electrode and activated carbon from cocoa as a negative electrode was fabricated. The activated carbon possessed obvious EDLC behavior with a specific capacitance of 123.78 F g^{-1} at 0.5 A g^{-1} and good cycling stability as shown in figure S1. Both Al-FumMOF//AC-Cocoa and CFA-FumMOF//AC-Cocoa devices had potential window of 0.0 to 1.5 V and exhibiting battery-type behavior corroborated with redox peaks. Al-FumMOF//AC-Cocoa possessed a specific capacity of 5.02 mAh g^{-1} and CFA-FumMOF possessed 4.74 mAh g^{-1} as presented in figure S2 and S3, respectively. Despite the change in the negative electrode, the devices did not improve in performance. Al-FumMOF//AC-Cocoa had coulombic efficiency of 99.00 % and 98.23% for CFA-FumMOF//AC-Cocoa indicating good cyclability after 5000 cycles. This is an indication that both Al-FumMOF and CFA-FumMOF struggle with synergy with a negative electrode. The prepared asymmetric devices did not exhibit good electrochemical performance in practical instances. It is noteworthy to the reader that there are no known reports on the utilization of aluminium fumarate MOF (Al-FumMOF) as a positive electrode for the use of SCs. In addition, CFA-FumMOF is a novel MOF obtained through green synthesis and was prepared as a mimic of aluminium fumarate MOF as means of cutting cost in MOF synthesis industry. This study is a proof of concept on the use of green prepared materials for SCs application. The improved performance of the three electrode measurements of the MOFs shows that if optimization processes such preparing a composite is achieved, the materials have a potential to outperform most known MOF. With different activated carbon materials utilized as negative electrode, the device can also have improve energy and power density.

Conclusion

The three electrode measurements of Al-FumMOF and novel CFA-FumMOF were successfully prepared with specific capacity of 28.62 mAh g^{-1} and 9.88 mAh g^{-1}, respectively at specific current of 0.5 A g^{-1}. Their respective MDCs, Al-MDC and CFA-MDC obtained a specific capacitance of 111.94 F g^{-1} and 306.59 F g^{-1}, respectively at 0.5 A g^{-1}. There are no known records on the use Al-FumMOF as an electrode or on carbonization in attempts to obtain, a porous carbon used as negative electrode in SCs. The asymmetric device did not provide good electrochemical performance. However, this study still serve as entry point in the utilization of cheap waste materials to obtain exceptional MOF materials that can in turn be used as parent materials to obtain porous carbons and used for SCs application. The high surface area and exceptional porosity of the MOFs and their carbon derivative enables then to be used also in other energy storage applications.

Experimental Section

Preparation and characterization methods of CFA-FumMOF, Al-FumMOF and their carbon derivatives (CFA-MDC and Al-MDC) has been described in our previous report [53]. AC-Cocoa was prepared as follows: The cocoa pod husks (CPH) waste was collected from a dumping site in a farmland and adopted as raw material. The CPH was repeatedly washed with acetone and distilled water to remove all the dirt and dried at 60 °C for 24 h in an electric oven. The cleaned and dried CPH was sliced into smaller pieces, 10 g of the sliced material was soaked in 100 mL of distilled water containing 10 mL of 0.5 M sulphuric acid and transferred into a 120 mL stainless steel autoclave unit which was then sealed and heated up at 160 °C for 12 h. The product was filtered and dried at 80 °C for another 48 h. The dried product was mixed together in an agate mortar with potassium hydroxide pellet in a mass ratio 1:1 before being carefully placed in a horizontal tube furnace for carbonization at a ramping rate of 5 °C min^{-1} to 700 °C under continuous flow of argon (300 sccm) for 60 minutes. Afterwards, the carbonized material was washed with 3 M hydrochloric acid and distilled water until a neutral pH value was reached. The final product was dried at 60 °C for 24 h in an electric oven, producing activated carbon named AC-Cocoa.

Three and two-electrode configuration systems were used to conduct the electrochemical measurements. The electrodes were prepared by mixing 80 % of the active material, 10 % of conductive carbon acetylene black (CB) and 10 % of Polyvinylidene fluoride (PVDF) as a binder and using few drops of 1-methyl 2-pyrollidone (NMP) to make a homogenous slurry. A clean nickel foam was used as a current collector and slurry was pasted on an area of 1.0 × 1.0 cm^2 and dried at 60 °C for 12 h. Their capacitive performance was performed with the aid of a Bio-Logic VMP300 potentiostat (Knoxville TN 37930, USA) controlled by EC-Lab V1.40 software in a three-electrode set-up. A glassy carbon was used as a counter electrode, Ag/AgCl as a reference electrode and working electrode consisting of the active material. The cyclic voltammetry (CV) of the as-prepared samples were performed at different scan rates ranging from 5 to 100 mV s^{-1} at a potential window ranging from 0.0 to 0.4 V vs. Ag/AgCl. The galvanostatic charge-discharge (GCD) was performed at specific current range of 0.5 to 10 A g^{-1} at a potential window range of 0.0 to 0.4 V. The specific capacity of a single electrode was calculated via a GCD profiles using equation (1) below [52],

$$Q_s = \frac{I_d \times \Delta t}{3.6} \quad (1)$$

Where Q_s is the specific capacity, I_d as specific current (A g^{-1}) and Δt is the discharge time (s). The specific capacitance C_s was calculated as follow:

$$C_s = \frac{\Delta t \times I_d}{\Delta V} \quad (2)$$

With Δt as change in discharge time and ΔV is potential difference. The coulombic efficiency C_E was calculated using equation below:

$$C_E = \frac{t_d}{t_c} \times 100\ \% \quad (3)$$

Where t_c is the charging time and t_d the discharging time.

The electrochemical impedance spectroscopy was measured using an open circuit potential of frequency range from 10 mHz - 100 kHz. The asymmetric hybrid device was assembled by using the as-prepared Al-fumMOF or CFA-FumMOF as positive electrode and their respective MDCs (Al-MDC and CFA-MDC) as negative electrode with a thickness and diameter of 0.2 and 16 mm, respectively in a standard 2032 grade coin cell using Watman Celgard paper-based separator and 6 M KOH as electrolyte. The charge balance $Q_+ = Q_-$ was used to balance the mass of each electrode. The MOF materials exhibited Faradic behaviour with specific capacity (Qs) calculated by using the GCD curve as shown in equation (1) above. The charge balancing equation was written as follows [52]:

$$Q_+ = Q_- \rightarrow m_+ \times 3.6 Q_{s+} = m_- \times \Delta V_- \times C_{s-} \rightarrow \frac{m_-}{m_+} = \frac{3.6 \times Q_{s+}}{\Delta V_- \times C_{s-}} \quad (4)$$

Where, Q_+ and Q_- is stored charge in positive and negative electrodes, respectively. Q_{s+} and C_{s-} are the specific capacity and capacitance for the positive and negative electrodes, respectively. ΔV_- is the potential window for the negative electrode and masses of the positive and negative electrodes are represented as m_+ and m_-, respectively. The prepared cell operated at a potential window of 0.0 to 1.5 V as influenced by the operating potential of the prepared electrodes. The specific capacity (Q_s) of the asymmetric device was calculated using equation (1).

The specific energy (E_d) and specific power (P_d) of the device were calculated as follows [52]:

$$E_d = \frac{1}{3.6m} \int V dt \quad (5)$$

$$P_d = \frac{E_d}{\Delta t} \times 3600 \quad (6)$$

Acknowledgements

KR would like to acknowledge the financial support from the South African Department of Science and Innovation (DSI) for research activities under the HySA Infrastructure as well as the National Research Foundation (NRF). KR also acknowledge the financial support by South African Research Chairs Initiatives (SARChI) of the Department of Science and Technology and the National Research Foundation (NRF) of South Africa (Grant No. 61056). Any opinions, findings and/or recommendations expressed here are those of the authors and not of the funding bodies.

Keywords: Coal fly ash derived MOFs • aluminium based MOFs • MOF derived carbons • Asymmetric capacitor

[1] D. J. Wuebbles, A. K. Jain, *Fuel Process. Technol.* **2001**, *71*, 99-119.
[2] T. Kåberger, *Global Energy Interconnection*, **2018**, *1*, 48-52.
[3] Z. Yang, J. Zhang, M. C. Kintner-Meyer, X. Lu, D. Choi, J. P. Lemmon, J. Liu, *Chem. Rev.*, **2011***111*, 3577-3613.
[4] F. Martins, C. Felgueiras, M. Smitková, *Energy Procedia*, **2018**, 153, 107-111.
[5] Ü. Ağbulut, S. Sarıdemir, *Int. J. Ambient Energy*, **2019**, 1-6.
[6] S. D. Musa, T. Zhonghua, A. O. Ibrahim, M. Habib, *Renew. Sustain. Energy Rev.*, **2018**, 81, 2281-2290.
[7] A. Cornelius, R. Bandyopadhyay, D. Patiño-Echeverri, *Renew. Sustain. Energy Rev.*, **2018**, 81, 2291-2298.
[8] N. Khan, S. Dilshad, R. Khalid, A. R. Kalair, N. Abas, *Energy Storage*, **2019**, 1, e49.
[9] D. Held, C. Roger, *Global Policy*, **2018**, 9, 527-537.
[10] J. H. Krug, *Carbon Balance Manag.*, **2018**, 13, 1-11.
[11] T. M. Gür, Energy Environ. Sci., **2018**, 11, 2696-2767.
[12] M. Salvia, D. Reckien, F. Pietrapertosa, P. Eckersley, N. A. Spyridaki, A. Krook-Riekkola, O. Heidrich, *Renew. Sustain. Energy Rev.*, **2021**,135, 110253.
[13] V. Ramanathan, J. Allison, M. Auffhammer, D. Auston, A. D. Barnosky, L. Chiang, J. Christensen, *Collabra*, **2016**, 2.
[14] D. O. Akinyele, R. K. Rayudu, *Sustain. Energy Technol.*, **2014**, 8, 74-91.
[15] J. P. Barton, D. G. Infield, *IEEE Trans. Energy Convers.* **2004**, 19, 441-448.
[16] A. Henriot, *Energy Econ.* **2015**, 49, 370-379.
[17] H. Zsiborács, N. H. Baranyai, A. Vincze, L. Zentkó, Z. Birkner, K. Máté G. Pintér, *Electronics*, **2019**, 8, 729.
[18] A. B. Gallo, J. R. Simões-Moreira, H. K. M. Costa, M. M. Santos, E. M. dos Santos, *Renew. Sustain. Energy Rev.*, **2016**, 65, 800-822.
[19] G. Notton, M. L. Nivet, C. Voyant, C. Paoli, C. Darras, F. Motte, A. Fouilloy, *Renew. Sustain. Energy Rev.*, **2018**, 87, 96-105.
[20] K. P. Kampouris, V. Drosou, C. Karytsas, M. Karagiorgas, *Earth Environ. Sci.*, **2020**, 410, 012033.
[21] S. Koohi-Fayegh, M. A, Rosen, *J. Energy Storage*, **2020**, 27, 101047.
[22] T. M. Gür, *Energy Environ. Sci.*, **2018**, 11, 2696-2767.
[23] A. G. Olabi, C. Onumaegbu, T. Wilberforce, M. Ramadan, M. A. Abdelkareem, A. H. Al–Alami, *Energy*, **2020**, 118987.
[24] M. S. Guney, Y. Tepe, *Renew. Sustain. Energy Rev.*, **2017**,75, 1187-1197.
[25] M. Faisal, M. A. Hannan, P. J. Ker, A. Hussain, M. B. Mansor, F. Blaabjerg, *Ieee Access*, **2018**,6, 35143-35164.
[26] L. Chang, W. Zhang, S. Xu, K. Spence, *IEEE Trans. Power Electron.*, **2017**, 2, 267-276.
[27] L. Zhang, X.Hu, Z. Wang, J. Ruan, C. Ma, Z. Song, M. G. Pecht, *Renew. Sustain. Energy Rev.*, **2020**,110581.
[28] G. Z. Chen, *Int. Mater. Rev*, **2017**, 62, 173-202.
[29] X. Gao, Y. Dong, S. Li, J. Zhou, L. Wang, B. Wang, *EER*, **2020**,3, 81-126.
[30] M. Fu, W. Chen, J. Ding, X. Zhu, Q. Liu, *J. Alloys Compd.*, **2019**, 782, 952-960.
[31] C. Ma, J. Min, J. Gong, X. Liu, X. Mu, X. Chen, T. Tang, *Chemosphere*, **2020**, 253, 126755.
[32] L. Li, C. Jia, X. Zhu, S. Zhang, *J. Clean. Prod.*, **2020**, 256, 120326.
[33] B. Xu, Y. Chen, G. Wei, G. Cao, H. Zhang, Y. Yang, *Mater. Chem. Phys.*, **2010**,124, 504-509.
[34] T. E. Rufford, D. Hulicova-Jurcakova, K. Khosla, Z. Zhu, G. Q. Lu, *J. Power Sources*, **2010**, 195, 912-918.
[35] U. Mueller, M. Schubert, F. Teich, H. Puetter, K. Schierle-Arndt, J. Pastre, *J. Mater. Chem.*, **2006**, 16, 626-636.
[36] H. Li, M. Eddaoudi, M. O'Keeffe, O. M. Yaghi, nature, *1999*, 402, 276-279.
[37] Y. Zhao, J. Liu, M. Horn, N. Motta, M. Hu, Y. Li, *Sci. China Mater.*, **2018**, 61, 159-184.
[38] X. Yan, X. Li, Z. Yan, S. Komarneni, *Appl. Surf. Sci.*, **2014**, 308, 306-310.
[39] M. S. Rahmanifar, H. Hesari, A. Noori, M. Y. Masoomi, A. Morsali, M. F. Mousavi, *Electrochimica. Acta*, **2018**, 275, 76-86.
[40] D. Zheng, H. Wen, X. Sun, X. Guan, J. Zhang, W. Tian, Y. Yao, *Chem. Eur. J*, **2020**,*26*, 17149-17155.
[41] F. Jeremias, A. Khutia, S. K. Henninger, C. Janiak, *J. Mater. Chem.*, **2012**, *22*, 10148-10151.
[42] J. Wang, Q. Zhong, Y. Xiong, D. Cheng, Y. Zeng, Y. Bu, *Appl. Surf. Sci.*, **2019**, *483*, 1158-1165.
[43] S. Zhang, X. Shi, D. Moszyński, T. Tang, P. K. Chu, X. Chen, E. Mijowska, *Electrochimica. Acta*, **2018**, *269*, 580-589.
[44] X. Yan, X. Li, Z. Yan,S. Komameni, *Appl. Surf. Sci.*, **2014**, 308, 306-310.
[45] D. Y. Momodu, F. Barzegar, A. Bello, J. Dangbegnon, T. Masikhwa, J. Madito, N. Manyala, *Electrochimica. Acta*, **2015**,*151*, 591-598.

[46] T. M. Masikhwa, F. Barzegar, J. K.Dangbegnon, A. Bello, M. J. Madito, D. Momodu, N. Manyala, *RSC advances*, **2016**, *6*, 38990-39000.
[47] M. S. Rahmanifar, H. Hesari, A. Noori, M. Y. Masoomi, A. Morsali, M. F. Mousavi, *Electrochimica. Acta*, **2018**, *275*, 76-86.
[48] M. Majumder, R. B.Choudhary, A. K. Thakur, A. Khodayari, M. Amiri, R. Boukherroub, S. Szunerits, *Electrochimica. Acta*, **2020**, *353*, 136609.
[49] T. Wu, N. Prasetya, K. Li, *J. Membr. Sci*, **2020**, 118493
[50] H. He, G.Wang, B. Shen, Y. Wang, Z. Lu, S. Guo, Z. Xiao, *J. Solid State Chem.*, **2020**, *288*, 121375.
[51] Y.Gong, J. Li, P. G. Jiang, Q. F. Li, J. H. Lin, *Dalton Transactions*, **2013**, *42*,1603-1611.
[52] D. J.Tarimo, K. O. Oyedotun, A. A. Mirghni, B.Mutuma, N. F. Sylla, P. Murovhi, N. Manyala, *Int. J. Hydrog. Energy*, **2020**, 45, 33059-33075.
[53] K.M. Rambau, N.M. Musyoka, R. Panek, W. Franus, M. Wdowin, N. Manyala, *Mater. Today Commun.* **2021**,102433.

Supporting information

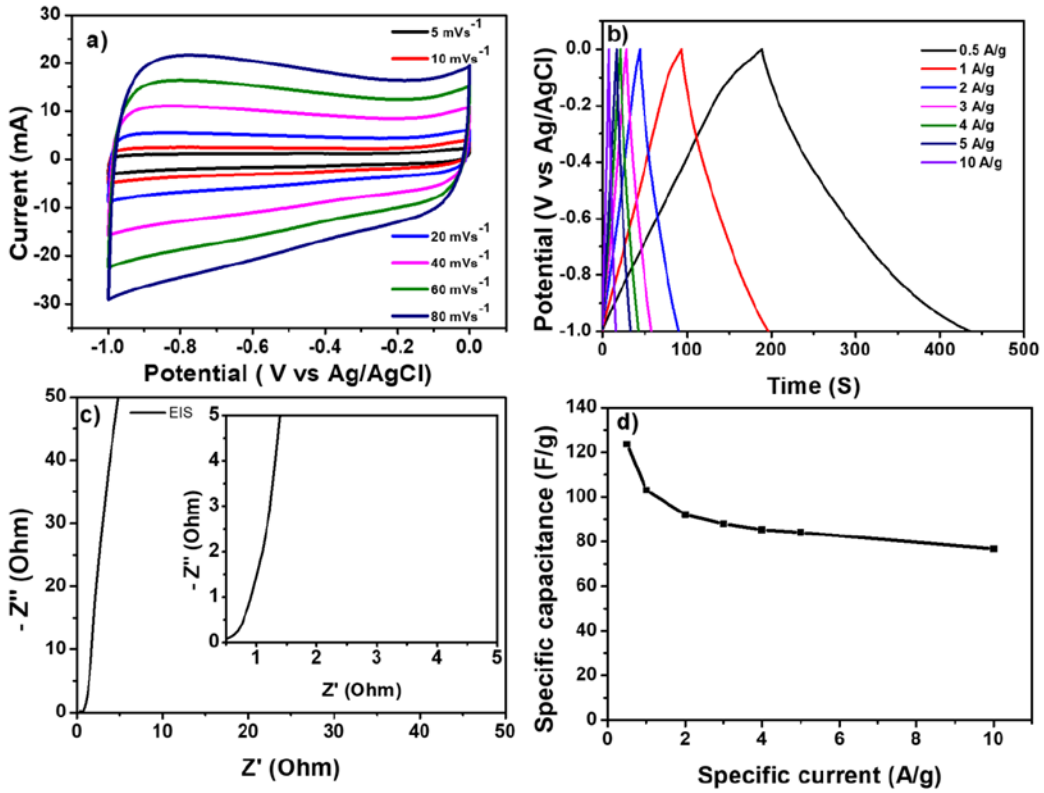

Figure S1: (a) CV curves at different scan rates, (b) GCD curves at different specific current and (c) EIS Nyquist plot and (d) Specific capacity versus specific current for AC-Cocoa in 6 M KOH in a negative potential window.

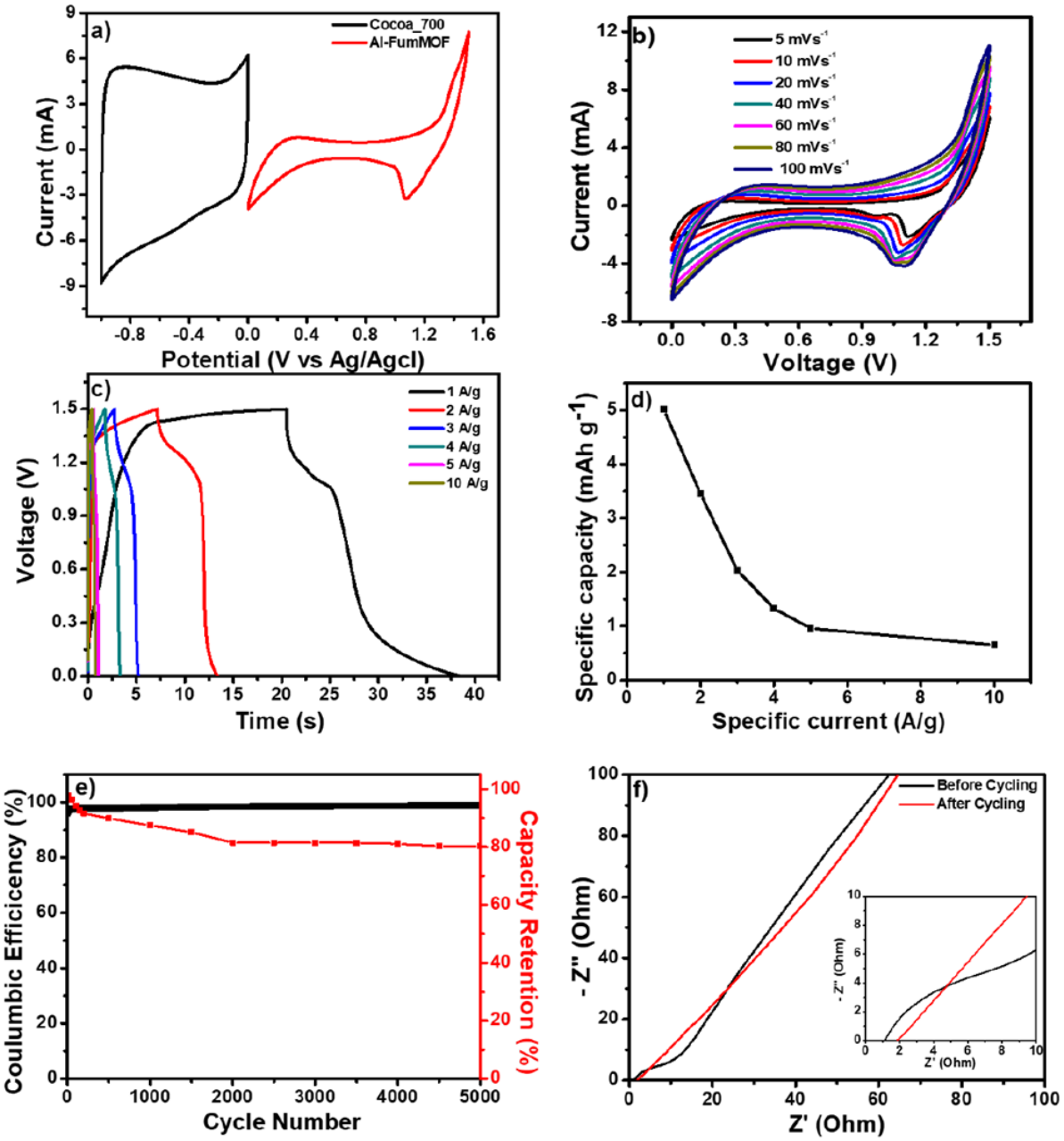

Figure S2: Al-FumMOF//AC-Cocoa700 asymmetric device: (a) CV curve of positive and negative electrodes at scan rate of 20 mV s^{-1}, (b) CV curves at different scan rates, (c) GCD curves at different specific currents, (d) Specific capacity versus specific current (e) Cycling stability and capacity retention versus cycle number for the device, (f) EIS Nyquist plot before and after cycling.

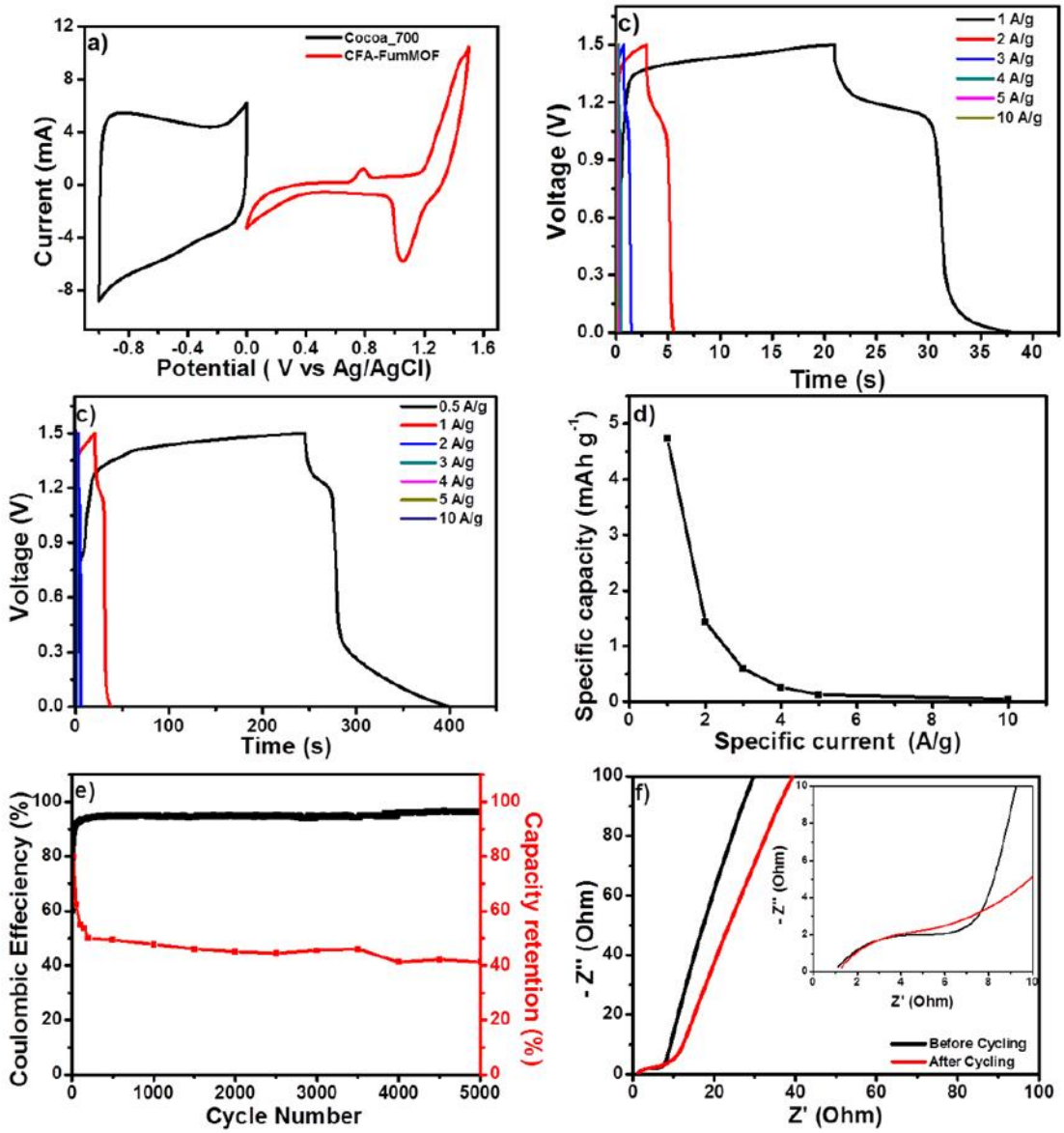

Figure S3: CFA-FumMOF//AC-Cocoa700 asymmetric device: (a) CV of positive and negative electrodes at scan rate of 20 mV s^{-1}, (b) CV curves at different scan rates, (c) GCD curves at different specific currents, (d) Specific capacity versus specific current (e) Cycling stability and capacity retention versus cycle number for the device, and (f) EIS Nyquist plot before and after cycling.

4.3.3. Conclusion

The three electrode measurements of Al-FumMOF and novel CFA-FumMOF were successfully prepared with specific capacity of 28.62 mAh g^{-1} and 9.88 mAh g^{-1}, respectively at specific current of 0.5 A g^{-1}. Their respective MDCs, Al-MDC and CFA-MDC obtained a specific capacitance of 111.94 F g^{-1} and 306.59 F g^{-1}, respectively at 0.5 A g^{-1}. There are no known records on the use Al-FumMOF as an electrode or on carbonization in attempts to obtain, a porous carbon used as negative electrode. The asymmetric device did not provide good electrochemical performance. However, this study still has the potential in utilization of cheap waste materials to obtain exceptional MOF materials that can in turn be used as parent materials to obtain porous carbons and used for SCs application. The exceptional porosity and high surface area of the MOFs and their carbon derivative enables them to be used also in other energy storage applications.

Chapter 5: Conclusion and Future Work

5. Introduction

The study on the preparation of MOFs from unconventional feedstock was successful conducted with prosperous electrochemical performance reported.

5.1. Conclusion

The thesis fully explored various methods on how to use waste such as coal fly ash (CFA) materials and spent Lithium-Ion batteries (LIBs) to extract metals. Chapter 2: Part A, gave a detailed methods on how coal fly ash is recycled and used in application of construction, ceramics, gas storage and others. Reclaiming of valuable metals were detailed in physical and chemical separation processes. The chapter also detailed how coal fly ash is utilized as metal feedstock in the preparation of porous materials such as zeolites and mesoporous silica, also indicating its potential as a metal source for the preparation of MOFs for electrochemical supercapacitors. Part B gives a detailed version of recycling spent LIBs through pyrometallurgical and hydrometallurgical processes also highlighting the leaching efficiency of metals. Spent cathode materials can also regenerated using sol-gel, sintering and co-precipitation methods. Various divalent MOFs and their application in spent LIBs are discussed, also highlighting how divalent MOFs can be synthesized from spent LIBs and utilized as positive electrode in LIBs application.

Al-based MOF from coal fly ash and Mn-based MOF from spent LIBs were successfully synthesized and used in Supercapacitors and LIBs applications, respectively. Chapter 3 discussed the structural, morphological and textural properties of the as-synthesized materials

and characterization using various techniques. Morphological properties of the prepared materials were obtained from SEM technique. The elemental composition, chemical composition and chemical states were analysed using EDS, EDXRF and XPS, respectively. The crystallographic nature, thermal response and textural properties of the materials were determined using XRD, TGA and N_2 BET sorption techniques, respectively. To determine the crystal lattice, molecular structure and functional groups, light-based principle spectroscopy namely FTIR and Raman spectroscopy were used.

For MOFs derived from spent LIBs, inorganic acids (HCl and H_2SO_4) were utilized to convert metal oxides to manganese salts. The salts were then mixed with commercial organic linker (benzene-1,4-dicarboxylic acid (H_2BDC)) in N, N-dimethylformamide solvent for solvothermal synthesis. The Mn-MOF(Cl_2) and Mn-MOF(SO_4) from spent LIBs were compared to Mn-MOF(Com) prepared from commercial $MnCl_2$ salt. The Mn-MOF(Cl_2) had superior morphological, structural and textural properties as compared to Mn-MOF(SO_4) but comparable to Mn-MOF(Com). When analysed for electrochemical performance, Mn-MOF(Cl_2) achieved coulombic efficiency of approximately 99% and discharge capacity of 1355 mAh g^{-1}, which is higher than Mn-MOF(Com) (772.55 mAh g^{-1}) after 100 cycles.

This exceptional performance is attributed to morphology consisting of small aggregates and structure of flaky sheets. This supports short ion diffusion length creating a high-rate capability. After full discharge to 0.01 V, Mn-MOF(Com) had amorphization and stability retention in an amorphous state. However, Mn-MOF(Cl_2) experienced amorphization but partially retained its structure. Despite the change in morphology the material maintained porosity to assist in the kinetic properties of the materials. There are reports on the use of Mn-MOF with a discharge capacity of 974 mAh g^{-1} after 100 cycles at 100 mA g^{-1} and one of 694 mAh g^{-1} at 400 mA g^{-1}. As far as the author's knowledge, the discharge values reported in this thesis are the highest.

Aluminium from coal fly ash was also extracted using improvised procedure. The leachate was utilized with fumaric acid as a linker to prepare CFA-FumMOF, which is a mimic of aluminium fumarate MOF (Al-FumMOF). The presence of other metals within the leachate were not detected in the overall structure of CFA-FumMOF. Except for Fe ions that had isomorphically substituted on the position in which Al ion would have presided. This did not affect any morphological, structural and textural properties rather exhibited similar characteristics to Al-FumMOF and achieving a surface area of 1236 m^2/g with respect to Al-FumMOF (1266 m^2/g).

For the purpose of application in electrochemical supercapacitors, the as-prepared MOFs went through direct carbonization process to obtain MOF derived carbons (MDC). The materials had the specific surface areas of 2017 m^2/g (CFA-MDC) and 2438 m^2/g (Al-MDC). The MOFs and their respective MDCs were tested for electrochemical performance in aqueous electrolyte. The MOFs were tested in the positive potential with Al-FumMOF achieving highest specific capacity value of 28.62 mAh g^{-1} and CFA-FumMOF with 9.88 mAh g^{-1} at specific current of 0.5 A g^{-1}. The electrochemical performance of Al-FumMOF and the novel CFA-FumMOF is relatively better when compared to other reported Al-based MOFs. Previous reports on MIL-53(Al) indicated the specific capacitance of 6.5 F g^{-1} at 0.5 A g^{-1}, this can also be attributed to its agglomerated morphology as opposed to the laminar structure possessed by both Al-FumMOF and CFA-FumMOF, which enables ease of transportation of electrolyte ion.

CFA-FumMOF did not perform better as compared to Al-FumMOF. It is expected that the presence of Fe in CFA-FumMOF would increase conductivity and stability; however, in this instance the opposite is true. Due to limited free holes created and as a result, Fe ion interact with the electrolyte ions as in any Fe-based MOF, by inhibiting the flow of electrons.

CFA-MDC possessed a high specific capacitance of 306.59 F g^{-1} at 0.5 A g^{-1} as compared to Al-MDC with the value of 111.94 mAh g^{-1}. These values are consistent with other reports of MOF derived carbons from aluminium based MOFs with highest value to be 298 F g^{-1} at 1 mV s^{-1} in 1 M H_2SO_4. However, despite the high performance of the MDCs, the asymmetric capacitors performed poorly. Al-FumMOF//Al-MDC had a value of 5.09 mAh g^{-1} and 4.0 mAh g^{-1} for CFA-FumMOF//CFA-MDC at current densities of 0.5 A g^{-1}. Despite the compatibility test with other carbons (AC-Cocoa) the prepared MOFs did not improve in performance. The improved performance of the three electrode measurements of the MOFs shows that if optimization processes such preparing a composite is achieved, the materials have a potential to outperform most known MOF. With different activated carbon materials utilized as negative electrode, the device can also have improve energy and power density. The obtained carbon materials can have better performance if paired with another positive material.

The study was successfully conducted and the developed recycling strategies has the potential for contributing to existing LIBs and CFA recycling strategies and as well to the circular economy. These innovative strategies have the potential to create a new route for value-addition of waste economy for many applications as well as cost reduction in MOFs preparation.

5.2. Future work

The study was successfully conducted, however, there is still room for improvement. The study using CFA leachate as metal feedstock for MOF synthesis leaves a gap on the in depth study of bimetallic or multivalent MOFs. The presence of other metals within the leachate can be used to prepare MOFs such Fe-based and Ti-based MOFs, which can be fine tuned for better performance in electrochemistry and other application. The introduced method of recycling spent LIBs can be open for study in terms of upscaling. The metal oxide obtained from

calcination stage can be used as pseudocapacitive materials in supercapacitor application.The coal fly ash derived MOFs and spent LIBs derived MOF can also be used as sacrificial templates for the preparation of aluminium metal oxides and manganese metal oxides, which are mainly used as catalyst and also in the use of SCs

Reference

[1] R. Haldar, N. Sikdar, T.K. Maji, Interpenetration in coordination polymers: Structural diversities toward porous functional materials, Mater. Today. 18 (2015) 97–116. https://doi.org/10.1016/j.mattod.2014.10.038.

[2] R. Seetharaj, P. V. Vandana, P. Arya, S. Mathew, Dependence of solvents, pH, molar ratio and temperature in tuning metal organic framework architecture, Arab. J. Chem. 12 (2019) 295–315. https://doi.org/10.1016/j.arabjc.2016.01.003.

[3] S. Soni 1, P.K. Bajpai 2, C. Arora 2, A review on metal-organic framework: synthesis, properties and application, Charact. Appl. Nanomater. 2 (2018). https://doi.org/10.24294/can.v2i2.551.

[4] M. Safaei, M.M. Foroughi, N. Ebrahimpoor, S. Jahani, A. Omidi, M. Khatami, A review on metal-organic frameworks: Synthesis and applications, TrAC - Trends Anal. Chem. 118 (2019) 401–425. https://doi.org/10.1016/j.trac.2019.06.007.

[5] V. Guillerm, D. Kim, J.F. Eubank, R. Luebke, X. Liu, K. Adil, M.S. Lah, M. Eddaoudi, A supermolecular building approach for the design and construction of metal-organic frameworks, Chem. Soc. Rev. 43 (2014) 6141–6172. https://doi.org/10.1039/c4cs00135d.

[6] Q. Wang, D. Astruc, State of the Art and Prospects in Metal-Organic Framework (MOF)-Based and MOF-Derived Nanocatalysis, Chem. Rev. 120 (2020) 1438–1511. https://doi.org/10.1021/acs.chemrev.9b00223.

[7] J. Ren, X. Dyosiba, N.M. Musyoka, H.W. Langmi, M. Mathe, S. Liao, Review on the current practices and efforts towards pilot-scale production of metal-organic frameworks (MOFs), Coord. Chem. Rev. 352 (2017) 187–219. https://doi.org/10.1016/j.ccr.2017.09.005.

[8] V. Ting, H. V Doan, Use of waste TPA in the synthesis of a metal organic framework (MOF) for use in hydrogen storage, ORPE. (2014) 47-53. https://research-information.bris.ac.uk/en/publications/use-of-waste-tpa-in-the-synthesis-of-a-metal-organic-framework-mo

[9] X. Dyosiba, J. Ren, N.M. Musyoka, H.W. Langmi, M. Mathe, M.S. Onyango, Preparation of value-added metal-organic frameworks (MOFs) using waste PET bottles as source of acid linker, Sustain. Mater. Technol. 10 (2016) 10–13. https://doi.org/10.1016/j.susmat.2016.10.001.

[10] F. Qi, R.S. Stein, T. Friščić, Mimicking mineral neogenesis for the clean synthesis of metal-organic materials from mineral feedstocks: Coordination polymers, MOFs and metal oxide separation, Green Chem. 16 (2014) 121–132. https://doi.org/10.1039/c3gc41370e.

[11] J. Zhao, W.T. Nunn, P.C. Lemaire, Y. Lin, M.D. Dickey, C.J. Oldham, H.J. Walls, G.W. Peterson, M.D. Losego, G.N. Parsons, Facile Conversion of Hydroxy Double Salts to Metal-Organic Frameworks Using Metal Oxide Particles and Atomic Layer Deposition Thin-Film Templates, J. Am. Chem. Soc. 137 (2015) 13756–13759. https://doi.org/10.1021/jacs.5b08752.

[12] N.J. Wagner, A. Matiane, Rare earth elements in select Main Karoo Basin (South Africa) coal and coal ash samples, Int. J. Coal Geol. 196 (2018) 82–92. https://doi.org/10.1016/j.coal.2018.06.020.

[13] S. Wang, H. Wu, Environmental-benign utilisation of fly ash as low-cost adsorbents, J. Hazard. Mater. 136 (2006) 482–501. https://doi.org/10.1016/j.jhazmat.2006.01.067.

[14] S. Hartuti, S. Kambara, A. Takeyama, F.F. Hanum, E.R. Desfitri, Chemical Stabilization of Coal Fly Ash for Simultaneous Suppressing of As, B, and Se Leaching, in: Coal Fly

Ash Benef. - Treat. Acid Mine Drain. with Coal Fly Ash, InTech, 2018. https://doi.org/10.5772/intechopen.72135.

[15] D.O. Akinyele, R.K. Rayudu, Review of energy storage technologies for sustainable power networks, Sustain. Energy Technol. Assessments. 8 (2014) 74–91. https://doi.org/10.1016/j.seta.2014.07.004.

[16] D. Parra, M. Swierczynski, D.I. Stroe, S.A. Norman, A. Abdon, J. Worlitschek, T. O'Doherty, L. Rodrigues, M. Gillott, X. Zhang, C. Bauer, M.K. Patel, An interdisciplinary review of energy storage for communities: Challenges and perspectives, Renew. Sustain. Energy Rev. 79 (2017) 730–749. https://doi.org/10.1016/j.rser.2017.05.003.

[17] K.M. Winslow, S.J. Laux, T.G. Townsend, A review on the growing concern and potential management strategies of waste lithium-ion batteries, Resour. Conserv. Recycl. 129 (2018) 263–277. https://doi.org/10.1016/j.resconrec.2017.11.001.

[18] L. Li, Y. Bian, X. Zhang, Y. Guan, E. Fan, F. Wu, R. Chen, Process for recycling mixed-cathode materials from spent lithium-ion batteries and kinetics of leaching, Waste Manag. 71 (2018) 362–371. https://doi.org/10.1016/j.wasman.2017.10.028.

[19] L. Yang, G. Xi, Y. Xi, Recovery of Co, Mn, Ni, and Li from spent lithium ion batteries for the preparation of LiNixCoyMnzO2 cathode materials, Ceram. Int. 41 (2015) 11498–11503. https://doi.org/10.1016/j.ceramint.2015.05.115.

[20] M. Inada, Y. Eguchi, N. Enomoto, J. Hojo, Synthesis of zeolite from coal fly ashes with different silica-alumina composition, Fuel. 84 (2005) 299–304. https://doi.org/10.1016/j.fuel.2004.08.012.

[21] M. Wang, J. Yang, H. Ma, J. Shen, J. Li, F. Guo, Extraction of aluminum hydroxide

from coal fly ash by pre-desilication and calcination methods, in: Adv. Mater. Res., 2012: pp. 706–710. https://doi.org/10.4028/www.scientific.net/AMR.396-398.706.

[22] L. Barbieri, I. Lancellotti, T. Manfredini, I. Queralt, J.M. Rincon, M. Romero, Design, obtainment and properties of glasses and glass-ceramics from coal fly ash, Fuel. 78 (1999) 271–276. https://doi.org/10.1016/S0016-2361(98)00134-3.

[23] Y. Yaping, Z. Xiaoqiang, Q. Weilan, W. Mingwen, Synthesis of pure zeolites from supersaturated silicon and aluminum alkali extracts from fused coal fly ash, Fuel. 87 (2008) 1880–1886. https://doi.org/10.1016/j.fuel.2007.12.002.

[24] C.Y. Wu, H.F. Yu, H.F. Zhang, Extraction of aluminum by pressure acid-leaching method from coal fly ash, Trans. Nonferrous Met. Soc. China (English Ed. 22 (2012) 2282–2288. https://doi.org/10.1016/S1003-6326(11)61461-1.

[25] L.-S. Li, Y.-S. Wu, Y.-Y. Liu, Y.-C. Zhai, The Chinese Journal of Process Engineering Extraction of Alumina from Coal Fly Ash with Sulfuric Acid Leaching Method, 2011.

[26] M. Gaab, N. Trukhan, S. Maurer, R. Gummaraju, U. Müller, The progression of Al-based metal-organic frameworks - From academic research to industrial production and applications, Microporous Mesoporous Mater. 157 (2012) 131–136. https://doi.org/10.1016/j.micromeso.2011.08.016.

[27] S. Karmakar, S. Bhattacharjee, S. De, Aluminium fumarate metal organic framework incorporated polyacrylonitrile hollow fiber membranes: Spinning, characterization and application in fluoride removal from groundwater, Chem. Eng. J. 334 (2018) 41–53. https://doi.org/10.1016/j.cej.2017.10.021.

[28] J. Ordoñez, E.J. Gago, A. Girard, Processes and technologies for the recycling and recovery of spent lithium-ion batteries, Renew. Sustain. Energy Rev. 60 (2016) 195–

205. https://doi.org/10.1016/j.rser.2015.12.363.

[29] C. Peng, C. Chang, Z. Wang, B.P. Wilson, F. Liu, M. Lundström, Recovery of High-Purity MnO2 from the Acid Leaching Solution of Spent Li-Ion Batteries, JOM. 72 (2020) 790–799. https://doi.org/10.1007/s11837-019-03785-1.

[30] D. Kim, J.R. Croy, M.M. Thackeray, Comments on stabilizing layered manganese oxide electrodes for Li batteries, Electrochem. Commun. 36 (2013) 103–106. https://doi.org/10.1016/j.elecom.2013.08.022.

[31] T. Horiba, K. Hironaka, T. Matsumura, T. Kai, M. Koseki, Y. Muranaka, Manganese-based lithium batteries for hybrid electric vehicle applications, in: J. Power Sources, Elsevier, 2003: pp. 893–896. https://doi.org/10.1016/S0378-7753(03)00202-7.

[32] J.G. Wang, D. Jin, H. Liu, C. Zhang, R. Zhou, C. Shen, K. Xie, B. Wei, All-manganese-based Li-ion batteries with high rate capability and ultralong cycle life, Nano Energy. 22 (2016) 524–532. https://doi.org/10.1016/j.nanoen.2016.02.051.

[33] S. Liu, L. Xiong, C. He, Long cycle life lithium ion battery with lithium nickel cobalt manganese oxide (NCM) cathode, J. Power Sources. 261 (2014) 285–291. https://doi.org/10.1016/j.jpowsour.2014.03.083.

[34] Q. Liu, L. Yu, Y. Wang, Y. Ji, J. Horvat, M.L. Cheng, X. Jia, G. Wang, Manganese-based layered coordination polymer: Synthesis, structural characterization, magnetic property, and electrochemical performance in lithium-ion batteries, Inorg. Chem. 52 (2013) 2817–2822. https://doi.org/10.1021/ic301579g.

[35] D.J. Wuebbles, A.K. Jain, Concerns about climate change and the role of fossil fuel use, Fuel Process. Technol. 71 (2001) 99–119. https://doi.org/10.1016/S0378-3820(01)00139-4.

[36] T. Kåberger, Progress of renewable electricity replacing fossil fuels, Glob. Energy Interconnect. 1 (2018) 48–52. https://doi.org/10.14171/j.2096-5117.gei.2018.01.006.

[37] Z. Yang, J. Zhang, M.C.W. Kintner-Meyer, X. Lu, D. Choi, J.P. Lemmon, J. Liu, Electrochemical energy storage for green grid, Chem. Rev. 111 (2011) 3577–3613. https://doi.org/10.1021/cr100290v.

[38] F. Martins, C. Felgueiras, M. Smitková, Fossil fuel energy consumption in European countries, in: Energy Procedia, Elsevier Ltd, 2018: pp. 107–111. https://doi.org/10.1016/j.egypro.2018.10.050.

[39] Ü. Ağbulut, S. Sarıdemir, A general view to converting fossil fuels to cleaner energy source by adding nanoparticles, Int. J. Ambient Energy. (2018) 1–6. https://doi.org/10.1080/01430750.2018.1563822.

[40] S.D. Musa, T. Zhonghua, A.O. Ibrahim, M. Habib, China's energy status: A critical look at fossils and renewable options, Renew. Sustain. Energy Rev. 81 (2018) 2281–2290. https://doi.org/10.1016/j.rser.2017.06.036.

[41] A. Cornelius, R. Bandyopadhyay, D. Patiño-Echeverri, Assessing environmental, economic, and reliability impacts of flexible ramp products in MISO's electricity market, Renew. Sustain. Energy Rev. 81 (2018) 2291–2298. https://doi.org/10.1016/j.rser.2017.06.037.

[42] N. Khan, S. Dilshad, R. Khalid, A.R. Kalair, N. Abas, Review of energy storage and transportation of energy, Energy Storage. 1 (2019) e49. https://doi.org/10.1002/est2.49.

[43] D. Held, C. Roger, Three Models of Global Climate Governance: From Kyoto to Paris and Beyond, Glob. Policy. 9 (2018) 527–537. https://doi.org/10.1111/1758-5899.12617.

[44] J.H.A. Krug, Accounting of GHG emissions and removals from forest management: A

long road from Kyoto to Paris, Carbon Balance Manag. 13 (2018) 1. https://doi.org/10.1186/s13021-017-0089-6.

[45] T.M. Gür, Review of electrical energy storage technologies, materials and systems: Challenges and prospects for large-scale grid storage, Energy Environ. Sci. 11 (2018) 2696–2767. https://doi.org/10.1039/c8ee01419a.

[46] M. Salvia, D. Reckien, F. Pietrapertosa, P. Eckersley, N.A. Spyridaki, A. Krook-Riekkola, M. Olazabal, S. De Gregorio Hurtado, S.G. Simoes, D. Geneletti, V. Viguié, P.A. Fokaides, B.I. Ioannou, A. Flamos, M.S. Csete, A. Buzasi, H. Orru, C. de Boer, A. Foley, K. Rižnar, M. Matosović, M. V. Balzan, M. Smigaj, V. Baštáková, E. Streberova, N.B. Šel, L. Coste, L. Tardieu, C. Altenburg, E.K. Lorencová, K. Orru, A. Wejs, E. Feliu, J.M. Church, S. Grafakos, S. Vasilie, I. Paspaldzhiev, O. Heidrich, Will climate mitigation ambitions lead to carbon neutrality? An analysis of the local-level plans of 327 cities in the EU, Renew. Sustain. Energy Rev. 135 (2021) 110253. https://doi.org/10.1016/j.rser.2020.110253.

[47] V. Ramanathan, J. Allison, M. Auffhammer, D. Auston, A.D. Barnosky, L. Chiang, W.D. Collins, S.J. Davis, F. Forman, S.B. Hecht, D.M. Kammen, C.-Y.C. Lin Lawell, T. Matlock, D. Press, D. Rotman, S. Samuelsen, G. Solomon, D. Victor, B. Washom, J. Christensen, Chapter 1. Bending the Curve: Ten Scalable Solutions for Carbon Neutrality and Climate Stability, Collabra. 2 (2016). https://doi.org/10.1525/collabra.55.

[48] D.O. Akinyele, R.K. Rayudu, Review of energy storage technologies for sustainable power networks, Sustain. Energy Technol. Assessments. 8 (2014) 74–91. https://doi.org/10.1016/j.seta.2014.07.004.

[49] J.P. Barton, D.G. Infield, Energy storage and its use with intermittent renewable energy, IEEE Trans. Energy Convers. 19 (2004) 441–448.

https://doi.org/10.1109/TEC.2003.822305.

[50] A. Henriot, Economic curtailment of intermittent renewable energy sources, Energy Econ. 49 (2015) 370–379. https://doi.org/10.1016/j.eneco.2015.03.002.

[51] H. Zsiborács, N.H. Baranyai, A. Vincze, L. Zentkó, Z. Birkner, K. Máté, G. Pintér, Intermittent renewable energy sources: The role of energy storage in the european power system of 2040, Electron. 8 (2019). https://doi.org/10.3390/electronics8070729.

[52] A.B. Gallo, J.R. Simões-Moreira, H.K.M. Costa, M.M. Santos, E. Moutinho dos Santos, Energy storage in the energy transition context: A technology review, Renew. Sustain. Energy Rev. 65 (2016) 800–822. https://doi.org/10.1016/j.rser.2016.07.028.

[53] G. Notton, M.L. Nivet, C. Voyant, C. Paoli, C. Darras, F. Motte, A. Fouilloy, Intermittent and stochastic character of renewable energy sources: Consequences, cost of intermittence and benefit of forecasting, Renew. Sustain. Energy Rev. 87 (2018) 96–105. https://doi.org/10.1016/j.rser.2018.02.007.

[54] K.P. Kampouris, V. Drosou, C. Karytsas, M. Karagiorgas, Energy storage systems review and case study in the residential sector, in: IOP Conf. Ser. Earth Environ. Sci., Institute of Physics Publishing, 2020: p. 12033. https://doi.org/10.1088/1755-1315/410/1/012033.

[55] S. Koohi-Fayegh, M.A. Rosen, A review of energy storage types, applications and recent developments, J. Energy Storage. 27 (2020) 101047. https://doi.org/10.1016/j.est.2019.101047.

[56] A.G. Olabi, C. Onumaegbu, T. Wilberforce, M. Ramadan, M.A. Abdelkareem, A.H. Al – Alami, Critical review of energy storage systems, Energy. 214 (2021) 118987. https://doi.org/10.1016/j.energy.2020.118987.

[57] M.S. Guney, Y. Tepe, Classification and assessment of energy storage systems, Renew. Sustain. Energy Rev. 75 (2017) 1187–1197. https://doi.org/10.1016/j.rser.2016.11.102.

[58] M. Faisal, M.A. Hannan, P.J. Ker, A. Hussain, M. Bin Mansor, F. Blaabjerg, Review of energy storage system technologies in microgrid applications: Issues and challenges, IEEE Access. 6 (2018) 35143–35164. https://doi.org/10.1109/ACCESS.2018.2841407.

[59] M. Mahmoud, M. Ramadan, A.G. Olabi, K. Pullen, S. Naher, A review of mechanical energy storage systems combined with wind and solar applications, Energy Convers. Manag. 210 (2020) 112670. https://doi.org/10.1016/j.enconman.2020.112670.

[60] A.K. Rohit, K.P. Devi, S. Rangnekar, An overview of energy storage and its importance in Indian renewable energy sector: Part I – Technologies and Comparison, J. Energy Storage. 13 (2017) 10–23. https://doi.org/10.1016/j.est.2017.06.005.

[61] A. V Olympios, J.D. McTigue, P. Farres-Antunez, A. Tafone, A. Romagnoli, Y. Li, Y. Ding, W.-D. Steinmann, L. Wang, H. Chen, C.N. Markides, Progress and prospects of thermo-mechanical energy storage—a critical review, Prog. Energy. 3 (2021) 022001. https://doi.org/10.1088/2516-1083/abdbba.

[62] Z. Ma, M.J. Li, K.M. Zhang, F. Yuan, Novel designs of hybrid thermal energy storage system and operation strategies for concentrated solar power plant, Energy. 216 (2021) 119281. https://doi.org/10.1016/j.energy.2020.119281.

[63] H. Chen, T.N. Cong, W. Yang, C. Tan, Y. Li, Y. Ding, Progress in electrical energy storage system: A critical review, Prog. Nat. Sci. 19 (2009) 291–312. https://doi.org/10.1016/j.pnsc.2008.07.014.

[64] S.T. Revankar, Chapter Six - Chemical Energy Storage, in: Storage Hybrid. Nucl. Energy Techno-Economic Integr. Renew. Nucl. Energy, Elsevier, 2018: pp. 177–227.

https://doi.org/10.1016/B978-0-12-813975-2.00006-5.

[65] L. Chang, Review on Distributed Energy Storage Systems for Utility Applications, CPSS Trans. Power Electron. Appl. 2 (2017) 267–276. https://doi.org/10.24295/cpsstpea.2017.00025.

[66] L. Zhang, X. Hu, Z. Wang, J. Ruan, C. Ma, Z. Song, D.G. Dorrell, M.G. Pecht, Hybrid electrochemical energy storage systems: An overview for smart grid and electrified vehicle applications, Renew. Sustain. Energy Rev. 139 (2021) 110581. https://doi.org/10.1016/j.rser.2020.110581.

[67] S. Sagadevan, A.R. Marlinda, Z.Z. Chowdhury, Y.B.A. Wahab, N.A. Hamizi, M.M. Shahid, F. Mohammad, J. Podder, M.R. Johan, Fundamental electrochemical energy storage systems, in: Adv. Supercapacitor Supercapattery, Elsevier, 2021: pp. 27–43. https://doi.org/10.1016/b978-0-12-819897-1.00001-x.

[68] Poonam, K. Sharma, A. Arora, S.K. Tripathi, Review of supercapacitors: Materials and devices, J. Energy Storage. 21 (2019) 801–825. https://doi.org/10.1016/j.est.2019.01.010.

[69] H. Ibrahim, A. Ilinc, Techno-Economic Analysis of Different Energy Storage Technologies, in: Energy Storage - Technol. Appl., InTech, 2013. https://doi.org/10.5772/52220.

[70] M. Isaac, D.P. van Vuuren, Modeling global residential sector energy demand for heating and air conditioning in the context of climate change, Energy Policy. 37 (2009) 507–521. https://doi.org/10.1016/j.enpol.2008.09.051.

[71] L. Suganthi, A.A. Samuel, Energy models for demand forecasting - A review, Renew. Sustain. Energy Rev. 16 (2012) 1223–1240. https://doi.org/10.1016/j.rser.2011.08.014.

[72] L. Huilin, Z. Guangbo, B. Rushan, C. Yongjin, D. Gidaspow, Coal combustion model for circulating fluidized bed boilers, Fuel. 79 (2000) 165–172. https://doi.org/10.1016/S0016-2361(99)00139-8.

[73] A. Molina, C.R. Shaddix, Ignition and devolatilization of pulverized bituminous coal particles during oxygen/carbon dioxide coal combustion, Proc. Combust. Inst. 31 II (2007) 1905–1912. https://doi.org/10.1016/j.proci.2006.08.102.

[74] K. Yan, Y. Guo, Z. Ma, Z. Zhao, F. Cheng, Quantitative analysis of crystalline and amorphous phases in pulverized coal fly ash based on the Rietveld method, J. Non. Cryst. Solids. 483 (2018) 37–42. https://doi.org/10.1016/j.jnoncrysol.2017.12.043.

[75] S.C. White, E.D. Case, Characterization of fly ash from coal-fired power plants, J. Mater. Sci. 25 (1990) 5215–5219. https://doi.org/10.1007/BF00580153.

[76] D. Zhang, Introduction to advanced and ultra-supercritical fossil fuel power plants, in: Ultra-Supercritical Coal Power Plants Mater. Technol. Optim., Elsevier Ltd, 2013: pp. 1–20. https://doi.org/10.1533/9780857097514.1.

[77] R.E. Desrosiers, J.W. Riehl, G.D. Ulrich, A.S. Chiu, Submicron fly-ash formation in coal-fired boilers, Symp. Combust. 17 (1979) 1395–1403. https://doi.org/10.1016/S0082-0784(79)80131-9.

[78] N. Ranjbar, C. Kuenzel, Cenospheres: A review, Fuel. 207 (2017) 1–12. https://doi.org/10.1016/j.fuel.2017.06.059.

[79] W.M. Gitari, O.O. Fatoba, L.F. Petrik, V.R.K. Vadapalli, Leaching characteristics of selected South African fly ashes: Effect of pH on the release of major and trace species, J. Environ. Sci. Heal. - Part A Toxic/Hazardous Subst. Environ. Eng. 44 (2009) 206–220. https://doi.org/10.1080/10934520802539897.

[80] J.L. Fernández-Turiel, W. de Carvalho, M. Cabañas, X. Querol, A. López-Soler, Mobility of heavy metals from coal fly ash, Environ. Geol. 23 (1994) 264–270. https://doi.org/10.1007/BF00766741.

[81] S. Beddu, M. Zainoodin, N.M. Kamal, D. Mohamad, S. Nabihah, F.M. Nazri, Material characterization of coal combustion product (cenosphere) generated from coal - Fired power plant in Malaysia, in: AIP Conf. Proc., American Institute of Physics Inc., 2018: p. 020259. https://doi.org/10.1063/1.5066900.

[82] Chapter 1 - Fly Ash - An Engineering Material - Fly Ash Facts for Highway Engineers - Recycling - Sustainability - Pavements - Federal Highway Administration, (n.d.). https://www.fhwa.dot.gov/pavement/recycling/fach01.cfm (accessed May 29, 2021).

[83] S. V. Vassilev, C.G. Vassileva, A new approach for the classification of coal fly ashes based on their origin, composition, properties, and behaviour, Fuel. 86 (2007) 1490–1512. https://doi.org/10.1016/j.fuel.2006.11.020.

[84] D.P. Mishra, S.K. Das, A study of physico-chemical and mineralogical properties of Talcher coal fly ash for stowing in underground coal mines, Mater. Charact. 61 (2010) 1252–1259. https://doi.org/10.1016/j.matchar.2010.08.008.

[85] A.R.K. Gollakota, V. Volli, C.M. Shu, Progressive utilisation prospects of coal fly ash: A review, Sci. Total Environ. 672 (2019) 951–989. https://doi.org/10.1016/j.scitotenv.2019.03.337.

[86] Fly Ash Market by Type, Application & Geography | COVID-19 Impact Analysis | MarketsandMarkets, (n.d.). https://www.marketsandmarkets.com/Market-Reports/fly-ash-market-76345803.html (accessed May 28, 2021).

[87] A. Malik, A. Thapliyal, Eco-friendly fly ash utilization: Potential for land application,

Crit. Rev. Environ. Sci. Technol. 39 (2009) 333–366. https://doi.org/10.1080/10643380701413690.

[88] D.C. Adriano, J.T. Weber, Influence of Fly Ash on Soil Physical Properties and Turfgrass Establishment, J. Environ. Qual. 30 (2001) 596–601. https://doi.org/10.2134/jeq2001.302596x.

[89] J.W.C. Wong, K.M. Lai, Effect of an artificial soil mix from coal fly ash and sewage sludge on soil microbial activity, Biol. Fertil. Soils. 23 (1996) 420–424. https://doi.org/10.1007/BF00335916.

[90] J. Vargas, A. Halog, Effective carbon emission reductions from using upgraded fly ash in the cement industry, J. Clean. Prod. 103 (2015) 948–959. https://doi.org/10.1016/j.jclepro.2015.04.136.

[91] A. Guerrero, S. Goñi, I. Campillo, A. Moragues, Belite cement clinker from coal fly ash of high Ca content. Optimization of synthesis parameters, Environ. Sci. Technol. 38 (2004) 3209–3213. https://doi.org/10.1021/es0351589.

[92] M. Cheriaf, J.C. Rocha, J. Péra, Pozzolanic properties of pulverized coal combustion bottom ash, Cem. Concr. Res. 29 (1999) 1387–1391. https://doi.org/10.1016/S0008-8846(99)00098-8.

[93] G.L. Golewski, Improvement of fracture toughness of green concrete as a result of addition of coal fly ash. Characterization of fly ash microstructure, Mater. Charact. 134 (2017) 335–346. https://doi.org/10.1016/j.matchar.2017.11.008.

[94] Optimizing the use of fly ash in concrete (Miscellaneous) | OSTI.GOV, (n.d.). https://www.osti.gov/biblio/21095693-optimizing-use-fly-ash-concrete (accessed May 28, 2021).

[95] A.K. Rai, B. Paul, G. Singh, A Study on Backfill Properties and Use of Fly Ash for Highway Embankments, J. Adv. Lab. Res. Biol. 1 (2010) 110–114. https://e-journal.sospublication.co.in/index.php/jalrb/article/view/44 (accessed May 28, 2021).

[96] A. Arulrajah, J. Piratheepan, M.M. Disfani, M.W. Bo, Geotechnical and Geoenvironmental Properties of Recycled Construction and Demolition Materials in Pavement Subbase Applications, J. Mater. Civ. Eng. 25 (2013) 1077–1088. https://doi.org/10.1061/(asce)mt.1943-5533.0000652.

[97] S. Attarde, UTILIZATION OF FLY ASH IN CONSTRUCTION INDUSTRIES FOR ENVIRONMENT MANAGEMENT, 2014. https://www.researchgate.net/publication/268740979 (accessed May 28, 2021).

[98] A.R. Boccaccini, M. Bücker, J. Bossert, K. Marszalek, Glass matrix composites from coal flyash and waste glass, Waste Manag. 17 (1997) 39–45. https://doi.org/10.1016/S0956-053X(97)00035-4.

[99] J. Sheng, Vitrification of borate waste from nuclear power plant using coal fly ash. (I) Glass formulation development, Fuel. 80 (2001) 1365–1369. https://doi.org/10.1016/S0016-2361(01)00022-9.

[100] J. Sheng, B.X. Huang, J. Zhang, H. Zhang, J. Sheng, S. Yu, M. Zhang, Production of glass from coal fly ash, Fuel. 82 (2003) 181–185. https://doi.org/10.1016/S0016-2361(02)00238-7.

[101] J. Zhang, W. Dong, J. Li, L. Qiao, J. Zheng, J. Sheng, Utilization of coal fly ash in the glass-ceramic production, J. Hazard. Mater. 149 (2007) 523–526. https://doi.org/10.1016/j.jhazmat.2007.07.044.

[102] Y. He, W. Cheng, H. Cai, Characterization of α-cordierite glass-ceramics from fly ash,

J. Hazard. Mater. 120 (2005) 265–269. https://doi.org/10.1016/j.jhazmat.2004.10.028.

[103] G. Itskos, N. Koukouzas, C. Vasilatos, I. Megremi, A. Moutsatsou, Comparative uptake study of toxic elements from aqueous media by the different particle-size-fractions of fly ash, J. Hazard. Mater. 183 (2010) 787–792. https://doi.org/10.1016/j.jhazmat.2010.07.095.

[104] S. Mohan, R. Gandhimathi, Removal of heavy metal ions from municipal solid waste leachate using coal fly ash as an adsorbent, J. Hazard. Mater. 169 (2009) 351–359. https://doi.org/10.1016/j.jhazmat.2009.03.104.

[105] C.L. Zhang, G.L. Qiao, F. Zhao, Y. Wang, Thermodynamic and kinetic parameters of ciprofloxacin adsorption onto modified coal fly ash from aqueous solution, J. Mol. Liq. 163 (2011) 53–56. https://doi.org/10.1016/j.molliq.2011.07.005.

[106] O.E. Abdel Salam, N.A. Reiad, M.M. ElShafei, A study of the removal characteristics of heavy metals from wastewater by low-cost adsorbents, J. Adv. Res. 2 (2011) 297–303. https://doi.org/10.1016/j.jare.2011.01.008.

[107] E. Sočo, J. Kalembkiewicz, Adsorption of nickel(II) and copper(II) ions from aqueous solution by coal fly ash, J. Environ. Chem. Eng. 1 (2013) 581–588. https://doi.org/10.1016/j.jece.2013.06.029.

[108] M.K. Jha, A. Kumari, R. Panda, J. Rajesh Kumar, K. Yoo, J.Y. Lee, Review on hydrometallurgical recovery of rare earth metals, Hydrometallurgy. 165 (2016) 2–26. https://doi.org/10.1016/j.hydromet.2016.01.035.

[109] A. Pol, T.R.M. Barends, A. Dietl, A.F. Khadem, J. Eygensteyn, M.S.M. Jetten, H.J.M. Op den Camp, Rare earth metals are essential for methanotrophic life in volcanic mudpots, Environ. Microbiol. 16 (2014) 255–264. https://doi.org/10.1111/1462-

2920.12249.

[110] A.R. Chakhmouradian, F. Wall, Rare earth elements: Minerals, mines, magnets (and more), Elements. 8 (2012) 333–340. https://doi.org/10.2113/gselements.8.5.333.

[111] M. Eichhorn, Quasi-three-level solid-state lasers in the near and mid infrared based on trivalent rare earth ions, Appl. Phys. B Lasers Opt. 93 (2008) 269–316. https://doi.org/10.1007/s00340-008-3214-0.

[112] Q. Tan, J. Li, X. Zeng, Rare Earth Elements Recovery from Waste Fluorescent Lamps: A Review, Crit. Rev. Environ. Sci. Technol. 45 (2015) 749–776. https://doi.org/10.1080/10643389.2014.900240.

[113] C.O. Iloeje, C.F. Jové Colón, J. Cresko, D.J. Graziano, Gibbs Energy Minimization Model for Solvent Extraction with Application to Rare-Earths Recovery, Environ. Sci. Technol. 53 (2019) 7736–7745. https://doi.org/10.1021/acs.est.9b01718.

[114] S. Massari, M. Ruberti, Rare earth elements as critical raw materials: Focus on international markets and future strategies, Resour. Policy. 38 (2013) 36–43. https://doi.org/10.1016/j.resourpol.2012.07.001.

[115] S. Dai, L. Zhao, S. Peng, C.L. Chou, X. Wang, Y. Zhang, D. Li, Y. Sun, Abundances and distribution of minerals and elements in high-alumina coal fly ash from the Jungar Power Plant, Inner Mongolia, China, Int. J. Coal Geol. 81 (2010) 320–332. https://doi.org/10.1016/j.coal.2009.03.005.

[116] T. Gupta, T. Ghosh, G. Akdogan, V.K. Srivastava, Characterizing rare earth elements in Alaskan coal and ash, Miner. Metall. Process. 34 (2017) 138–145. https://doi.org/10.19150/mmp.7614.

[117] L. Jing, C.Y. Kwok, Y.F. Leung, Micromechanical Origin of Particle Size Segregation,

Phys. Rev. Lett. 118 (2017) 118001. https://doi.org/10.1103/PhysRevLett.118.118001.

[118] S. V. Vassilev, R. Menendez, A.G. Borrego, M. Diaz-Somoano, M.R. Martinez-Tarazona, Phase-mineral and chemical composition of coal fly ashes as a basis for their multicomponent utilization. 3. Characterization of magnetic and char concentrates, in: Fuel, Elsevier, 2004: pp. 1563–1583. https://doi.org/10.1016/j.fuel.2004.01.010.

[119] A.S. Shoumkova, Magnetic separation of coal fly ash from Bulgarian power plants, Waste Manag. Res. 29 (2011) 1078–1089. https://doi.org/10.1177/0734242X10379494.

[120] A. Shoumkova, PHYSICO-CHEMICAL CHARACTERIZATION AND MAGNETIC SEPARATION OF COAL FLY ASHES FROM "VARNA", "BOBOV DOL" AND "MARITZA-ISTOK I" POWER PLANTS, BULGARIA. II-MAGNETIC SEPARATION, 2006. https://dl.uctm.edu/journal/node/j2006-2/14-a.shoumkova.pdf (accessed May 29, 2021).

[121] C. Tian, J. Zhang, Y. Zhao, R. Gupta, Understanding of mineralogy and residence of trace elements in coals via a novel method combining low temperature ashing and float-sink technique, Int. J. Coal Geol. 131 (2014) 162–171. https://doi.org/10.1016/j.coal.2014.06.005.

[122] I. Acar, M.U. Atalay, Recovery potentials of cenospheres from bituminous coal fly ashes, Fuel. 180 (2016) 97–105. https://doi.org/10.1016/j.fuel.2016.04.013.

[123] Y.M.S. Meor, Rate of rare earths leaching in HCI, H_2SO_4 AND HNO_3, in: Adv. Mater. Res., Trans Tech Publications Ltd, 2013: pp. 1–4. https://doi.org/10.4028/www.scientific.net/AMR.795.1.

[124] A. Kolker, C. Scott, J.C. Hower, J.A. Vazquez, C.L. Lopano, S. Dai, Distribution of rare earth elements in coal combustion fly ash, determined by SHRIMP-RG ion microprobe,

Int. J. Coal Geol. 184 (2017) 1–10. https://doi.org/10.1016/j.coal.2017.10.002.

[125] A. Kumari, R. Parween, S. Chakravarty, K. Parmar, D.D. Pathak, J. chun Lee, M.K. Jha, Novel approach to recover rare earth metals (REMs) from Indian coal bottom ash, Hydrometallurgy. 187 (2019) 1–7. https://doi.org/10.1016/j.hydromet.2019.04.024.

[126] M. Tang, C. Zhou, N. Zhang, J. Pan, S. Cao, T. Hu, W. Ji, Z. Wen, T. Nie, Extraction of rare earth elements from coal fly ash by alkali fusion–acid leaching: Mechanism analysis, Int. J. Coal Prep. Util. (2019). https://doi.org/10.1080/19392699.2019.1623206.

[127] R.K. Taggart, J.C. Hower, H. Hsu-Kim, Effects of roasting additives and leaching parameters on the extraction of rare earth elements from coal fly ash, Int. J. Coal Geol. 196 (2018) 106–114. https://doi.org/10.1016/j.coal.2018.06.021.

[128] M. Tang, C. Zhou, J. Pan, N. Zhang, C. Liu, S. Cao, T. Hu, W. Ji, Study on extraction of rare earth elements from coal fly ash through alkali fusion – Acid leaching, Miner. Eng. 136 (2019) 36–42. https://doi.org/10.1016/j.mineng.2019.01.027.

[129] A Review of the Chemistry, Structure, Properties and Applications of Zeolites, (n.d.). http://article.sapub.org/10.5923.j.materials.20170705.12.html (accessed May 28, 2021).

[130] E. Polat, M. Karaca, H. Demir, A.N. Onus, USE OF NATURAL ZEOLITE (CLINOPTILOLITE) IN AGRICULTURE, 2004.

[131] C.J. Rhodes, Properties and applications of zeolites, Sci. Prog. 93 (2010) 223–284. https://doi.org/10.3184/003685010X12800828155007.

[132] N. Murayama, H. Yamamoto, J. Shibata, Zeolite synthesis from coal fly ash by hydrothermal reaction using various alkali sources, in: J. Chem. Technol. Biotechnol., John Wiley & Sons, Ltd, 2002: pp. 280–286. https://doi.org/10.1002/jctb.604.

[133] G.G. Hollman, G. Steenbruggen, M. Janssen-Jurkovičová, Two-step process for the synthesis of zeolites from coal fly ash, Fuel. 78 (1999) 1225–1230. https://doi.org/10.1016/S0016-2361(99)00030-7.

[134] J.L.X. Hong, T. Maneerung, S.N. Koh, S. Kawi, C.H. Wang, Conversion of Coal Fly Ash into Zeolite Materials: Synthesis and Characterizations, Process Design, and Its Cost-Benefit Analysis, Ind. Eng. Chem. Res. 56 (2017) 11565–11574. https://doi.org/10.1021/acs.iecr.7b02885.

[135] M. Inada, H. Tsujimoto, Y. Eguchi, N. Enomoto, J. Hojo, Microwave-assisted zeolite synthesis from coal fly ash in hydrothermal process, Fuel. 84 (2005) 1482–1486. https://doi.org/10.1016/j.fuel.2005.02.002.

[136] N. Koshy, D.N. Singh, Fly ash zeolites for water treatment applications, J. Environ. Chem. Eng. 4 (2016) 1460–1472. https://doi.org/10.1016/j.jece.2016.02.002.

[137] M. Chigondo, U. Guyo, M. Shumba, F. Chigondo, B.C. Nyamunda, M. Moyo, T. Nharingo, Synthesis and characterisation of Zeolites from Coal Fly Ash (CFA), (2013). http://ir.msu.ac.zw:8080/xmlui/handle/11408/1111 (accessed May 28, 2021).

[138] G. Verrecchia, L. Cafiero, B. de Caprariis, A. Dell'Era, I. Pettiti, R. Tuffi, M. Scarsella, Study of the parameters of zeolites synthesis from coal fly ash in order to optimize their CO2 adsorption, Fuel. 276 (2020) 118041. https://doi.org/10.1016/j.fuel.2020.118041.

[139] O.B. Pagar, H.S. Nagare, Y.M. Chine, R.R. Autade, P.R. Narode, V.M. Sanklecha, Mesoporous Silica: A Review, Int. J. Pharm. DRUG Anal. 6 (2018) 1–12.

[140] R. Narayan, U.Y. Nayak, A.M. Raichur, S. Garg, Mesoporous silica nanoparticles: A comprehensive review on synthesis and recent advances, Pharmaceutics. 10 (2018). https://doi.org/10.3390/pharmaceutics10030118.

[141] P. Kumar, N. Mal, Y. Oumi, K. Yamana, T. Sano, Mesoporous materials prepared using coal fly ash as the silicon and aluminium source, J. Mater. Chem. 11 (2001) 3285–3290. https://doi.org/10.1039/b104810b.

[142] H. Lin, L. Wan, Y. Yang, Aluminium hydroxide ultrafine powder extracted from fly ash, in: Adv. Mater. Res., 2012: pp. 1548–1553. https://doi.org/10.4028/www.scientific.net/AMR.512-515.1548.

[143] R. Singh, L. Singh, S.V. Singh, Beneficiation of iron and aluminium oxides from fly ash at lab scale, Int. J. Miner. Process. 145 (2015) 32–37. https://doi.org/10.1016/j.minpro.2015.08.001.

[144] S. Sangita, C.R. Panda, Acid leaching technique for the possible recovery of aluminium and other metal values from coal fly ashes, 2016. https://www.researchgate.net/publication/321361599 (accessed May 28, 2021).

[145] Study of recovery of highly pure super-fine powdered... - Google Scholar, (n.d.). https://scholar.google.com/scholar?hl=en&as_sdt=0%2C5&q=Study+of+recovery+of+highly+pure+super-fine+powdered+aluminum+oxide+from+fly+ash+by+way+of+lime+sintered+self+powdering&btnG= (accessed May 29, 2021).

[146] R. Padilla, H.Y. Sohn, Sodium aluminate leaching and desilication in lime-soda sinter process for alumina from coal wastes, Metall. Trans. B. 16 (1985) 707–713. https://doi.org/10.1007/BF02667507.

[147] R.H. Matjie, J.R. Bunt, J.H.P. Van Heerden, Extraction of alumina from coal fly ash generated from a selected low rank bituminous South African coal, Miner. Eng. 18 (2005) 299–310. https://doi.org/10.1016/j.mineng.2004.06.013.

[148] A. Shemi, S. Ndlovu, V. Sibanda, L.D. Van Dyk, Extraction of alumina from coal fly ash using an acid leach-sinter-acid leach technique, Hydrometallurgy. 157 (2015) 348–355. https://doi.org/10.1016/j.hydromet.2015.08.023.

[149] N. Stock, S. Biswas, Synthesis of metal-organic frameworks (MOFs): Routes to various MOF topologies, morphologies, and composites, Chem. Rev. 112 (2012) 933–969. https://doi.org/10.1021/cr200304e.

[150] S. Yuan, L. Feng, K. Wang, J. Pang, M. Bosch, C. Lollar, Y. Sun, J. Qin, X. Yang, P. Zhang, Q. Wang, L. Zou, Y. Zhang, L. Zhang, Y. Fang, J. Li, H.C. Zhou, Stable Metal–Organic Frameworks: Design, Synthesis, and Applications, Adv. Mater. 30 (2018) 1704303. https://doi.org/10.1002/adma.201704303.

[151] Y.R. Lee, J. Kim, W.S. Ahn, Synthesis of metal-organic frameworks: A mini review, Korean J. Chem. Eng. 30 (2013) 1667–1680. https://doi.org/10.1007/s11814-013-0140-6.

[152] M. Bosch, M. Zhang, H.-C. Zhou, Increasing the Stability of Metal-Organic Frameworks, Adv. Chem. 2014 (2014) 1–8. https://doi.org/10.1155/2014/182327.

[153] P. Coppens, Y. Chen, E. Trzop, Crystallography and properties of polyoxotitanate nanoclusters, Chem. Rev. 114 (2014) 9645–9661. https://doi.org/10.1021/cr400724e.

[154] C. Serre, J.A. Groves, P. Lightfoot, A.M.Z. Slawin, P.A. Wright, N. Stock, T. Bein, M. Haouas, F. Taulelle, G. Férey, Synthesis, structure and properties of related microporous N,N′-piperazinebismethylenephosphonates of aluminum and titanium, Chem. Mater. 18 (2006) 1451–1457. https://doi.org/10.1021/cm052149l.

[155] H. Wang, X. Yuan, Y. Wu, G. Zeng, X. Chen, L. Leng, Z. Wu, L. Jiang, H. Li, Facile synthesis of amino-functionalized titanium metal-organic frameworks and their superior

visible-light photocatalytic activity for Cr(VI) reduction, J. Hazard. Mater. 286 (2015) 187–194. https://doi.org/10.1016/j.jhazmat.2014.11.039.

[156] C. Hon Lau, R. Babarao, M.R. Hill, A route to drastic increase of CO2 uptake in Zr metal organic framework UiO-66, Chem. Commun. 49 (2013) 3634–3636. https://doi.org/10.1039/c3cc40470f.

[157] L. Zou, D. Feng, T.F. Liu, Y.P. Chen, S. Yuan, K. Wang, X. Wang, S. Fordham, H.C. Zhou, A versatile synthetic route for the preparation of titanium metal-organic frameworks, Chem. Sci. 7 (2016) 1063–1069. https://doi.org/10.1039/c5sc03620h.

[158] I. Senkovska, F. Hoffmann, M. Fröba, J. Getzschmann, W. Böhlmann, S. Kaskel, New highly porous aluminium based metal-organic frameworks: Al(OH)(ndc) (ndc = 2,6-naphthalene dicarboxylate) and Al(OH)(bpdc) (bpdc = 4,4′-biphenyl dicarboxylate), Microporous Mesoporous Mater. 122 (2009) 93–98. https://doi.org/10.1016/j.micromeso.2009.02.020.

[159] G. Férey, M. Latroche, C. Serre, … F.M.-C., undefined 2003, Hydrogen adsorption in the nanoporous metal-benzenedicarboxylate M (OH)($O_2C–C_6H_4–CO_2$)($M= Al^{3+}$, Cr^{3+}), MIL-53, Pubs.Rsc.Org. (n.d.). https://pubs.rsc.org/fa/content/articlehtml/2003/cc/b308903g (accessed May 29, 2021).

[160] T. Loiseau, C. Serre, C. Huguenard, G. Fink, F. Taulelle, M. Henry, T. Bataille, G. Férey, A Rationale for the Large Breathing of the Porous Aluminum Terephthalate (MIL-53) Upon Hydration, Chem. - A Eur. J. 10 (2004) 1373–1382. https://doi.org/10.1002/chem.200305413.

[161] D.T.C. Nguyen, H.T.N. Le, T.S. Do, V.T. Pham, D.L. Tran, V.T.T. Ho, T. Van Tran, D.C. Nguyen, T.D. Nguyen, L.G. Bach, H.K.P. Ha, V.T. Doan, Metal-Organic Framework MIL-53(Fe) as an adsorbent for ibuprofen drug removal from aqueous

solutions: Response surface modeling and optimization, J. Chem. 2019 (2019). https://doi.org/10.1155/2019/5602957.

[162] E. Yilmaz, E. Sert, F.S. Atalay, Synthesis, characterization of a metal organic framework: MIL-53 (Fe) and adsorption mechanisms of methyl red onto MIL-53 (Fe), J. Taiwan Inst. Chem. Eng. 65 (2016) 323–330. https://doi.org/10.1016/j.jtice.2016.05.028.

[163] M. Ma, A. Bétard, I. Weber, N.S. Al-Hokbany, R.A. Fischer, N. Metzler-Nolte, Iron-based metal-organic frameworks MIL-88B and NH_2-MIL-88B: High quality microwave synthesis and solvent-induced lattice "breathing," Cryst. Growth Des. 13 (2013) 2286–2291. https://doi.org/10.1021/cg301738p.

[164] I. Ahmed, J. Jeon, N.A. Khan, S.H. Jhung, Synthesis of a metal-organic framework, iron-benezenetricarboxylate, from dry gels in the absence of acid and salt, Cryst. Growth Des. 12 (2012) 5878–5881. https://doi.org/10.1021/cg3014317.

[165] E. Haque, N.A. Khan, H.J. Park, S.H. Jhung, Synthesis of a metal-organic framework material, iron terephthalate, by ultrasound, microwave, and conventional electric heating: A kinetic study, Chem. - A Eur. J. 16 (2010) 1046–1052. https://doi.org/10.1002/chem.200902382.

[166] N. Tannert, S. Gökpinar, E. Hastürk, S. Nießing, C. Janiak, Microwave-assisted dry-gel conversion-a new sustainable route for the rapid synthesis of metal-organic frameworks with solvent re-use, Dalt. Trans. 47 (2018) 9850–9860. https://doi.org/10.1039/c8dt02029a.

[167] L. Ai, C. Zhang, L. Li, J. Jiang, Iron terephthalate metal-organic framework: Revealing the effective activation of hydrogen peroxide for the degradation of organic dye under visible light irradiation, Appl. Catal. B Environ. 148–149 (2014) 191–200.

https://doi.org/10.1016/j.apcatb.2013.10.056.

[168] Y.K. Seo, J.W. Yoon, J.S. Lee, U.H. Lee, Y.K. Hwang, C.H. Jun, P. Horcajada, C. Serre, J.S. Chang, Large scale fluorine-free synthesis of hierarchically porous iron(III) trimesate MIL-100(Fe) with a zeolite MTN topology, Microporous Mesoporous Mater. 157 (2012) 137–145. https://doi.org/10.1016/j.micromeso.2012.02.027.

[169] P. Horcajada, F. Salles, S. Wuttke, T. Devic, D. Heurtaux, G. Maurin, A. Vimont, M. Daturi, O. David, E. Magnier, N. Stock, Y. Filinchuk, D. Popov, C. Riekel, G. Férey, C. Serre, How linker's modification controls swelling properties of highly flexible iron(III) dicarboxylates MIL-88, J. Am. Chem. Soc. 133 (2011) 17839–17847. https://doi.org/10.1021/ja206936e.

[170] S. Bauer, C. Serre, T. Devic, P. Horcajada, J. Marrot, G. Férey, N. Stock, High-throughput assisted rationalization of the formation of metal organic frameworks in the iron(III) aminoterephthalate solvothermal system, Inorg. Chem. 47 (2008) 7568–7576. https://doi.org/10.1021/ic800538r.

[171] H. Wu, T. Yildirim, W. Zhou, Exceptional mechanical stability of highly porous zirconium metal-organic framework UiO-66 and its important implications, J. Phys. Chem. Lett. 4 (2013) 925–930. https://doi.org/10.1021/jz4002345.

[172] J.H. Cavka, S. Jakobsen, U. Olsbye, N. Guillou, C. Lamberti, S. Bordiga, K.P. Lillerud, A new zirconium inorganic building brick forming metal organic frameworks with exceptional stability, J. Am. Chem. Soc. 130 (2008) 13850–13851. https://doi.org/10.1021/ja8057953.

[173] D. Zou, D. Liu, Understanding the modifications and applications of highly stable porous frameworks via UiO-66, Mater. Today Chem. 12 (2019) 139–165. https://doi.org/10.1016/j.mtchem.2018.12.004.

[174] C. Kutzscher, G. Nickerl, I. Senkovska, V. Bon, S. Kaskel, Proline Functionalized UiO-67 and UiO-68 Type Metal-Organic Frameworks Showing Reversed Diastereoselectivity in Aldol Addition Reactions, Chem. Mater. 28 (2016) 2573–2580. https://doi.org/10.1021/acs.chemmater.5b04575.

[175] J.D. Evans, B. Garai, H. Reinsch, W. Li, S. Dissegna, V. Bon, I. Senkovska, R.A. Fischer, S. Kaskel, C. Janiak, N. Stock, D. Volkmer, Metal–organic frameworks in Germany: From synthesis to function, Coord. Chem. Rev. 380 (2019) 378–418. https://doi.org/10.1016/j.ccr.2018.10.002.

[176] A. Schaate, P. Roy, A. Godt, J. Lippke, F. Waltz, M. Wiebcke, P. Behrens, Modulated synthesis of Zr-based metal-organic frameworks: From nano to single crystals, Chem. - A Eur. J. 17 (2011) 6643–6651. https://doi.org/10.1002/chem.201003211.

[177] J. Ren, H.W. Langmi, B.C. North, M. Mathe, D. Bessarabov, Modulated synthesis of zirconium-metal organic framework (Zr-MOF) for hydrogen storage applications, Int. J. Hydrogen Energy. 39 (2014) 890–895. https://doi.org/10.1016/j.ijhydene.2013.10.087.

[178] H. Wu, Y.S. Chua, V. Krungleviciute, M. Tyagi, P. Chen, T. Yildirim, W. Zhou, Unusual and highly tunable missing-linker defects in zirconium metal-organic framework UiO-66 and their important effects on gas adsorption, J. Am. Chem. Soc. 135 (2013) 10525–10532. https://doi.org/10.1021/ja404514r.

[179] G. Zhan, W.C. Ng, W.Y. Lin, S.N. Koh, C.H. Wang, Effective Recovery of Vanadium from Oil Refinery Waste into Vanadium-Based Metal-Organic Frameworks, Environ. Sci. Technol. 52 (2018) 3008–3015. https://doi.org/10.1021/acs.est.7b04989.

[180] J.N. Joshi, C.M. Moran, H.P. Feininger, J.M. Dow, K.S. Walton, Household Aluminum Products as Insoluble Precursors for Directed Growth of Metal-Organic Frameworks,

Cryst. Growth Des. 19 (2019) 5097–5104. https://doi.org/10.1021/acs.cgd.9b00452.

[181] K. Song, X. Qiu, B. Han, S. Liang, Z. Lin, Efficient upcycling electroplating sludge and waste PET into Ni-MOF nanocrystals for the effective photoreduction of CO2, Environ. Sci. Nano. 8 (2021) 390–398. https://doi.org/10.1039/d0en01061h.

[182] G. Gautham Prasad, N. Shetty, S. Thakur, Rakshitha, K.B. Bommegowda, Supercapacitor technology and its applications: A review, in: IOP Conf. Ser. Mater. Sci. Eng., Institute of Physics Publishing, 2019: p. 012105. https://doi.org/10.1088/1757-899X/561/1/012105.

[183] A.A. Mirghni, K.O. Oyedotun, B.A. Mahmoud, A. Bello, S.C. Ray, N. Manyala, Nickel-cobalt phosphate/graphene foam as enhanced electrode for hybrid supercapacitor, Compos. Part B Eng. 174 (2019) 106953. https://doi.org/10.1016/j.compositesb.2019.106953.

[184] B.K. Kim, S. Sy, A. Yu, J. Zhang, Electrochemical Supercapacitors for Energy Storage and Conversion, in: Handb. Clean Energy Syst., John Wiley & Sons, Ltd, 2015: pp. 1–25. https://doi.org/10.1002/9781118991978.hces112.

[185] T.M. Masikhwa, M.J. Madito, A. Bello, J. Lekitima, N. Manyala, Microwave-assisted synthesis of cobalt sulphide nanoparticle clusters on activated graphene foam for electrochemical supercapacitors, RSC Adv. 7 (2017) 20231–20240. https://doi.org/10.1039/c7ra02204b.

[186] Y. Tan, W. Zhang, Y. Gao, J. Wu, B. Tang, Facile synthesis and supercapacitive properties of Zr-metal organic frameworks (UiO-66), RSC Adv. 5 (2015) 17601–17605. https://doi.org/10.1039/c4ra11896k.

[187] K.F. Babu, M.A. Kulandainathan, I. Katsounaros, L. Rassaei, A.D. Burrows, P.R.

Raithby, F. Marken, Electrocatalytic activity of BasoliteTM F300 metal-organic-framework structures, Electrochem. Commun. 12 (2010) 632–635. https://doi.org/10.1016/j.elecom.2010.02.017.

[188] M. Majumder, R.B. Choudhary, A.K. Thakur, A. Khodayari, M. Amiri, R. Boukherroub, S. Szunerits, Aluminum based metal-organic framework integrated with reduced graphene oxide for improved supercapacitive performance, Electrochim. Acta. 353 (2020) 136609. https://doi.org/10.1016/j.electacta.2020.136609.

[189] Y. Zhang, B. Lin, Y. Sun, X. Zhang, H. Yang, J. Wang, Carbon nanotubes@metal–organic frameworks as Mn-based symmetrical supercapacitor electrodes for enhanced charge storage, RSC Adv. 5 (2015) 58100–58106. https://doi.org/10.1039/c5ra11597c.

[190] F. Marpaung, M. Kim, J.H. Khan, K. Konstantinov, Y. Yamauchi, M.S.A. Hossain, J. Na, J. Kim, Metal–Organic Framework (MOF)-Derived Nanoporous Carbon Materials, Chem. - An Asian J. 14 (2019) 1331–1343. https://doi.org/10.1002/asia.201900026.

[191] L. Radhakrishnan, J. Reboul, S. Furukawa, P. Srinivasu, S. Kitagawa, Y. Yamauchi, Preparation of microporous carbon fibers through carbonization of al-based porous coordination polymer (Al-PCP) with furfuryl alcohol, Chem. Mater. 23 (2011) 1225–1231. https://doi.org/10.1021/cm102921y.

[192] P. Su, L. Jiang, J. Zhao, J. Yan, C. Li, Q. Yang, Mesoporous graphitic carbon nanodisks fabricated via catalytic carbonization of coordination polymers, Chem. Commun. 48 (2012) 8769–8771. https://doi.org/10.1039/c2cc34234k.

[193] X. Yan, X. Li, Z. Yan, S. Komarneni, Porous carbons prepared by direct carbonization of MOFs for supercapacitors, Appl. Surf. Sci. 308 (2014) 306–310. https://doi.org/10.1016/j.apsusc.2014.04.160.

[194] J.K. Sun, Q. Xu, From metal-organic framework to carbon: Toward controlled hierarchical pore structures via a double-template approach, Chem. Commun. 50 (2014) 13502–13505. https://doi.org/10.1039/c4cc06212d.

[195] E.K. Heidari, A. Kamyabi-gol, M.H. Sohi, A. Ataie, Electrode Materials for Lithium Ion Batteries : A Review, 51 (2018) 1–12. https://doi.org/10.22059/JUFGNSM.2018.01.01.

[196] B. N, D. H, Review on Synthesis, Characterizations, and Electrochemical Properties of Cathode Materials for Lithium Ion Batteries, J. Mater. Sci. Eng. 5 (2016). https://doi.org/10.4172/2169-0022.1000258.

[197] N. Nitta, F. Wu, J.T. Lee, G. Yushin, Li-ion battery materials: Present and future, Mater. Today. 18 (2015) 252–264. https://doi.org/10.1016/j.mattod.2014.10.040.

[198] X. Chen, W. Shen, T.T. Vo, Z. Cao, A. Kapoor, An overview of lithium-ion batteries for electric vehicles, in: 10th Int. Power Energy Conf. IPEC 2012, 2012: pp. 230–235. https://doi.org/10.1109/ASSCC.2012.6523269.

[199] C.M. Julien, A. Mauger, K. Zaghib, H. Groult, Comparative issues of cathode materials for Li-ion batteries, Inorganics. 2 (2014) 132–154. https://doi.org/10.3390/inorganics2010132.

[200] B. N, D. H, Review on Synthesis, Characterizations, and Electrochemical Properties of Cathode Materials for Lithium Ion Batteries, J. Mater. Sci. Eng. 5 (2016). https://doi.org/10.4172/2169-0022.1000258.

[201] G. Griffiths, Review of developments in lithium secondary battery technology, Underw. Technol. 33 (2016) 153–163. https://doi.org/10.3723/ut.33.153.

[202] D. Liu, W. Zhu, J. Trottier, C. Gagnon, F. Barray, A. Guerfi, A. Mauger, H. Groult, C.M. Julien, J.B. Goodenough, K. Zaghib, Spinel materials for high-voltage cathodes in

Li-ion batteries, RSC Adv. 4 (2014) 154–167. https://doi.org/10.1039/c3ra45706k.

[203] X. Yuan, H. Liu, J. Zhang, Lithium-ion batteries: advanced materials and technologies, 2011. https://books.google.com/books?hl=en&lr=&id=uruKWWpWYewC&oi=fnd&pg=PP1&dq=Lithium-ion+batteries:+advanced+materials+and+technologies.&ots=Tlms8pC3S-&sig=LbXB3VKF08GAzkuu7mOrmFODXaA (accessed May 29, 2021).

[204] BU-216: Summary Table of Lithium-based Batteries – Battery University, (n.d.). https://batteryuniversity.com/learn/article/bu_216_summary_table_of_lithium_based_batteries (accessed May 28, 2021).

[205] Lithium Batteries, Materials & Compound Market Research Report 2023, (n.d.). https://www.bccresearch.com/market-research/fuel-cell-and-battery-technologies/lithium-batteries.html (accessed May 28, 2021).

[206] L. Lu, X. Han, J. Li, J. Hua, M. Ouyang, A review on the key issues for lithium-ion battery management in electric vehicles, J. Power Sources. 226 (2013) 272–288. https://doi.org/10.1016/j.jpowsour.2012.10.060.

[207] P. Ribière, S. Grugeon, M. Morcrette, S. Boyanov, S. Laruelle, G. Marlair, Investigation on the fire-induced hazards of Li-ion battery cells by fire calorimetry, Energy Environ. Sci. 5 (2012) 5271–5280. https://doi.org/10.1039/c1ee02218k.

[208] M.M. Archuleta, Toxicity of materials used in the manufacture of lithium batteries, J. Power Sources. 54 (1995) 138–142. https://doi.org/10.1016/0378-7753(94)02054-7.

[209] D. Lisbona, T. Snee, A review of hazards associated with primary lithium and lithium-ion batteries, Process Saf. Environ. Prot. 89 (2011) 434–442.

https://doi.org/10.1016/j.psep.2011.06.022.

[210] X. Zeng, J. Li, N. Singh, Recycling of Spent Lithium-Ion Battery: A Critical Review, Crit. Rev. Environ. Sci. Technol. 44 (2014) 1129–1165. https://doi.org/10.1080/10643389.2013.763578.

[211] C.K. Lee, K.I. Rhee, Preparation of LiCoO2 from spent lithium-ion batteries, J. Power Sources. 109 (2002) 17–21. https://doi.org/10.1016/S0378-7753(02)00037-X.

[212] M. Zhang, J. Du, L. Liu, A. Stefanopoulou, J. Siegel, L. Lu, X. He, X. Xie, M. Ouyang, Internal Short Circuit Trigger Method for Lithium-Ion Battery Based on Shape Memory Alloy, J. Electrochem. Soc. 164 (2017) A3038–A3044. https://doi.org/10.1149/2.0731713jes.

[213] D. Ren, X. Feng, L. Lu, M. Ouyang, S. Zheng, J. Li, X. He, An electrochemical-thermal coupled overcharge-to-thermal-runaway model for lithium ion battery, J. Power Sources. 364 (2017) 328–340. https://doi.org/10.1016/j.jpowsour.2017.08.035.

[214] E. Cabrera-Castillo, F. Niedermeier, A. Jossen, Calculation of the state of safety (SOS) for lithium ion batteries, J. Power Sources. 324 (2016) 509–520. https://doi.org/10.1016/j.jpowsour.2016.05.068.

[215] S. Koch, A. Fill, K.P. Birke, Comprehensive gas analysis on large scale automotive lithium-ion cells in thermal runaway, J. Power Sources. 398 (2018) 106–112. https://doi.org/10.1016/j.jpowsour.2018.07.051.

[216] X. Feng, J. Sun, M. Ouyang, F. Wang, X. He, L. Lu, H. Peng, Characterization of penetration induced thermal runaway propagation process within a large format lithium ion battery module, J. Power Sources. 275 (2015) 261–273. https://doi.org/10.1016/j.jpowsour.2014.11.017.

[217] T. Yokoshima, D. Mukoyama, F. Maeda, T. Osaka, K. Takazawa, S. Egusa, S. Naoi, S. Ishikura, K. Yamamoto, Direct observation of internal state of thermal runaway in lithium ion battery during nail-penetration test, J. Power Sources. 393 (2018) 67–74. https://doi.org/10.1016/j.jpowsour.2018.04.092.

[218] B. Mao, H. Chen, Z. Cui, T. Wu, Q. Wang, Failure mechanism of the lithium ion battery during nail penetration, Int. J. Heat Mass Transf. 122 (2018) 1103–1115. https://doi.org/10.1016/j.ijheatmasstransfer.2018.02.036.

[219] M. Vanitha, N. Balasubramanian, Waste minimization and recovery of valuable metals from spent lithium-ion batteries–a review, Environ. Technol. Rev. 2 (2013) 101–115. https://doi.org/10.1080/21622515.2013.853105.

[220] X. Wang, G. Gaustad, C.W. Babbitt, Targeting high value metals in lithium-ion battery recycling via shredding and size-based separation, Waste Manag. 51 (2016) 204–213. https://doi.org/10.1016/j.wasman.2015.10.026.

[221] M.M. Wang, C.C. Zhang, F.S. Zhang, Recycling of spent lithium-ion battery with polyvinyl chloride by mechanochemical process, Waste Manag. 67 (2017) 232–239. https://doi.org/10.1016/j.wasman.2017.05.013.

[222] X. Zheng, Z. Zhu, X. Lin, Y. Zhang, Y. He, H. Cao, Z. Sun, A Mini-Review on Metal Recycling from Spent Lithium Ion Batteries, Engineering. 4 (2018) 361–370. https://doi.org/10.1016/j.eng.2018.05.018.

[223] F. Wang, T. Zhang, Y. He, Y. Zhao, S. Wang, G. Zhang, Y. Zhang, Y. Feng, Recovery of valuable materials from spent lithium-ion batteries by mechanical separation and thermal treatment, J. Clean. Prod. 185 (2018) 646–652. https://doi.org/10.1016/j.jclepro.2018.03.069.

[224] J. Xiao, J. Li, Z. Xu, Novel Approach for in Situ Recovery of Lithium Carbonate from Spent Lithium Ion Batteries Using Vacuum Metallurgy, Environ. Sci. Technol. 51 (2017) 11960–11966. https://doi.org/10.1021/acs.est.7b02561.

[225] N.E.A. Latif, A.M. Ahmed, Recovery of Cobalt and Lithium from Spent Lithium Ion Batteries, 2017.

[226] F. Saloojee, J. Lloyd, CRUNDWELL MANAGEMENT SOLUTIONS (PTY) LTD, t/a CM SOLUTIONS (PTY) LTD LITHIUM BATTERY RECYCLING PROCESS Desktop Study, 2014. https://www.sagreenfund.org.za/wordpress/wp-content/uploads/2015/07/Lithium-Battery-Recycling-Literature-Review-CM-Solutions.pdf (accessed May 28, 2021).

[227] A.A. Nayl, R.A. Elkhashab, S.M. Badawy, M.A. El-Khateeb, Acid leaching of mixed spent Li-ion batteries, Arab. J. Chem. 10 (2017) S3632–S3639. https://doi.org/10.1016/j.arabjc.2014.04.001.

[228] D. Song, X. Wang, E. Zhou, P. Hou, F. Guo, L. Zhang, Recovery and heat treatment of the Li(Ni1/3Co 1/3Mn1/3)O2 cathode scrap material for lithium ion battery, J. Power Sources. 232 (2013) 348–352. https://doi.org/10.1016/j.jpowsour.2012.10.072.

[229] J. Senćanski, D. Bajuk-Bogdanović, D.M.-J. of P., undefined 2017, The synthesis of Li (CoMnNi) O2 cathode material from spent-Li ion batteries and the proof of its functionality in aqueous lithium and sodium electrolytic, Elsevier. (n.d.). https://www.sciencedirect.com/science/article/pii/S0378775316318183?casa_token=unK_kWbWGIsAAAAA:dgPCoeaZRCcKeUltabXYurjIoXtaQr1qJ0E8WYvcSTwzorrVNJNFHjyKmdLeGQy32kAxGII4 (accessed May 28, 2021).

[230] L.P. He, S.Y. Sun, X.F. Song, J.G. Yu, Recovery of cathode materials and Al from spent lithium-ion batteries by ultrasonic cleaning, Waste Manag. 46 (2015) 523–528.

https://doi.org/10.1016/j.wasman.2015.08.035.

[231] Y. Yang, G. Huang, S. Xu, Y. He, X. Liu, Thermal treatment process for the recovery of valuable metals from spent lithium-ion batteries, Hydrometallurgy. 165 (2016) 390–396. https://doi.org/10.1016/j.hydromet.2015.09.025.

[232] A. Nasser, U. Mingelgrin, Mechanochemistry: A review of surface reactions and environmental applications, Appl. Clay Sci. 67–68 (2012) 141–150. https://doi.org/10.1016/j.clay.2011.11.018.

[233] P. Baláž, A. Aláčová, M. Achimovičová, J. Ficeriová, E. Godočíková, Mechanochemistry in hydrometallurgy of sulphide minerals, in: Hydrometallurgy, Elsevier, 2005: pp. 9–17. https://doi.org/10.1016/j.hydromet.2004.09.009.

[234] P. Baláž, E. Dutková, Fine milling in applied mechanochemistry, Miner. Eng. 22 (2009) 681–694. https://doi.org/10.1016/j.mineng.2009.01.014.

[235] X. Guo, D. Xiang, G. Duan, P. Mou, A review of mechanochemistry applications in waste management, Waste Manag. 30 (2010) 4–10. https://doi.org/10.1016/j.wasman.2009.08.017.

[236] M.M. Wang, C.C. Zhang, F.S. Zhang, An environmental benign process for cobalt and lithium recovery from spent lithium-ion batteries by mechanochemical approach, Waste Manag. 51 (2016) 239–244. https://doi.org/10.1016/j.wasman.2016.03.006.

[237] J.S. Sohn, S.M. Shin, D.H. Yang, S.K. Kim, C.K. Lee, Comparison of two acidic leaching processes for selecting the effective recycle process of spent lithium ion battery, Geosystem Eng. 9 (2006) 1–6. https://doi.org/10.1080/12269328.2006.10541246.

[238] M. Joulié, R. Laucournet, E. Billy, Hydrometallurgical process for the recovery of high value metals from spent lithium nickel cobalt aluminum oxide based lithium-ion

batteries, J. Power Sources. 247 (2014) 551–555. https://doi.org/10.1016/j.jpowsour.2013.08.128.

[239] M. Contestabile, S. Panero, B. Scrosati, Laboratory-scale lithium-ion battery recycling process, J. Power Sources. 92 (2001) 65–69. https://doi.org/10.1016/S0378-7753(00)00523-1.

[240] L. Li, J. Lu, L. Zhai, X. Zhang, L. Curtiss, Y. Jin, F. Wu, R. Chen, K. Amine, A facile recovery process for cathodes from spent lithium iron phosphate batteries by using oxalic acid, CSEE J. Power Energy Syst. 4 (2018) 219–225. https://doi.org/10.17775/cseejpes.2016.01880.

[241] X. Chen, L. Cao, D. Kang, J. Li, T. Zhou, H. Ma, Recovery of valuable metals from mixed types of spent lithium ion batteries. Part II: Selective extraction of lithium, Waste Manag. 80 (2018) 198–210. https://doi.org/10.1016/j.wasman.2018.09.013.

[242] D. Dutta, A. Kumari, R. Panda, S. Jha, D. Gupta, S. Goel, M.K. Jha, Close loop separation process for the recovery of Co, Cu, Mn, Fe and Li from spent lithium-ion batteries, Sep. Purif. Technol. 200 (2018) 327–334. https://doi.org/10.1016/j.seppur.2018.02.022.

[243] J. Xu, H.R. Thomas, R.W. Francis, K.R. Lum, J. Wang, B. Liang, A review of processes and technologies for the recycling of lithium-ion secondary batteries, J. Power Sources. 177 (2008) 512–527. https://doi.org/10.1016/j.jpowsour.2007.11.074.

[244] W.S. Chen, H.J. Ho, Recovery of valuable metals from lithium-ion batteries NMC cathode waste materials by hydrometallurgical methods, Metals (Basel). 8 (2018). https://doi.org/10.3390/met8050321.

[245] Y. Zou, C. Zhang, X. Ju, Z. Wang, Y. Wu, J. Yuan, W. Chen, R. He, Effect of removing

cadmium with citric acid on the physicochemical and microstructure properties of rice bran, Food Control. 98 (2019) 290–296. https://doi.org/10.1016/j.foodcont.2018.11.044.

[246] J. Li, X. Yang, Z. Yin, Recovery of manganese from sulfuric acid leaching liquor of spent lithium-ion batteries and synthesis of lithium ion-sieve, J. Environ. Chem. Eng. 6 (2018) 6407–6413. https://doi.org/10.1016/j.jece.2018.09.044.

[247] L. Li, Y. Bian, X. Zhang, Q. Xue, E. Fan, F. Wu, R. Chen, Economical recycling process for spent lithium-ion batteries and macro- and micro-scale mechanistic study, J. Power Sources. 377 (2018) 70–79. https://doi.org/10.1016/j.jpowsour.2017.12.006.

[248] L. Li, E. Fan, Y. Guan, X. Zhang, Q. Xue, L. Wei, F. Wu, R. Chen, Sustainable Recovery of Cathode Materials from Spent Lithium-Ion Batteries Using Lactic Acid Leaching System, ACS Sustain. Chem. Eng. 5 (2017) 5224–5233. https://doi.org/10.1021/acssuschemeng.7b00571.

[249] W. Xiang, Y. Tang, Y.Y. Wang, B.H. Zhong, W.M. Fang, H. Liu, X.D. Guo, Influence of pH value and chelating reagent on performance of Li 3V2(PO4)3/C cathode material, Trans. Nonferrous Met. Soc. China (English Ed. 23 (2013) 1395–1402. https://doi.org/10.1016/S1003-6326(13)62609-6.

[250] H. Liu, Y.P. Wu, E. Rahm, R. Holze, H.Q. Wu, Cathode materials for lithium ion batteries prepared by sol-gel methods, J. Solid State Electrochem. 8 (2004) 450–466. https://doi.org/10.1007/s10008-004-0521-1.

[251] R. Qadir, F. Gulshan, Reclamation of Lithium Cobalt Oxide from Waste Lithium Ion Batteries to Be Used as Recycled Active Cathode Materials, Mater. Sci. Appl. 09 (2018) 142–154. https://doi.org/10.4236/msa.2018.91010.

[252] Q. Meng, Y. Zhang, P. Dong, A combined process for cobalt recovering and cathode material regeneration from spent LiCoO2 batteries: Process optimization and kinetics aspects, Waste Manag. 71 (2018) 372–380. https://doi.org/10.1016/j.wasman.2017.10.030.

[253] Y. Weng, S. Xu, G. Huang, C. Jiang, Synthesis and performance of Li[(Ni1/3Co1/3Mn1/3)1-xMgx]O2 prepared from spent lithium ion batteries, J. Hazard. Mater. 246–247 (2013) 163–172. https://doi.org/10.1016/j.jhazmat.2012.12.028.

[254] X. Meng, J. Hao, H. Cao, X. Lin, P. Ning, X. Zheng, J. Chang, X. Zhang, B. Wang, Z. Sun, Recycling of LiNi1/3Co1/3Mn1/3O2 cathode materials from spent lithium-ion batteries using mechanochemical activation and solid-state sintering, Waste Manag. 84 (2019) 54–63. https://doi.org/10.1016/j.wasman.2018.11.034.

[255] W. Yan, L.J. Han, H.L. Jia, K. Shen, T. Wang, H.G. Zheng, Three Highly Stable Cobalt MOFs Based on “y”-Shaped Carboxylic Acid: Synthesis and Absorption of Anionic Dyes, Inorg. Chem. 55 (2016) 8816–8821. https://doi.org/10.1021/acs.inorgchem.6b01328.

[256] G. Sargazi, D. Afzali, A. Ghafainazari, H. Saravani, Rapid Synthesis of Cobalt Metal Organic Framework, J. Inorg. Organomet. Polym. Mater. 24 (2014) 786–790. https://doi.org/10.1007/s10904-014-0042-z.

[257] I. Strauss, A. Mundstock, M. Treger, K. Lange, S. Hwang, C. Chmelik, P. Rusch, N.C. Bigall, T. Pichler, H. Shiozawa, J. Caro, Metal-Organic Framework Co-MOF-74-Based Host-Guest Composites for Resistive Gas Sensing, ACS Appl. Mater. Interfaces. 11 (2019) 14175–14181. https://doi.org/10.1021/acsami.8b22002.

[258] O.M. Yaghi, H. Li, T.L. Groy, Construction of porous solids from hydrogen-bonded metal complexes of 1,3,5-benzenetricarboxylic acid, J. Am. Chem. Soc. 118 (1996)

9096–9101. https://doi.org/10.1021/ja960746q.

[259] M. Ranjbar, M.A. Taher, A. Sam, Facile hydrothermal synthesis of manganese-metal organic framework nanostructures in the presence of various organic ligands for SO2 and CO_2 gas adsorption, J. Porous Mater. 23 (2016) 375–380. https://doi.org/10.1007/s10934-015-0090-y.

[260] K. Vellingiri, D.C.W. Tsang, K.H. Kim, A. Deep, T. Dutta, D.W. Boukhvalov, The utilization of zinc recovered from alkaline battery waste as metal precursor in the synthesis of metal-organic framework, J. Clean. Prod. 199 (2018) 995–1006. https://doi.org/10.1016/j.jclepro.2018.07.233.

[261] E. Perez, R. Navarro Amador, M. Carboni, D. Meyer, In-situ precipitation of Metal-Organic Frameworks from a simulant battery waste solution, Mater. Lett. 167 (2016) 188–191. https://doi.org/10.1016/j.matlet.2015.12.129.

[262] X. Zhang, A. Chen, M. Zhong, Z. Zhang, X. Zhang, Z. Zhou, X.-H. Bu, Metal–Organic Frameworks (MOFs) and MOF-Derived Materials for Energy Storage and Conversion, Electrochem. Energy Rev. 2 (2019) 29–104. https://doi.org/10.1007/s41918-018-0024-x.

[263] Y. Zhang, Y. Bin Niu, T. Liu, Y.T. Li, M.Q. Wang, J. Hou, M. Xu, A nickel-based metal-organic framework: A novel optimized anode material for Li-ion batteries, Mater. Lett. 161 (2015) 712–715. https://doi.org/10.1016/j.matlet.2015.09.079.

[264] T. An, Y. Wang, J. Tang, Y. Wang, L. Zhang, G. Zheng, A flexible ligand-based wavy layered metal-organic framework for lithium-ion storage, J. Colloid Interface Sci. 445 (2015) 320–325. https://doi.org/10.1016/j.jcis.2015.01.012.

[265] L. Gou, L.M. Hao, Y.X. Shi, S.L. Ma, X.Y. Fan, L. Xu, D.L. Li, K. Wang, One-pot

synthesis of a metal-organic framework as an anode for Li-ion batteries with improved capacity and cycling stability, J. Solid State Chem. 210 (2014) 121–124. https://doi.org/10.1016/j.jssc.2013.11.014.

[266] X. Hu, H. Hu, C. Li, T. Li, X. Lou, Q. Chen, B. Hu, Cobalt-based metal organic framework with superior lithium anodic performance, J. Solid State Chem. 242 (2016) 71–76. https://doi.org/10.1016/j.jssc.2016.07.021.

[267] S. Maiti, A. Pramanik, U. Manju, S. Mahanty, Reversible Lithium Storage in Manganese 1,3,5-Benzenetricarboxylate Metal-Organic Framework with High Capacity and Rate Performance, ACS Appl. Mater. Interfaces. 7 (2015) 16357–16363. https://doi.org/10.1021/acsami.5b03414.

[268] H. Hu, X. Lou, C. Li, X. Hu, T. Li, Q. Chen, M. Shen, B. Hu, A thermally activated manganese 1,4-benzenedicarboxylate metal organic framework with high anodic capability for Li-ion batteries, New J. Chem. 40 (2016) 9746–9752. https://doi.org/10.1039/c6nj02179d.

[269] X. Li, F. Cheng, S. Zhang, J. Chen, Shape-controlled synthesis and lithium-storage study of metal-organic frameworks Zn4O(1,3,5-benzenetribenzoate)2, J. Power Sources. 160 (2006) 542–547. https://doi.org/10.1016/j.jpowsour.2006.01.015.

[270] B. Tang, S. Huang, Y. Fang, J. Hu, C. Malonzo, D.G. Truhlar, A. Stein, Mechanism of electrochemical lithiation of a metal-organic framework without redox-active nodes, J. Chem. Phys. 144 (2016) 194702. https://doi.org/10.1063/1.4948706.

[271] G. Férey, F. Millange, M. Morcrette, C. Serre, M.L. Doublet, J.M. Grenèche, J.M. Tarascon, Mixed-valence Li/Fe-based metal-organic frameworks with both reversible redox and sorption properties, Angew. Chemie - Int. Ed. 46 (2007) 3259–3263. https://doi.org/10.1002/anie.200605163.

[272] C. Combelles, M. Ben Yahia, L. Pedesseau, M.L. Doublet, Design of electrode materials for lithium-ion batteries: The example of metal-organic frameworks, J. Phys. Chem. C. 114 (2010) 9518–9527. https://doi.org/10.1021/jp1016455.

[273] Y. Wang, Q. Qu, G. Liu, V.S. Battaglia, H. Zheng, Aluminum fumarate-based metal organic frameworks with tremella-like structure as ultrafast and stable anode for lithium-ion batteries, Nano Energy. 39 (2017) 200–210. https://doi.org/10.1016/j.nanoen.2017.06.007.

[274] Sedres, G. (2016). Recovery of SiO2 and Al2O3 from... - Google Scholar, (n.d.). https://scholar.google.com/scholar?hl=en&as_sdt=0%2C5&q=Sedres%2C+G.+%282016%29.+Recovery+of+SiO2+and+Al2O3+from+coal+fly+ash+%28Masters+Dissertation%2C+University+of+Western+Cape%2C+South+Africa%29.+Retrieved+from+https%3A%2F%2Fetd.uwc.ac.za%2Fbitstream%2Fhandle%2F11394%2F5651%2FSedras_g_msc_ns_2016&btnG= (accessed May 28, 2021).

[275] J. Dechnik, C. Janiak, S.D.-J. of hazardous materials, undefined 2016, Aluminium fumarate metal-organic framework: a super adsorbent for fluoride from water, Elsevier. (n.d.). https://www.sciencedirect.com/science/article/pii/S0304389415301588?casa_token=uDL61SYwASAAAAAA:xWJgf3DYf_v82uIaiSZKmOz7X62gcw2VvPVBQuHAr8rywN-z_ZUaYLPMBTUxmYQs6zysRrf0 (accessed May 28, 2021).

[276] R. Cherrington, J.L.-D. and M. of Plastic, undefined 2015, 2 Materials and Deposition Processes for Multifunctionality, Books.Google.Com. (n.d.). https://books.google.com/books?hl=en&lr=&id=RzROBQAAQBAJ&oi=fnd&pg=PA19&dq=Materials+and+Deposition+Processes+for+Multifunctionality&ots=RNNQbQCQ_h&sig=C8hGP8FlKOn1Izw6Ju4Tj196zd8 (accessed May 29, 2021).

[277] W. Zhou, R. Apkarian, Z.L. Wang, D. Joy, Fundamentals of scanning electron microscopy (SEM), in: Scanning Microsc. Nanotechnol. Tech. Appl., Springer New York, 2007: pp. 1–40. https://doi.org/10.1007/978-0-387-39620-0_1.

[278] A.E. Vladár, M.T. Postek, The Scanning Electron Microscope *, in: Handb. Charg. Part. Opt., CRC Press, 2017: pp. 437–496. https://doi.org/10.1201/9781420045550-9.

[279] O.D. Neikov, N.A. Yefimov, Powder Characterization and Testing, in: Handb. Non-Ferrous Met. Powders, Elsevier, 2019: pp. 3–62. https://doi.org/10.1016/b978-0-08-100543-9.00001-4.

[280] A.K. Singh, Experimental Methodologies for the Characterization of Nanoparticles, in: Eng. Nanoparticles, Elsevier, 2016: pp. 125–170. https://doi.org/10.1016/b978-0-12-801406-6.00004-2.

[281] A.A. Bunaciu, E. Gabriela Udriştioiu, H.Y. Aboul-Enein, E.G. Udri¸stioiuudri¸ Udri¸stioiu, Critical Reviews in Analytical Chemistry X-Ray Diffraction: Instrumentation and Applications X-Ray Diffraction: Instrumentation and Applications, Crit. Rev. Anal. Chem. 45 (2015) 289–299. https://doi.org/10.1080/10408347.2014.949616.

[282] J. Epp, X-Ray Diffraction (XRD) Techniques for Materials Characterization, in: Mater. Charact. Using Nondestruct. Eval. Methods, Elsevier Inc., 2016: pp. 81–124. https://doi.org/10.1016/B978-0-08-100040-3.00004-3.

[283] J. Patel, … P.P.B.P., undefined 2018, Biodegradable and Biocompatible Polymer Composites, n.d. http://repository.um-palembang.ac.id/id/eprint/9233/1/Biodegradable and Biocompatible Polymer Composites Processing%2C Properties and Applications %28 PDFDrive.com %29.pdf#page=80 (accessed May 29, 2021).

[284] W.M. Doyle, Principles and Applications of Fourier Transform Infra-red (FTIR) Process Analysis, (2017).

[285] N. Jaggi, D.R. Vij, FOURIER TRANSFORM INFRARED SPECTROSCOPY, in: Handb. Appl. Solid State Spectrosc., Springer US, Boston, MA, n.d.: pp. 411–450. https://doi.org/10.1007/0-387-37590-2_9.

[286] D. Titus, E. James Jebaseelan Samuel, S.M. Roopan, Nanoparticle characterization techniques, in: Green Synth. Charact. Appl. Nanoparticles, Elsevier, 2019: pp. 303–319. https://doi.org/10.1016/b978-0-08-102579-6.00012-5.

[287] G. BR, Application of Scanning Electron Microscopy and Fourier-Transform Infrared Spectroscopy to Study Surface Design and Chemical Group Components of Merino Wool, Paschmina and Angora Fibers, Curr. Trends Fash. Technol. Text. Eng. 3 (2018). https://doi.org/10.19080/ctftte.2018.03.555607.

[288] Z.W. Chen, W.M. Gibson, H. Huang, High Definition X-Ray Fluorescence: Principles and Techniques, Downloads.Hindawi.Com. 10 (2008). https://doi.org/10.1155/2008/318171.

[289] A. Markowicz, An overview of quantificationmethods in energy-dispersive X-ray fluorescence analysis, Pramana - J. Phys. 76 (2011) 321–329. https://doi.org/10.1007/s12043-011-0045-z.

[290] K. Janssens, F. Adams, A. Rindby, Microscopic X-ray fluorescence analysis, 2000. https://analyticalscience.wiley.com/do/10.1002/sepspec.9780471974260 (accessed May 28, 2021).

[291] O. Olubiyi, F. Lu, D. Calligaris, F.J.-…-G. Neurosurgery, undefined 2015, Advances in molecular imaging for surgery, Elsevier. (n.d.).

https://www.sciencedirect.com/science/article/pii/B9780128008706000170 (accessed May 28, 2021).

[292] P. Vandenabeele, Practical Raman Spectroscopy - An Introduction, John Wiley & Sons, Ltd, 2013. https://doi.org/10.1002/9781119961284.

[293] P.G. Zambonin, E. Desimoni, X-Ray Photoelectron Spectroscopy: Principles, Instrumentation, Data Processing and Molten Salt Applications, in: Molten Salt Chem., Springer Netherlands, 1987: pp. 425–445. https://doi.org/10.1007/978-94-009-3863-2_21.

[294] G. Greczynski, L.H.-P. in M. Science, undefined 2020, X-ray photoelectron spectroscopy: Towards reliable binding energy referencing, Elsevier. (n.d.). https://www.sciencedirect.com/science/article/pii/S0079642519300738 (accessed May 28, 2021).

[295] P. Gabbott, Principles and Applications of Thermal Analysis, Blackwell Publishing Ltd, 2008. https://doi.org/10.1002/9780470697702.

[296] G. Fagerlund, Determination of specific surface by the BET method, Matériaux Constr. 6 (1973) 239–245. https://doi.org/10.1007/BF02479039.

[297] J. H. De Boer, The structure and properties of porous... - Google Scholar, (n.d.). https://scholar.google.com/scholar?hl=en&as_sdt=0%2C5&q=J.+H.+De+Boer%2C+The+structure+and+properties+of+porous+materials%3B+Butterworth+%26+Co+Publishers+Ltd%3A+London%2C+1958%2C+pp.68–94&btnG= (accessed May 28, 2021).

[298] P. Liu, L. Xiao, Y. Tang, Y. Zhu, H. Chen, Y.C.- Vacuum, undefined 2018, Resynthesis and electrochemical performance of LiNi0. 5Co0. 2Mn0. 3O2 from spent cathode material of lithium-ion batteries, Elsevier. (n.d.).

https://www.sciencedirect.com/science/article/pii/S0042207X18310406?casa_token=GnOYD3XsWuIAAAAA:tDcv0Yi0X2Tvlzvd-pkyfyGwLP-pISjqcBY21C4BdjRGYnrAMIVX6Maf5lYRW4KQrKtqqcaU (accessed May 28, 2021).

[299] G. Wang, P. Jensen, H. Wu, F.F.- Fuel, undefined 2019, KOH capture by coal fly ash, Elsevier. (n.d.). https://www.sciencedirect.com/science/article/pii/S0016236118321574?casa_token=V1QevtqqlDYAAAAA:Py4RRTFJ3lVBPzecY1LBd8-vPi0XuZvTH49ejN53mk0Xq2i0_WT8fbZ1dmj2g-jiZGkYCCFa (accessed May 28, 2021).

[300] N. Wagner, A.M.-I.J. of C. Geology, undefined 2018, Rare earth elements in select Main Karoo Basin (South Africa) coal and coal ash samples, Elsevier. (n.d.). https://www.sciencedirect.com/science/article/pii/S0166516218301708?casa_token=q04V2UfGRXAAAAAA:m31UbbgLIV0jO9cjWJV7wprUM-ci3nhdCJ8GCmJqUw5Ig9FPn3i75nxrX6UlYhUZWDpT9BBX (accessed May 28, 2021).

[301] S. Wang, H.W.-J. of hazardous materials, undefined 2006, Environmental-benign utilisation of fly ash as low-cost adsorbents, Elsevier. (n.d.). https://www.sciencedirect.com/science/article/pii/S0304389406000690?casa_token=UDT7Sjd9OqgAAAAA:PafI69SV2tbDKySFMd02-x_JucGBrDKZ5DenHGHKUvm5MkzC2q0OTN6h9G39W_9cvZ0DKIvm (accessed May 28, 2021).

[302] B. Lokeshappa, A.D.-A. Procedia, undefined 2012, Behaviour of metals in coal fly ash ponds, Elsevier. (n.d.).

https://www.sciencedirect.com/science/article/pii/S2212670812000085 (accessed May 28, 2021).

[303] G. Singh, S. Kumar, M. Singh, S.M. journal of, undefined 2016, Environmental impact assessment of ash disposal system of a thermal power plant, Elsevier. (n.d.). https://www.sciencedirect.com/science/article/pii/S036031991631000X?casa_token=ng4-dL04718AAAAA:WUmzfEB08EfBFs7brUVG1V-2gksUL6yycI2GtmhFKTVcEgBLzovfD-EpJDa0SSHyyDtP1OM4 (accessed May 28, 2021).

[304] D.K. Gupta, U.N. Rai, R.D. Tripathi, D.K. Gupta, • M Inouhe, • U N Rai, • R D Tripathi, S. Jpn, S. -Verlagminireview, Impacts of fly-ash on soil and plant responses, MINIREVIEW J Plant Res. 115 (2002) 401–409. https://doi.org/10.1007/s10265-002-0057-3.

[305] W. Franus, M.M. Wiatros-Motyka, M. Wdowin, Coal fly ash as a resource for rare earth elements, Environ. Sci. Pollut. Res. 22 (2015) 9464–9474. https://doi.org/10.1007/s11356-015-4111-9.

[306] A. Chatterjee, X. Hu, F.L.-C. Today, undefined 2018, Catalytic activity of an economically sustainable fly-ash-metal-organic-framework composite towards biomass valorization, Elsevier. (n.d.). https://www.sciencedirect.com/science/article/pii/S092058611830018X?casa_token=JZYB0ckMe_YAAAAA:hZJO8My7poHtxbMaAbSD8XO9wZYcEg-fCQ44J4fS_cUii825Md3PcSIv0J52Yf0bzokOB2Bi (accessed May 28, 2021).

[307] X. Yan, X. Li, Z. Yan, S.K.-A. surface science, undefined 2014, Porous carbons prepared by direct carbonization of MOFs for supercapacitors, Elsevier. (n.d.). https://www.sciencedirect.com/science/article/pii/S0169433214009362?casa_token=

WEBm-tGbKLQAAAAA:agen2OCyUdjIpJ8_wForKN-Alf9OcOAWcuf86_BKWQfDwvSopcobrHWk8ek1iRKePiWciN6H (accessed May 28, 2021).

[308] M. Fu, W. Chen, J. Ding, X. Zhu, Q.L.-J. of A. and Compounds, undefined 2019, Biomass waste derived multi-hierarchical porous carbon combined with CoFe2O4 as advanced electrode materials for supercapacitors, Elsevier. (n.d.). https://www.sciencedirect.com/science/article/pii/S092583881834800X?casa_token=vXzB4XsO95cAAAAA:OuaT26FYWcKqi6WQ1_CgOGoxjCel4U1yxrdkjcmJow_b56qmz0TiDiDG2B9RlaEFk2z-apAt (accessed May 28, 2021).

[309] C. Ma, J. Min, J. Gong, X. Liu, X. Mu, X. Chen, T.T.- Chemosphere, undefined 2020, Transforming polystyrene waste into 3D hierarchically porous carbon for high-performance supercapacitors, Elsevier. (n.d.). https://www.sciencedirect.com/science/article/pii/S0045653520309486?casa_token=20rbkQLVCT0AAAAA:qXz0Ml2mhAY4bH8gZNkq9U3ZVqbq0lERbHTRjDZa9-B2nN5CCd0c4gfz2cHmqLkhzES2Fjyq (accessed May 28, 2021).

[310] L. Li, C. Jia, X. Zhu, S.Z.-J. of C. Production, undefined 2020, Utilization of cigarette butt waste as functional carbon precursor for supercapacitors and adsorbents, Elsevier. (n.d.). https://www.sciencedirect.com/science/article/pii/S0959652620303735?casa_token=Dm_5NhnKWNgAAAAA:bu9epeGSJkilAadA9tE_q_9BTar-sToKW5zuRW0Hy5MGOLq5fJUKURZT2XphAHCIz2hO4yvd (accessed May 28, 2021).

[311] B. Xu, Y. Chen, G. Wei, G. Cao, … H.Z.-M.C. and, undefined 2010, Activated carbon with high capacitance prepared by NaOH activation for supercapacitors, Elsevier. (n.d.).

https://www.sciencedirect.com/science/article/pii/S025405841000533X?casa_token=fwEVPU8O7okAAAAA:cRrOgwYsh4wV0e9f8h3CrTDs_rE7Mqzgfgm4O5enI6hGFKtt1mlcOGF93x4fYvxqq9k_ELiX (accessed May 28, 2021).

[312] T. Rufford, D. Hulicova-Jurcakova, … K.K.-J. of P., undefined 2010, Microstructure and electrochemical double-layer capacitance of carbon electrodes prepared by zinc chloride activation of sugar cane bagasse, Elsevier. (n.d.). https://www.sciencedirect.com/science/article/pii/S0378775309014372?casa_token=N-fXuSdtfzwAAAAA:81nyMsSlwXi9ZDicdmqHmXyECa-WrF8k2i-emv2QdFIrc0p5jjEnIHyFewA8HTunxernf4Zg (accessed May 28, 2021).

[313] U. Mueller, M. Schubert, F. Teich, … H.P.-J. of M., undefined 2006, Metal–organic frameworks—prospective industrial applications, Pubs.Rsc.Org. (n.d.). https://pubs.rsc.org/en/content/articlehtml/2006/jm/b511962f?casa_token=xRvAu7veyQcAAAAA:IzfliRlRxkpfn6ODkXvpXcmzc03RCxOUt-lC3uVUoN4ziKMCeiV9qTnBTdFKT3EHx_ZVruZ85UPxnw (accessed May 28, 2021).

[314] H. Li, M. Eddaoudi, M. O'Keeffe, O.Y.- nature, undefined 1999, Design and synthesis of an exceptionally stable and highly porous metal-organic framework, Nature.Com. (n.d.). https://idp.nature.com/authorize/casa?redirect_uri=https://www.nature.com/articles/46248&casa_token=ypuXDNLAR_YAAAAA:aF_ofCnlHq9rQtJBBmysjQ0kklphvu6BmBXhvxDsDisT5ue30YqbAZ9rO-laVAfLFY8XFkKZ5sVSHZfJ (accessed May 28, 2021).

[315] Y. Zhao, J. Liu, M. Horn, N. Motta, M. Hu, Y. Li, Recent advancements in metal organic framework based electrodes for supercapacitors, Sci. China Mater. 61 (2018) 159–184.

https://doi.org/10.1007/s40843-017-9153-x.